Laboratory-based Tender X-ray Emission Spectroscopy: Instrumental, Experimental, and Theoretical Advances and Application to the Study of Phosphorus and Sulfur Electronic Structure

William M. Holden

A dissertation

submitted in partial fulfillment of the

requirements for the degree of

Doctor of Philosophy

University of Washington
2019

Reading Committee:

Gerald T. Seidler, Chair

Marjorie Olmstead

Joshua J. Kas

Program Authorized to Offer Degree:

Physics

University of Washington

Abstract

Laboratory-based Tender X-ray Emission Spectroscopy: Instrumental, Experimental, and Theoretical Advances and Application to the Study of Phosphorus and Sulfur Electronic Structure

William M. Holden

Chair of the Supervisory Committee:
Professor Gerald T. Seidler
Physics

Tender x-ray emission spectroscopy (XES) is a powerful, element-specific, atomically local probe of chemical and electronic structure. Taking advantage of advances in every component of spectrometer systems including crystal analyzers, color x-ray cameras, and bremsstrahlung x-ray tubes, I designed, built, and demonstrated a new, laboratory-based tender x-ray emission spectrometer. This apparatus creates an opportunity for more widespread access to tender XES measurements, which in recent years have been largely restricted to a limited number of beamlines at synchrotron facilities. Using the developed spectrometer, I performed lab-based XES studies on phosphorus and sulfur, whose emission lines lie in the energy range of optimal performance, and are of significant experimental value due to their chemical sensitivity and the ubiquity of phosphorus and sulfur in environmental, material, and fundamental science. I conducted analytical

applications, demonstrating the speciation of phosphorus in indium phosphide quantum dots and the speciation of sulfur in biochars at low concentration. These studies illustrate the strength of P Kα XES as an alternative to solid-state nuclear magnetic resonance (SSNMR), and the ability for S Kα XES to yield information comparable and complementary to synchrotron x-ray absorption near edge structure (XANES). Supplementing these new experimental capabilities, I utilized linear-response time-dependent density functional theory (LR-TDDFT) for theoretical prediction and analysis of Kα core-to-core and Kβ valence-to-core emission lines of sulfur. The strong quantitative agreement between this theoretical approach and the observed results supports future applications in both analytical and theoretical investigations. With the establishment of these experimental and theoretical capabilities by the work in this thesis, tender XES is primed to grow into a powerful and routine analytical tool in both academia and industry.

TABLE OF CONTENTS

LIST OF FIGURES

LIST OF TABLES

ACKNOWLEDGEMENTS

My wife, Izumi, is the sturdy foundation on which this thesis was built. With her support, the last five years have been an incredible journey. It's hard to imagine the young traveler who set out on this journey looking into the fog of an unknown future, putting one foot in front of the other one step at a time in an apparent line, only to look back and see the twists and turns and stumbles clearly. It is with her steady hand and encouragement that the steps forward could continue unabated. With the publishing of this dissertation, I look forward to continuing together as we bring along this new traveler who is so far seven months in the making.

My parents, Therese and Nelson, and my brothers and sister, Steven, Jason, and Annette, are the joinery of this thesis. Behind the words of this writing is their influence and shared experience.

My advisor, Jerry, and my labmates, Evan, Alex, Oliver, Ryan, Devon, and John, are the team from which this thesis was built, both in terms of literal collaboration and in terms of motivation, shared knowledge and experience. Although my hands typed the words, they are not mine alone. This thesis is the product of our combined knowledge and collective experience, and I could not have done it without them.

I would also like to acknowledge the community at the University of Washington. I am deeply grateful to our collaborators in chemistry: Jenny, Brandi, Christine and Alexandra. Bob, Ron, and the UW machine shop helped tremendously in actualizing our designs. Catherine was always available for support and guidance. I had the pleasure of working with and mentoring a number of undergraduate researchers in our lab. I am also very thankful to our collaborators from other institutions; Niri, Stosh, and the beamline scientists and staff at APS, ALS, and SSRL.

CHAPTER 1 INTRODUCTION TO X-RAY EMISSION SPECTROSCOPY

1.1 WHAT IS X-RAY EMISSION SPECTROSCOPY?

X-ray emission spectroscopy (XES) is a term used to describe x-ray fluorescence spectroscopy studied with a very high energy resolution, i.e., comparable to the intrinsic linewidths of the features being measured. Atoms in a sample of interest are excited with some type of radiation source (e.g. incident x-rays from a bremsstrahlung x-ray tube or synchrotron) and the resulting fluorescence x-rays are detected and interpreted.

Whereas traditional x-ray fluorescence spectroscopy (XRF) has a resolution typically >100 eV, XES commonly achieves <1 eV resolution or better. The change in terminology is justified by the vastly increased amount of information attainable. The most common application of XRF is in elemental analysis. With the lower resolution, there is typically enough discrimination between emission lines of different elements that the relative proportion of each element in a given sample can be quantified using proper calibration with reference standards.

In contrast, whereas XRF only gives information about elemental presence, XES instead interrogates chemical changes of a single elemental species out of a complex mixture, including information about oxidation state, bonding configurations, symmetry, and coordination. This increased information content has led to the use of XES in many high profile applications, including the identification of carbon as the central atom in the nitrogenase iron-molybdenum cofactor,[1] the investigation of Fe-O_2 bonding in myoglobin/hemoglobin,[2,3] the study of density fluctuations in water,[4,5] identification of spin transition of iron at pressures comparable to the

earth's mantle,[6] as well as numerous studies of catalysis,[7] and electrical energy storage,[8,9] to name a few prominent examples.

An illustrative comparison of the difference in information accessible by these techniques is given in Figure 1.1. While the typical XRF measurement might be used to identify the nature of the material (Figure 1.1 left, a simulated spectrum of InP quantum dots), the additional sensitivity of XES allows for the discrimination of different phosphorus species within the InP quantum dots (Figure 1.1 right, actual XES data from InP quantum dots from the study reported in chapter 9). In this case, in addition to the reduced phosphorus species in the core of the quantum dot (P bonded to In is in the reduced, nominally -2 oxidation state), we see a fraction of phosphorus atoms in an oxidized environment. This oxidized phosphorus is a signature of P – O bonding impurities developing on the surface of the InP quantum dots during synthesis. This capability was used in an extensive study of phosphorus surface oxidation defects in InP quantum dots for a range of synthetic procedures, discussed in detail in chapter 9.

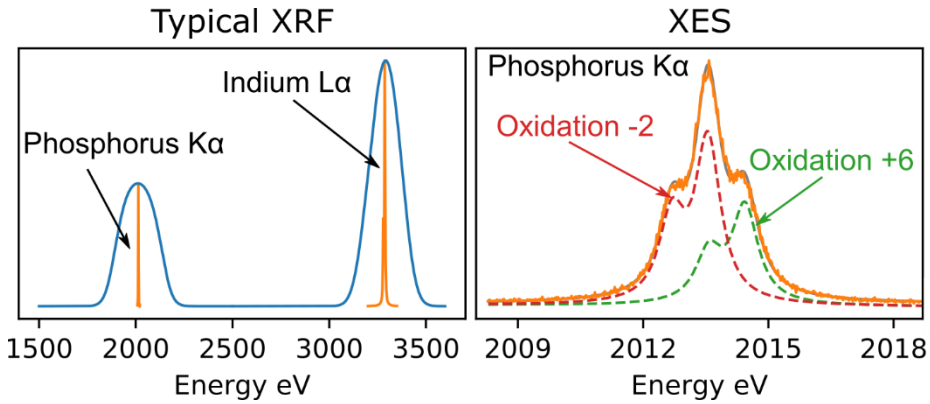

Figure 1.1: (Left) Simulated typical x-ray fluorescence (XRF) of InP sample with resolution 150 eV FWHM. (Right) Actual XES data of InP quantum dots with resolution < 1 eV showing the ability to distinguish oxidation state distribution, from chapter 9. Measurements were taken with the spectrometer reported in chapter 5.

In addition to the information content available with the increased energy resolution, there are a few key features that make XES a powerful experimental and analytical tool:

- **Element-specificity:** As with other x-ray spectroscopies, XES probes characteristic transitions of the elements. The energies of these transitions are well separated compared to experimental resolutions, and therefore by tuning to an energy of a specific transition, an element-specific measurement can be made.
- **Bulk sensitivity and penetrating capability:** In the tender x-ray energy range, penetration depths of x-rays in common materials are on the order of 1–100 μm. XES measurements therefore represent a bulk average over these length scales. Though the penetration lengths are shorter for tender x-rays than for hard x-rays, with some care in sample cell design this bulk averaging capability can be utilized for *in-situ* and *in-operando* measurements. For example, Kavčič et al.[8] made *in-operando* measurements of sulfur in a Li–S battery using an cell with a thin aluminized mylar window.
- **Atomically local:** XES is an atomically local probe of the electronic structure. In other words, the measurements depend only on the element being measured and its immediate environment. Thus, there is no restriction on sample phase or order/crystallinity, as would be the case in x-ray diffraction (XRD). XES measurements can be performed on solutions, liquids, gases, plasmas, and solids.

1.2 Historical context for XES

With the development of bremsstrahlung x-rays in 1895,[10] it was not long until Charles G. Barkla found a connection between x-rays radiating from a sample and its atomic weight.[11] Soon after in 1913, Henry G. J. Moseley observed that the K-line transitions in an x-ray spectrum moved

the same amount with subsequent increases in atomic number; Moseley used this discovery to number the elements, and he is credited with revising the periodic table to be based on atomic number instead of atomic weight.[11] This historical development was the birth of XRF techniques, including modern XES.

Amazingly, by 1932, the development of a double-crystal vacuum spectrometer[12] by Lyman G. Parratt allowed spectra to be measured with a resolution near enough to the intrinsic natural linewidth to properly be called x-ray emission spectroscopy, though the term was not used until much later. Parratt used the spectrometer to make possibly the first tender x-ray emission measurement of sulfur,[13] and even identified the chemical shift of the sulfur Kα emission line with change in oxidation state.

Application of the technique, particularly in the tender x-ray regime (1–5 keV), was somewhat sparse in the mid-1900s, though a large effort was made by Sugiura,[14] Yasuda,[15] and others in Japan[16,17] in the 1970s and 1980s with double-crystal spectrometers working on the same principle as Parratt.

The 1970s also brought the development of what would become modern synchrotron x-ray radiation light-sources. With an extremely brilliant source of x-rays, an appropriately designed monochromator selects a narrow slice of energy and, by tuning this incident energy, it became easy to quickly measure x-ray absorption fine-structure (XAFS) spectra with higher fidelity and sensitivity than had been available in lab-based instruments of that era.[18] The rapid development of synchrotrons and the relative ease with which XAFS spectra could be obtained became an extremely powerful tool and launched a broad use of XAFS, resulting in more than 100 synchrotron endstations worldwide that now regularly offer this technique. With these capabilities, XAFS use at synchrotron facilities became considerably more widespread, while

laboratory spectrometers saw some continued interest but, on the whole, a great decrease in their use, in part because the synchrotron work showed that lab-based instruments of this era frequently had uncontrolled systematic errors, such as from harmonic contamination.

At synchrotron endstations, in addition to XAFS, XES can also be performed, though it requires an additional crystal analyzer or grating to disperse the fluorescence from the sample, making XES measurements both more instrumentally complex and less efficient. Even so, synchrotron-based XES has had high impact, discussed above, and in parallel there has been strong progress made with the technique itself and the underlying theoretical framework.

Presently (2019), XES is having somewhat of a renaissance with the advent of modern laboratory-based x-ray spectrometers. One of these spectrometers, tuned to work especially well in the tender x-ray regime, is the foundation of this thesis. This "renaissance" is fueled by the recognition that modern bremsstrahlung x-ray tubes, modern solid-state detectors, and the availability of high quality x-ray crystal analyzers allow XES to be performed in laboratory facilities with count rates comparable to synchrotron sources and with instrumental energy resolution that is *the same* as what is achieved at synchrotron facilities.

1.3 The modern case for laboratory XES

1.3.1 Laboratory spectrometers in 1932 and 2017

To understand the modern case for laboratory XES systems, it helps to briefly consider the spectrometer used by Parratt for his pioneering measurements of sulfur x-ray emission.[12,13] The resolution of Parratt's original measurements is quite comparable with modern capabilities and is sufficiently close to the natural linewidth of the sulfur emission lines that his measurements can rightly be called XES. A diagram and photograph of Parratt's original spectrometer are shown in Figure 1.2.

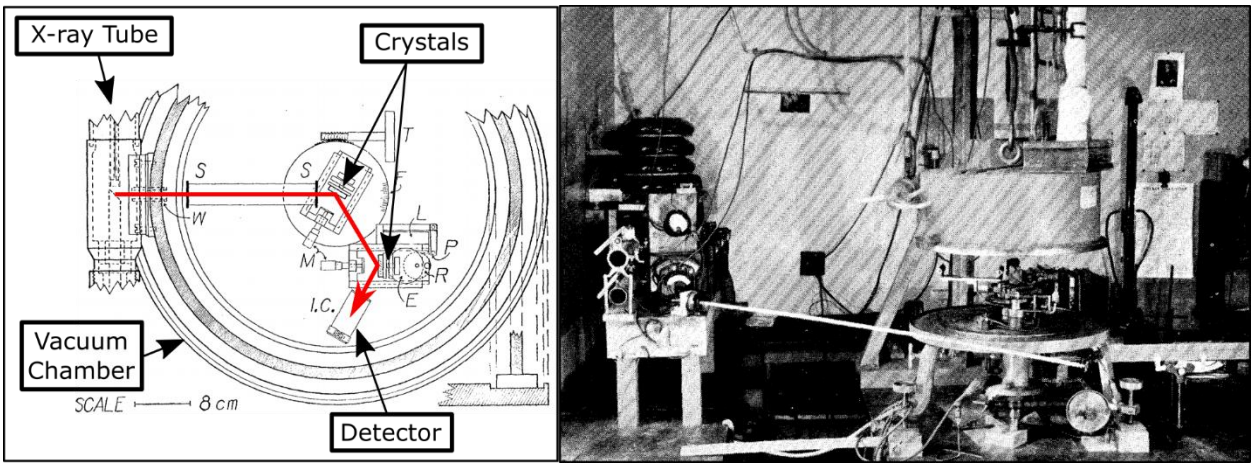

Figure 1.2: (Left) Diagram of the double-crystal spectrometer used by Parratt. Additional text annotations and the red beampath have been added for clarity. (Right) Original photograph of the spectrometer setup.[12]

The original setup used an x-ray tube in which the x-ray fluorescence of a target was generated by direct electron excitation. High-voltage electrons from the filament of the tube directly struck the target stimulating it to emit x-rays. The emitted x-rays were collimated by two slits (both labelled S in Figure 1.2 left), which were then analyzed by two calcite crystals and captured by the ionization chamber detector. The entire setup was operated inside of a vacuum chamber.

In comparison, the modern tender x-ray emission spectrometer (reported in chapter 5) is shown in Figure 1.3. A small vacuum (or helium back-filled) chamber contains a sample mounted above the nozzle of a low-powered, large beamspot x-ray tube. X-rays from the tube stimulate fluorescence in the sample. Using a dispersive refocusing Rowland (DRR) geometry, these fluorescence rays travel to a cylindrically bent silicon crystal analyzer and are analyzed and refocused onto the detector, which is an energy-resolving position-sensitive CMOS-based x-ray camera.

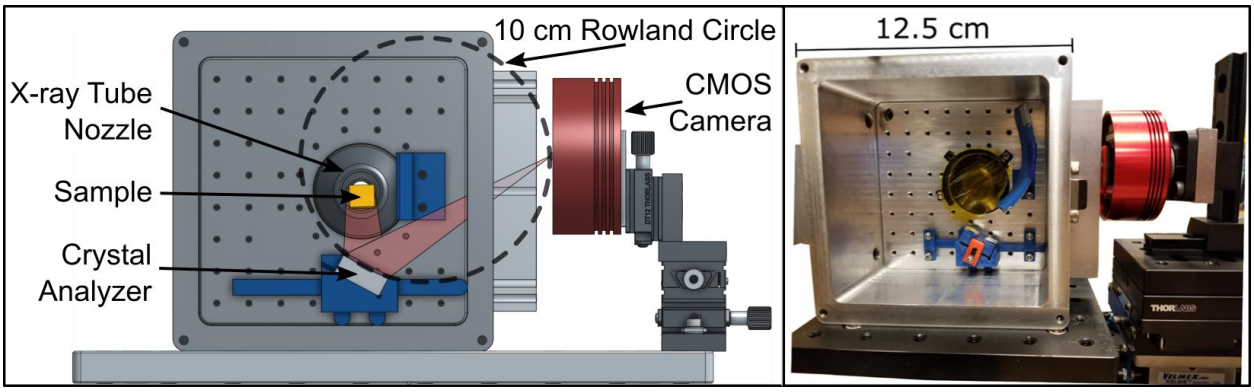

Figure 1.3: (Left) Labelled CAD rendering of the modern x-ray spectrometer reported in Chapter 5. (Right) Picture of the x-ray spectrometer with sample holder removed.

1.3.2 Advances in spectrometer components

The advances made between the original double crystal x-ray spectrometer and the modern dispersive refocusing Rowland spectrometer come from improved technology of nearly every component of the system. With the widespread use of traditional XRF systems, modern x-ray tubes and high voltage power supplies have become inexpensive, reliable, and extremely efficient. Improvements in the anode geometries and proper selection of anode material (e.g. Pd-anode x-ray tubes generate strong Pd fluorescence at 2.84 keV, an energy close to P and S K-edges, which generates strong fluorescence) allow very efficient stimulation of fluorescence in the samples. Combined with the DRR geometry to allow for efficient collection of the large beamspot on the sample, efficient measurements can be taken with relatively low incident flux, limiting possible radiation damage to sample (which was an issue observed by Parratt in his original measurements[13]).

Crystal analyzers have also seen enormous improvements. Modern x-ray crystal analyzers are commonly made from curved silicon crystal wafers of different Miller indices. The first single crystals of silicon were grown by crucible pulling in 1950,[19] just two years after the invention of the transistor. The huge demand for silicon wafer-based electronic devices has made

monocrystalline silicon commonplace and inexpensive. With the ability to produce thin wafers, silicon has become a choice material for bent crystal analyzers. Cylindrically bent and spherically bent crystal analyzers were heavily developed and improved during the growth of synchrotron x-ray science. Now such analyzers are commercially available, and modern laboratory-based spectrometers can take advantage of these incredible advances and perform XES measurements with resolutions identical to what is achievable at synchrotron beamlines.

Advances in x-ray detectors have also greatly contributed to the performance of modern spectrometers. The ionization chamber detectors used in the double-crystal spectrometer designs had little to no energy resolving capabilities. As such, they required low background signals in order to achieve good signal-to-noise measurements. Fortunately, to achieve high resolution, the double-crystal design required collimating slits and two crystal diffractions, which inherently reduced the background signals reaching the detector. The focusing, curved analyzers in the modern XES system have the advantage of being much more efficient, but does not necessarily have the intrinsically low background signals of the double-crystal design.

The detector used in the modern DRR design is an x-ray camera based on a complementary metal-oxide-semiconductor (CMOS) camera sensor. Full details of the x-ray camera are covered in chapter 6. The sensor is a visible light sensor adapted to work with x-rays be removal of the protective glass covering. The camera detects both the position of the x-rays striking the sensor (with high position resolution from the small 2.9 μm pixels) and the energies with relatively high resolution (~ 86 eV FWHM for photons at 2014 eV, near the Fano noise limit). With the DRR design being dispersive, the energy spectrum is captured in the spatial pattern of the image. Using the energy-resolving capabilities of the camera, only photons in the energy region of interest are captured into the final image, vastly reducing backgrounds. The other advantage of the dispersive

spectrometer and position-sensitive detector is that the entire energy range is captured simultaneously with no moving parts. This is a great simplification compared to the double-crystal spectrometers which required complicated mechanical scanning mechanisms.

1.3.3 Relation to synchrotron XES

Most of the high-profile applications of XES in modern science have been done at spectrometers at synchrotron beamlines. In a sense, this is in line with the synchrotron access model. Synchrotron x-ray beamlines are truly marvels of modern science, using electron storage rings hundreds of meters in diameter to send high energy electrons through series of alternating magnets, producing the most brilliant x-rays available to experimenters. They're capabilities are truly astounding and are often at the forefront of scientific discovery in a wide variety of fields.

With that level of capability, however, comes expense and complexity. There are currently only five synchrotron facilities in the United States that have beamlines available to experimenters, and around fifty worldwide. Thus, access to experiments at synchrotron beamlines is a limited, finite resource. In order to perform experiments at beamlines, researchers must submit proposals for their experiments, wait for them to be reviewed, and then wait for their experimental time to be allocated in the schedule. We refer to this as the "synchrotron access model," and it is a natural result that studies with high potential impact are often favored.

As discussed in section 1.2, there was rapid growth in synchrotron technology since the 1970s, which also fueled the development of x-ray spectrometer technology, such as the crystal analyzers and detectors necessary for XES measurements. XES technology thus increased in step with synchrotron development, and this has led to many of the high-profile XES studies mentioned previously.

From this historical development, XES as a technique has been available to experimenters predominantly at synchrotron facilities. With increasing knowledge of the technique, it has become apparent that there are many possible applications of XES that do not fit the synchrotron access model and which could be better served by laboratory-based XES instruments. A few examples include routine characterization of materials, such as our recent study of InP quantum dots (QDs)(see chapter 9) in which several different synthetic procedures were measured to address the presence of oxygen surface impurities. After some measurements, we were able to synthesize new batches or adjust the synthetic procedure and repeat the measurement. Such a follow-up study at a synchrotron facility would require submitting an additional proposal, and may be difficult to justify. Another example of an application outside of the synchrotron access model is the possibility of environmental or industrial process monitoring. A recent publication by our group demonstrates the ability to use laboratory XES to determine hexavalent chromium speciation.[20] With a laboratory XES spectrometer, hexavalent chromium could be monitored at environmental sites or in the factory where chromium-containing products are produced.

While synchrotron XES has capabilities beyond what is possible in a laboratory instrument (e.g. resonant studies, microscopy, see section 3.3.2), for samples that do not require a focused beam, it turns out that laboratory-based instruments can achieve comparable count rates with equally high resolution. As discussed in section 1.3.2, the achievable resolution is the same because laboratory spectrometers make use of the same crystal analyzers as at the synchrotron. To achieve comparable count rates, however, is at first glance not as straightforward given that synchrotrons have much higher brilliance than the x-ray tube of laboratory instruments. Synchrotron beamlines have very high incident flux in a very narrow bandwidth, while bremsstrahlung x-ray tubes have a relatively high flux over a broad range of energies along with

characteristic fluorescence lines from the x-ray tube anode material. This comparison is illustrated schematically in Figure 1.4. The key realization is that, for an XES measurement, all energies of x-rays above the absorption edge of the atom being studied are capable of generating a core hole and thus causing fluorescence. Thus, for an x-ray tube in a laboratory instrument, despite having much less peak flux than a synchrotron beamline, the integrated flux of the bremsstrahlung and anode fluorescence lines of an x-ray tube is capable of a similar core-hole generation rate, and thus a similar amount of fluorescence.

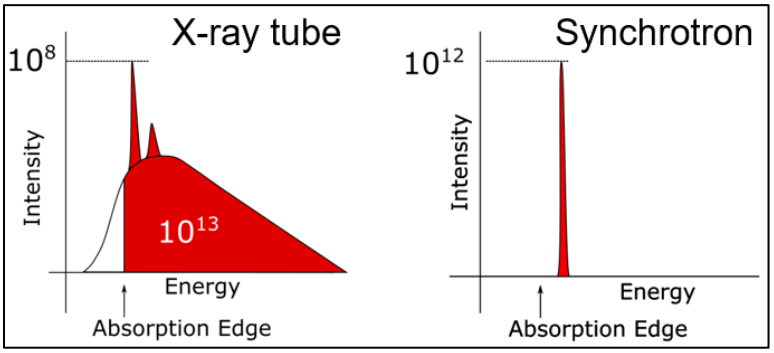

Figure 1.4: Schematic illustration of useful flux for non-resonant XES of a bremsstrahlung x-ray tube compared to a typical insertion-device synchrotron beamline. Indicated values are only approximate for purposes of illustration.

1.4 Overview of recent laboratory XES instruments and applications

In the last decade, a large variety of effort has been made developing and applying laboratory based XES systems. Here, we give a brief review of our efforts at the University of Washington and of the instruments and applications of other research groups.

The main spectrometer developed and used in this thesis, described in detail in chapter 5, is a dispersive refocusing Rowland spectrometer that works best in the 2–5 keV energy range. The primary applications of this spectrometer have been for measuring XES of phosphorus and sulfur compounds. In Chapter 7, XES is applied to the question of speciation of sulfur in biochars, which

has an effect on potential bioavailability of sulfur. In Chapter 9, phosphorus XES is used to address the role of speciation of P in InP quantum dots with the aim of understanding the effect of different shelling procedures used to improve quantum yields for use in emissive applications, e.g. display technologies. In Chapter 10, sulfur valence-to-core XES (VtC-XES) of a wide array of compounds is investigated using linear-response time-dependent density functional theory.

Our group at the University of Washington also developed a laboratory spectrometer capable of performing XES (as well as transmission-mode XAFS) at higher energies (5–12 keV and above).[21,22] This spectrometer is based on a 1-meter Johann-type spectrometer using an x-ray tube, spherically bent crystal analyzer, and silicon drift diode detector. Some applications include measurement of hexavalent chromium in plastics,[20] measurement of nickel XES in nickel-manganese- cobalt- (NMC) oxide battery cathode laminates,[22] measurement of arsenic Kα XES of trivalent and pentavalent arsenic oxide,[22] as well as measurements of valence-to-core XES of vanadium in vanadyl phosphate-based battery materials.[23]

In the past few decades, other groups around the world have also developed a number of laboratory XES spectrometers. The majority of these have been based on the von Hamos geometry (discussed in section 3.7.2).[24-29] These have been used in applications such as studying the role of iron in nitrogenase model systems[30] as well as spin crossover complexes.[31] The energy ranges of these spectrometers vary and are typically in the hard x-ray range (>5 keV), though some[24] have been used for applications in the tender x-ray range as well, such as measurements of sulfur valence-to-core.[32] A different instrument using a Laue-type DuMond spectrometer[33] has demonstrated XES measurements as high in energy as the Au K-edge (78 keV).

Based on the efforts demonstrated in this thesis, from our group at the University of Washington, and the developments of other systems from labs around the world, the future is

promising for laboratory based XES instrumentation and their application to a wide range of problems from fundamental physics to routine analysis and characterization of materials. Indeed, with the growing number of instruments and ongoing commercialization of the technology, it's clear that the use and prevalence of laboratory XES will continue to increase, and it is likely only a matter of time before XES capabilities are a mainstay of analytical laboratories in universities and industries around the world.

1.5 REFERENCES

1 Lancaster, K. M. *et al.* X-ray Emission Spectroscopy Evidences a Central Carbon in the Nitrogenase Iron-Molybdenum Cofactor. *Science* **334**, 974-977, doi:10.1126/science.1206445 (2011).

2 Schuth, N. *et al.* Effective intermediate-spin iron in O2-transporting heme proteins. *Proceedings of the National Academy of Sciences* **114**, 8556-8561, doi:10.1073/pnas.1706527114 (2017).

3 Koster, A. S. Electronic State of Iron in Hemoglobin, Myoglobin, and Derivatives, as Inferred from X-Ray Fluorescence Spectra. *The Journal of Chemical Physics* **56**, 3161-3164, doi:10.1063/1.1677655 (1972).

4 Guo, J. H. *et al.* Molecular Structure of Alcohol-Water Mixtures. *Physical Review Letters* **91**, doi:10.1103/PhysRevLett.91.157401 (2003).

5 Huang, C. *et al.* The inhomogeneous structure of water at ambient conditions. *Proceedings of the National Academy of Sciences* **106**, 15214-15218, doi:10.1073/pnas.0904743106 (2009).

6 Lin, J.-F. *et al.* Spin transition of iron in magnesiowüstite in the Earth's lower mantle. *Nature* **436**, 377-380, doi:10.1038/nature03825 (2005).

7 Lomachenko, K. A. *et al.* The Cu-CHA deNOx Catalyst in Action: Temperature-Dependent NH3-Assisted Selective Catalytic Reduction Monitored by Operando XAS and XES. *Journal of the American Chemical Society* **138**, 12025-12028, doi:10.1021/jacs.6b06809 (2016).

8 Kavčič, M. *et al.* Operando Resonant Inelastic X-ray Scattering: An Appropriate Tool to Characterize Sulfur in Li–S Batteries. *The Journal of Physical Chemistry C* **120**, 24568-24576, doi:10.1021/acs.jpcc.6b06705 (2016).

9 Robba, A. *et al.* Mechanistic Study of Magnesium–Sulfur Batteries. *Chemistry of Materials* **29**, 9555-9564, doi:10.1021/acs.chemmater.7b03956 (2017).

10 Rontgen, W. C. On a New Kind of Rays. *Science* **3**, 227-231, doi:10.1126/science.3.59.227 (1896).

11 Shackley, M. S. X-Ray Fluorescence Spectrometry (XRF). 1-5, doi:10.1002/9781119188230.saseas0620 (2018).

12 Parratt, L. G. Design of a Double-Crystal X-Ray Vacuum Spectrometer. *Physical Review* **41**, 553-560, doi:10.1103/PhysRev.41.553 (1932).

13 Parratt, L. G. Effects of Chemical Binding on the X-RayKα1, 2Doublet Lines of Sulphur Studied with a Two-Crystal Spectrometer. *Physical Review* **49**, 14-16, doi:10.1103/PhysRev.49.14 (1936).
14 Sugiura, C., Gohshi, Y. & Suzuki, I. SulfurKβx-ray emission spectra and electronic structures of some metal sulfides. *Physical Review B* **10**, 338-343, doi:10.1103/PhysRevB.10.338 (1974).
15 Yasuda, S. & Kakiyama, H. Chemical effects in X-ray Kα and Kβ emission spectra of sulfur in organic compounds. *Spectrochimica Acta Part A: Molecular Spectroscopy* **35**, 485-493, doi:10.1016/0584-8539(79)80164-6 (1979).
16 Sato, T., Takahashi, Y. & Yabe, K. An X-Ray Emission Spectroscopic Investigation of the Chemical Bond of Sulfur. I. The Peak Shift ofKα and the Number of Valence Electrons of the Sulfur Atom in Compounds. *Bulletin of the Chemical Society of Japan* **40**, 298-301, doi:10.1246/bcsj.40.298 (1967).
17 Gohshi, Y., Hukao, Y. & Hori, K. A wide-range, single-axis, vacuum two-crystal spectrometer for fluorescent X-ray analysis. *Spectrochimica Acta Part B: Atomic Spectroscopy* **27**, 135-142, doi:10.1016/0584-8547(72)80016-8 (1972).
18 Lytle, F. W. The EXAFS family tree: a personal history of the development of extended X-ray absorption fine structure. *Journal of Synchrotron Radiation* **6**, 123-134, doi:10.1107/s0909049599001260 (1999).
19 Zulehner, W. Historical overview of silicon crystal pulling development. *Materials Science and Engineering: B* **73**, 7-15, doi:10.1016/s0921-5107(99)00427-4 (2000).
20 Jahrman, E. P., Seidler, G. T. & Sieber, J. R. Determination of Hexavalent Chromium Fractions in Plastics Using Laboratory-Based, High-Resolution X-ray Emission Spectroscopy. *Analytical Chemistry* **90**, 6587-6593, doi:10.1021/acs.analchem.8b00302 (2018).
21 Seidler, G. T. *et al.* A laboratory-based hard x-ray monochromator for high-resolution x-ray emission spectroscopy and x-ray absorption near edge structure measurements. *Review of Scientific Instruments* **85**, 113906, doi:10.1063/1.4901599 (2014).
22 Jahrman, E. P. *et al.* An improved laboratory-based x-ray absorption fine structure and x-ray emission spectrometer for analytical applications in materials chemistry research. *Review of Scientific Instruments* **90**, 024106, doi:10.1063/1.5049383 (2019).
23 Jahrman, E. P. *et al.* Valence-to-core X-ray Emission Spectroscopy of Vanadium Oxide and Lithiated Vanadyl Phosphate Materials. *Chemistry of Materials* **Submitted** (2019).
24 Hoszowska, J., Dousse, J. C., Kern, J. & Rhême, C. High-resolution von Hamos crystal X-ray spectrometer. *Nuclear Instruments and Methods in Physics Research Section A: Accelerators, Spectrometers, Detectors and Associated Equipment* **376**, 129-138, doi:10.1016/0168-9002(96)00262-8 (1996).
25 Anklamm, L. *et al.* A novel von Hamos spectrometer for efficient X-ray emission spectroscopy in the laboratory. *Review of Scientific Instruments* **85**, 053110, doi:10.1063/1.4875986 (2014).
26 Kayser, Y. *et al.* Laboratory-based micro-X-ray fluorescence setup using a von Hamos crystal spectrometer and a focused beam X-ray tube. *Review of Scientific Instruments* **85**, 043101, doi:10.1063/1.4869340 (2014).
27 Németh, Z., Szlachetko, J., Bajnóczi, É. G. & Vankó, G. Laboratory von Hámos X-ray spectroscopy for routine sample characterization. *Review of Scientific Instruments* **87**, 103105, doi:10.1063/1.4964098 (2016).

28 Malzer, W. *et al.* A laboratory spectrometer for high throughput X-ray emission spectroscopy in catalysis research. *Review of Scientific Instruments* **89**, 113111, doi:10.1063/1.5035171 (2018).
29 Błachucki, W., Czapla-Masztafiak, J., Sá, J. & Szlachetko, J. A laboratory-based double X-ray spectrometer for simultaneous X-ray emission and X-ray absorption studies. *Journal of Analytical Atomic Spectrometry* **34**, 1409-1415, doi:10.1039/c9ja00159j (2019).
30 Kalläne, S. I. *et al.* Spectroscopic and Quantum Chemical Investigation of Benzene-1,2-dithiolate-Coordinated Diiron Complexes with Relevance to Dinitrogen Activation. *Inorganic Chemistry* **58**, 5111-5125, doi:10.1021/acs.inorgchem.9b00177 (2019).
31 Wolny, J. A., Schünemann, V., Németh, Z. & Vankó, G. Spectroscopic techniques to characterize the spin state: Vibrational, optical, Mössbauer, NMR, and X-ray spectroscopy. *Comptes Rendus Chimie* **21**, 1152-1169, doi:10.1016/j.crci.2018.10.001 (2018).
32 Kavčič, M., Dousse, J. C., Szlachetko, J. & Cao, W. Chemical effects in the Kβ X-ray emission spectra of sulfur. *Nuclear Instruments and Methods in Physics Research Section B: Beam Interactions with Materials and Atoms* **260**, 642-646, doi:10.1016/j.nimb.2007.04.290 (2007).
33 Szlachetko, M., Berset, M., Dousse, J. C., Hoszowska, J. & Szlachetko, J. High-resolution Laue-type DuMond curved crystal spectrometer. *Review of Scientific Instruments* **84**, 093104, doi:10.1063/1.4821621 (2013).

CHAPTER 2 TENDER X-RAY SPECTROSCOPY

2.1 INTERACTION OF PHOTONS WITH MATTER

In the tender x-ray energy range (1–5 keV), the dominant mechanism for the interaction of photons with matter is the photoelectric effect, in which the entire energy of a photon is absorbed by an electron in an atom causing the electron to be ejected. Figure 2.1 shows the total interaction cross section of photons with matter for carbon. Below the photoelectric effect, at 3-4 orders of magnitude lower intensity are the coherent (elastic) scattering and incoherent (inelastic) scattering processes. At photon energies much higher than are relevant here and with even lower cross-section, other processes such as pair production and nuclear photoabsorption become possible. Thus, the anatomy of a tender x-ray experiment is remarkably dependent on essentially one interaction: the photoelectric effect and subsequent decay of the photoexcited atom. In the next sections, some details of this interaction are discussed.

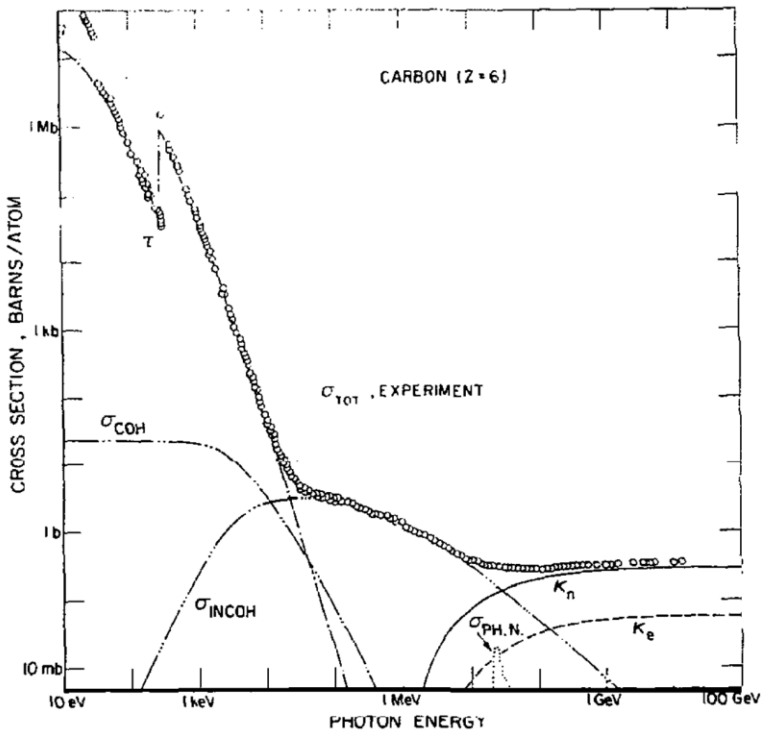

Figure 2.1: Contributions of different scattering mechanisms to the total interaction cross section of electromagnetic radiation with carbon. The scattering mechanisms are the photoelectric effect (τ), coherent scattering (σ_{COH}), incoherent scattering (σ_{INCOH}), nuclear-field pair production (κ_n), electron-field pair production (κ_e), and nuclear photoabsorption ($\sigma_{PH.N.}$). Figure from Hubbell et al.[1]

2.1.1 Interaction Hamiltonian with electromagnetic field

In a nonrelativistic approach, the interaction of electromagnetic radiation with matter can be obtained by considering the electronic and electromagnetic contributions to the Hamiltonian, along with the interaction between them. A standard approach to including the interaction of charged particles with the electromagnetic field is through modifying the momentum and energy of the particle as:

$$p \rightarrow p - q A, \quad E \rightarrow E - q \phi \tag{1}$$

Where A is the vector potential, ϕ is the scalar potential, q is the charge of the particle and c is the speed of light. With this replacement, the nonrelativistic Hamiltonian becomes:

$$H = \frac{1}{2m}(p - q\,A)^2 + V(r) + q\,\phi \tag{2}$$

Now expanding the square and adding in the contribution of the electromagnetic field to the Hamiltonian, $H_{photons}$:

$$H = \frac{p^2}{2m} + V(r) - \frac{q}{2m}(p \cdot A + A \cdot p) + \frac{q^2A^2}{2m} + q\,\phi + H_{photons} \tag{3}$$

Choosing the gauge of the electromagnetic field such that $\nabla \cdot A = 0$ and $\phi = 0$, this implies that $p \cdot A = A \cdot p$, which yields:

$$H = \frac{p^2}{2m} + V(r) - \frac{q}{m}(A \cdot p) + \frac{q^2A^2}{2m} + H_{photons} \tag{4}$$

Separating the Hamiltonian into two pieces, a ground state Hamiltonian H_0 and a perturbing (i.e. interaction) Hamiltonian H_1 gives:

$$H = H_0 + H_1 \tag{5}$$

$$H_0 = \frac{p^2}{2m} + V(r) + H_{photons} \tag{6}$$

$$H_1 = -\frac{q}{m}(A \cdot p) + \frac{q^2A^2}{2m} \tag{7}$$

The interaction contains two terms, one linear in the vector potential, and one quadratic. In first order perturbation theory, the linear term gives rise to absorption and emission of photons, while the quadratic term gives rise to scattering.[2] One way to see this is to examine the vector potential A in a quantized picture of the electromagnetic field, as follows:

$$A(r,t) = \sqrt{\frac{\hbar}{2V\epsilon_0}} \sum_{k,\alpha} \frac{1}{\sqrt{\omega_k}} \left[\hat{\epsilon}_{k\alpha} a_{k\alpha}(t) e^{ik\cdot r} + \hat{\epsilon}^{\dagger}_{k\alpha} a^{\dagger}_{k\alpha}(t) e^{-ik\cdot r}\right] \tag{8}$$

where V is the volume of the box over which quantization is considered, k is the wavevector, α is the polarization index, $\hat{\epsilon}_{k\alpha}$ is the unit vector representing the polarization direction, and $\omega_k = c|k|$

is the angular frequency. In the quantized framework, $a^{\dagger}_{k\alpha}$ is the creation operator that creates a photon with polarization α with wavevector k, and $a_{k\alpha}$ is the annihilation operator that annihilates a photon with polarization α with wavevector k. They obey the commutation relations:

$$[a_{k\alpha}, a_{k'\alpha'}] = 0 \tag{9}$$

$$[a^{\dagger}_{k\alpha}, a^{\dagger}_{k'\alpha'}] = 0 \tag{10}$$

$$\left[a_{k\alpha}, a^{\dagger}_{k'\alpha'}\right] = \delta_{k,k'}\delta_{\alpha\alpha'} \tag{11}$$

Such that the contribution of the electromagnetic field to the Hamiltonian is:

$$H_{photons} = \sum_{k,\alpha} \hbar\omega_k \left(a^{\dagger}_{k\alpha}a_{k\alpha} + \frac{1}{2}\right) \tag{12}$$

With this framework in mind, the two terms in the interaction Hamiltonian H_1 can be interpreted. The first term is linear in A and therefore is capable of connecting two states with photon number different by one in first-order perturbation theory, i.e. connecting a state where a single photon is either created or destroyed. These two processes are emission and absorption of a photon. The second term in H_1 is quadratic in A even in first-order perturbation theory, and therefore always contains terms quadratic in the annihilation and creation operators, i.e. the second term can connect initial and final states whose number of photons differs by zero or two. This does not represent single photon absorption or emission processes, but rather other processes such as elastic Thomson scattering.

The final piece needed to derive the expressions for rates of absorption and emission is Fermi's golden rule. Using the standard result of first-order time-dependent perturbation theory, Fermi's golden rule is:[3]

$$\Gamma_{i\to f} = \frac{2\pi}{\hbar}|\langle f|H_1|i\rangle|^2 \rho(E)\delta(E_f - E_i) \tag{13}$$

Now substituting the perturbing Hamiltonian H_1, keeping only the first term based on the arguments above:

$$\Gamma_{i\to f} = \frac{2\pi}{\hbar}\left|\left\langle f\left|\left(-\frac{q}{m}(A\cdot p)\right)\right|i\right\rangle\right|^2 \rho(E)\delta(E_f - E_i) \tag{14}$$

Which, upon substituting the expression for A gives:

$$\Gamma_{i\to f} = \left(\frac{q}{m}\right)^2 \frac{\pi}{V\epsilon_0\omega_k}\left|\left\langle f\left|\left(\sum_{k,\alpha}\left[\hat{\epsilon}_{k\alpha}a_{k\alpha}(t)e^{ik\cdot r} + \hat{\epsilon}^{\dagger}_{k\alpha}a^{\dagger}_{k\alpha}(t)e^{-ik\cdot r}\right]\cdot p\right)\right|i\right\rangle\right|^2 \rho(E)\delta(E_f - E_i) \tag{15}$$

This can be separated into two pieces:

$$\text{absorption: } \Gamma_{i\to f} = \left(\frac{q}{m}\right)^2 \frac{\pi}{V\epsilon_0\omega_k}\left|\left\langle f\left|\left(\sum_{k,\alpha} a_{k\alpha}(t)e^{ik\cdot r}\,\hat{\epsilon}_{k\alpha}\cdot p\right)\right|i\right\rangle\right|^2 \rho(E)\delta(E_f - E_i) \tag{16}$$

$$\text{emission: } \Gamma_{i\to f} = \left(\frac{q}{m}\right)^2 \frac{\pi}{V\epsilon_0\omega_k}\left|\left\langle f\left|\left(\sum_{k,\alpha} a^{\dagger}_{k\alpha}(t)e^{-ik\cdot r}\,\hat{\epsilon}^{\dagger}_{k\alpha}\cdot p\right)\right|i\right\rangle\right|^2 \rho(E)\delta(E_f - E_i) \tag{17}$$

The presence of the annihilation and creation operators ($a_{k\alpha}$ and $a^{\dagger}_{k\alpha}$) connects initial and final states whose photon numbers differ by one. This leads to expressions containing the matrix elements:

$$\text{absorption: } |\langle n_{k\alpha} - 1|a_{k\alpha}|n_{k\alpha}\rangle|^2 = n_{k\alpha} \tag{18}$$

$$\text{emission: } \left|\langle n_{k\alpha} + 1\left|a^{\dagger}_{k\alpha}\right|n_{k\alpha}\rangle\right|^2 = n_{k\alpha} + 1 \tag{19}$$

Thus absorption depends on the number (i.e. intensity) of photons through $n_{k\alpha}$, and emission contains two pieces, one of which depends on the intensity (stimulated emission from the $n_{k\alpha}$ term) and the other of which does not (spontaneous emission through the $+1$ term).

Considering only the case of spontaneous emission from the $+1$ term in equation (19) and using that in equation (17) gives:

$$\Gamma_{i\to f,k\alpha} = \left(\frac{q}{m}\right)^2 \frac{\pi}{V\epsilon_0\omega_k} \left|\langle\psi_f|\left(e^{-i(k\cdot r-\omega_k t)}\,\hat{\epsilon}^{\dagger}_{k\alpha}\cdot p\right)|\psi_i\rangle\right|^2 \rho(E)\delta(E_f - E_i + \hbar\omega_k) \tag{20}$$

Where the substitution $a^{\dagger}_{k\alpha}(t) = a^{\dagger}_{k\alpha,0}e^{i\omega t}$ has been implicitly performed. Also, E_f and E_i have been redefined as the energy of the initial and final states $|\psi_i\rangle$ and $|\psi_f\rangle$ with the $+\hbar\omega_k$ to account for the emitted photon.

In the dipole approximation, the replacement $e^{-i\,k\cdot r} \approx 1$ is made, keeping only the lowest order term. Next, the momentum operator p is replaced using the relation:

$$p = \frac{im}{\hbar}[H_0, r] \tag{21}$$

Which gives:

$$\langle\psi_f|\hat{\epsilon}^{\dagger}_{k\alpha}\cdot p|\psi_i\rangle = \frac{im}{\hbar}\hat{\epsilon}^{\dagger}_{k\alpha}\cdot\langle\psi_f|[H_0, r]|\psi_i\rangle = im\frac{E_f - E_i}{\hbar}\hat{\epsilon}^{\dagger}_{k\alpha}\cdot\langle\psi_f|r|\psi_i\rangle \tag{22}$$

Defining $\omega_k = \frac{E_f - E_i}{\hbar}$ and substituting into (20) gives:

$$\Gamma_{i\to f,k\alpha} \approx \frac{\pi\omega_k}{V\epsilon_0}\left|\langle\psi_f|\hat{\epsilon}^{\dagger}_{k\alpha}\cdot d|\psi_i\rangle\right|^2 \rho(E)\delta(E_f - E_i + \hbar\omega_k) \tag{23}$$

With the definition of the dipole operator, $d = q\cdot r$. Next, integrating the transition rate associated with a small solid angle $d\Omega$ in direction k:

$$d\Gamma_{i\to f,\alpha} = \sum_{k\in d\Omega}\Gamma_{i\to f,k\alpha} = d\Omega\frac{V}{(2\pi)^3}\int \Gamma_{i\to f,k\alpha}\,k^2\,dk \tag{24}$$

Where the standard result for the density of photon states in a box of volume V has been used. Using the dispersion relationship $\omega_k = c|k|$ yields:

$$\frac{d\Gamma_{i\to f,\alpha}}{d\Omega} = \frac{\omega_k}{8\pi^2c^3\epsilon_0}\int \left|\langle\psi_f|\hat{\epsilon}^{\dagger}_{k\alpha}\cdot d|\psi_i\rangle\right|^2 \delta(E_f - E_i + \hbar\omega_k)\omega_k{}^2\,d\omega_k \tag{25}$$

$$\frac{d\Gamma_{i\to f,\alpha}}{d\Omega} = \frac{\omega_k^3}{8\pi^2c^3\epsilon_0\hbar}\left|\langle\psi_f|\hat{\epsilon}^{\dagger}_{k\alpha}\cdot d|\psi_i\rangle\right|^2 \tag{26}$$

The $\hbar$ in the denominator appears from the evaluation of the integral with the delta function. Equation (26) is the defining equation of the differential spontaneous emission rate. Note that separate rates occur for each polarization α, such that the total is the sum over two independent polarizations.

To find the total transition rate, the differential rate can be summed over polarizations and integrated over emission direction. Using the relationship between emission direction and polarization directions (see Sakurai Advanced QM,[4] page 43):

$$\sum_{a}\int\left|\langle\psi_f|\hat{\epsilon}_{k\alpha}^{\dagger}\cdot d|\psi_i\rangle\right|^2 d\Omega = \int\left(\hat{\epsilon}_{k1}^{\dagger}\cdot|\langle\psi_f|d|\psi_i\rangle|^2+\hat{\epsilon}_{k2}^{\dagger}\cdot|\langle\psi_f|d|\psi_i\rangle|^2\right)d\Omega$$

$$= \int|\langle\psi_f|d|\psi_i\rangle|^2\sin^2\theta\, d\Omega \tag{27}$$

$$= \frac{8\pi}{3}|\langle\psi_f|d|\psi_i\rangle|^2$$

Which gives the total integrated transition rate for spontaneous emission to be:

$$\Gamma_{i\to f} = \sum_{a}\int\frac{d\Gamma_{i\to f,\alpha}}{d\Omega}d\Omega = \frac{\omega_k^3}{3\pi c^3\epsilon_0\hbar}|\langle\psi_f|d|\psi_i\rangle|^2 \tag{28}$$

The rightmost term is commonly defined as the transition dipole moment μ_{if}:

$$\mu_{if} = \langle\psi_f|d|\psi_i\rangle = \langle\psi_f|q\ r|\psi_i\rangle \tag{29}$$

Sometimes, the transition rate is rewritten in terms of the oscillator strength f_{12} defined as:[5]

$$f_{12} = \frac{2m\omega_{12}}{3\hbar q^2}|\langle\psi_f|d|\psi_i\rangle|^2 = \frac{2m\omega_{12}}{3\hbar}|\langle\psi_f|r|\psi_i\rangle|^2 \tag{30}$$

2.1.2 Photoelectric absorption process

Photoelectric absorption is the process by which a photon is absorbed by an atom, resulting in the ejection of an electron, leaving the atom in an ionized state. The strength of the absorption of photons by an atom is characterized by the absorption cross section σ_a. The absorption cross

section of matter has two strong and important dependencies: the cross section increases with atomic number approximately as Z^4, and the cross section decreases with energy approximately as E^{-3}. The absorption cross section of various atoms is shown in Figure 2.2, in which the cross sections have been scaled by their approximate dependencies.

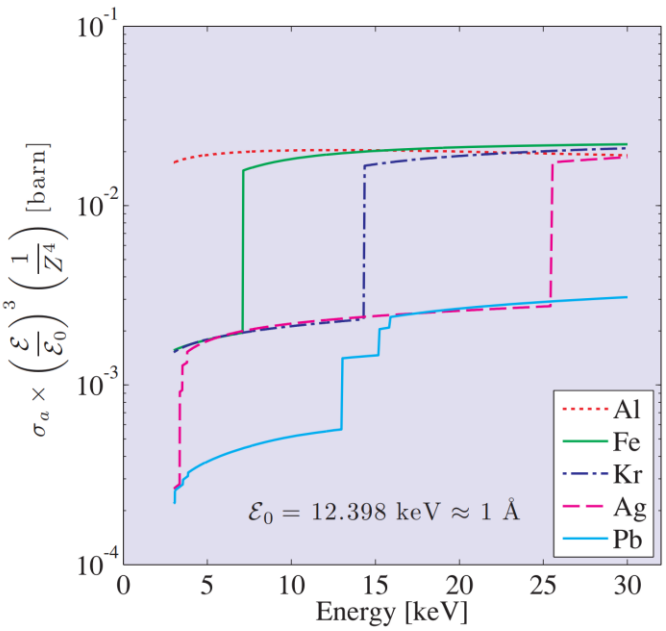

Figure 2.2: Scaled absorption cross section of various elements as a function of photon energy. The absorption cross section has been scaled by the approximate dependencies, namely, dividing by the ~Z^4 dependence on atomic number, and dividing by the ~E^{-3} dependence on energy. Figure reproduced from Als-Nielsen and McMorrow.[2]

As seen in the figure, the atoms (other than Pb) share an upper plateau, in which the cross section, after scaling by Z^4 and E^{-3}, is nearly constant. Moreover, by around 25 keV, the atoms depicted (except Pb) converge on nearly the same value of the scaled absorption cross section. In addition, another plateau is seen approximately one decade less in intensity. Taking Fe as an example, the transition in absorption from the higher to lower plateaus is seen to occur at ~7110 eV, the binding energy of the K-shell (1s) electrons. This discontinuous jump in absorption is referred to as an absorption edge and will be discussed in more detail in section 2.7.

A quantum mechanical description of photoelectric absorption was laid out in section 2.1.1. Similar to the derivation for emission, for the case of absorption, combining equations (16) and (18), the resulting expression is:

$$\Gamma_{i\to f,k\alpha} = \left(\frac{q}{m}\right)^2 \frac{\pi n_{k\alpha}}{V\epsilon_0\omega_k} \left|\langle\psi_f|e^{ik\cdot r}\hat{\epsilon}_{k\alpha}\cdot p|\psi_i\rangle\right|^2 \rho(E)\delta(E_f - E_i - \hbar\omega_k) \tag{31}$$

Where it is observed that the absorption transition rate depends on $n_{k\alpha}$, the number of photons with wavevector k and polarization α. Making the dipole approximation and changing the momentum operator to position operator (equation (21)) yields:

$$\Gamma_{i\to f,k\alpha} \approx \frac{\pi\omega_k}{V\epsilon_0} n_{k\alpha} |\langle\psi_f|\hat{\epsilon}_{k\alpha}\cdot d|\psi_i\rangle|^2 \rho(E)\delta(E_f - E_i - \hbar\omega_k) \tag{32}$$

This is the primary result for the absorption transition rate. It remains, of course, to evaluate the matrix element $\langle\psi_f|\hat{\epsilon}_{k\alpha}\cdot d|\psi_i\rangle$ to obtain the cross section. Various levels of approximation yield different approximate results, and such computations are often approximated using quantum chemical calculations such as density functional theory. For the simplified case of approximating the initial state $|i\rangle$ as either a free electron or the hydrogenic 1*s* wavefunction, a detailed discussion is presented in Als-Nielsen and McMorrow[2].

2.1.3 Relaxation after creation of core-hole

After a photoelectric absorption event, the atom is left in an unstable state with a hole in the orbital from which the electron was ejected. This unstable state is rapidly filled, with decay lifetimes for *K* shell core holes on the order of femtoseconds. For a *K* shell core-hole, there are only two decay channels: x-ray fluorescence and Auger emission.[6] These are illustrated in Figure 2.3. In both cases, an electron from a higher shell decays to fill the core hole; in x-ray fluorescence, the energy of the falling electron is radiated as a photon (termed radiative emission), and in Auger

emission, the energy is instead transferred to another electron which is ejected from the atom (termed non-radiative emission).

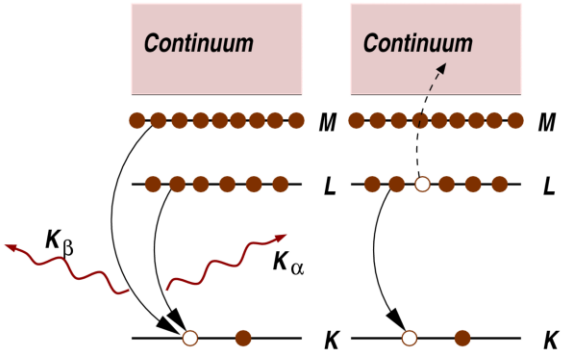

Figure 2.3: (Left) Schematic of fluorescence decay of the K-shell core hole excited state. (Right) Schematic of Auger decay of the K-shell core hole excited state. Figure from Newville.[7]

These two decay processes are competing, and the probability of either process depends on atomic number. The fraction of core hole events that result in radiative emission (x-ray fluorescence) is referred to as the fluorescence yield. The fluorescence yields of *K* and *L* shell core holes and the atomic number dependence is shown in Figure 2.4. In the context of tender x-ray emission spectroscopy, the elements that have K-shell fluorescence energies in the 1 – 5 keV range have atomic numbers 11 – 23 (Na – V), and thus have fluorescence yields from 3 – 25 %.

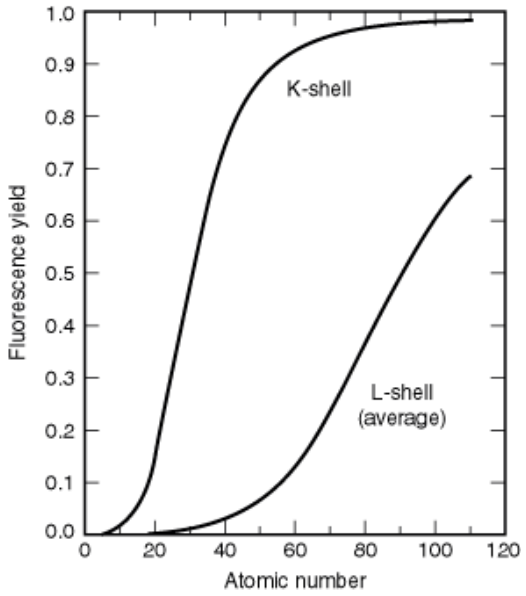

Figure 2.4: Dependence of the fluorescence yield (probability of radiative emission) on atomic number for *K* shell and *L* shell core holes. The *L* shell curve is the average of L_1, L_2, and L_3 core holes. Figure from x-ray data booklet, section 1.3,[8] using experimental data compiled by Krause.[6]

2.1.4 X-ray fluorescence process

X-ray fluorescence occurs when the core hole left behind in a photoexcited atom is filled by an electron from a higher shell with concomitant emission of a photon. Relaxation of the photoexcited atom occurs spontaneously, and thus x-ray fluorescence is a case of spontaneous emission and can be understood in the context of typical quantum mechanics approaches for calculation spontaneous emission rates, as was derived in section 2.1.1. The expression for the spontaneous emission rate, summed over polarizations is given in equation (28). From the expression, the primary dependence of the transition rate is on the dipole matrix element $\langle\psi_f|d|\psi_i\rangle$. Thus, calculating this matrix element is the task of computational approaches when modelling XES spectra. In chapter 10, linear response time-dependent density functional theory (LR-

TDDFT) computations are used to calculate these matrix elements for molecules to simulate the XES spectra.

This transition rate is related to the lifetime of the transition, and therefore also to the natural linewidth. From Fermi's golden rule, $\Gamma_{i\to f}$ is the constant transition rate, leading to exponential decay of the population of the excited state over time with radiative lifetime $\tau = 1 / \Gamma_{i\to f}$. In energy space, this translates to a Lorentzian distribution in energy, with a full-width half-maximum of $\hbar\Gamma_{i\to f}$.

2.2 X-RAY EMISSION SPECTROSCOPY (XES) OVERVIEW

X-ray emission spectroscopy (XES) is the measurement of the x-ray fluorescence energy spectrum with an energy resolution comparable to the natural linewidths of the transitions being measured. As discussed in section 2.1.4, the natural linewidth of XES features is related to their radiative decay rates, as understood in the context of Fermi's golden rule and time-dependent perturbation theory. For phosphorus and sulfur *K*-shell emission in the tender x-ray range, the *K*-shell lifetimes are on the order of ~ 1 femtosecond, corresponding to linewidths of ~0.5 eV. Thus, for XES measurements on these elements, high resolution and therefore high resolving power instruments are required: e.g. for P Kα fluorescence, the resolving power (E/ΔE) is 2014 eV / 0.5 eV ≈ 4000.

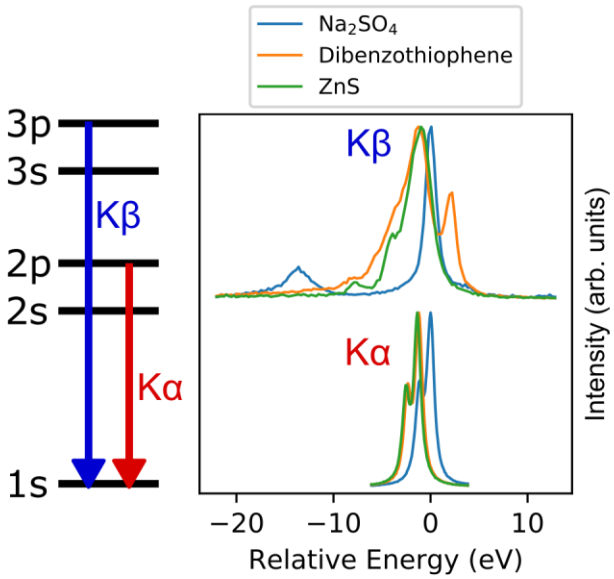

Figure 2.5: Kα and valence-to-core Kβ XES of sulfur in various compounds on an energy scale relative to the spectral positions of Na_2SO_4. Figure from chapter 10.

Representative spectra are shown in Figure 2.5 for Kα and Kβ XES of some sulfur compounds. From the energy scale, it is apparent that a high resolution is needed to discern the changes between the compounds for both emission lines.

The later chapters of this thesis explore the use of tender XES primarily on phosphorus and sulfur compounds, though the behavior of the emission lines is also similar for nearby third-row elements on the periodic table. Therefore, the following sections focus discussion on Kα and Kβ XES of phosphorus and sulfur, with some indications to references where similar effects have been demonstrated for other elements, such as chlorine, silicon and aluminum.

2.3 Kα XES OF PHOSPHORUS, SULFUR, AND NEARBY ELEMENTS

2.3.1 Kα Overview

When a 1*s* core hole (*K*-shell) is filled by an electron from the 2*p* shell, the fluorescence photon emitted is referred to as Kα emission. The Kα emission energies for different elements are

well separated in energy and have a nearly quadratic dependence on atomic number. The energies are well approximated by the formula:[2]

$$E_{K_\alpha}[\text{keV}] \approx 1.017 \times 10^{-2}(Z\text{-}1)^2$$

where Z is the atomic number of the element.

High resolution XES measurements of P Kα radiation of several compounds is shown in Figure 2.6. The Kα spectra in the figure is observed to consist of two main peaks, labelled $K\alpha_1$ and $K\alpha_2$, separated by ~0.86 eV in energy. These peaks are split by the spin-orbit interaction, and correspond to emission from the $2p_{3/2}$ and $2p_{1/2}$ levels with total angular momentum J of 3/2 and 1/2, respectively. The degeneracy of the levels is given by $2J + 1$, and is thus in the ratio of 4:2 for the levels $2p_{3/2}$:$2p_{1/2}$. Thus, as seen in Figure 2.6, the $K\alpha_1$ and $K\alpha_2$ components are in the approximate ratio of 2:1 in intensity. Though there are some deviations from the ideal 2:1 ratio, as noted in Mori et al. for the case of sulfur,[9] the cause of these deviations is not fully understood, but may be due to additional multiplet effects[10] or otherwise due to the presence of satellite features buried under the main $K\alpha_{1,2}$ peaks arising from 3*d* spectator holes or radiative Auger emission processes.[11]

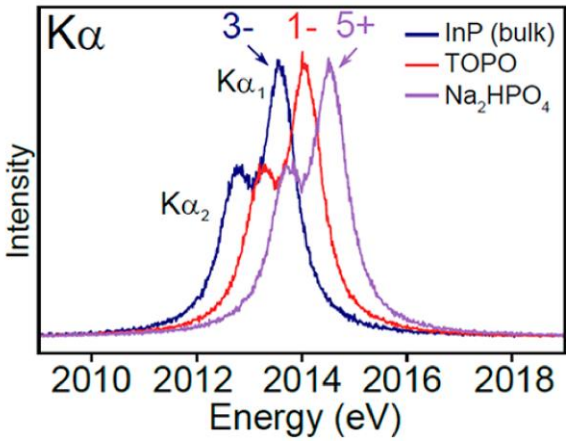

Figure 2.6: Kα XES measurements of phosphorus in a variety of compounds. The numerical labels at the top indicate formal oxidation states of P in the different compounds. These spectra are from the study described in detail in chapter 9.

2.3.2 Kα chemical shifts and sensitivity to oxidation state

For third-row elements, the 2*p* shell is a core shell, and the Kα emission is a core-to-core transition. Thus, changes in the chemical environment of the emitting atoms have only indirect effects on the Kα spectra. Indeed, despite the three phosphorus compounds of Figure 2.6 having drastically different bonding environments, covalencies, and formal oxidation states, the shape of the Kα spectra is seen to be unchanged. One effect that is clear, however, is a shift towards higher energies with increasing oxidation state. This can be qualitatively understood as changes in the amount of screening of the nuclear charge with changes in the valence population.

As illustrated in Figure 2.7, the 3*p* valence electrons of phosphorus have a finite probability of being found at distances between the nucleus and the 2*p* electrons (and the 1*s* electrons). This finite probability corresponds to some electronic repulsion which can slightly counteract the nuclear charge being experienced by the 2*p* electrons. Since oxidation state is an indication of the amount of charge in the valence shell localized around an atom, a higher oxidation state represents an atom with a reduced charge in the valence population. This reduced valence population reduces

the screening of the nuclear charge and increases the binding energy of the 2*p* and 1*s* shells. Since Kα emission corresponds to 2*p* → 1*s* transitions, the shift in the Kα energy represents the difference in the shifts of the 2*p* and 1*s* shells. For higher oxidation state, evidently the 1*s* shell shifts by a larger amount than the 2*p* shell, resulting in a shift of the Kα spectrum to higher energy. For phosphorus, the energy shift is ~0.8 eV between the oxidation state extremes of -3 and +5. The phosphorus Kα energy shift is very much related to the energy shift observed in 2*p* x-ray photoelectron spectroscopy (XPS, see section 2.8), though since XPS directly measures the effective binding energy of the 2*p* electrons (and not the 2*p* – 1*s* energy difference), a larger shift of ~ 8 eV is observed.

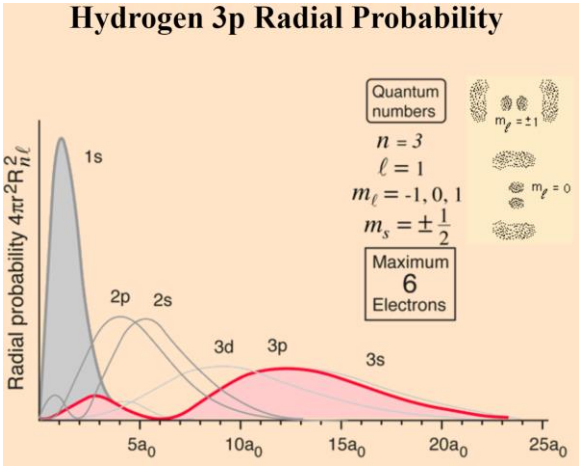

Figure 2.7: Radial probabilities of the hydrogen wavefunctions. Figure from Hyperphysics by Carl Nave.[12]

Though the above considerations were made in the context of phosphorus Kα XES, they hold equally well in the case of sulfur and chlorine, as summarized well by the results of Petric and Kavčič[13] shown in Figure 2.8. Similar effects have also been observed for silicon,[14,15] aluminum[16,17] and magnesium.[17,18]

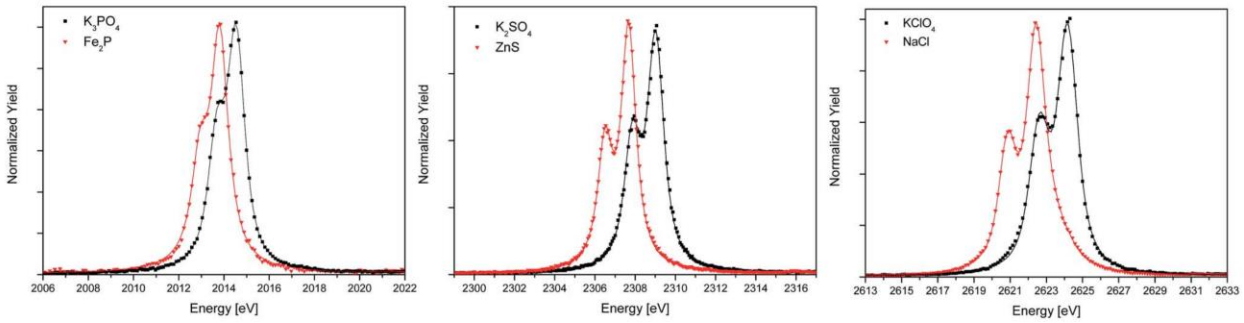

Figure 2.8: Proton-induced Kα XES of (left) phosphorus, (center) sulfur, and (right) chlorine, showing the energy shift towards higher energy between compounds of reduced and oxidized species of each element. Figure from Petric and Kavčič.[13]

The discussion above is made more concrete by comparing Kα energy shifts with theoretical calculations of valence electron populations. Petric et al.[19] have compared the Kα shifts of a number of phosphorus compounds with valence electronic configurations calculated by DFT, and observed strong correlation. Mori et al.[9] performed a similar comparison for Kα energy shifts of sulfur compounds, and found similar good agreement with DFT calculated valence populations. In chapter 10, we compare Kα energy shifts of a wide range of sulfur compounds with theoretical calculations made using linear response time-dependent density functional theory (LR-TDDFT), and find stronger agreement with the magnitude of energy shifts made by LR-TDDFT compared to a ground-state DFT approach.

With the clear Kα energy dependence on oxidation state, one opportunity presents itself immediately. If a sample contains a population of mixed oxidation states, a measurement of the Kα spectrum can be used to quantitatively measure the proportion of each component. Such a measurement of P Kα on a sample of ZnS-shelled InP quantum dots is illustrated in Figure 2.9, from the study described in chapter 9. The spectrum shows clearly three peaks which can be fit by two shifted Kα lineshapes, one representing phosphorus in a reduced oxidation state and one

representing oxidized phosphorus. By this fitting procedure, the relative components are measured quantitatively, and in this case matched well with measurements made by ^{31}P SSNMR.

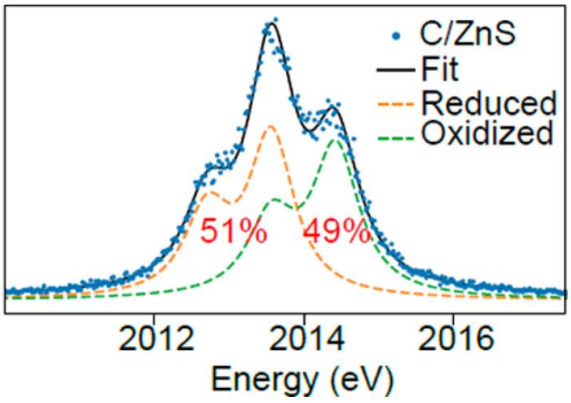

Figure 2.9: Phosphorus Kα XES of a ZnS-shelled InP quantum dot sample, illustrating the quantitative decomposition into reduced and oxidized components. Figure from chapter 9.

2.3.3 Kα satellite features

In addition to the main doublet $K\alpha_{1,2}$ spectrum, satellite features exist at higher energy that are several times less intense. These features include the Kα', $K\alpha_3$ and $K\alpha_4$ shown in Figure 2.10, and are a result of multiple ionization events in which additional electrons are ejected along with the ejection of a 1*s* electron. It should be noted that the probability of two independent x-ray photons ejecting two electrons within the lifetime of the excited state (~1 fs) is vanishingly small for typical x-ray fluxes (though these nonlinear effects may be possible with x-ray free electron lasers[20]), thus these events occur when a single photon (or incident charged particle) ejects two core electrons. This implies that the photon energy required for such events is the sum of the two binding energies of the electrons, and for incident photons below this threshold, these satellite features would not be observed.[21,22] The relative intensities of these features are discussed in detail by Graeffe et al.[14] in the context of silicon Kα satellites. Additional Kα satellites beyond those shown in Figure 2.10 have been measured by Heirwegh et al.[23] for magnesium, aluminum, and

silicon using proton-induced XES, and shows features from triple and quadruple ionization events. There is some conjecture that these satellite features could have increased chemical sensitivity, though Yasuda and Kakiyama[24] in their observations of satellite features in S Kα were unable to observe significant effects.

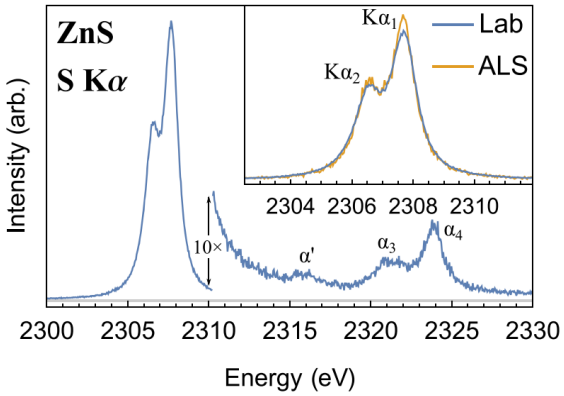

Figure 2.10: ZnS S Kα spectrum showing satellite features at energies above the main $K\alpha_{1,2}$ transitions. Figure from chapter 5.

2.4 Kβ Valence-to-Core XES of Phosphorus, Sulfur, and Nearby Elements

In addition to the Kα $2p \rightarrow 1s$ transition, the next strongest emission that is possible for a core-hole in the *K*-shell (1*s*) is the dipole-allowed $3p \rightarrow 1s$ transition, referred to as Kβ. For the elements Al – Cl, this transition is of particular interest because the 3*p* shell is the valence shell, so that the transitions that make up the Kβ emission come from the valence electrons involved in bonding and chemical interactions.

The following discussion focuses on Kβ XES features of third-row elements, in particular phosphorus and sulfur, as those elements are the focus of later chapters of this thesis. The Kβ XES features of nearby third-row elements have also been shown to have significant similarity, especially in the work by Takahashi[18] for silicon and aluminum, and the work by Taniguchi[25] in the case of chlorine. For these elements, the 3*p* shell corresponds to valence electrons, and

therefore the Kβ spectrum corresponding to $3p \rightarrow 1s$ transitions directly probes the valence electronic states.

As discussed in section 2.1.4, the transition rates can be expressed in the context of Fermi's golden rule as $\Gamma \propto \sum_{i,f} |\langle f|r|i\rangle|^2$. In a single-particle picture, the transitions can be thought of as electrons initially in a valence state transitioning to the available 1*s* state of the core-hole. Thus, in principle, if the wave-functions of all initially occupied valence states were known, the transition rate from each could simply be calculated by evaluating the coordinate operator r against the wave-function overlaps with the atomic-like 1*s* state. The relative energies of the initial valence states and the strength of the wave-function overlap matrix elements would yield the shape of the spectral transitions and combined with broadening effects from the finite lifetime of the 1*s* state, the Kβ spectrum would be completely predicted.

The challenge then lies in the knowledge of the initial valence states. For molecules or compounds with more than a few atoms, exact quantum mechanical calculations are infeasible, and exact structure of valence states is thus not known. This is a core problem in chemistry and is the subject of much effort in the field of computational quantum chemistry. There are many approaches used to model electronic structure, and several of these have been applied in the computation of valence-to-core XES spectra, including molecular orbital calculations,[26] *ab initio* multiple scattering calculations FEFF[27-29] ground-state density-functional theory (DFT) methods,[30-32] and linear-response time-dependent density functional theory[29,33,34] (LR-TDDFT) techniques. A full analysis of these techniques is beyond the scope of this work, but useful discussions can be found in the works of Rehr et al.[27] (FEFF), Lee et al.[30] (DFT), and Zhang et al.[33] (LR-TDDFT).

The following sections focus on a phenomenological description of spectral features in the Kβ emission. Detailed discussion of theoretical results using LR-TDDFT and a comparison with experimental spectra in the case of the sulfur is the subject of chapter 10.

2.4.1 Kβ intensity relative to Kα

The Kβ emission is lower in intensity than the Kα transition. The ratio of intensities of Kβ/ Kα has a complicated dependence on atomic number Z, as shown in Figure 2.11. For the elements Al – Cl the intensity increases from ~ 2 – 10 % as the number of 3*p* electrons increases. The intensity ratio is relatively constant throughout the transition metals, then continues to increase.

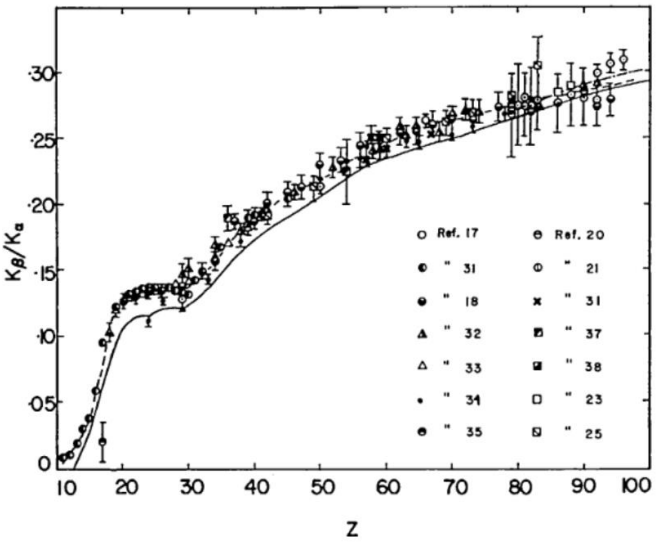

Figure 2.11: Ratio of intensities of x-ray emission lines, Kβ/ Kα, plotted with dependence on atomic number. Figure from Salem et al.[35]

The reason for the lower intensity of Kβ relative to Kα has a simple explanation. From the discussion in section 2.1.4 of x-ray emission in first-order time-dependent perturbation theory, recall that the transition rate is proportional to the square of matrix elements of the form $\langle f|r|i\rangle$, for initial and final states i and f. Expanding in a coordinate basis, the expression becomes:

$$\langle f|r|i\rangle \rightarrow \int r\langle f|r\rangle\langle r|i\rangle \, d^3r \rightarrow \int r \, \Psi_f(r)\Psi_i(r) \, d^3r$$

where Ψ_i (Ψ_f) is the initial (final) wave function. Thus the transition rate depends on the dipole character of spatial overlap of the initial and final state wave functions. This overlap is smaller for wave functions that have larger differences in principal quantum number.

A calculation in terms of hydrogenic wave functions gives a reasonable first estimate:

$$\int z\, \Psi_{100}(r)\Psi_{210}(r)\, d^3r \approx 0.37$$

$$\int z\, \Psi_{100}(r)\Psi_{310}(r)\, d^3r \approx 0.15$$

$$\frac{0.15^2}{0.37^2} \approx 0.16$$

which is seen to be a reasonable estimate of the Kβ/Kα intensity ratio for elements with filled 3*p* shells.

Though the behavior can be approximately understood with a simplified description, the precise nature of the Kβ/Kα intensity ratio depends on the details of the initial and final states, and several authors have attempted to use small changes in Kβ/Kα intensity ratios as signatures for information regarding the chemical state of the element in question.[36-39]

2.4.2 Kβ XES spectral features and sensitivities

Sulfur Kβ spectra of a variety of compounds are shown in Figure 2.12. As already seen with these few examples, the spectral features and range of energies are very different than the Kα spectrum. In contrast to S Kα XES, where the spectra had identical shapes shifted in energy, in the Kβ spectrum a variety of features emerge between compounds. The energy span of the spectral features is also much larger. In the case of S Kα, spectra of a single oxidation state were around 2 eV wide and the spectra shifted by around 1.4 eV going from -2 to +6 oxidation state. As seen in the case of the Kβ spectrum of Na_2SO_3 (Figure 2.12, middle-bottom), between the highest and lowest energy features is a span of around 20 eV. It should be noted that these features are not multiple-ionization satellites such as those observed in section 2.3.3 for S Kα. As will be

elaborated further below, these features in the Kβ spectrum originate from the valence electronic structure. Thus, the information about chemical state, and in particular the valence electronic configuration, is much more direct in the case of Kβ spectra as compared with Kα.

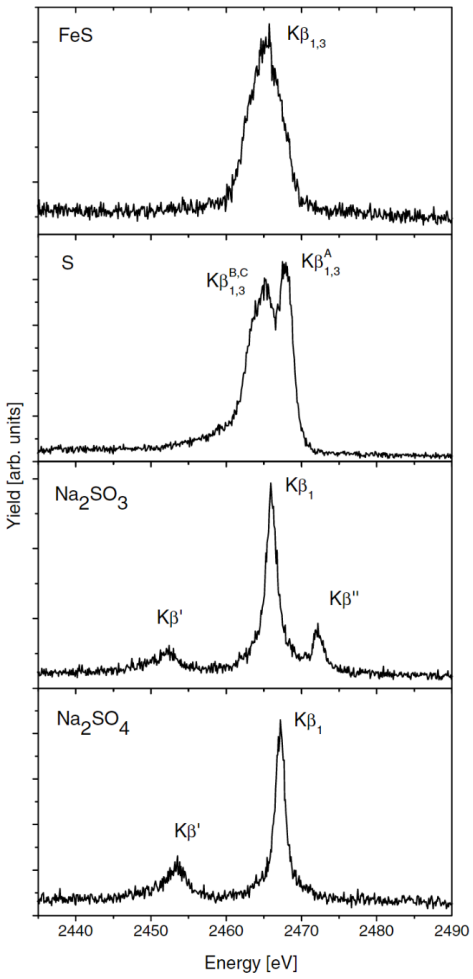

Figure 2.12: Sulfur valence-to-core Kβ spectrum of a number of compounds. Figure from Kavčič et al.[40]

As observed in Figure 2.12, the sulfur Kβ spectrum generally consists of a dominant feature known as $K\beta_{1,3}$ near 2464 eV, with some compounds showing isolated satellites lower in energy known as Kβ', and some compounds with a high energy satellite feature referred to as Kβ''. The main $K\beta_{1,3}$ feature can have a variety of additional structure, including shoulders (e.g. FeS, Figure 2.12 top) and separate, clearly defined peaks (e.g. S, Figure 2.12 middle-top).

For sulfur in organic compounds, the Kβ spectra contain a rich variety of spectral features. Figure 2.13 show Kβ experimental and theoretically calculated spectra for a variety of organosulfur compounds. The data shown is a subset from the study discussed in detail in chapter 10. For these compounds, it's evident that the changes in the valence electronic structure produce a variety of transitions and spectral features. The spectra are observed to be sensitive to the valence electronic structure, and thus the detailed bonding environment of the sulfur being measured. For example, comparing the spectra for dibenzothiophene and thianthrene, despite the sulfur being bonded directly to two phenyl groups in both cases, the change in bonding structure of the rings causes a different electronic structure, which produces clear changes in the spectra, including the width of the main feature and the energy separation of the high-energy shoulder. Similarly, comparing dimethyl sulfone and diphenyl sulfone, despite identical nearest bonding neighbors of the sulfur, the spectra vary in the relative intensities of peaks and the shoulders of the main feature. For 2-mercaptopyridine and 4-mercaptopyridine, the spectra seem to be driven mostly by the sulfur-carbon double bond, producing nearly identical spectra.

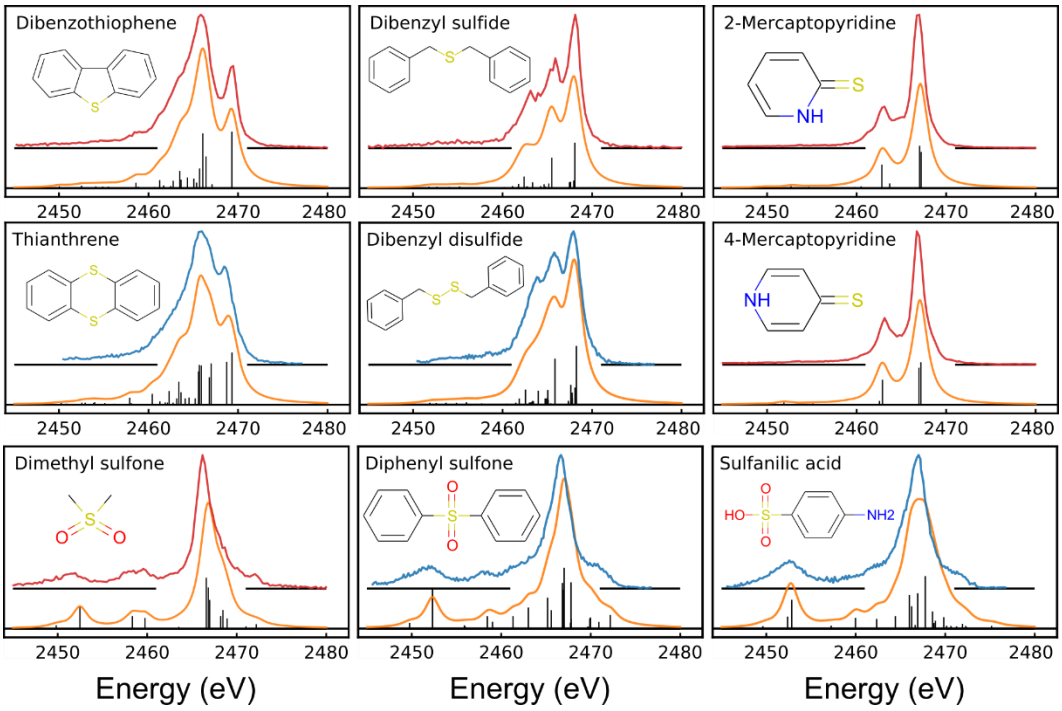

Figure 2.13: Sulfur valence-to-core Kβ spectrum of organosulfur compounds. Experimental spectra (red and blue) are compared with theoretical calculations with LR-TDDFT (black sticks are individual transitions, Lorentzian-broadened spectra in orange). These figures are a subset of data from the study in chapter 10.

Figure 2.13 also compares the experimentally observed spectra with theoretical calculations using linear-response time-dependent density functional theory (LR-TDDFT). As apparent in the figure, the theoretical predictions agree very well with the observed spectra. The theoretical calculations allow finer interpretation of the variety of spectral features observed and their differing origins. The subject of the interpretation of the calculations and a further analysis of the spectra is given in detail in chapter 10.

Alonso-Mori et al.[31] measured a number of inorganic sulfide compounds and observed a variety of fine structure, as seen in their spectra shown in Figure 2.14. Similar to the organic compounds discussed above, the fine details of the spectra depend on the details of the electronic structure. They observe some clear trends in spectral features, including in particular the very

similar spectra of ZnS, CdS (not included in Figure 2.14, see original work[31]), and HgS which all have filled valence *d*-shells: Zn $3d^{10}$, Cd $4d^{10}$, and Hg $5d^{10}$, suggesting a similar valence electronic structure even with different cations and despite different local symmetries (T_d for ZnS and CdS; distorted O_h for HgS). Among the five Cu/Fe containing sulfides, similar spectral features are also observed, for example the high-energy shoulder feature D that is not well-separated in the sulfides that do not contain Cu/Fe. Interestingly, they note that the among the Cu/Fe sulfides, only $(Cu,Fe)_{12}Sb_4S_{13}$ shows the low-energy feature labelled A. Since $(Cu,Fe)_{12}Sb_4S_{13}$ is the only Cu/Fe compound that contains a full *d*-orbital provided by the Sb atoms, and the same A feature is observed among the filled *d*-shell compounds ZdS, CdS, and HgS, it seems apparent that feature A is likely related to the presence of a filled *d*-orbital.

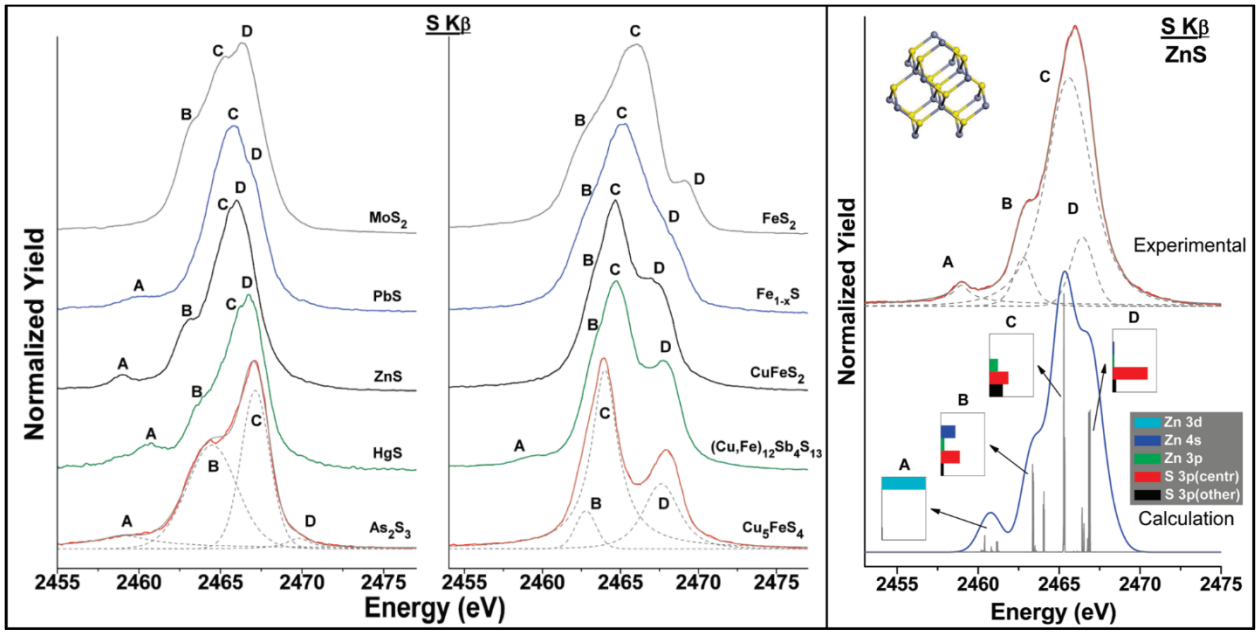

Figure 2.14: Sulfur valence-to-core Kβ spectrum of inorganic sulfide compounds. Figure from Alonso-Mori et al.[31]

To further investigate the valence structure, Alonso-Mori et al. also performed calculations using a ground-state DFT approach, shown in Figure 2.14 right. Their computations reproduce

the experimental spectra well and, as seen in the atomic basis character of the transitions in the bottom of the figure, their computations are consistent with their observations about the relation of the feature A with the cation *d*-shell electrons. Of the compounds in Figure 2.14, those authors were only able to achieve convergence for the ZnS system, and they remark upon the difficulty of modelling the sulfide compounds in their approach. In chapter 10, theoretical modelling is performed for additional sulfide compounds using the LR-TDDFT approach applied above to the organosulfur compounds.

Though a complete understanding of fine spectral details generally requires quantum chemical calculations, there are a few general features of Kβ spectra of third-row elements that serve as signatures of the atomic environment of the emitting atoms. Perhaps the most apparent and well-known is the Kβ' peak which appears as an isolated feature around ~15 eV lower than the main $K\beta_{1,3}$ peak. This feature appears in particular in compounds with oxygen bonds to third row elements. Spectra of XO_4 and XO_3 (X = P, S, Cl) compounds are shown in Figure 2.15. Comparing the spectra of the P, S, and Cl compounds also shows the similarity of spectral shapes for similar chemical environments for the different third-row elements. Similar spectra for oxide compounds of Si and Al are reported by Takahashi.[18] The XO_4 compounds with T_d symmetry show a main $K\beta_{1,3}$ peak with weak low- and high-energy shoulders, along with the well-separated Kβ' peak. The XO_3 compounds with C_{3v} symmetry show those same features, with an additional high energy feature labelled $K\beta_{xx}$ for S and Cl, though not for P.

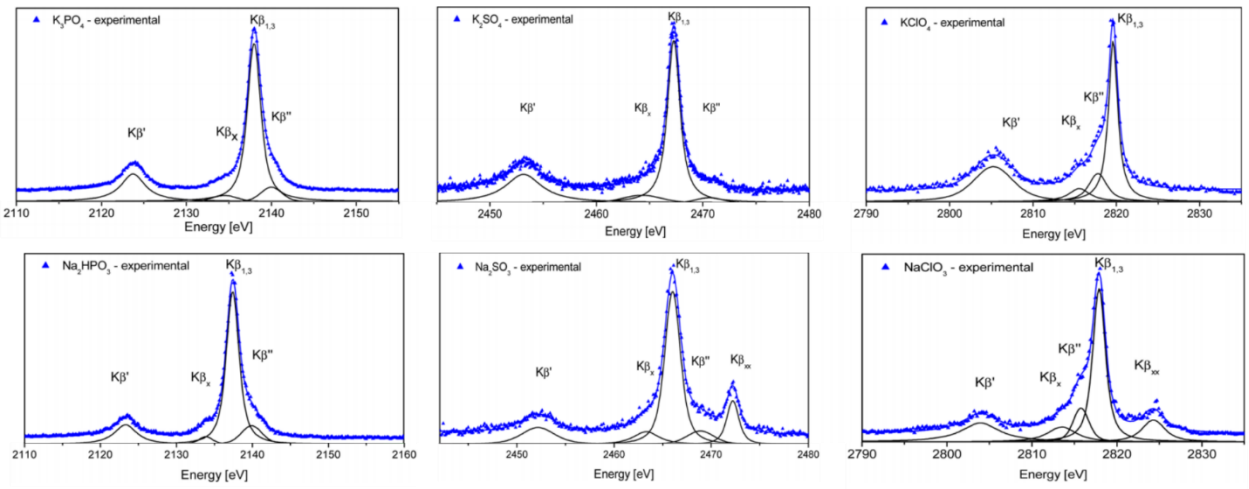

Figure 2.15: Valence-to-core Kβ spectrum of oxide anions of P, S, and Cl. Figure adapted from Petric et al.[32]

Supported by DFT calculations, the Kβ' feature of the oxide compounds is observed to originate due to hybridization of the oxygen 2*s* orbitals with the phosphorus 3*p* valence. One question that arises is whether other bonded atoms can similarly hybridize and demonstrate isolated features in the Kβ spectrum. Indeed, such features occur, as shown in Figure 2.16 for the case of phosphorus compounds containing P–N, P–O, and P–F bonds.

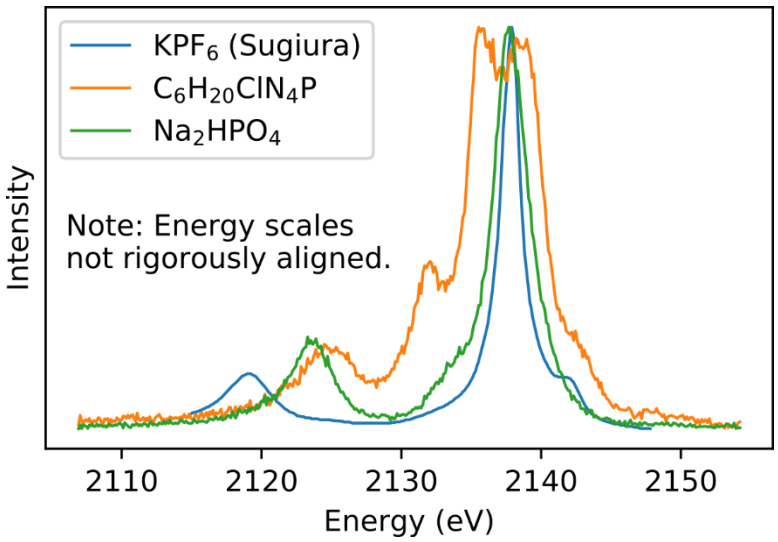

Figure 2.16: Phosphorus valence-to-core Kβ spectrum of compounds with P–N, P–O, and P–F bonds. Spectra of aminotris-(dimethylamino)phosphonium chloride ($C_6H_{20}ClN_4P$) and Na_2HPO_4 were measured on the spectrometer of chapter 5. The KPF_6 spectra was digitized from the data of Sugiura et al.[41] The note in the figure indicates that the energy scale between the measurement of Sugiura et al. and the other measurements were not rigorously aligned. The energy scale of Sugiura et al. is from the digitized figure, and the other measurements were aligned using the reported energy positions of Na_2HPO_4 by Petric et al.[19]

Figure 2.17 shows the Kβ spectra from compounds of silicon, aluminum, and sulfur. The similarity across these spectra shows the similar sensitivities of the spectra for different third-row elements, as well as the similar effect of the spectra from changes in bonding neighbors. The spectra are reversed because the x-axis is given as wavelength, so the Kβ' features appears as a peak on the right-hand side of the spectra. Similar to Figure 2.16, the Kβ' peak shifts in energy for different bonding atom such as oxygen, chlorine, and fluorine.

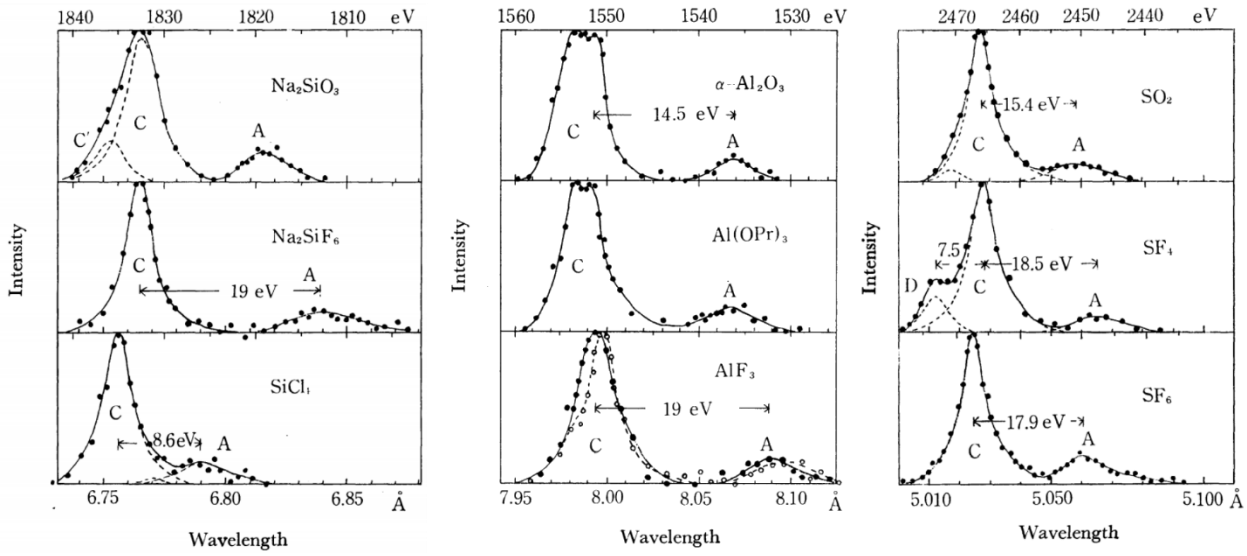

Figure 2.17: Valence-to-core Kβ spectrum of Si, Al, and S compounds. Similar spectral features are seen among the different emitting elements, along with similar sensitivities of the Kβ' satellite (labelled A). Figures from Takahashi.[18]

In addition to the Kβ' feature which can give information about the identity of bonded neighbors, the Kβ spectrum is also sensitive to the symmetry of compounds relative to the emitting atom. One example of this manifests in the spectra shown in Figure 2.15 between the T_d symmetry of XO_4 ions and the C_{3v} symmetry of XO_3 ions (X = P, S, Cl). For sulfur and chlorine, the C_{3v} symmetric SO_3^{2-} and ClO_3^{1-} ions both exhibit a $K\beta_{xx}$ peak on the high energy side of the spectrum. Petric et al.[32] show that this peak arises from a π-antibonding MO, which is created from the X $3p_z$ and O $2p_z$ atomic orbitals in a way which is allowed by the C_{3v} symmetry but does not occur in the T_d case. The $K\beta_{xx}$ peak does not arise in the Na_2HPO_3 spectra, which the authors demonstrate is due to the hydrogen being bonded directly to the P atom in the HPO_3^{2-} ion, modifying the electronic structure in a way that the $K\beta_{xx}$ disappears despite the C_{3v} symmetry. It may be the case that the spectrum of a compound such as $P(OCH_3)_3$, in which the P is bonded directly only to three oxygen atoms without the perturbing hydrogen, could show the $K\beta_{xx}$ peak as well.

Another demonstration of symmetry effects is shown in the Kβ spectra of sulfuric acid in the study of Niskanen et al.[42] They found that shoulders on the low energy side (named $K\beta_x$) and on the high energy side (named Kβ'') of the main $K\beta_{1,3}$ change intensity with changes in concentration of the sulfuric acid. Their measured spectra are shown in Figure 2.18, along with calculations of the spectrum using DFT of sulfuric acid at different concentrations based on *ab initio* molecular dynamics simulations. In particular, Niskanen et al. reported that the lowest energy portion of the $K\beta_x$ shoulder is present in H_2SO_4 system but not in the purely symmetric SO_4^{2-} ion. They showed that the $K\beta_x$ peak in H_2SO_4 arises from a molecular orbital that is spherically symmetric in the case of the SO_4^{2-} ion and therefore dipole-forbidden, whereas the addition of the two protons in H_2SO_4 breaks the symmetry of the molecular orbital and allows a dipole transition.

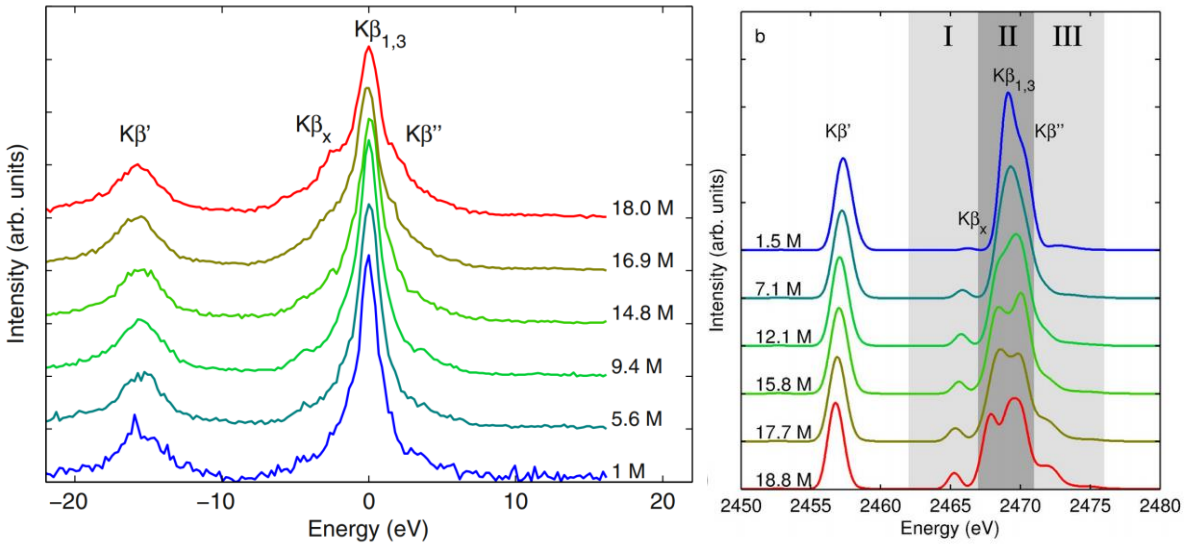

Figure 2.18: (left) Sulfur Kβ experimental spectra of sulfuric acid at different concentrations. (right) DFT calculated S Kβ spectra of sulfuric acid based on *ab initio* molecular dynamics simulations.

2.4.3 Polarization effects and anisotropic emission

In most valence-to-core XES measurements, the samples being measured are unoriented and thus the resulting fluorescence is isotropic. However, in oriented samples such as single crystals, anisotropic emission can occur. Such an example is shown in Figure 2.19 for the case of Fe emission in a single crystal of $[Rh(En)_3][Mn(N)(CN)_5]\cdot H2O$ measured by Bergmann et al.[43] As the emission angle of the detector relative to the symmetry axis of the crystal is changed, the spectra changes, most distinctly in the 'cross-over' Kβ'' satellite peak, which is known to be due to mixing of the ligand 2*s* (in this case N) with the metal. In the bottom of Figure 2.19, the intensity of the Kβ'' feature is observed to follow a $\sin^2\theta$ dependence for angle θ between emission direction and direction of the Fe–N bond, i.e. the pattern of a linearly polarized dipole transition.

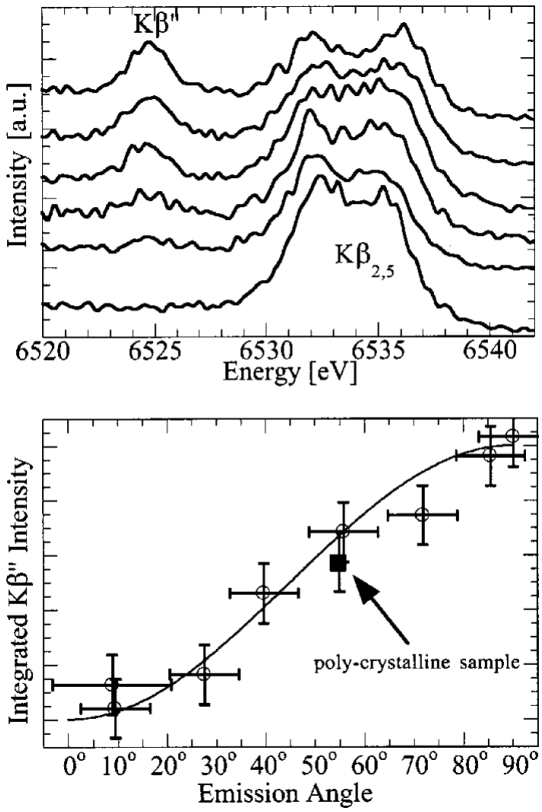

Figure 2.19: (top) Anisotropic valence-to-core XES of Fe in a single crystal of $[Rh(En)_3][Mn(N)(CN)_5]\cdot H2O$. Emission angles relative to the C_6 axis of the crystal for the

above spectra are, top-to-bottom: 90°, 72°, 56°, 39°, 26°, 8°. (bottom) Integrated intensity of the Kβ'' satellite feature relative to emission angle. Figure from Bergmann et al.[43]

From the above example, it's clear that additional information can be obtained about the valence electronic states by analyzing the polarization of valence emission features, sometimes referred to as polarized XES (PXES). Such observations have been reported by several authors,[44-49] including the notable review by Dräger and Brümmer.[50]

In the tender x-ray energy range, PXES has been performed on single crystal black phosphorus by Hayasi et al.[49] Figure 2.20 shows the PXES spectra of single crystal black phosphorus measured with polarizations along the symmetry axes of the black phosphorus layered crystal structure. Hayasi et al. also compared their results to theoretical calculations based on self-consistent pseudopotential methods and found good qualitative agreement. In particular, the strong polarization of the highest energy peak (~2141.5 eV) along the z-axis direction which is almost absent along the y-axis direction was well reproduced.

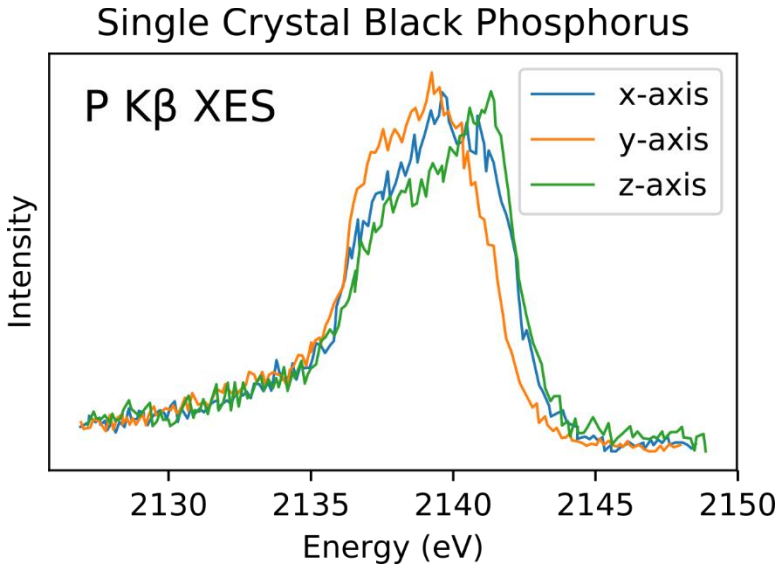

Figure 2.20: Valence-to-core polarized XES measurement of P in single crystal black phosphorus. The x, y, and z axes are relative to the crystal axes of black phosphorus; for an

illustration of these orientations relative to the crystal structure, see the original work. Figure produced from digitized data from Hayasi et al.[49]

With the LR-TDDFT theoretical approach to calculating XES spectra employed in chapter 10, it is possible to extract information about the transition dipole moment vector directions which in principle contain information about the polarization of spectral features. In chapter 10, figures are produced projecting these directions onto coordinate axes which may correspond to such a PXES measurement. That being said, an interesting open question remains. The projection procedure in chapter 10 implicitly assumes that each feature acts as a linear polarized dipole oscillator with $\sin^2\theta$ dependence on the emission direction. However, in pure atomic transitions, dipole emission can occur with linear polarization ($\Delta m = 0$) or circular polarization ($\Delta m = \pm 1$). These different cases produce anisotropic emissions with distinct patterns illustrated in Figure 2.21. At present, no distinction is made between these possibilities in the calculations of chapter 10. Such a distinction is also not clearly made in the literature, for example the work by Bergmann et al.[43] tacitly assumes the $\sin^2\theta$ dependence. Recent work by Maganas et al.[51] briefly mentions the effect of the phase of the transition dipole moment relative to *z* and *xy* directions of molecules in their study, but the connection to nonresonant PXES is not directly addressed. Thus, additional theoretical interpretation and experimental measurement of PXES and the associated anisotropies may be required to fully understand this issue.

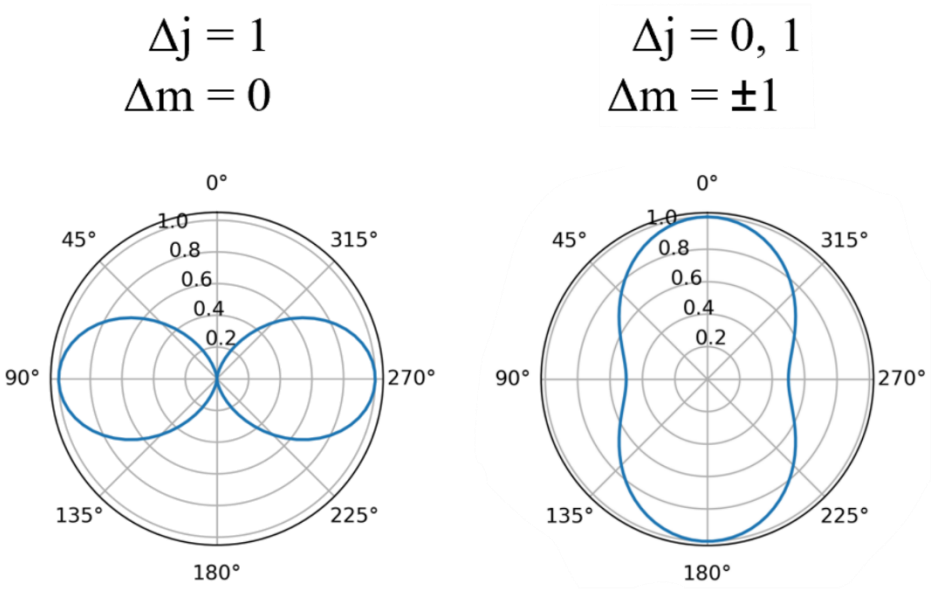

Figure 2.21: Polar plot of emission intensity for dipole transitions that are (left) linear polarized along the z-axis and (right) circularly polarized with rotation in the xy-plane. In both plots, the emission angle is the polar angle relative to the z-axis, and the patterns are azimuthally symmetric.

2.4.4 Kβ satellites

In analogy to the Kα satellites discussed in section 2.3.3, multiple-ionization satellites can also occur in the Kβ spectrum. These Kβ satellites are significantly weaker than the Kβ main spectral features, and therefore difficult to observe. Despite their low intensity, measurements have been reported for multiple-ionization Kβ satellites for sulfur by several authors.[11,52]

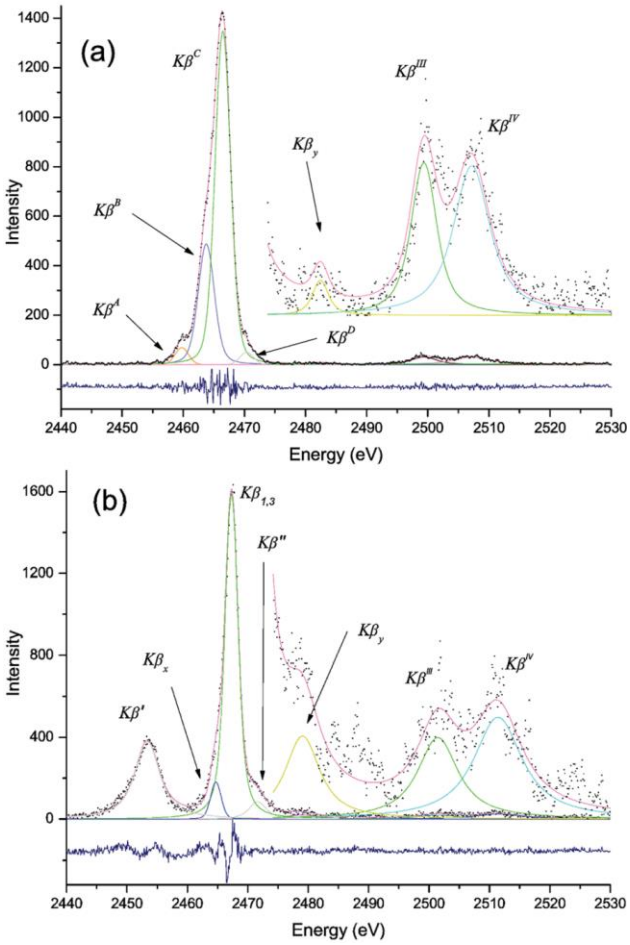

Figure 2.22: Kβ spectra of sulfur in ZnS and $CaSO_4$ measured using a spectrometer coupled to a scanning electron microscope. The $K\beta^{III}$ and $K\beta^{IV}$ lines are multiple-ionization satellites from double vacancies. Figure from Sánchez et al.[11]

2.5 Non-resonant vs. resonant (XES, RXES, & RIXS)

The discussion of XES in this thesis is focused on non-resonant XES; that is, XES measurements of atoms that are excited with broadband incident x-rays or x-rays that are tuned far above the absorption edge. If the incident x-rays used to stimulate the fluorescence are monochromatic (e.g. synchrotron beamline radiation) and tuned very close to the absorption edge of an atom, resonant effects can be observed.

One example of this is resonant XES measurements (RXES) of lithium sulfur battery materials by Kavčič et al.[53] Shown in Figure 2.23 are RXES measurements of elemental sulfur

and Li_2S_4 made at two different excitation energies centered at 2470.7 eV and 2473.0 eV. The incident excitation energies are of course not perfectly monochromatic, and in this case have a width of ~0.36 eV. The measurements were made at beamline ID26 at the European Synchrotron Radiation Facility (ESRF), using a beamline with a cryogenically cooled Si(111) double crystal monochromator with energy resolution of 0.36 eV at the sulfur K-edge energy (2472 eV).

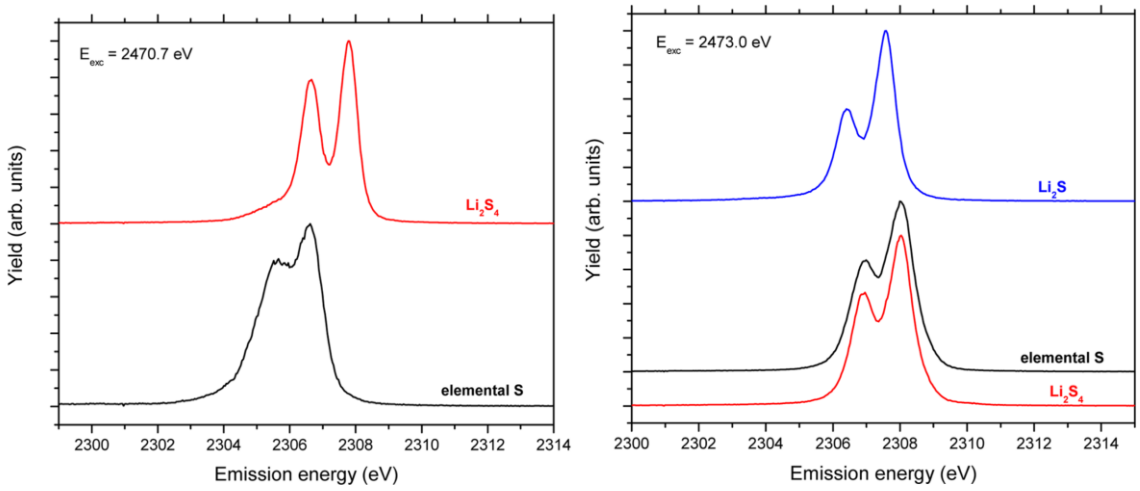

Figure 2.23: Resonant-XES (RXES) of elemental sulfur and lithium sulfide materials relevant to lithium-sulfur battery research. Figure from Kavčič et al.[53]

As seen in Figure 2.23 (right), at an excitation energy of 2473.0 eV, the elemental sulfur and Li_2S_4 RXES spectra are nearly indistinguishable, whereas at an excitation energy of 2470.7 eV (left), there is a pronounced change in both spectra, allowing them to be distinguished. This change in response allowed Kavčič et al. to monitor the transformation of sulfur in an operando study of lithium-sulfur batteries. Using these two energies, they were able to monitor the formation of lithium polysulfide (Li_2S_X) from sulfur at energy 2470.7 eV, as well as specifically monitoring the formation of Li_2S compared to Li_2S_X using the shift in energy between the spectra at 2473.0 eV.

If RXES spectra are taken in energy steps over the whole range of energies around an absorption edge, a 2D dataset is obtained, as shown in Figure 2.24 for the measurement of Li_2S_4 by Kavčič et al.[53] This type of measurement is referred to as resonant inelastic x-ray scattering (RIXS), and the plot is termed the "RIXS plane." With simultaneous control of both the exciting and emitting energies, both the energy and the momentum of the scattered photons is measured, yielding information about a range of excitations and their momentum dependence, including charge-transfer excitations, plasmons, *dd* excitations, magnons and phonons. Detailed discussions of RIXS experimental setups and the information available in such measurements are given in the review articles by Ament et al.[54] and Glatzel and Bergmann.[55] It should be noted that RIXS plane measurements are costly, as they require full integration of emission spectra at a full range of incident energies, and are thus a "photon-hungry" experiment that is limited by the availability of incident flux. That being said, upgrades of many existing synchrotron beamlines are seeing large increases in flux available that increase the accessibility of these techniques.

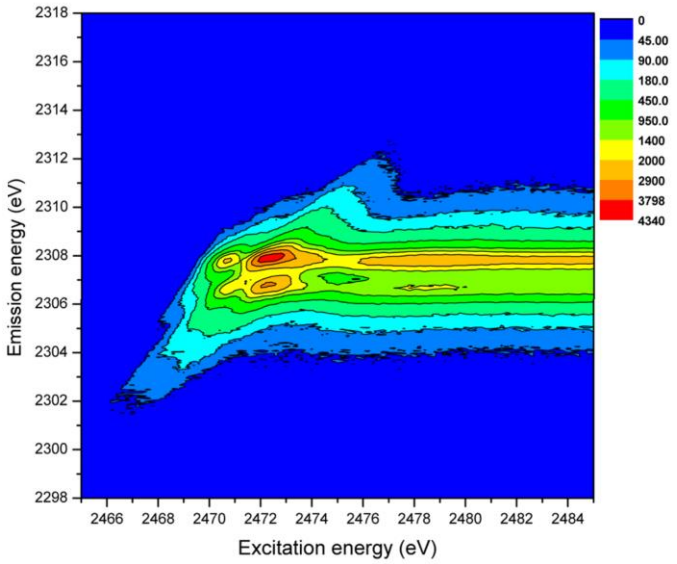

Figure 2.24: Resonant inelastic x-ray scattering (RIXS) measurement of Li_2S_4. The vertical axis represents the emission energy being measured, tuned to the energy of sulfur Kα emission. The horizontal axis corresponds to the incident excitation energy which is scanned through the sulfur K-edge absorption energy. When the full range of energies for both emission and excitation is measured, the resultant figure is commonly referred to as the "RIXS plane." Figure from Kavčič et al.[53]

Given a complete RIXS plane or, alternatively a direct measurement of the emission intensity at one fluorescence energy as a function of incident photon energy, it is possible to obtain an enhanced absorption spectrum, a technique referred to as high energy resolution fluorescence detected (HERFD) XAS. In a typical XANES measurement, the resolution of observed features is limited by the natural linewidth (i.e. finite lifetime) of the core-hole created in the excitation. Because of the effects of resonant excitation in the RIXS measurement, it is possible to reduce the lifetime broadening by taking a slice through the RIXS plane. For example, taking a horizontal slice through Figure 2.24 yields the HERFD spectrum for Li_2S_4 shown in Figure 2.25. A discussion of this reduction in broadening from lifetime effects is given in Glatzel and Bergmann,[55] and details of the HERFD technique are discussed by several authors.[56-58]

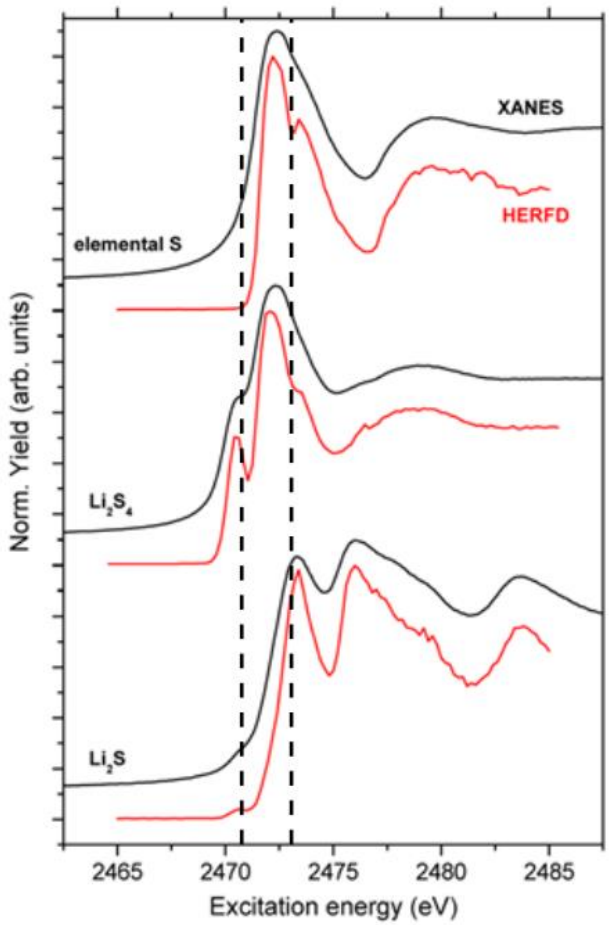

Figure 2.25: XANES and HERFD measurements of elemental sulfur and lithium sulfide materials relevant to lithium-sulfur battery research. Vertical lines have been added at the excitation energies (2470.7 eV and 2473.0 eV) of the two RXES spectra of Figure 2.23. Figure from Kavčič et al.[53]

2.6 XES OF OTHER ELEMENTS AND OTHER EMISSION LINES

The previous sections discuss Kα and Kβ emission lines with a focus on third-row elements, where chemical effects in the spectra are very similar. It should be noted that *K*-shell emission lines are only a subset of possible x-ray emissions. For phosphorus and sulfur, *L*-shell (2*p* core-hole) x-ray emission is also possible and occurs at lower energy (~160 eV for sulfur). These emission have been measured, for example by Taniguchi.[59]

For other elements, the chemical sensitivities of emission lines can vary quite dramatically, and in many cases depend on the specific element being measured. Moreover, not all elements and emission lines have been systematically measured at high energy resolution to investigate what sensitivities they may possess, so there are many open questions about other possible utilities of XES measurements.

The elements which have been most commonly studied by XES are the fourth-row (3*d*) transition metals. This includes the most highly cited XES papers such as the identification of carbon as the central atom in the nitrogenase iron-molybdenum cofactor,[60] the identification of spin transition of iron at pressures comparable to the earth's mantle,[61] and the investigation of Mn in the oxygen-evolving complex of photosystem II.[62] Figure 2.26 shows the three main regions of interest in 3*d* transition metal XES measurements. Generally, the Kα emission may contain information about the valence shell spin state with low sensitivity, the Kβ main line emission has much higher sensitivity to the metal spin state, and the Kβ satellite emission lines probe the valence electrons directly and can have increased sensitivity to spin state, ligand identity, and symmetry. Extensive reviews of transition metal XES include the works of Glatzel and Bergmann[55,63] and Kowalska and DeBeer.[64]

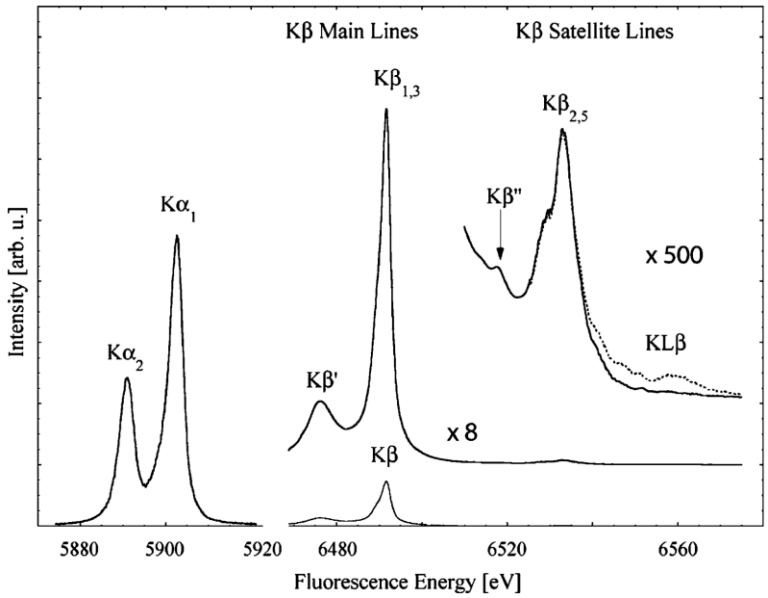

Figure 2.26: *K*-shell x-ray emission lines of Mn in MnO. For the fourth-row transition metals there are three main regions of interest: Kα, Kβ main lines, and the valence-to-core Kβ satellites. Figure from Glatzel and Bergmann.[55]

2.7 X-RAY ABSORPTION SPECTROSCOPIES

Photoelectric absorption is the dominant interaction between x-rays and matter in the tender x-ray energy range (see Figure 2.1). While the general behavior of the x-ray photoelectric cross-section is discussed in section 2.1.2, here we focus on the spectroscopies that arise from a more detailed analysis of changes in absorption. The general name for spectroscopies making use of x-ray absorption is x-ray absorption fine structure (XAFS).

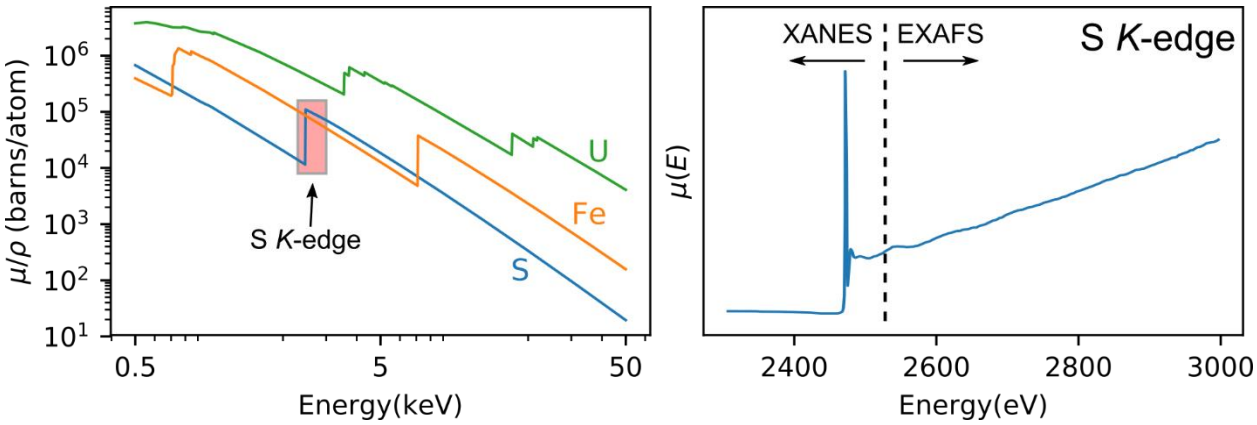

Figure 2.27: (left) X-ray absorption cross section versus photon energy over a wide energy range for different elements. (right) A close-up view of one of the discontinuous jumps in absorption (S *K*-edge), showing the fine structure of the absorption edge. Data adapted from Aquilanti et al.[65]

Figure 2.27 (left) shows the absorption cross section of several elements over a wide energy range. The first feature of importance are the discontinuous jumps in photoelectric absorption cross section that occur at energies equal to the binding energies of electrons of each atom. Similar to emission lines in XES, these discontinuities vary greatly in energy between elements, and thus can be used to fingerprint individual elements in a complex mixture. Figure 2.27 (right) shows an enlarged view of one of these absorption discontinuities, revealing that it is not a simple discontinuity but instead has an additional fine structure that is only revealed when measured at high resolution. As indicated in the figure, there are two main regions of interest that give rise to two different types of measurement: x-ray absorption near-edge spectroscopy (XANES) which is measured within around 50 eV of the absorption edge, and extended x-ray absorption fine structure (EXAFS) which typically extends several hundred eV above the absorption edge.

2.7.1 X-ray absorption near-edge spectroscopy (XANES)

XANES measurements reveal fine structure in the amount of absorption of x-rays for energies within ~50 eV of the absorption edge and often have similar as well as complementary

information relative to XES. For present purposes, there are two main differences between XES and XANES. First, whereas XES measures electronic transitions from occupied states to the core-hole, XANES measures the transitions of electrons from core shells to unoccupied bound or (relatively) near-Fermi-level continuum states. Second, while the final state rule tells us that the core hole can largely be ignored and ground-state calculations suffice for much of XES, the same is not true for XANES, and correct treatment of the core-hole effect is a major topic of theoretical effort for XANES. For simplicity of presentation in this survey, in the remainder of this section the excited state effects on the XANES are not addressed. To frame the discussion and highlight the similarities and differences between XANES and XES, the information content of *K*-edge XANES in the context of sulfur is briefly reviewed. The case is similar for *K*-edge XANES of other third-row elements, and much of the general discussion hold for XANES of transition metals as well.

In Figure 2.28, sulfur XANES spectra are shown for compounds with varying oxidation states. The most apparent feature of the spectra is the shift in energy of the absorption edge between the compounds, with shifts towards higher energy for increasing oxidation state. This shift in the XANES spectra is complementary to the energy shift that occurs in the Kα XES (see Figure 2.6). The physical origin of these two effects is the same: for increasing oxidation state of the sulfur atom, the local electronic density decreases and therefore the screening of the nuclear charge decreases. In XANES, this causes the 1*s* shell to have a larger binding energy and therefore the absorption edge occurs at higher energy. That contrasts with the Kα XES, which measures the relative change in the 2*p* and 1*s* binding energies, though the effect on the spectra is qualitatively the same, causing an increase in Kα energy.

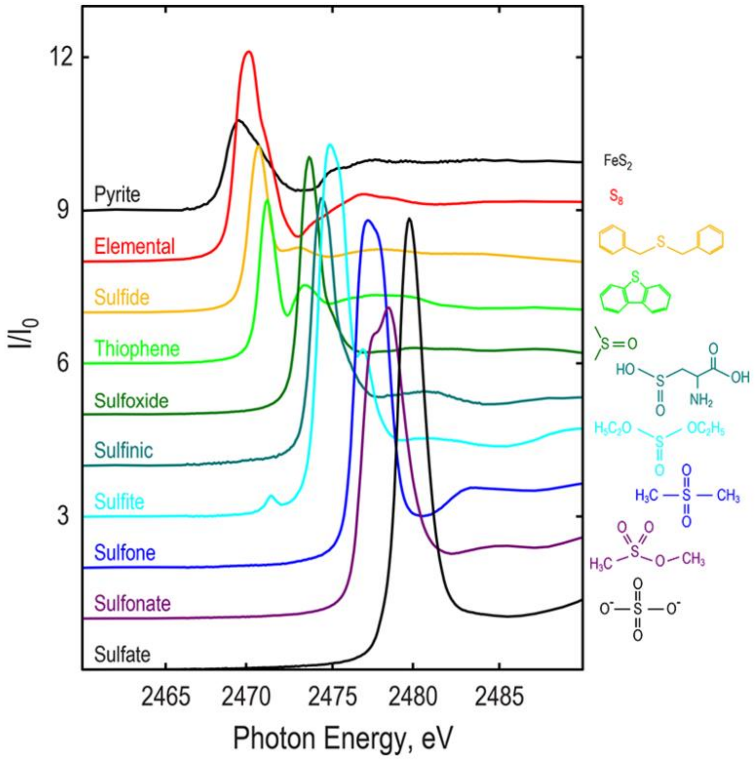

Figure 2.28: Sulfur XANES spectra of compounds with varying sulfur oxidation state. Figure from Craddock et al.[66]

Aside from the shift in edge position, the varying compounds of Figure 2.28 show a variety of additional spectral features. These features reflect the *unoccupied* electronic structure of the systems being measured, i.e. the unoccupied density of states near the valence level. Thus, the additional information carried by the fine structure of these features is complementary to VtC-XES (Kβ for S, P) where the information encoded in the spectrum related to the *occupied* valence states. Therefore, the VtC-XES and XANES spectra share similar chemical sensitivities, such as encoding information about symmetry, covalency, and electronic state.

As in VtC-XES, the complete details of the XANES spectra cannot be generally related to simple descriptors of the compounds being measured. In order to capture the many physical phenomena that affect the XANES spectra, computational approaches are required. Common approaches for simulating XANES spectra include *ab initio* multiple scattering calculations

(FEFF)[27] and time-dependent density functional theory (TDDFT) methods.[67-69] A comparison by Ray et al.[68] of experimentally measured and theoretical spectra calculated by TDDFT is shown in Figure 2.29. The computational approach aims to capture the peaks that make up the features XANES spectra, disregarding the smooth atomic background absorption, which shows up in the normalized spectra as a constant absorption level above the absorption edge (e.g. the nonzero absorption of the experimental spectra at 2473 eV and above). In the study by Ray et al. shown in Figure 2.29, they were able to achieve excellent agreement between their calculations and experimental data.

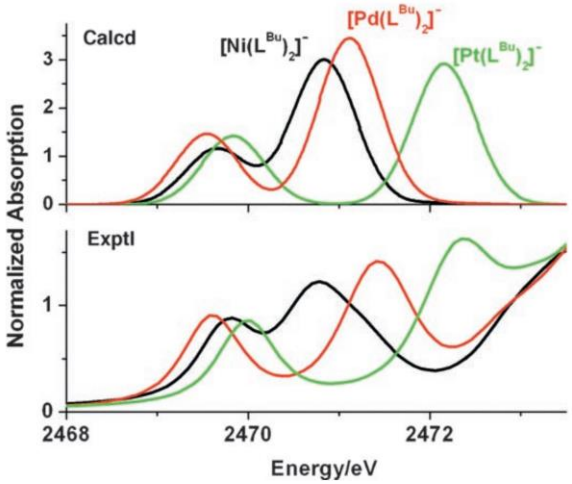

Figure 2.29: Experimental (bottom) and theoretical (top) sulfur *K*-edge XANES spectra of Bis(dithiolato) transition-metal complexes. The theoretical spectrum was calculating using a TDDFT protocol.[67] Figure from Ray et al.[68]

Other than studying the electronic structure with comparison to theoretical calculations, XANES spectra have also been commonly applied for fingerprinting of chemical species within a complex mixture. If suitable reference compounds that represent the possible forms of an element in a given material, the spectrum of a mixture can be analyzed by linear-combination fitting to mixtures of spectra of the reference compounds.[70] Alternatively, analytic functions such as

Gaussian profiles and arctangents can be used to approximate XANES spectral features, and those can subsequently be used to fit a mixture in terms of components of the references.[70] In the case of sulfur, these approaches have been used with *K*-edge XANES to characterize the forms of sulfur in coal,[71] soil organic matter,[72] petroleum,[73,74] and basaltic glasses.[75] One recent study by Robba et al. applied this approach to the study of sulfur in magnesium-sulfur batteries.[76] Their linear-combination fitting of sulfur XANES spectra is shown in Figure 2.30. Using this technique, they were able to track the conversion of sulfur to MgS and polysulfides MgS_x for different charge states in an operando battery. While the study of Robba et al. shows fits with a high degree of agreement and confidence, it is well known that care must be taken in this approach. In particular, for this approach to work well, there must be a proper selection of reference compounds that are representative of forms that may show up in the sample of interest. Also, differences in crystallinity between reference and sample compounds, as well as possible self-absorption distortion effects of the XANES spectra must be taken into account.[70,77]

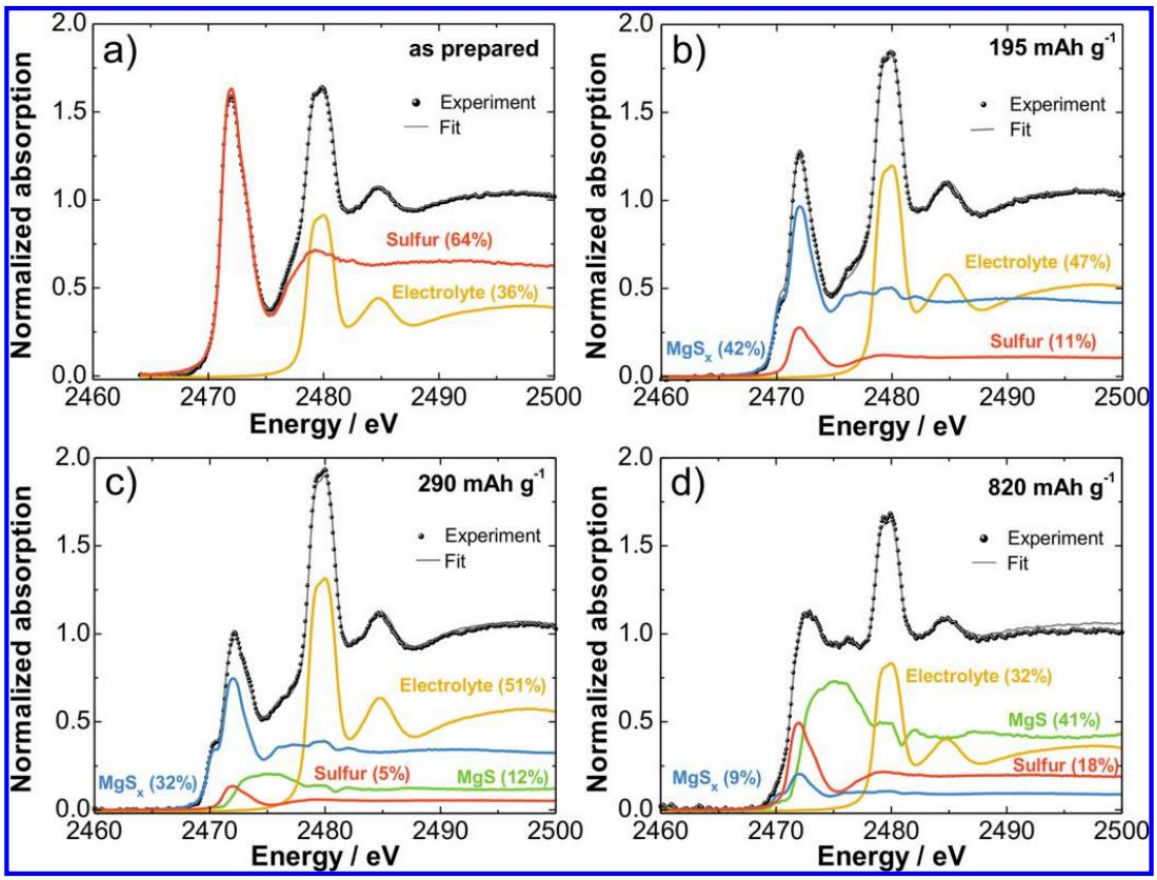

Figure 2.30: Linear combination fitting of sulfur *K*-edge XANES spectra measured at four different charge states of an operando magnesium-sulfur battery. Figure from Robba et al.[76]

2.7.2 Extended x-ray absorption fine structure (EXAFS)

In contrast to XANES features which occur because of the detailed electronic structure of the unoccupied valence levels that participate in modulating absorption, the extended x-ray absorption fine structure (EXAFS) extends to photon energies up to several hundred electron-volts above the absorption edge. At these higher energies, the outgoing photoelectron has appreciable kinetic energy (energy of absorbed photon minus binding edge energy), and thus is excited at levels significantly above the valence. In this case, the details of the interaction do not depend on the valence electronic structure, but rather the local atomic structure around the absorbing atom. A

detailed derivation of EXAFS effects is beyond the scope of this thesis. For a more detailed discussion, see the introduction by Newville.[7]

A heuristic explanation of the origin of EXAFS effects is shown in Figure 2.31. When an x-ray of energy E is absorbed, an outgoing photoelectron with kinetic energy equal to the incident photon energy minus the binding energy $\left(E\text{-}E_{binding}\right)$ is created. The wavefunction of the outgoing photoelectron is then $\lambda\sim\left(E\text{-}E_{binding}\right)^{-1/2}$ and depends on the energy of the incident photon. The outgoing photoelectron is then scattered by neighboring atoms, and the scattered wavefunction modulates the amplitude of the wavefunction at the absorbing atom, thereby modulating the absorption probability. This effect is summarized by Newville as: "The EXAFS is proportional to the amplitude of the scattered photo-electron at the absorbing atom."[7] The net effect is small changes (peaks and troughs) in the absorption spectrum extending far above the absorption edge.

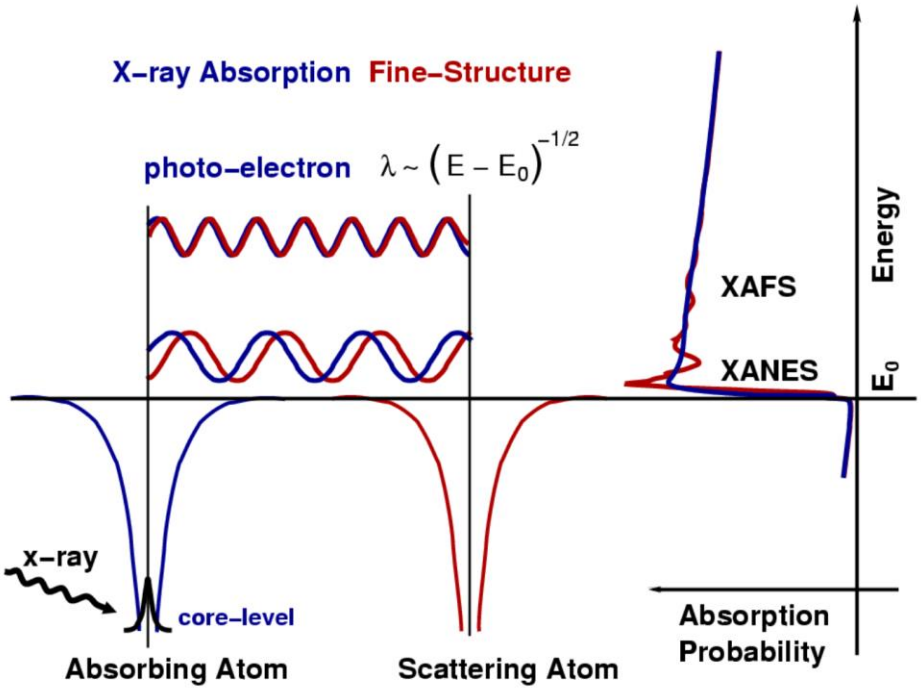

Figure 2.31: Schematic illustration of the origin of EXAFS effects. The photoelectron created by x-ray absorption has a wavefunction with wavelength dependent on the energy of the incoming photon. The photo-electron wave-function is scattered by neighboring atoms which modulates the amplitude of the wavefunction at the absorbing atom, which modulates the absorption probability. Figure from Newville.[7]

Though sulfur *K*-edge XANES is applied much more commonly than sulfur EXAFS, there are several studies making use of sulfur *K*-edge EXAFS,[65,73,78-85] including studies such as *operando* measurements of sulfur in lithium-sulfur batteries.[65,83] An example measurement of sulfur *K*-edge EXAFS is shown in Figure 2.32. The raw spectrum in the top of the figure illustrates the wide energy range required in an EXAFS measurement. Standard EXAFS data processing techniques serve to highlight the small changes in absorption (bottom-left of figure), and a Fourier transform of those oscillations (bottom-right of figure) in the analysis.

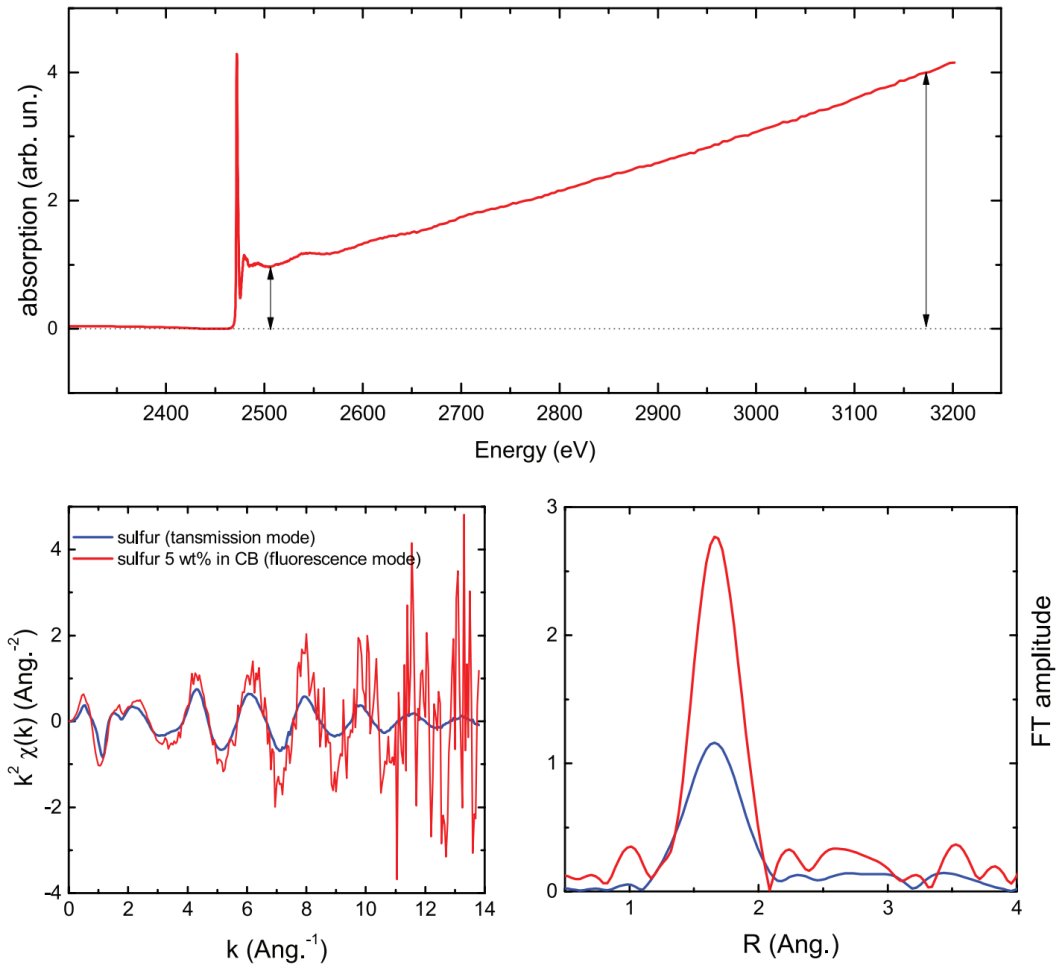

Figure 2.32: Example spectra of sulfur *K*-edge EXAFS. (top) Full spectrum illustrating the wide energy range that is scanned in an EXAFS measurement. (bottom) Standard EXAFS analysis procedure showing the processed *k*-weighted oscillations (left) and the Fourier transform of the oscillations (right). Figure from Aquilanti et al.[65]

From the Fourier transform of the data, using EXAFS theory and fitting the spectra using computational models (typically based on FEFF[27]) allows the extraction of information about bond lengths and coordination number. Such capabilities were used by Dominko et al.[83] to measure the change in coordination number of S in an *operando* lithium-sulfur battery, as shown in Figure 2.33.

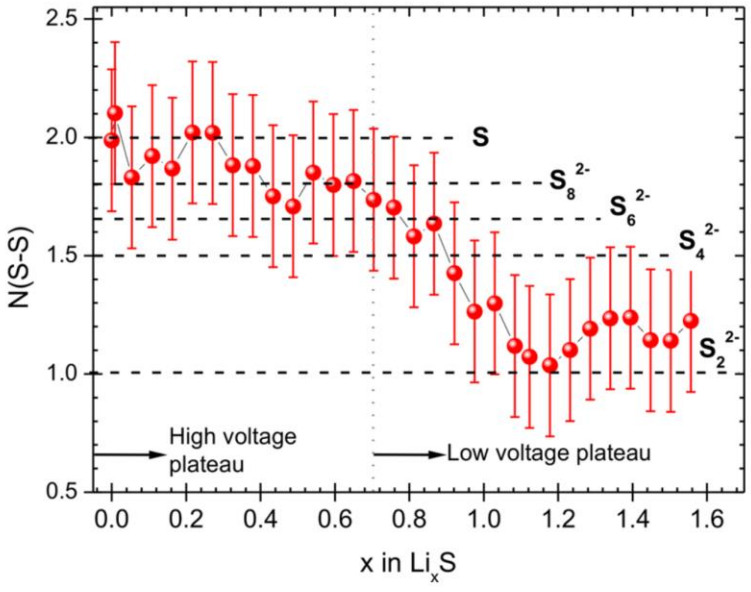

Figure 2.33: Variation of average S coordination number extracted from sulfur EXAFS data measured on an *operando* lithium-sulfur battery. Figure from Dominko et al.[83]

2.8 X-RAY PHOTOELECTRON SPECTROSCOPY (XPS)

X-ray photoelectron spectroscopy (XPS), or ultraviolet photoelectron spectroscopy (UPS) when used with ultraviolet light, is an x-ray spectroscopic technique in which x-rays incident upon a sample are absorbed generating photoexcited electron. Some are able to leave the sample, and the energy of the emitted electrons is then measured using an electron energy analyzer to give the resulting XPS spectrum. A diagram outlining an XPS measurement and the instrumental components is shown in Figure 2.34. As indicated in the figure, the incident x-rays can come either from a synchrotron beamline or with a conventional x-ray tube. In order for the photoexcited electrons to be able to reach the analyzer without being absorbed, measurements are typically performed in ultra-high vacuum to prevent the electrons from scattering from air molecules and thus changing their energy. However, there has recently been a large growth in the availability of near-ambient pressure (<2500 Pa) XPS systems using differential pumping in which the sample is

at near-ambient pressure while the electrons escape a very short distance through the higher-pressure region into an ultra-high vacuum electron energy analyzer.[86]

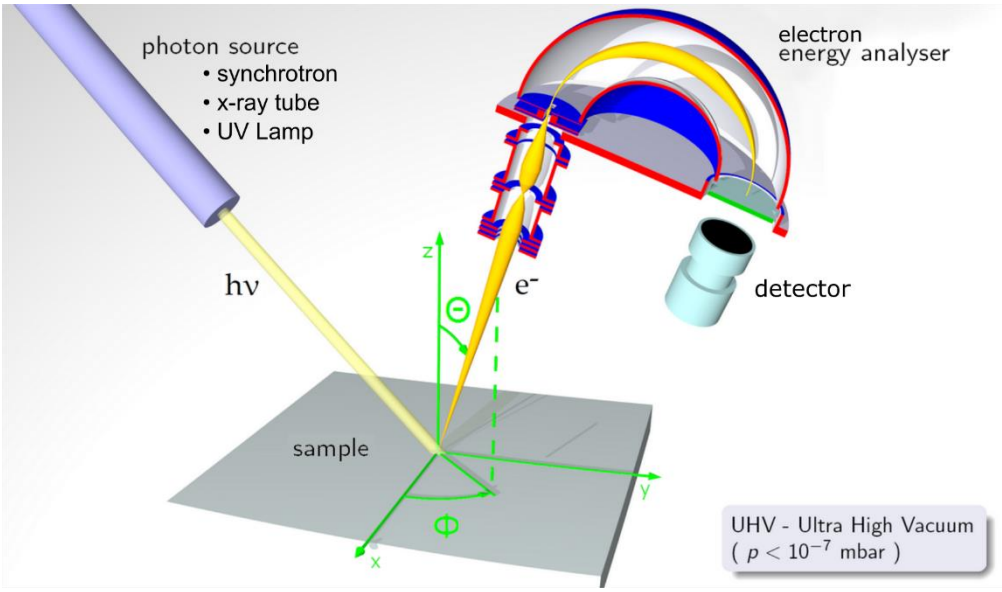

Figure 2.34: Diagram outlining the components of an XPS instrument. Figure from Saiht with annotations added.[87]

For a proper measurement of the XPS spectrum, the energies that the electrons have while leaving the sample must be measured, i.e., if the electron undergoes any scattering or other interaction events before being measured by the analyzer, the electrons may not be captured by the detector or the measured spectrum will be distorted. In addition to the vacuum requirements mentioned above, this also affects what portions of the sample can contribute to the measured signal. The relevant parameter describing from what depth electrons can escape a sample without losing energy in a scattering event is the electron inelastic mean free path. Figure 2.35 shows electron inelastic mean free paths at different kinetic energies for a range of different materials. Note from the figure that the elements presented span a wide range of atomic number, and therefore the dashed line represents the nearly universal trend of electron inelastic mean free paths in matter. From the y-axis of the figure, the inelastic mean free path is on the order of ~5–100 Å. Therefore,

the sampling depths of XPS measurements is on the order of several nanometers depending on the electron energies being measured as well as the takeoff angle used in the experiment. Thus, XPS is a very surface sensitive technique, in contrast with XES and XAFS measurements which are more bulk sensitive. The surface sensitivity is often an advantage when surface measurements are desired. In other cases the surface sensitivity can cause challenges, for example in the study in chapter 9 when XPS measurements were performed on shelled-InP quantum dots, the XPS signal could not see the InP core through the shells. Often XPS surface-sensitive measurements can be combined with XES/XAFS bulk measurements to get contrasting information about the sample at different sampling depths.

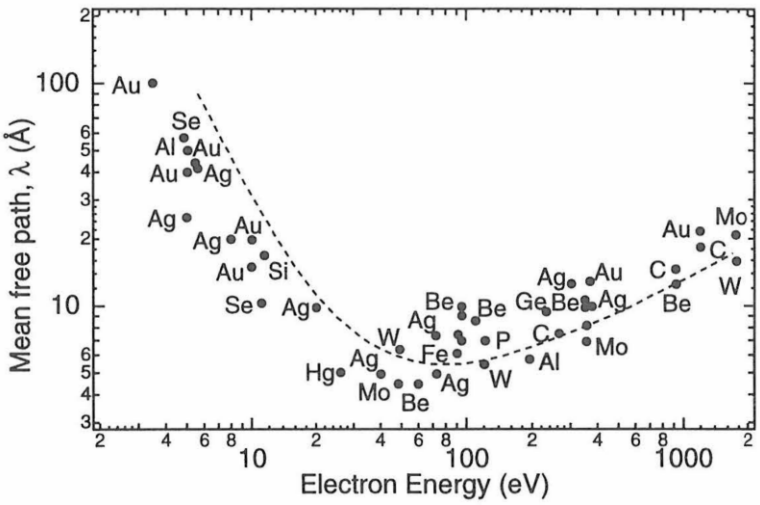

Figure 2.35: Electron inelastic mean free paths in various materials. Note that the indicated elements span both low- and high-Z atoms, and the dashed line indicates the nearly universal curve that approximates the behavior for most materials. Figure from Magnuson.[88]

By measuring the energies of electrons excited with a fixed (relatively narrow) incident x-ray energy, the binding energies of the electrons in the material can be determined as ($E_{binding} = E_{incident}$-$E_{measured}$). Thus, XPS probes the occupied electronic states in a sample, and therefore shares many similarities with XES. This is most apparent in comparing sulfur 2*p* XPS and sulfur

Kα XES. An example sulfur 2*p* XPS measurement is shown in Figure 2.36 for the measurement of sulfur in magnesium-sulfur batteries.[89] In the top of the figure, two components of a doublet represent the binding energies of the spin-orbit split $2p_{1/2}$ and $2p_{3/2}$ levels for sulfur in a nominal oxidation state S^0. This doublet spectrum is in exact analogy of the spin-orbit split doublet $K\alpha_1$ and $K\alpha_2$ components of the sulfur Kα XES spectrum (see Figure 2.10). In the bottom of Figure 2.36, a separate doublet at higher binding energy is labelled as SO_x, representing the shifted electron binding energies from sulfur bonded to oxygen and therefore in a higher oxidation state. This energy shift with oxidation state is a key feature of XPS and is also analogous to the shift in energy with oxidation state observed in Kα XES (see Figure 2.6 and Figure 2.8). However, in the case of XPS, the energy shift is about an order of magnitude larger than XES. The reason for this was discussed in section 2.3.2, but briefly, XPS measures the change in the 2*p* binding energy directly, whereas XES measures the relative change in the 2*p* and 1*s* binding energies, which results in a weaker sensitivity to oxidation state because both the 2*p* and 1*s* levels shift in the same direction upon change in oxidation state.

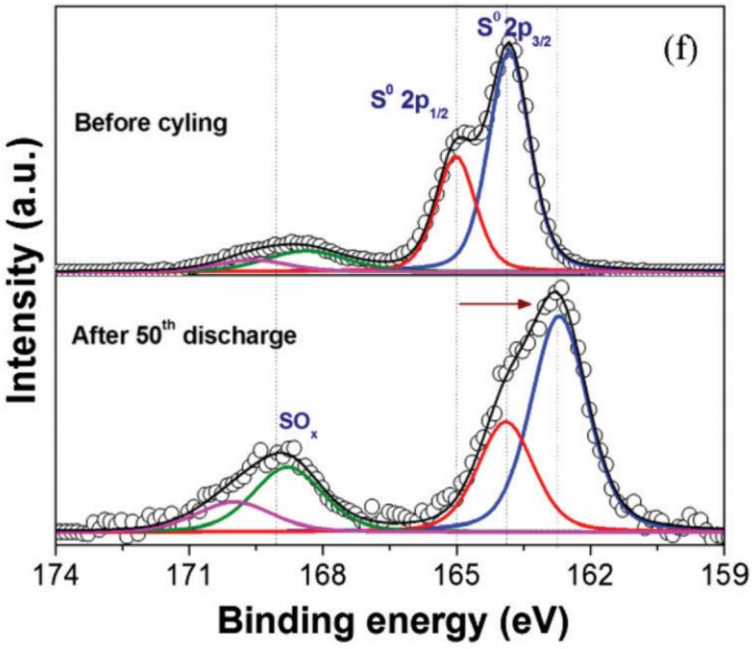

Figure 2.36: Sulfur 2*p* XPS spectrum of magnesium-sulfur battery material before and after cycling. Figure from Vinayan et al.[89]

One major advantage that XPS has over XES at present is an established presence, both at universities and in industries. With the availability of laboratory XPS instruments, XPS is performed very commonly in far-reaching branches of science. One tool that aids in the widespread usage of XPS is the freely available NIST XPS database[90] with compiled information on XPS line positions, chemical shifts, doublet splittings, and energy separations of photoelectron and Auger-electron lines. With the similar information content of XES, such a database should be a goal in the near future for the XES community as well, in particular as the technique becomes more common with increasing presence of laboratory instruments such as the one in chapter 5.

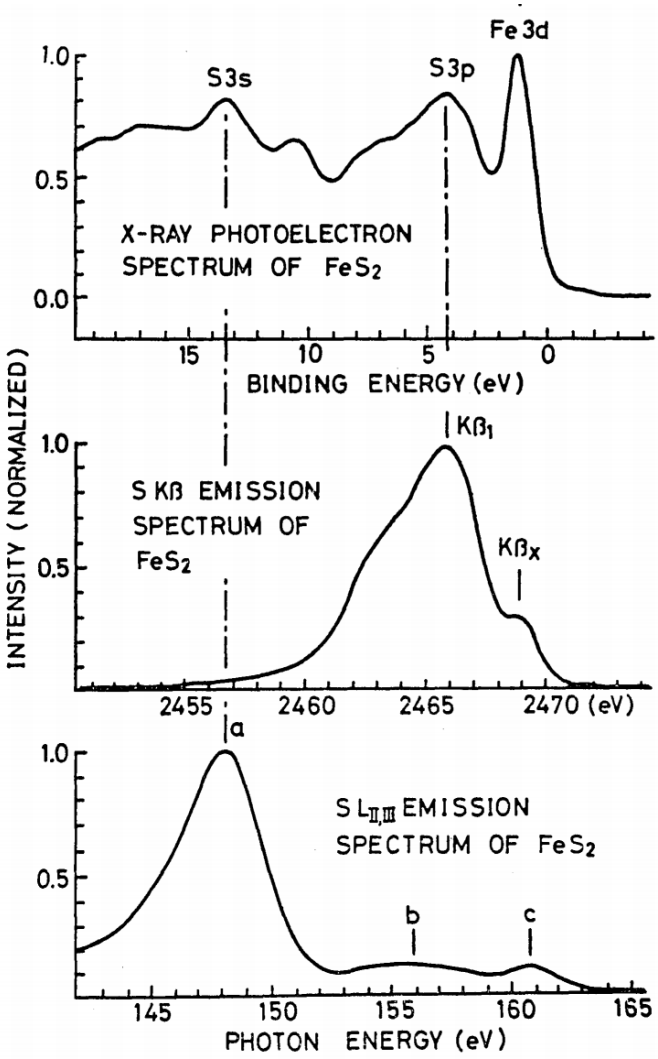

Figure 2.37: Comparison of (top) valence photoelectron spectrum, (middle) S Kβ XES spectrum, and (bottom) S $L_{2,3}$ XES spectrum of FeS_2. Figure from Sugiura et al.[91]

In addition to the 2*p* XPS of sulfur in Figure 2.36, it is also possible to use photoelectron spectroscopy to measure the valence electrons as well. Since the valence binding energies are very low, the technique uses ultraviolet light instead of x-rays and thus is referred to as ultraviolet photoelectron spectroscopy (UPS). An example of a valence UPS spectrum of FeS_2 is shown in Figure 2.37 with comparisons to sulfur Kβ and $L_{2,3}$ XES spectra. Since UPS measures the valence electrons, it has similar sensitivity to the Kβ XES discussed in section 2.4.2 with one important distinction: sulfur Kβ XES measures transitions from valence orbitals to the sulfur 1*s* core-hole

and thus measures an element-specific view of the valence orbitals, whereas UPS measures all of the valence electrons present in the system. In contrast to 2*p* XPS and Kα XES which have strong similarities, valence UPS and Kβ XES are drastically different. Though both techniques yield views into the valence electronic structure, UPS probes all of the electrons whereas Kβ XES maintains element-specificity and only probes a specific atom's (e.g. sulfur in Figure 2.37 middle) local view of the valence electronic structure.

2.9 References

1 Hubbell, J. H., Gimm, H. A. & O/verbo, I. Pair, Triplet, and Total Atomic Cross Sections (and Mass Attenuation Coefficients) for 1 MeV-100 GeV Photons in Elements Z=1 to 100. *Journal of Physical and Chemical Reference Data* **9**, 1023-1148, doi:10.1063/1.555629 (1980).

2 Als-Nielsen, J. & McMorrow, D. *Elements of modern X-ray physics*. 2nd edn, (Wiley, 2011).

3 Grynberg, G., Aspect, A. & Fabre, C. *Introduction to quantum optics : from the semi-classical approach to quantized light*. (Cambridge University Press, 2010).

4 Sakurai, J. J. *Advanced Quantum Mechanics*. (Addison-Wesley Publishing Co., 1967).

5 Fox, M. *Quantum optics : an introduction*. (Oxford University Press, 2006).

6 Krause, M. O. Atomic radiative and radiationless yields for K and L shells. *Journal of Physical and Chemical Reference Data* **8**, 307-327, doi:10.1063/1.555594 (1979).

7 Newville, M. Fundamentals of XAFS. *Reviews in Mineralogy and Geochemistry* **78**, 33-74, doi:10.2138/rmg.2014.78.2 (2014).

8 Kortright, J. B. (Lawrence Berkeley National Laboratory, 2001).

9 Alonso Mori, R. *et al.* Electronic Structure of Sulfur Studied by X-ray Absorption and Emission Spectroscopy. *Analytical Chemistry* **81**, 6516-6525, doi:10.1021/ac900970z (2009).

10 Groot, F. d. Multiplet effects in X-ray spectroscopy. *Coordination Chemistry Reviews* **249**, 31-63, doi:10.1016/j.ccr.2004.03.018 (2005).

11 Sánchez, E., Torres Deluigi, M. & Castellano, G. Binding effects in sulfur Kα and Kβ X-ray emission spectra. *Journal of Analytical Atomic Spectrometry* **34**, 274-283, doi:10.1039/c8ja00345a (2019).

12 Nave, C. R. *Hyperphysics: Hydrogen 3p Radial Probability*, <http://hyperphysics.phy-astr.gsu.edu/hbase/hydwf.html> (2019).

13 Petric, M. & Kavčič, M. Chemical speciation via X-ray emission spectroscopy in the tender X-ray range. *Journal of Analytical Atomic Spectrometry* **31**, 450-457, doi:10.1039/c5ja00394f (2016).

14 Graeffe, G., Juslen, J. & Karras, M. Si KαX-ray emission spectra of Si, SiC, SiO2and Si3N4. *Journal of Physics B: Atomic and Molecular Physics* **10**, 3219-3227, doi:10.1088/0022-3700/10/16/017 (1977).

15 Dolenko, G. N. X-ray determination of effective charges on sulphur, phosphorus, silicon and chlorine atoms. *Journal of Molecular Structure* **291**, 23-57, doi:10.1016/0022-2860(93)80253-r (1993).
16 Yamamoto, T., Kudo, T., Yamamoto, T. & Kawai, J. Analysis of coordination environment of aluminum species in zeolites and amorphous silica-alumina by X-ray absorption and emission spectroscopy. *Microporous and Mesoporous Materials* **182**, 239-243, doi:10.1016/j.micromeso.2013.03.047 (2013).
17 Fukushima, S., Iida, A., Gohshi, Y. & Fujima, K. Molecular orbital calculation of Al and Mg Kα chemical shifts. *Spectrochimica Acta Part B: Atomic Spectroscopy* **39**, 77-83, doi:10.1016/0584-8547(84)80008-7 (1984).
18 Takahashi, Y. The X-Ray Emission Spectra of the Compounds of Third-period Elements. VI. The Relationship between theKα andKβ Spectra. *Bulletin of the Chemical Society of Japan* **46**, 2039-2044, doi:10.1246/bcsj.46.2039 (1973).
19 Petric, M. *et al.* Chemical State Analysis of Phosphorus Performed by X-ray Emission Spectroscopy. *Analytical Chemistry* **87**, 5632-5639, doi:10.1021/acs.analchem.5b00782 (2015).
20 Zhang, Y., Bergmann, U., Schoenlein, R., Khalil, M. & Govind, N. Double core hole valence-to-core x-ray emission spectroscopy: A theoretical exploration using time-dependent density functional theory. *The Journal of Chemical Physics* **151**, 144114, doi:10.1063/1.5111141 (2019).
21 Parratt, L. G. Excitation Potential, Relative Intensities and Wave-Lengths of theKα′′X-Ray Satellite Line. *Physical Review* **49**, 502-507, doi:10.1103/PhysRev.49.502 (1936).
22 Mikkola, E., Keski-Rahkonen, O. & Kuoppala, R. KαhHypersatellite Spectrum and Electron Double Ionization Cross Section of theK-Shell in Magnesium. *Physica Scripta* **19**, 29-32, doi:10.1088/0031-8949/19/1/007 (1979).
23 Heirwegh, C. M. *et al.* Multiple ionization X-ray satellites of magnesium, aluminum and silicon in alpha particle PIXE. *Nuclear Instruments and Methods in Physics Research Section B: Beam Interactions with Materials and Atoms* **428**, 9-16, doi:10.1016/j.nimb.2018.05.005 (2018).
24 Yasuda, S. & Kakiyama, H. Chemical effects in X-ray Kα and Kβ emission spectra of sulfur in organic compounds. *Spectrochimica Acta Part A: Molecular Spectroscopy* **35**, 485-493, doi:10.1016/0584-8539(79)80164-6 (1979).
25 Taniguchi, K. Chemical-state Analysis by Means of Soft X-Ray Spectroscopy. II.Kβ Spectra for Phosphorus, Sulfur, and Chlorine in Various Compounds. *Bulletin of the Chemical Society of Japan* **57**, 915-920, doi:10.1246/bcsj.57.915 (1984).
26 Kawai, J. DV-Xα Calculation of X-Ray Emission Spectra. **29**, 329-355, doi:10.1016/s0065-3276(08)60277-4 (1998).
27 Rehr, J. J. *et al.* Ab initio theory and calculations of X-ray spectra. *Comptes Rendus Physique* **10**, 548-559, doi:10.1016/j.crhy.2008.08.004 (2009).
28 Ankudinov, A. L., Elam, W. T., Sieber, J. R. & Rehr, J. J. Chemical speciation via X-ray emission spectra. *X-Ray Spectrometry* **35**, 312-318, doi:10.1002/xrs.913 (2006).
29 Mortensen, D. R. *et al.* Benchmark results and theoretical treatments for valence-to-core x-ray emission spectroscopy in transition metal compounds. *Physical Review B* **96**, doi:10.1103/PhysRevB.96.125136 (2017).

30 Lee, N., Petrenko, T., Bergmann, U., Neese, F. & DeBeer, S. Probing Valence Orbital Composition with Iron Kβ X-ray Emission Spectroscopy. *Journal of the American Chemical Society* **132**, 9715-9727, doi:10.1021/ja101281e (2010).

31 Mori, R. A. *et al.* Sulfur-Metal Orbital Hybridization in Sulfur-Bearing Compounds Studied by X-ray Emission Spectroscopy. *Inorganic Chemistry* **49**, 6468-6473, doi:10.1021/ic100304z (2010).

32 Petric, M. *et al.* Electronic Structure of Third-Row Elements in Different Local Symmetries Studied by Valence-to-Core X-ray Emission Spectroscopy. *Inorganic Chemistry* **55**, 5328-5336, doi:10.1021/acs.inorgchem.6b00237 (2016).

33 Zhang, Y., Mukamel, S., Khalil, M. & Govind, N. Simulating Valence-to-Core X-ray Emission Spectroscopy of Transition Metal Complexes with Time-Dependent Density Functional Theory. *Journal of Chemical Theory and Computation* **11**, 5804-5809, doi:10.1021/acs.jctc.5b00763 (2015).

34 Wadey, J. D. & Besley, N. A. Quantum Chemical Calculations of X-ray Emission Spectroscopy. *Journal of Chemical Theory and Computation* **10**, 4557-4564, doi:10.1021/ct500566k (2014).

35 Salem, S. I., Panossian, S. L. & Krause, R. A. Experimental K and L relative x-ray emission ratess. *Atomic Data and Nuclear Data Tables* **14**, 91-109, doi:10.1016/s0092-640x(74)80017-3 (1974).

36 Mukoyama, T., Taniguchi, K. & Adachi, H. Chemical effect onKβ:Kαx-ray intensity ratios. *Physical Review B* **34**, 3710-3716, doi:10.1103/PhysRevB.34.3710 (1986).

37 Küçükönder, A., Sąhín, Y. & Büyükkasap, E. Dependence of the Kβ/Kα intensity ratio on the oxidation state. *Journal of Radioanalytical and Nuclear Chemistry Articles* **170**, 125-132, doi:10.1007/bf02134583 (1993).

38 Raj, S., Padhi, H. C. & Polasik, M. Influence of chemical effect on the Kβ-to-Kα x-ray intensity ratios of Cr, Mn and Co in CrSe, MnSe, MnS and CoS. *Nuclear Instruments and Methods in Physics Research Section B: Beam Interactions with Materials and Atoms* **160**, 443-448, doi:10.1016/s0168-583x(99)00626-6 (2000).

39 Sogut, O., Büyükkasap, E. & Erdoğan, H. Chemical-effect variation of Kβ/Kα X-ray intensity ratios in 3d elements. *Radiation Physics and Chemistry* **64**, 343-348, doi:10.1016/s0969-806x(01)00644-2 (2002).

40 Kavčič, M., Dousse, J. C., Szlachetko, J. & Cao, W. Chemical effects in the Kβ X-ray emission spectra of sulfur. *Nuclear Instruments and Methods in Physics Research Section B: Beam Interactions with Materials and Atoms* **260**, 642-646, doi:10.1016/j.nimb.2007.04.290 (2007).

41 Sugiura, C. Kβ X-Ray Emission Spectra and Chemical Environments of Phosphorus and Sulfur in Various Compounds. *Journal of the Physical Society of Japan* **64**, 3840-3852, doi:10.1143/jpsj.64.3840 (1995).

42 Niskanen, J. *et al.* Sulphur Kβ emission spectra reveal protonation states of aqueous sulfuric acid. *Scientific Reports* **6**, doi:10.1038/srep21012 (2016).

43 Bergmann, U., Bendix, J., Glatzel, P., Gray, H. B. & Cramer, S. P. Anisotropic valence→core x-ray fluorescence from a [Rh(en)3][Mn(N)(CN)5]·H2O single crystal: Experimental results and density functional calculations. *The Journal of Chemical Physics* **116**, 2011-2015, doi:10.1063/1.1419062 (2002).

44 Kaneyoshi, T., Kowada, Y., Tanaka, T., Kawai, J. & Motoyama, M. Molecular orbital calculation of graphite K-V X-ray emission spectra. *Spectrochimica Acta Part B: Atomic Spectroscopy* **54**, 189-196, doi:10.1016/s0584-8547(98)00194-3 (1999).
45 Lindle, D. W. *et al.* Polarized x-ray emission studies of methyl chloride and the chlorofluoromethanes. *Physical Review A* **43**, 2353-2366, doi:10.1103/PhysRevA.43.2353 (1991).
46 Kottmann, A. *et al.* Partial densities of states with polarized oxygen Kα X-ray emission of YBa2Cu3O7−δ. *Physica C: Superconductivity* **178**, 125-136, doi:10.1016/0921-4534(91)90167-w (1991).
47 Dräger, G. & Leiro, J. A. Electronic structure of α-Al2O3studied by polarized x-ray-emission spectroscopy. *Physical Review B* **41**, 12919-12921, doi:10.1103/PhysRevB.41.12919 (1990).
48 Simunek, A., Drager, G., Czolbe, W., Brummer, O. & Levy, F. Polarised K emission bands of SnS2and TiS2. *Journal of Physics C: Solid State Physics* **18**, 1605-1011, doi:10.1088/0022-3719/18/8/008 (1985).
49 Hayasi, Y. *et al.* Electronic structure of black phosphorus studied by polarized soft-x-ray emission and absorption spectroscopy. *Physical Review B* **30**, 1891-1895, doi:10.1103/PhysRevB.30.1891 (1984).
50 Dräger, G. & Brümmer, O. Polarized X-Ray Emission Spectra of Single Crystals. *physica status solidi (b)* **124**, 11-28, doi:10.1002/pssb.2221240102 (1984).
51 Maganas, D., DeBeer, S. & Neese, F. A Restricted Open Configuration Interaction with Singles Method To Calculate Valence-to-Core Resonant X-ray Emission Spectra: A Case Study. *Inorganic Chemistry* **56**, 11819-11836, doi:10.1021/acs.inorgchem.7b01810 (2017).
52 Pérez, P. D., Carreras, A. C. & Trincavelli, J. C. Structure of the sulfurKx-ray emission spectrum: influence of the oxidation state. *Journal of Physics B: Atomic, Molecular and Optical Physics* **45**, 025004, doi:10.1088/0953-4075/45/2/025004 (2012).
53 Kavčič, M. *et al.* Operando Resonant Inelastic X-ray Scattering: An Appropriate Tool to Characterize Sulfur in Li–S Batteries. *The Journal of Physical Chemistry C* **120**, 24568-24576, doi:10.1021/acs.jpcc.6b06705 (2016).
54 Ament, L. J. P., van Veenendaal, M., Devereaux, T. P., Hill, J. P. & van den Brink, J. Resonant inelastic x-ray scattering studies of elementary excitations. *Reviews of Modern Physics* **83**, 705-767, doi:10.1103/RevModPhys.83.705 (2011).
55 Glatzel, P. & Bergmann, U. High resolution 1s core hole X-ray spectroscopy in 3d transition metal complexes—electronic and structural information. *Coordination Chemistry Reviews* **249**, 65-95, doi:10.1016/j.ccr.2004.04.011 (2005).
56 Safonova, O. V. *et al.* Identification of CO Adsorption Sites in Supported Pt Catalysts Using High-Energy-Resolution Fluorescence Detection X-ray Spectroscopy. *The Journal of Physical Chemistry B* **110**, 16162-16164, doi:10.1021/jp063416t (2006).
57 Glatzel, P., Sikora, M., Smolentsev, G. & Fernández-García, M. Hard X-ray photon-in photon-out spectroscopy. *Catalysis Today* **145**, 294-299, doi:10.1016/j.cattod.2008.10.049 (2009).
58 Bauer, M. HERFD-XAS and valence-to-core-XES: new tools to push the limits in research with hard X-rays? *Phys. Chem. Chem. Phys.* **16**, 13827-13837, doi:10.1039/c4cp00904e (2014).

59 Taniguchi, K. Chemical-state Analysis by Means of Soft X-Ray Spectroscopy. I.L2,3-Emission Spectra for Phosphorus, Sulfur, and Chlorine in Various Compounds. *Bulletin of the Chemical Society of Japan* **57**, 909-914, doi:10.1246/bcsj.57.909 (1984).
60 Lancaster, K. M. *et al.* X-ray Emission Spectroscopy Evidences a Central Carbon in the Nitrogenase Iron-Molybdenum Cofactor. *Science* **334**, 974-977, doi:10.1126/science.1206445 (2011).
61 Lin, J.-F. *et al.* Spin transition of iron in magnesiowüstite in the Earth's lower mantle. *Nature* **436**, 377-380, doi:10.1038/nature03825 (2005).
62 Kern, J. *et al.* Simultaneous Femtosecond X-ray Spectroscopy and Diffraction of Photosystem II at Room Temperature. *Science* **340**, 491-495, doi:10.1126/science.1234273 (2013).
63 Bergmann, U. & Glatzel, P. X-ray emission spectroscopy. *Photosynthesis Research* **102**, 255-266, doi:10.1007/s11120-009-9483-6 (2009).
64 Kowalska, J. & DeBeer, S. The role of X-ray spectroscopy in understanding the geometric and electronic structure of nitrogenase. *Biochimica et Biophysica Acta (BBA) - Molecular Cell Research* **1853**, 1406-1415, doi:10.1016/j.bbamcr.2014.11.027 (2015).
65 Aquilanti, G. *et al.* Operandocharacterization of batteries using x-ray absorption spectroscopy: advances at the beamline XAFS at synchrotron Elettra. *Journal of Physics D: Applied Physics* **50**, 074001, doi:10.1088/1361-6463/aa519a (2017).
66 Craddock, P. R., Bake, K. D. & Pomerantz, A. E. Chemical, Molecular, and Microstructural Evolution of Kerogen during Thermal Maturation: Case Study from the Woodford Shale of Oklahoma. *Energy & Fuels* **32**, 4859-4872, doi:10.1021/acs.energyfuels.8b00189 (2018).
67 DeBeer George, S., Petrenko, T. & Neese, F. Time-dependent density functional calculations of ligand K-edge X-ray absorption spectra. *Inorganica Chimica Acta* **361**, 965-972, doi:10.1016/j.ica.2007.05.046 (2008).
68 Ray, K., DeBeer George, S., Solomon, E. I., Wieghardt, K. & Neese, F. Description of the Ground-State Covalencies of the Bis(dithiolato) Transition-Metal Complexes from X-ray Absorption Spectroscopy and Time-Dependent Density-Functional Calculations. *Chemistry - A European Journal* **13**, 2783-2797, doi:10.1002/chem.200601425 (2007).
69 DeBeer George, S., Petrenko, T. & Neese, F. Prediction of Iron K-Edge Absorption Spectra Using Time-Dependent Density Functional Theory†. *The Journal of Physical Chemistry A* **112**, 12936-12943, doi:10.1021/jp803174m (2008).
70 Prietzel, J. r. *et al.* Sulfur Speciation in Soil by SK-Edge XANES Spectroscopy: Comparison of Spectral Deconvolution and Linear Combination Fitting. *Environmental Science & Technology* **45**, 2878-2886, doi:10.1021/es102180a (2011).
71 Huffman, G. P. *et al.* Quantitative analysis of all major forms of sulfur in coal by x-ray absorption fine structure spectroscopy. *Energy & Fuels* **5**, 574-581, doi:10.1021/ef00028a008 (1991).
72 Solomon, D., Lehmann, J. & Martínez, C. E. Sulfur K-edge XANES Spectroscopy as a Tool for Understanding Sulfur Dynamics in Soil Organic Matter. *Soil Science Society of America Journal* **67**, 1721, doi:10.2136/sssaj2003.1721 (2003).
73 George, G. N. & Gorbaty, M. L. Sulfur K-edge x-ray absorption spectroscopy of petroleum asphaltenes and model compounds. *Journal of the American Chemical Society* **111**, 3182-3186, doi:10.1021/ja00191a012 (1989).

74 Pomerantz, A. E. *et al.* Sulfur Chemistry of Asphaltenes from a Highly Compositionally Graded Oil Column. *Energy & Fuels* **27**, 4604-4608, doi:10.1021/ef400773f (2013).
75 Jugo, P. J., Wilke, M. & Botcharnikov, R. E. Sulfur K-edge XANES analysis of natural and synthetic basaltic glasses: Implications for S speciation and S content as function of oxygen fugacity. *Geochimica et Cosmochimica Acta* **74**, 5926-5938, doi:10.1016/j.gca.2010.07.022 (2010).
76 Robba, A. *et al.* Mechanistic Study of Magnesium–Sulfur Batteries. *Chemistry of Materials* **29**, 9555-9564, doi:10.1021/acs.chemmater.7b03956 (2017).
77 Pongpiachan, S. *et al.* Parameters Influencing Sulfur Speciation in Environmental Samples Using Sulfur K-Edge X-Ray Absorption Near-Edge Structure. *Journal of Analytical Methods in Chemistry* **2012**, 1-12, doi:10.1155/2012/659858 (2012).
78 Li, D. *et al.* Sulfur K- and L-edge X-ray absorption spectroscopy of sphalerite, chalcopyrite and stannite. *Physics and Chemistry of Minerals* **20**, doi:10.1007/bf00203219 (1994).
79 Gui, Z., Green, A. R., Kasrai, M., Bancroft, G. M. & Stillman, M. J. Sulfur K-Edge EXAFS Studies of Cadmium-, Zinc-, Copper-, and Silver-Rabbit Liver Metallothioneins. *Inorganic Chemistry* **35**, 6520-6529, doi:10.1021/ic951624m (1996).
80 Pattrick, R. A. D. *et al.* The structure of amorphous copper sulfide precipitates: An X-ray absorption study. *Geochimica et Cosmochimica Acta* **61**, 2023-2036, doi:10.1016/s0016-7037(97)00061-6 (1997).
81 Hibble, S. J., Walton, R. I., Feaviour, M. R. & Smith, A. D. Sulfur–sulfur bonding in the amorphous sulfides WS3, WS5, and Re2S7 from sulfur K-edge EXAFS studies. *Journal of the Chemical Society, Dalton Transactions*, 2877-2883, doi:10.1039/a903918j (1999).
82 Hayter, C. E., Evans, J., Corker, J. M., Oldman, R. J. & Peter Williams, B. Sulfur K-edge X-ray absorption spectroscopy study of the reaction of zinc oxide with hydrogen sulfide. *Journal of Materials Chemistry* **12**, 3172-3177, doi:10.1039/b203426n (2002).
83 Dominko, R. *et al.* Analytical Detection of Polysulfides in the Presence of Adsorption Additives by Operando X-ray Absorption Spectroscopy. *The Journal of Physical Chemistry C* **119**, 19001-19010, doi:10.1021/acs.jpcc.5b05609 (2015).
84 Wang, X., Gu, C., Feng, X. & Zhu, M. Sulfate Local Coordination Environment in Schwertmannite. *Environmental Science & Technology* **49**, 10440-10448, doi:10.1021/acs.est.5b02660 (2015).
85 Gu, C., Wang, Z., Kubicki, J. D., Wang, X. & Zhu, M. X-ray Absorption Spectroscopic Quantification and Speciation Modeling of Sulfate Adsorption on Ferrihydrite Surfaces. *Environmental Science & Technology* **50**, 8067-8076, doi:10.1021/acs.est.6b00753 (2016).
86 Arble, C., Jia, M. & Newberg, J. T. Lab-based ambient pressure X-ray photoelectron spectroscopy from past to present. *Surface Science Reports* **73**, 37-57, doi:10.1016/j.surfrep.2018.02.002 (2018).
87 Saiht. *General Principle of ARPES with description*, <https://commons.wikimedia.org/wiki/File:ARPESgeneral.png> (2009).
88 Magnuson, M. *Electronic Structure Studies Using Resonant X-ray and Photemission Spectroscopy* 452 thesis, Uppsala University, (1999).
89 Vinayan, B. P. *et al.* Performance study of magnesium–sulfur battery using a graphene based sulfur composite cathode electrode and a non-nucleophilic Mg electrolyte. *Nanoscale* **8**, 3296-3306, doi:10.1039/c5nr04383b (2016).

90 Lee, A. Y., Blakeslee, D. M., Powell, C. J. & Rumble, J. J. R. Development of the web-based NIST X-ray Photoelectron Spectroscopy (XPS) Database. *Data Science Journal* **1**, 1-12, doi:10.2481/dsj.1.1 (2002).

91 Sugiura, C., Suzuki, I., Kashiwakura, J. & Gohshi, Y. SulfurKβ X-Ray Emission Bands and Valence-Band Structures of Transition-Metal Disulfides. *Journal of the Physical Society of Japan* **40**, 1720-1724, doi:10.1143/jpsj.40.1720 (1976).

CHAPTER 3 TENDER XES INSTRUMENTATION

3.1 Overview

Tender x-ray emission spectroscopy instruments come in a wide variety, but all approaches have a few common requirements. Tender XES generally refers to the energy range of around 1–5 keV fluorescence photons. This range encompasses the Kα and Kβ fluorescence lines of period 3 elements and period 4 up to around titanium, as well as the L-edge fluorescence lines of second row transition metals and M-edge emission lines of actinides and many lanthanides.

In contrast to hard x-rays (> 5 keV), the absorption length in air for the tender x-ray range is considerably reduced, around 1-2 cm in the energy range of phosphorus and sulfur XES. This generally requires the use of vacuum chambers or helium-filled spaces for x-rays to travel through the spectrometer. The requirements are not as severe as for soft x-rays (< 1 keV), however, and in the case of the tender XES spectrometer in chapter 5, a small (~2–5 mm) air gap is tolerated between the exit of the vacuum chamber and the surface of the x-ray camera sensor.

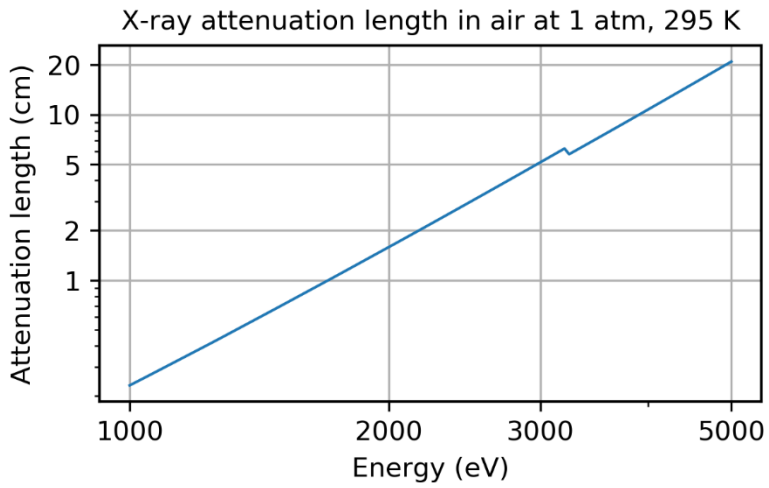

Figure 3.1: Attenuation length in air of x-rays in the tender x-ray energy range. Data generated using CXRO online calculator.[1]

Working in this energy range also affects the types of samples that can be investigated. Whereas hard x-ray techniques are known for the penetrating capabilities and are therefore able to easily perform measurements through material extraneous to the sample (e.g. *in situ* battery studies, where transition metals are probed through the entire working battery material), tender x-rays are not as penetrating and require additional consideration. It is still possible to design *in situ* experiments in this energy, for example with the use of thin encapsulating materials such as very thin polyimide films or silicon nitride windows.

3.2 EDXRF, WDXRF, AND XES

It is important to understand the connection between XES and other forms of x-ray fluorescence (XRF) measurements. All of these techniques are measurements of the same physical phenomenon: the x-ray fluorescence released when an excited atom undergoes radiative relaxation. The only distinction between the techniques is the energy resolution with which the fluorescence is measured. The information available at different resolutions varies dramatically, which is why they are commonly viewed as separate techniques. A schematic illustration comparing the measurements from the different techniques is given in Figure 3.2, with summary explanation of the spectral features in the caption.

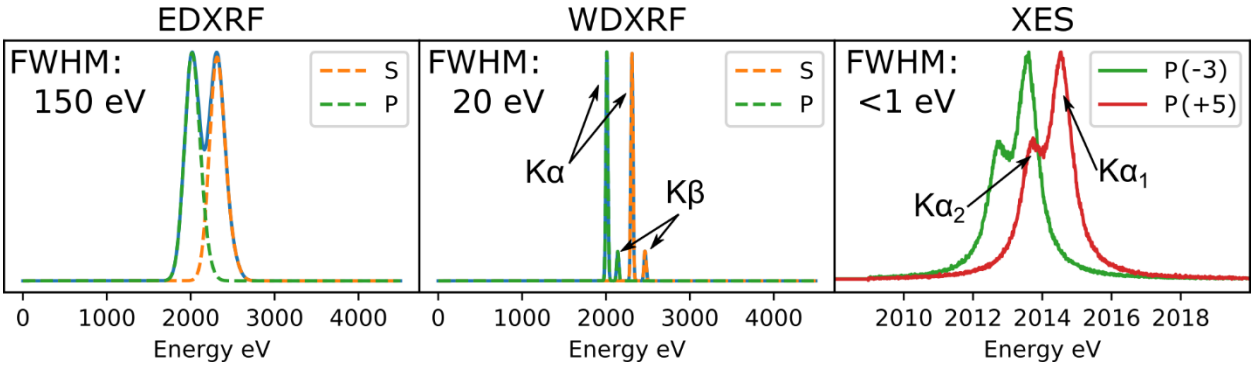

Figure 3.2: Comparison of different x-ray fluorescence measurement techniques. (left) Simulated EDXRF spectrum of a sample of mixed sulfur and phosphorus with resolution 150 eV FWHM, demonstrating the identification of both elements from their characteristic emission lines. (center) Simulated WDXRF spectrum with resolution 20eV FWHM of the same sample as the EDXRF spectrum on the left. Both Kα and Kβ characteristic lines are visible for both P and S. (right) Actual XES data measured with resolution <1 eV on the spectrometer described in chapter 5, showing the energy shift for materials of different oxidation state. The P^{-3} sample was GaP, and the P^{5+} sample was Na_2HPO_4.

3.3 Excitation Sources

For x-ray fluorescence to occur, an inner-shell electron hole must be generated in the atomic species being studied (e.g. for phosphorus and sulfur *K*-shell fluorescence, the 1*s* electron must be ejected). Perhaps the most common method of excitation is to use incident x-rays that are above the binding energy of the electronic shell being studied. These incident rays can come from a multitude of sources, including bremsstrahlung x-ray tubes, synchrotrons, free electron lasers, and decay of radioactive elements, to name a few. Another means of generating an inner-shell electron hole is by bombardment with charged particles such as protons or electrons. The following sections discuss these different excitation sources in more detail.

3.3.1 X-ray tubes

When a charged particle undergoes acceleration, electromagnetic radiation is created. In the case of an x-ray tube, the charged particle is an electron and the acceleration is actually an

abrupt *deceleration* when the electron strikes a stationary anode material. Radiation created in this manner is known as bremsstrahlung, coming from the German language and literally meaning "braking radiation." This was the source of the very first x-rays discovered by German physicist Wilhelm Conrad Röntgen in 1895.[2]

A full description of the quantum mechanics of bremsstrahlung radiation is outside of the scope of this work, though it is useful to highlight some of the key characteristics of bremsstrahlung radiation and how they relate to the output of x-ray tubes used in x-ray spectrometers. For a more detailed review of bremsstrahlung radiation, see the work of Agarwal.[3]

In a classical picture, for a near-instantaneous deceleration of a charged particle, a discontinuity in the electromagnetic field lines develops, as shown in Figure 3.3. For an observer, the electric field is seen to change suddenly, with a near delta function change of the field in the tangential direction. Fourier transforming to frequency space, taking the complex magnitude of the electric field to yield the Poynting vector, and integrating over all directions yields an intensity spectrum independent of frequency (see Agarwal[3] chapter 1). Therefore, in this simple picture, the idealized bremsstrahlung spectrum from a thin target is a flat intensity spectrum when plotted against frequency (i.e. energy); in other words, equal intensity at *all* energies of electromagnetic radiation, not just x-rays. This simple idealization agrees with the more careful calculation of Kramers,[4] with the additional dependence of a sharp cutoff at the energy equal to the kinetic energy of the electron before the collision. With this in mind, it is quite interesting that bremsstrahlung radiation is associated most strongly with x-rays since that is where it is most commonly used, though the actual intensity distribution for thin targets is even intensity across all energies up to the cutoff energy.

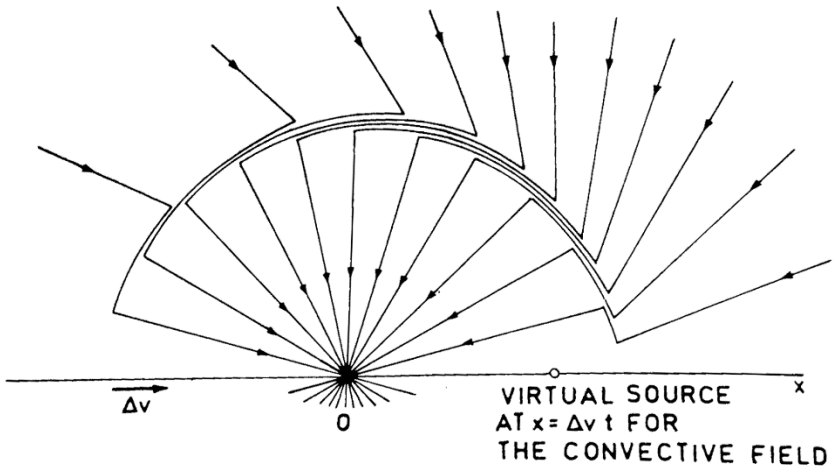

Figure 3.3: Illustration of discontinuity of electric field lines from a near-instantaneous acceleration of a charged particle. Figure from Agarwal.[3]

For a thick target, the spectrum is altered by the fact that the electron undergoes multiple collisions generating radiation in multiple steps, and that the emitted radiation must travel back out through the material to escape. The idealized spectrum of a thick target can be understood as made up of a series of thin targets, in which the cutoff energy is lower at each subsequent stage, since the electron loses a fraction of its energy in previous collisions as it travels deeper into the material. As shown in Figure 3.4, the resulting ideal thick target spectrum is a downward-sloped line, with an x-intercept representing a sharp cutoff in produced intensity at an energy equal to the initial incident electron energy. Although the ideal thick target spectrum represents what is being produced, the question more relevant to the experimenter is what spectrum will be observable from the outside of the target. As the x-rays leave the target material, some absorption occurs, and emission from deeper inside of the target is attenuated more. This attenuation is from absorption, which as discussed in section 2.1.2, has an E^{-3} energy dependence, and therefore the attenuation is much stronger at lower energies, resulting in the "actual thick target spectrum" trace shown in Figure 3.4.

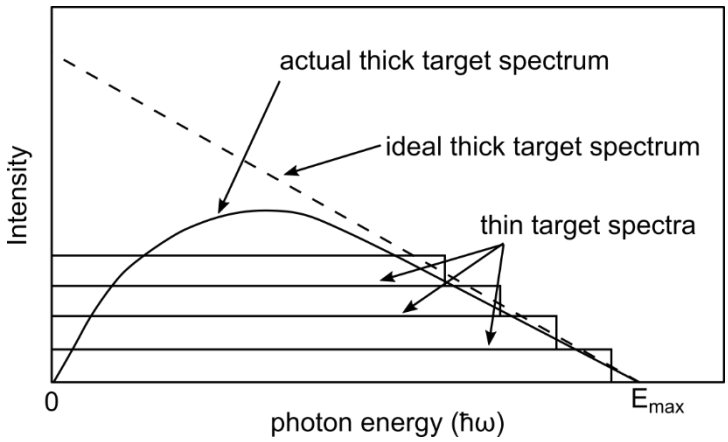

Figure 3.4: Schematic energy spectrum of bremsstrahlung radiation, showing how the spectrum from a thick target is understood as a series of combined thin target spectra.

Lastly, in addition to the smooth bremsstrahlung spectrum, electrons striking the anode material can also cause impact ionization, which upon subsequent decay leads to characteristic x-ray fluorescence, as discussed in section 2.1.4. The result is that on top of the smooth bremsstrahlung signal there are strong, narrow increases in intensity from these fluorescence lines. In x-ray emission experiments, such as the x-ray spectrometer described in chapter 5, the choice of anode material with strong emission lines can be utilized to increase the amount of sample fluorescence (and therefore signal) in the experiment. As an example, for sulfur *K*-shell fluorescence, the sulfur 1*s* electron with a binding energy of ~2472 eV must be ejected. In the spectrometer of chapter 5, the x-ray tube has a palladium anode, which has strong *L*-shell emission lines at 2838 eV (Lα) and 2990 eV (Lβ). These fluorescence lines have a good balance of being far enough above the absorption edge to avoid resonant effects (see section 2.5), but still close enough to the absorption energy to allow strong absorption. With the E^{-3} decrease in absorption cross section, sulfur absorption is much stronger at ~2900 eV from the palladium emission lines

than it would be, for example, at ~8400 eV for the strong emission lines of tungsten, which is another common x-ray tube anode material.

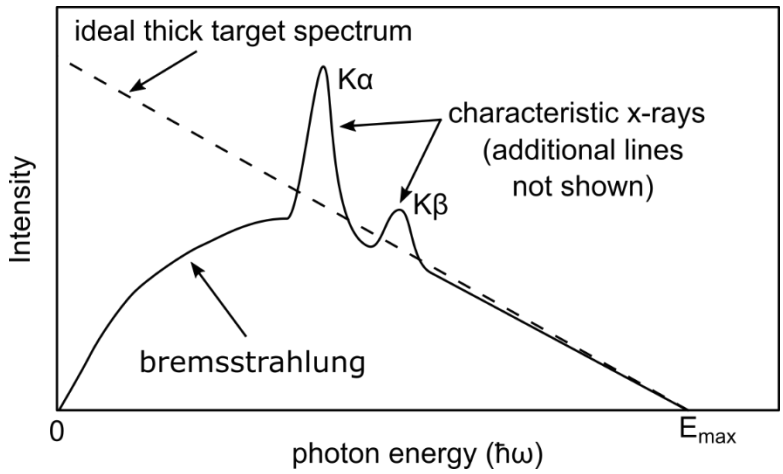

Figure 3.5: Schematic spectrum of the output of a "real" x-ray tube, showing the smooth bremsstrahlung with the characteristic emission lines of the anode material.

Now, with the understanding of the shape of the bremsstrahlung spectrum and dependence on the accelerating potential (i.e. electron kinetic energy), the last major feature of x-ray tubes is the power in the electron beam. The power of the electron beam is simply the accelerating potential of the electrons multiplied by the current in the electron beam. The shape of the spectrum produced is independent of the current, and more electrons just emits more radiation with the same spectrum, such that the intensity of the spectrum scales directly with the electron beam power.

The major challenge in the construction of x-ray tubes is stabilizing the electron beam and preventing the electron beam from overheating and destroying the tube. Higher powers are desired to generate more flux, but the x-ray tubes must be constructed to withstand the additional heating from the electron beam. Therefore, x-ray tubes can be generically categorized by how they are cooled. Modern air-cooled x-ray tubes can achieve powers of up to a few hundred watts. Combined with electron-beam spot sizes on the order of ~1 mm, there is thus a very large heat flux into the anode material that needs to be cooled. For powers up to ~1–2 kW, air cooling is

insufficient, and water-cooled anodes are required. For even higher powered tubes (up to several kW), rotating anodes can be used, thus spreading the electron beam power over a circle of the rotating anode material instead of a single spot.

The last major point to consider when choosing an x-ray tube for a fluorescence experiment is the geometry of the electron beam spot relative to the tube window and where the sample can be positioned. The electron beam travels in vacuum, and so an x-ray window separates the vacuum from atmosphere (typically a beryllium window to reduce absorption). As the flux (intensity per area) of x-rays drops as the inverse square of the distance, to get the most flux on a sample in a fluorescence experiment, the sample must be brought as close as possible to the electron beam spot. With modern XRF-style x-ray tubes, the beam spot can be as close as ~5 mm from the x-ray window, allowing a large flux to be captured by the sample.

3.3.2 Synchrotron beamlines

In the history of XES development, discussed in section 1.2, many of the developments of advanced x-ray spectroscopies were carried out synchrotron facilities after their rapid development in the 1970s. At synchrotrons, x-rays are generated by high energy electrons that are centripetally accelerated by magnetic fields. The physical principle of x-ray generation, namely, the acceleration of electrons, is the same in a synchrotron as in an x-ray tube. At a synchrotron however, instead of accelerating electrons by abruptly stopping them in a piece of metal, electrons are accelerated by travelling through regions of strong magnetic fields.

There are three main types of synchrotron beamlines that use different magnet configurations to generate x-rays: bending magnets, wigglers, and undulators. Illustrations of these magnet configurations are shown in Figure 3.6, along with a contrast schematic of how x-

rays are generated in an x-ray tube. Illustrative spectra of the radiation generated from each type are shown in Figure 3.7.

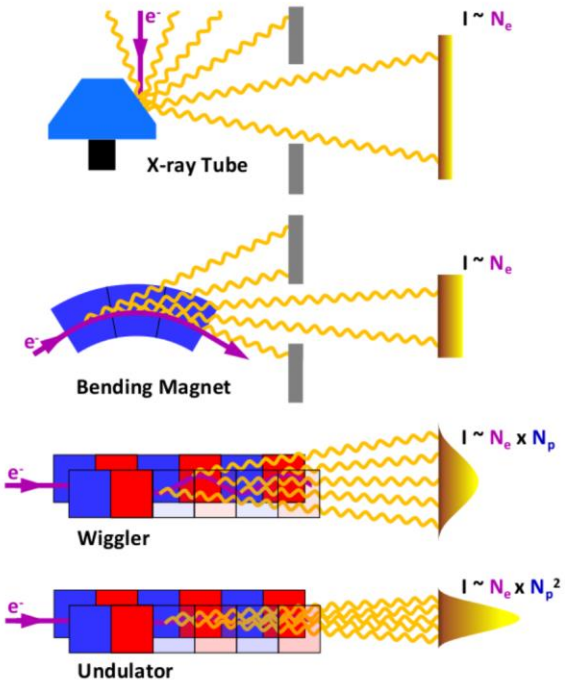

Figure 3.6: Diagrams of the different magnet configurations of bending magnets, wigglers, and undulators used at synchrotron facilities to generate x-rays. Also shown for contrast is a schematic of x-ray generation in an x-ray tube. Figure from Shabalin.[5]

A bending magnet beamline generates x-rays in the process of bending the beam in one direction. Radiation of this type is produced every time an electron in the storage ring of a synchrotron facility is steered. A wiggler has alternating poles of magnets that steer the beam with strong deviation in direction. The radiation from a wiggler can be thought of as being generated by a series of bending magnets, with a total spectrum of generally the same shape as a bending magnet beamline but higher in intensity. An undulator has alternating poles of magnets, but in contrast to a wiggler, the maximum deviation of the direction of the beam is much reduced and the spacing of the poles is different. The result is that the radiation generated at each set of magnet poles interferes with the radiation generated from the others, such that the sum total radiation from

the undulator is peaked at an energy related to the magnetic pole spacing. Radiation peaks also occur at higher energy due to harmonics of the magnetic pole spacing. The result is that undulator radiation has much higher peak brilliance, but at the cost of having a narrow bandwidth.

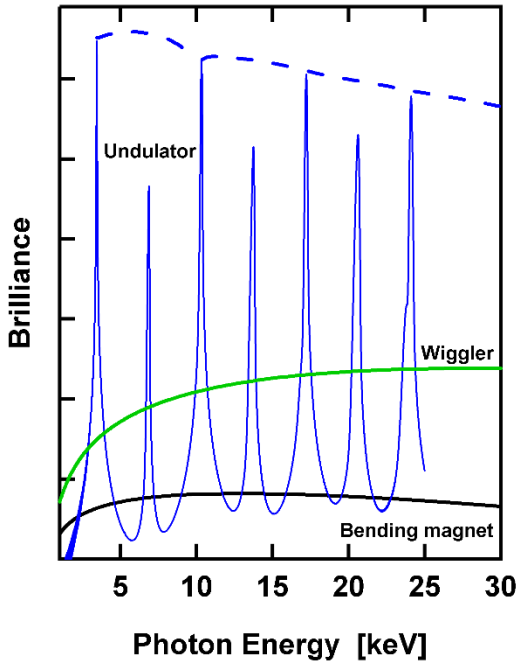

Figure 3.7: Schematic illustration of the relative brilliance of different magnet configurations for x-ray generation. Figure from DESY website.[6]

For tender and hard x-ray operations, as is relevant for this dissertation, the raw spectrum of the beam is almost always monochromatized using a double-crystal monochromator, so that the output beam typically has a relative energy resolution of $\sim 1*10^{-4}$, i.e. high energy resolution with a narrow bandwidth. In addition to a monochromator, many additional elements are typically included in synchrotron beamlines, such as slits to control beam size, focusing mirrors to allow micro-focused beam spots, and chemical filters for suppressing harmonics. An illustration of the beamline components of 4-BM at NSLS-II is shown in Figure 3.8.

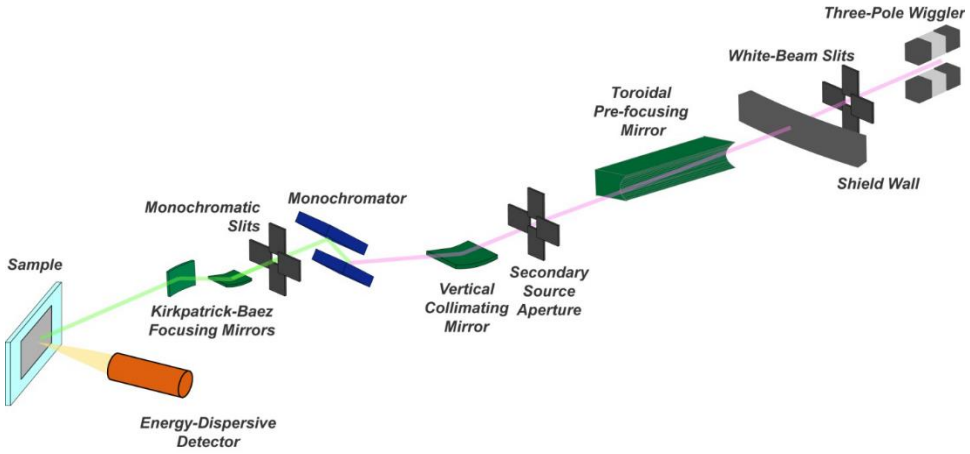

Figure 3.8: Illustration of beamline components of beamline 4-BM X-ray Fluorescence Microprobe (XFM) at NSLS-II.[7]

Radiation from synchrotron beamlines is not continuous in time, but comes in bursts due to the electron bunches travelling in the storage rings. By coordinating these bursts with accurately timed laser pulses, it is also possible to do studies with time resolution, for example pump-probe experiments where samples are pumped with a laser beam to a high energy state and subsequently probed with the x-ray pulse from the beamline.

To conclude this section, it's useful to highlight the major differences in capabilities for performing an XES experiment using a synchrotron beamline as a source instead of an x-ray tube. First and foremost, beamlines allow monochromatic incident flux on the sample. Thus, in addition to a high-resolution measurement of emitted energies with XES, the spectrum can be measured at different incident energies. These incident energies can be scanned through important features in the absorption spectrum (XANES), and changes in the XES coming from resonant effects can be observed. This topic, i.e., resonant XES, is discussed in more detail in section 2.5. Second, many synchrotron beamlines have optical elements that focus the beam spot to small dimensions on the sample, often down to several microns or even nanometers. With small focal spots, it is possible to raster the sample underneath the beam and thus get position-dependent measurements. Thus it

would be possible to make XES maps of features on a sample, or selectively take measurements from an interesting feature (like the nucleus of a cell (!), as was demonstrated in the case of micro-XANES for arsenic speciation in cellular compartments.[8]). Third, as indicated above, synchrotron beamline output is pulsed in time, and by coordinating the x-ray pulses with laser pulses, studies of laser-excited time-resolved XES have been made in this manner.[9-11]

3.3.3 Other excitation sources

In addition to x-ray tubes and synchrotron beamlines, other recent advances have been made in x-ray generation techniques that may be used to stimulate fluorescence for an XES experiment. One method that has been demonstrated in a study of XES is x-ray generation with a laser driven plasma for a time-resolved study.[12] Other recent methods of x-ray generation also make use of high-powered lasers, including betatron radiation from laser wakefield acceleration[13] and high-harmonic generation where harmonics of the incident laser of order >5000 have been utilized to generated x-rays energies up to 1.6 keV.[14] These techniques have been demonstrated in XANES experiments[13,15] at soft x-ray energies (~ 400 – 1000 eV), where these sources have clear advantage due to challenges generating these energies with conventional bremsstrahlung x-ray tubes. It is possible that they could be used as well in soft x-ray energy XES experiments, where they may offer the ability for time-resolved measurements.

Outside of stimulating fluorescence with incident x-rays, it is also possible to use beams of charged particles as excitation sources. Electron or proton beams incident on samples can cause ejection of core-level electrons, stimulating subsequent fluorescence. This is very common when paired with scanning electron microscopes, in a technique known as scanning electron microscopy energy dispersive x-ray fluorescence (SEM-EDX). This is typically done at low resolution (> 100 eV) for elemental analysis and elemental mapping. Notably, some higher resolution (~3 eV

FWHM) measurements, in particular for sulfur Kα and Kβ, have been reported by Sánchez et al.[16] and Pérez et al.[17] with a crystal analyzer-based spectrometer coupled to an SEM. In their studies, very narrow slits were required for high resolution measurement, and in addition to measuring the main Kα and Kβ features, a number of multielectron excitation satellites (see sections 2.3.3 and 2.4.4) were also reported. Though some studies with XES-like information can be studied at that resolution, retrieving full information from the techniques such as Kα linear combination fitting and comparison of fine structure of the Kβ spectrum with theoretical results require XES resolution (<1 eV). In the future, it could be possible to use a spectrometer like the one in chapter 5 to achieve higher resolution in combination with an SEM, and perhaps without too much lost signal. As described in chapter 5, one of the advantages of the spectrometer is that no slits are required and the spectrometer is relatively insensitive to the means of sample illumination. One reason for this is the position-sensitive detector, which combined with the crystal, serve to define the possible resolution without need for a slit that decreases signal. In contrast, the spectrometers in the systems of Sánchez et al. and Pérez et al. operate in step-scanning modes which require narrow slits to achieve high resolution at each point.

XES when combined with particle beam excitation, such as protons or alpha particles, is known as particle-induced x-ray emission (PIXE), though some authors use PIXE to refer specifically to proton-induced x-ray emission. There are many studies using the PIXE technique, often in the tender x-ray range.[18-24] One feature that alpha particle PIXE has been used to investigate are multiple ionization satellites,[19] where the strength of multiple ionization features is observed to be much larger in response to alpha particle induced radiation, in contrast to proton-induced or x-ray excited measurements.

3.4 DETECTORS

A large variety of detector technologies are commonly used in x-ray spectrometers. Indirect detectors, such as scintillator/photomultiplier combinations, rely on conversion of x-rays to visible light which is then detected. They have the advantage of relatively high count rates before saturation (i.e. short decay time)[25], but with the disadvantage of relatively low energy resolution. They can also be used at higher energies than other detection types, such as in the Laue-type spectrometer of Szlachetko et al.[26] that used a scintillation detector for XES measurements as high as gold Kα (78 keV).

Direct detectors, in which the x-rays are converted directly into electronic charges which are subsequently recorded by electronics, have higher energy resolution and are therefore more common in x-ray spectrometers, where the energy resolution allows background and stray signal to be rejected. Direct detectors take on forms such as ionization chambers, where x-rays travel through a sparse gas and cause ionization of the gas, as well as solid-state devices where x-rays are absorbed directly into active layers of solids, such as silicon in the case of silicon drift diodes (SDDs) and charge-coupled device cameras (CCD) and complementary metal-oxide-semiconductor cameras (CMOS).

Direct detectors in which the x-rays are absorbed in active silicon layers typically offer higher resolutions and, especially in laboratory-based instrumentation, are typically the preferred detectors for x-ray spectrometers. For point-to-point focusing spectrometers, where a single energy is measured at each point, SDDs are common since they offer no spatial resolution and are essentially a large single pixel; this approach is used in the spectrometer of Jahrman et al.[27] For dispersive approaches that require position sensitivity, in which the intensity is measured at a range of positions corresponding to a range of energies, x-ray cameras and stripline detectors are

common. CCDs are typically manufactured with larger pixel thicknesses and have higher quantum efficiencies as a result, and offer spatial resolution and some energy resolution; these are especially common in laboratory spectrometers using the von Hamos geometry[28-31] (see section 3.7.2). CMOS sensors are a rising alternative to CCDs and rely on the same approach of x-ray absorption in an active silicon layer, but differ in the electronics scheme used to process the created amount of charge. One advantage of the CMOS scheme is that it is often a less expensive alternative to CCDs, since CCD production requires dedicated processing facilities whereas CMOS-based sensors can often be manufactured at the same facilities as other microelectronics products. In addition, CMOS detectors can often function with low noise even at room temperature, whereas CCD require cooling to achieve low dark counts. Chapter 6 details our efforts to make a homemade CMOS x-ray camera, which, despite thinner active regions still maintains reasonable quantum efficiencies (~50 %) in the tender x-ray range and is therefore very suitable for spectrometers such as the one discussed in chapter 5.

One exciting detector technology for x-ray spectroscopies is the rapidly developing example of transition edge sensor arrays.[32,33] This technology uses an array of superconducting sensors on small reference masses, such that these units are maintained precisely at the temperature of their superconducting transition edges. In this state, the energy deposited by a single photon changes the temperature of the element and causes a measurable change in resistance of the superconducting temperature sensor because the superconductor is on the steepest slope of its transition region. By accurately measuring this change in resistance with the use of another technology, superconducting quantum interference devices (SQUIDs), one can accurately determine the energy deposited and thus the energy of the incident photon. This approach has demonstrated detector resolutions as high as 1.6 eV at 5.9 keV incident photon energy.[34] This

resolution is close to the level of the natural linewidths of x-ray transitions being measured. The main advantage of this approach is extremely high measurement efficiency, as the photons are detected directly without the need for a dispersive element like a crystal analyzer. As this technology is further developed, it could allow x-ray spectroscopy to be performed in a number of situations where measurement with traditional spectrometers would be too inefficient to be practical.

3.5 Crystal analyzers

To achieve higher energy resolution than what is possible with direct x-ray detectors, dispersive elements are required. Similar to a prism with optical light, x-ray dispersive elements take an otherwise polychromatic incident beam of radiation and disperse it in space based on energy. Changes in refractive index for different x-ray energies are extremely small, however, and prisms are impractical for dispersive purposes with hard x-rays. There are various approaches for x-ray dispersive components, including zone-plates,[35] diffraction gratings,[36] and crystal analyzers. In the tender x-ray range, crystal analyzers are typically used for their high performance in terms of energy resolution and efficiency, as well as their ease of manufacture.

Crystal analyzers rely on Bragg diffraction of x-rays from crystalline materials. At the simplest level, Bragg diffraction is understood as coherent scattering from repeating planes of a periodic material, as illustrated in Figure 3.9. Geometric considerations based on the figure lead to the form of Bragg's law:

$$n\lambda = 2d \sin\theta$$

where λ is the wavelength, d is the periodic spacing of the material, θ is the scattering angle, and n is the diffraction order.

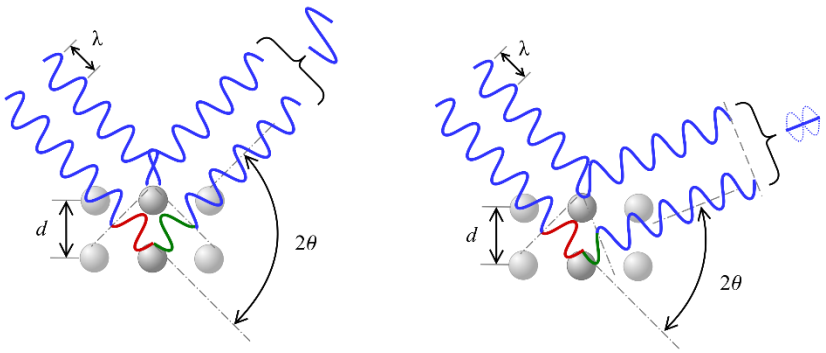

Figure 3.9: Illustration of geometric relationship of the Bragg diffraction condition. Figure by Christophe Chan.[37]

While Bragg's law is relatively simple to understand and is useful for quickly calculating angles for aligning spectrometers, some information is needed beyond this simple equation to understand the performance of crystal analyzer. For example, Bragg's law gives the approximate condition for scattering to occur but yields no information about the strength of the diffraction. In particular, depending on the crystal symmetry, not all orders of diffraction (n) are allowed, and many are not observable or have drastically reduced intensity. Bragg's law would also imply that a monochromatic beam incident on a crystal would only diffract at a single, precise angle, and thus from a vanishingly small region of the crystal corresponding to that exact angle. If the diffraction strength was not infinitely strong (in the manner of a delta function), then no appreciable intensity would be scattered.

The solution to these issues and a full description of the phenomenon of diffraction from perfect crystals is known as dynamical diffraction. A full account of dynamical diffraction is beyond the scope of this work. A thorough discussion is given in chapter 6 of Als-Nielsen.[38] Here, a few key results of dynamical diffraction and their effect on the use crystal analyzers in spectrometers are discussed.

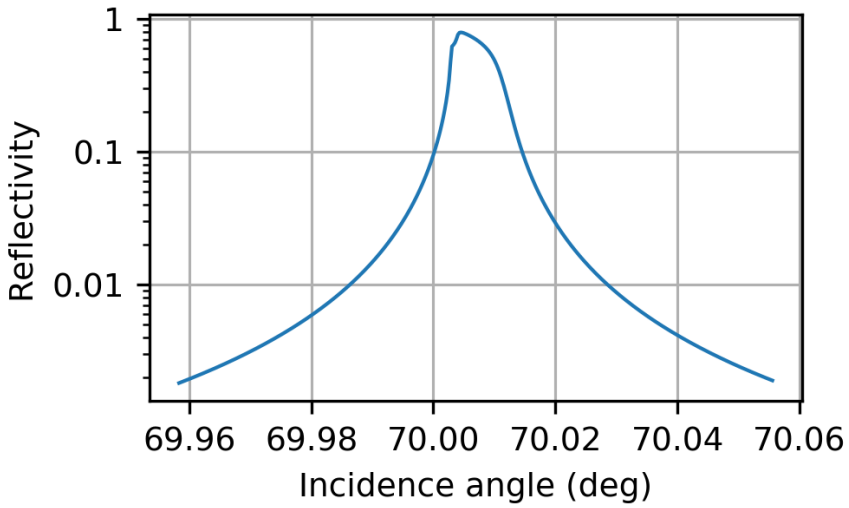

Figure 3.10: Reflectivity curve of silicon (220), at the Bragg condition for 70 degrees, for incident radiation of mixed polarization. Calculated using Sergey Stepanov's X-ray Server.[39,40]

An example of a crystal reflectivity curve is shown in Figure 3.10, for a silicon crystal with surface along the (220) Miller indices direction, at incident angle 70 degrees and for an incident beam of mixed polarization in a symmetric reflection condition. There are several interesting features of the reflectivity curve to remark upon. First, remarkably, the reflectivity can approach unity such that nearly all incident intensity in a narrow angle or energy range is diffracted. Second, as anticipated, there is a finite range of angles over which reflection occurs significantly, in this case on the order of 0.01 degree. Note that while the geometry of the calculation is set to what would be predicted to be a Bragg angle of 70 degrees based on the silicon lattice spacing and Miller indices, the actual center of the diffraction occurs slightly offset from the idealized Bragg condition. Third, the reflectivity curve depends on the polarization of the incident beam, which affects the shape of the curve and also allows this difference in reflectivity to be utilized to control beam polarization. Lastly, the reflectivity curve is asymmetric, and is reduced on the high-angle side compared to the low-angle side. This occurs because above the ideal angle, the diffracting

wavefield is in phase with the atomic planes, leading to more absorption than below the ideal angle where destructive interference reduces the intensity at the atomic planes. Also, the properties described above vary with energy, two important effects being that the asymmetry decreases at higher energies and the overall width of the curve decreases at higher energies, in both cases because of diminished absorption.

All these properties can play important roles in the design of crystal analyzer spectrometers. Perhaps most importantly is knowing the overall strength of diffraction, so that crystal analyzer materials can be chosen to have strong reflections and therefore make efficient spectrometers. Computational codes (like Sergey Stepanov's X-ray Server or XRayTracer) making use of dynamical diffraction can be used to calculate the total intensity of a diffraction to aid in analyzer selection. Additionally, knowing the offset between the ideal Bragg angle and actual angle of reflection can play a role in energy calibration of spectrometers.

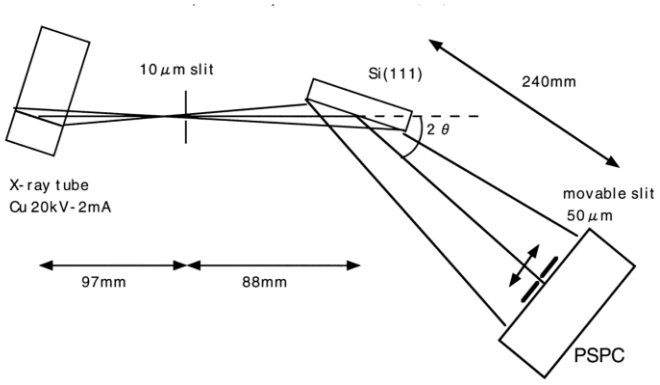

Figure 3.11: Schematic of a single flat-crystal x-ray spectrometer. X-rays travel from the source on the left (x-ray tube) to the crystal, and different rays making different angles with the crystal return to different positions on the position-sensitive detector. In this design, a small source size is needed. In the diagram, this is achieved with a small slit on the output of the x-ray tube. In practical implementation, this approach was designed to be used with a microfocused x-ray beam from a synchrotron beamline, where the slit is used to define the beam but does not drastically

reduce the incident flux as would occur with an x-ray tube as illustrated. Figure from Hayakawa et al.[41]

From the properties of Bragg diffraction, a single flat crystal alone can be used as a dispersive element in an x-ray spectrometer. One such design is illustrated in Figure 3.11. The energy resolution for a single flat-crystal spectrometer depends heavily on the source size of the x-rays, as the angle from the source to crystal can vary over the size of the source. For applications with small source sizes, such as synchrotron beamlines with micro-focused beams, flat crystal spectrometers have been utilized for x-ray spectrometers.[41,42]

Generally speaking, a single flat-crystal spectrometer has several drawbacks, namely low efficiency of collected x-rays, relatively low energy resolution, and strong sensitivity of resolution to size of the source. As such, several spectrometer geometries making use of different crystal analyzer configurations exist to drastically improve energy resolution and efficiency. One common geometry, the Rowland circle geometry, will be discussed in the next section. Some alternatives are discussed in section 3.7.

3.6 Rowland focusing geometry

One very common approach to crystal analyzer-based x-ray spectrometers is the Rowland circle geometry. This geometry is named after Henry Augustus Rowland, the first president of the American Physical Society. Rowland first published a short note describing the geometry in 1882[43] in the context of its application with visible light spectrometers making use of curved diffraction gratings. The geometry and focusing circle arrangement became known as the "Rowland circle," and the name was later applied to the very analogous situation in x-ray spectroscopy where the diffraction grating is instead replaced a crystal analyzer.

3.6.1 Overview of Rowland circle concepts

The Rowland circle geometry is illustrated in Figure 3.12. The illustration is of the most common form encountered in x-ray spectroscopy, namely the symmetric geometry where both left and right focal points are symmetrically placed on the circle. The symmetric condition occurs because when utilized with a bent crystal analyzer for x-rays, the diffraction angles are symmetric with respect to the surface normal of the crystal. Notable, with diffraction gratings for visible light, the angle of incidence and angle of reflection are generally not equal, and thus the focal points can occur at different locations on the focusing circle.

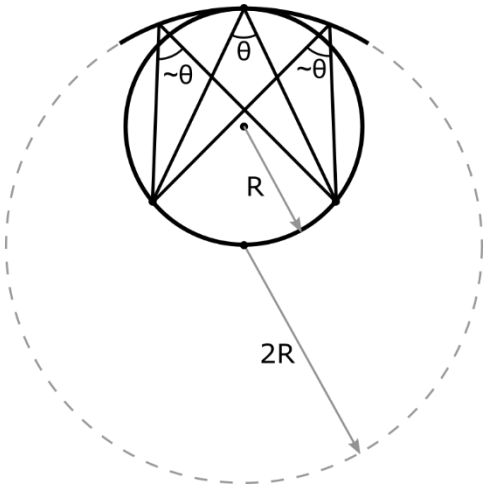

Figure 3.12: Illustration of the Rowland circle geometry. The diffracting / reflecting element at the top (crystal analyzer in the case of x-rays) is bent to a radius 2R with the resulting focusing circle having radius R.

The clever innovation of the focusing circle (radius R) is the use of the basic geometrical fact that for two points on a circle, any two chords that extend to another point on the circle make a constant angle between them. For the three rays considered in Figure 3.12, because they make nearly the same angle with the surface of the crystal (radius= 2R), by Bragg's law the energy of diffracted rays is nearly the same. Note that at the edges of the crystal, the angle is only approximately equal. This refocusing error is known as "Johann error" and is the topic of section

3.6.3. This error can be mitigated by further processing of the crystal analyzer to create a "Johansson" analyzer, as discussed in the next section.

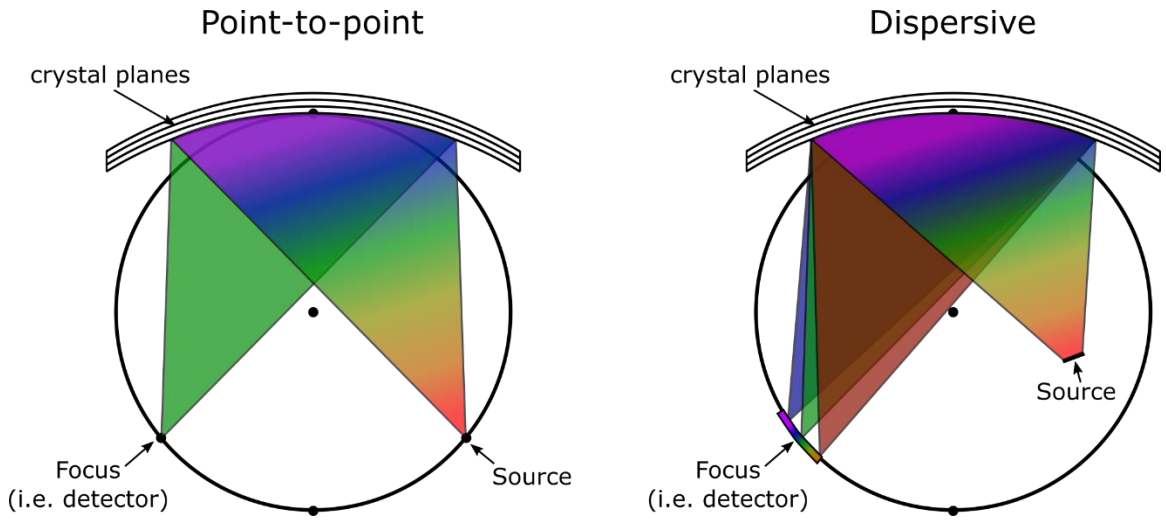

Figure 3.13: Illustration of the Rowland circle geometry in the case of point-to-point and dispersive setups, depending on location of the source. Colors represent that all energies are emitted from the source, and only selective energies are focused back onto the Rowland circle.

There are two ways to operate a Rowland circle geometry, either in a point-to-point focusing mode, where from a polychromatic radiation source only a single energy is refocused, then to measure different energies the location of the source and focus would be symmetrically scanned. Alternatively, with the source located inside of the Rowland circle, a range of energies can be refocused onto the circle, and with a position sensitive detector, multiple energies can be measured simultaneously. This dispersive approach is employed in the spectrometer in chapter 5, where additional details of the dispersive refocusing geometry is discussed.

3.6.2 Johann and Johansson geometries

With Johann-type[44] Rowland circle spectrometers a Bragg-angle dependent aberration occurs due to the details of the Johann analyzer geometry (Figure 3.14 left). In order to satisfy the Bragg condition, the normal direction of the crystal planes must be aimed at the center of the

bottom of the focusing circle. For a constant radius bend, in order to achieve this direction, the crystal cannot lie exactly along the circle of radius R, but rather must be bent to radius 2R. This gap between the focusing circle and the crystal analyzer creates an aberration in the focal spot F. This aberration (colloquially referred to as the "Johann error") increases as Bragg angle decreases (away from backscatter) and in practice limits the angle range usable in Johann-type spectrometers.

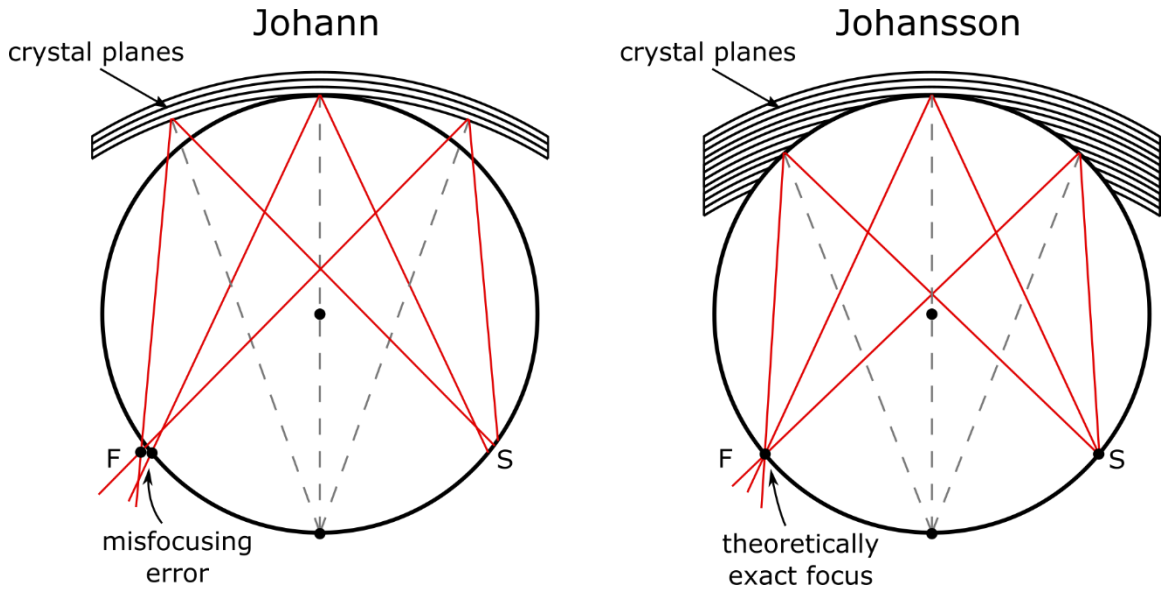

Figure 3.14: Illustration of Johann vs. Johansson x-ray crystal analyzer geometry. All rays shown are for the same energy. Note that in the Johann case, the fact that the source *S* is not coming from a single point is not an artifact, but an actual feature, showing that the Johann distortion effects both the focal point *F* as well as the sampled source locations *S*.

The Johann error can be solved by suitable modification of the crystal analyzer, and the result is the Johansson geometry[45] shown on the right in Figure 3.14. The tradeoff of this geometry is the increased complexity of the crystal analyzer. The crystal analyzer must be bent such that the crystal planes are oriented to the proper radii (radius 2R at the top of the circle, but $< 2R$ at other points along the circle), then portions of the crystal must be removed such that the surface of the crystal lies exactly along the circle of radius R. In practice there are multiple approaches to manufacturing a crystal in such a geometry. Two such approaches are shown in Figure 3.15. The

increased expense of the Johansson geometry is often justified, and Johansson optics are commonly used in synchrotron spectrometers.[24]

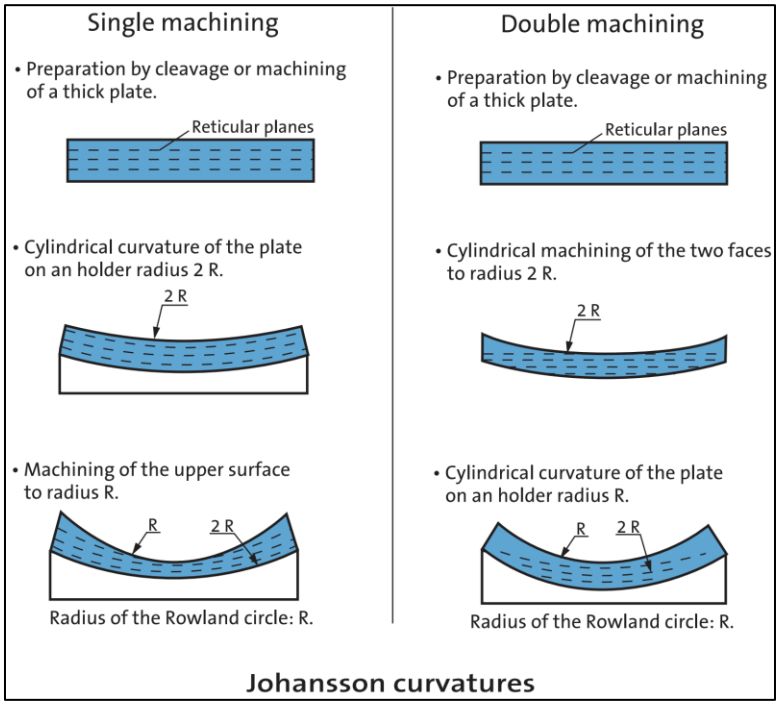

Figure 3.15: Illustrations of two approaches for producing crystal analyzers of the Johansson geometry. Figure from Saint-Gobain website.[46]

Depending on the energy range being studied, it is not always possible to find a crystal analyzer with suitable d-spacing to work near backscatter in the Johann geometry, and in such cases Johansson crystals are important components. One example in the tender x-ray regime is the sulfur Kβ emission lines 2464 eV (5.03 Å). Consulting the list of common crystalline and multilayer materials for use as analyzers in the x-ray data booklet[47] shows that the crystal with nearest 2d spacing is NaCl (2d = 5.641 Å, yielding Bragg angle 72°), and the more commonly used Si(111) (2d = 6.2712 Å, yielding Bragg angle 59°) is also nearby. Use of NaCl as a crystal analyzer material creates obvious challenges of degradation from humidity in the atmosphere for a spectrometer that is not permanently installed in vacuum, thus typically Si(111) is used instead

even at the less favorable Bragg angle. In Johann-type spectrometers, resolution can be maintained by masking the edges of the crystal which have the largest aberration, whereas Johansson-type spectrometers maintain energy resolution while still utilizing the entire crystal, thus allowing for more efficient measurements.

Despite imperfect focusing of the Johann-type spectrometers, the relative ease and simplicity with which the crystal analyzers can be manufactured makes them the practical choice in many situations. In particular, the spectrometer discussed in chapter 5 of this thesis makes use of a cylindrically bent crystal analyzer with radius of curvature of 100 mm. Typically, silicon is used, and the manufacture of such a small radius requires a thin wafer. The thin wafer thickness allows the Johann-type analyzer to be produced relatively simply, but complicates attempts to perform the machining steps required for production of the Johansson geometry.

3.6.3 Johann error

It is useful to elaborate on the effects of Johann error on the Johann-type cylindrical analyzer spectrometers such as the one utilized in Chapter 5. Investigations of the Johann error have been made in the literature,[48] in particular by Lu and Stern for comparing Johann vs. Johansson geometries,[49] and the effects have also been discussed in the context of spectrometer design and performance.[50,51] The discussion of Johann error effects however is often complicated by the mode of operation of the spectrometer. In the case of Wang et al, they investigate effects of an extended source with a detector that is not tangent to the Rowland circle but rather pointed at the analyzer. Lu and Stern discuss the case of a polychromatic point source on the Rowland circle. In the following, a simplified view is taken and limited to the analysis of singly curved crystals in two dimensions. For comprehensive analyses of monochromators including all manner

of doubly-curved analyzers, see the incredibly thorough works of Wittry and Sun,[52] and Suortti et al.[53]

The problem can be analyzed from two perspectives: (1) for a single point on the detector, what are all of the energies that can be refocused from the crystal analyzer onto that point (for polychromatic source), and (2) for a single energy being refocused (monochromatic source), what are the range of positions of the detector onto which radiation can be focused. Here, I take case (2), the idealized case of a monochromatic extended source on the source-side of the Rowland circle, with radiation being analyzed back onto Rowland circle on the focusing-side (Figure 3.16). Furthermore, the problem is analyzed in the 2d-plane, ignoring effects of rays with angles into or out of the plane which may also effect the Bragg angle. Beyond the scope of this work, full inclusion of all effects on spectrometer resolutions including Johann error could be more rigorously investigated with a full simulation using modern x-ray ray-tracing software such as the Python-based XRayTracer.[54]

The problem is laid out as follows: for radiation of energy E being diffracted by the crystal at angle α, if the radiation is diffracted by a point on the crystal analyzer some distance from the center (characterized by angle θ_0), the radiation will be focused to point B (add label) which makes an "effective" bragg angle of β with the center of the crystal, therefore the energy assigned by a detector on the circle would assign the energy refocused from that point to be at the energy for Bragg angle β instead of the true Bragg angle α. Therefore, the aim is to find the relation between the distance of a point on the crystal analyzer from the center and the energy error ($E(\alpha) - E(\beta)$).

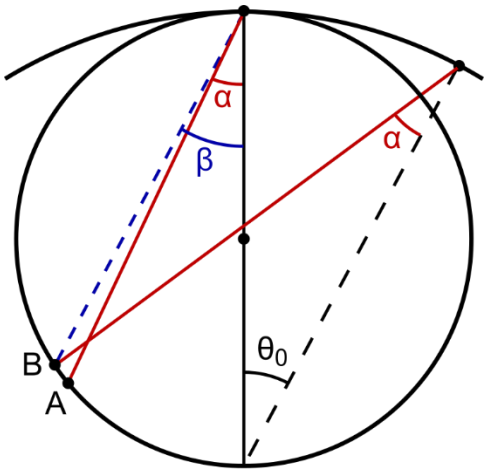

Figure 3.16: Schematic of geometry used for analyzing the effects of Johann error.

This problem was solved in *Mathematica*, and the code and solution are shown in Figure 3.17. The solution shown was simplified using *Mathematica*'s simplification algorithms.

```
p1 = R * {Sin[θ], Cos[θ]} + s * {-Sin[α + θ], -Cos[α + θ]};

p2 = {0, R/2} + R/2 {-Sin[2 β], -Cos[2 β]};

sol = Solve[p1 == p2, {s, β}];
```

$$\beta \to \frac{1}{2}\,\text{ArcTan}\Big[1 - 2\,\text{Cos}[\theta] - \text{Cos}[2\,(\alpha+\theta)] + \sqrt{2}\,\text{Abs}[\text{Cos}[\alpha+\theta]]\,\sqrt{-3 + 4\,\text{Cos}[2\,\alpha] + 4\,\text{Cos}[\theta] + \text{Cos}[2\,(\alpha+\theta)] - 4\,\text{Cos}[2\,\alpha+\theta]} + 2\,\text{Cos}[2\,\alpha+\theta],\ 4\,\text{Cos}[\alpha+\theta]\,\text{Sin}[\alpha] - \text{Sin}[2\,(\alpha+\theta)] + \sqrt{2}\,\text{Abs}[\text{Cos}[\alpha+\theta]]\,\sqrt{-3 + 4\,\text{Cos}[2\,\alpha] + 4\,\text{Cos}[\theta] + \text{Cos}[2\,(\alpha+\theta)] - 4\,\text{Cos}[2\,\alpha+\theta]}\,\text{Tan}[\alpha+\theta]\Big]$$

Figure 3.17: *Mathematica* code and solution for the misfocused effective Bragg angle β.

With the solution for the parameter β, it is possible to calculate the Johann error. The Johann error, taken as the difference in energy as assigned by the detector and the true energy of the refocused radiation, is plotted in Figure 3.18. It is clear from the plots that Johann error increases quickly with distance from the center of the analyzer, and Johann error is much more pronounced at lower angles. For measurements of sulfur Kα as reference, the emission line is only ~1.5 eV wide, so deviations on the order of 1 eV or more greatly distort the spectral shapes.

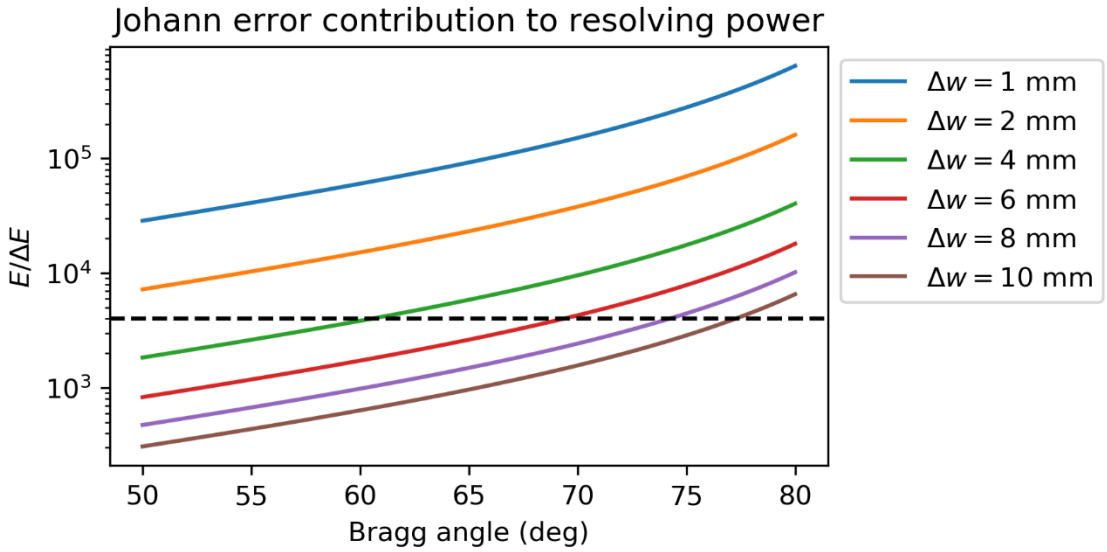

Figure 3.18: Plots of Johann error contribution to the resolving power, showing dependence on Bragg angle and width of the analyzer. Δw represents the distance between the center of the analyzer and the edge point considered. The black dashed line represents a resolving power of 4000 corresponding to 0.5 eV resolution near P Kα (2014 eV). The plot represents the maximum deviation that occurs between the center and a region at the edge of the analyzer. Thus the actual resolving power in an experiment, being the average over the entire region of the analyzer, would be somewhat less.

Figure 3.19 shows that the dependence of Johann error on distance from the center of the crystal analyzer is fit well by a quadratic polynomial. Interestingly however, the fit is not perfect, and it is not obvious from the form of the solution for β that the dependence should be exact.

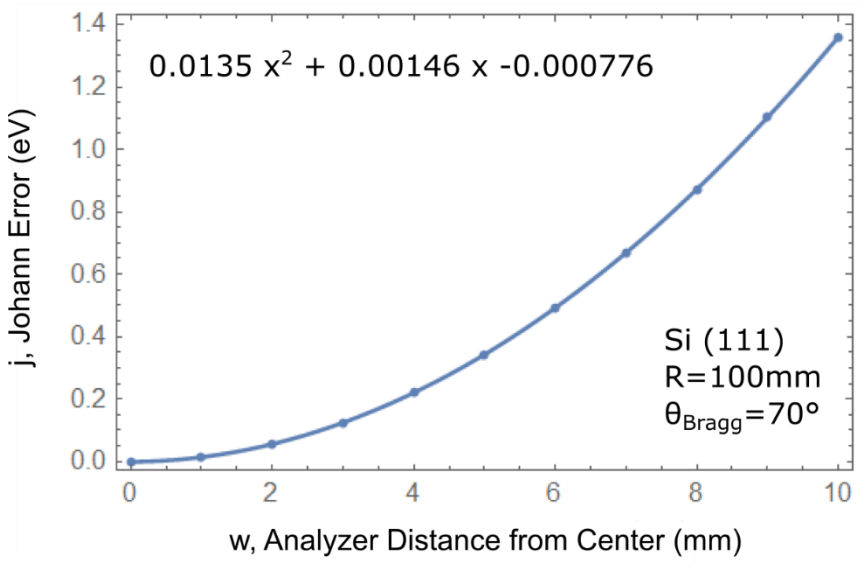

Figure 3.19: Fit of the dependence of Johann error on distance from the center of the crystal analyzer using the approach described in the text.

3.6.4 Johann error effects on spectrometer response function

With the general form of the dependence of the Johann error on the distance of the point on the crystal from the center, it's possible to find the response function of a cylindrical crystal analyzer with respect to the Johann error contribution. Using a quadratic function to model the Johann error j as a function of distance from the crystal center w, we can invert the equation to solve for w(j), taking only the positive root to look at one half of the crystal analyzer:

$$j(w) = aw^2 + bw + c \tag{33}$$

$$w(j) = \frac{-b + \sqrt{b^2-4a(j-c)}}{2a} \tag{34}$$

To get the response function from the integrated width of the analyzer, we assert that the measured intensity at a Johann error j is proportional to the differential width dw corresponding to that j, with some proportionality constant k related to the crystal reflectivity.

$$\text{totalsignal} = \int I(w)dw = \int k\,dw = k\int \frac{dw}{dj}dj \equiv k\int I(j)dj \tag{35}$$

We use this definition to identify the response function which gives the intensity reflected from the crystal for a given magnitude of Johann error:

$$I(j) = \frac{dw}{dj} = \frac{1}{\sqrt{b^2 + 4a(j-c)}} \tag{36}$$

The resulting response function is shown in Figure 3.20. It's clear that the Johann error is asymmetric with tails only on the high-energy side of the response, in agreement with Figure 3.16. Thus, the center-of-mass of the response is also not centered on the input energy but shifted towards higher energy. From Figure 3.19, it's clear that the regions near the center of the analyzer contribute the portion of the response closest to the input signal, and that the high energy tail is due towards the outer extremities of the crystal analyzer. Thus, the high-energy tail of the response can be trimmed by use of a mask over the analyzer.

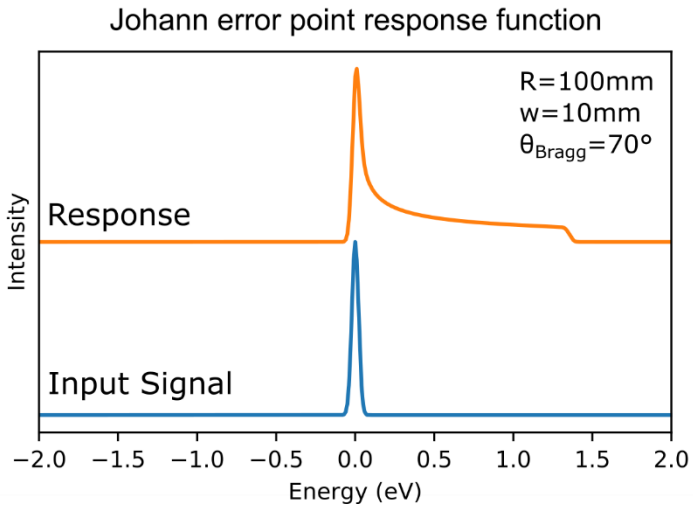

Figure 3.20: Illustration of the response function of a spectrometer operating at 70 degrees Bragg angle with silicon (111), showing the distortion caused by Johann error for a crystal analyzer 20mm wide on a 100mm-radius Rowland circle.

In Figure 3.21, the spectra from masked and unmasked measurements of sulfur Kα radiation are shown. The response function agrees qualitatively with results observed comparing masked and unmasked spectra measured on the spectrometer described in Chapter 5.

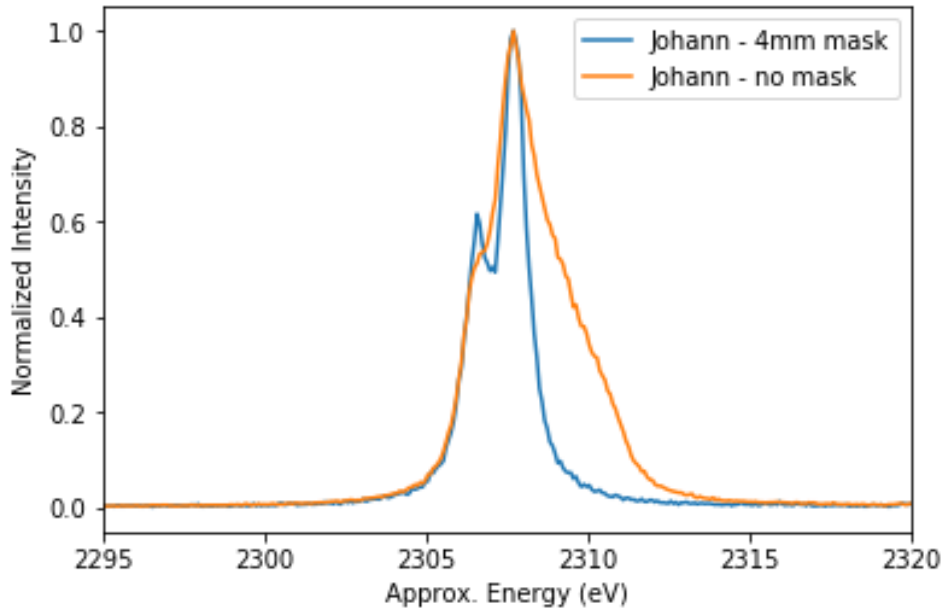

Figure 3.21: Comparison of masked and unmasked measurements of sulfur Kα radiation showing the distortion caused by Johann error. The spectra were peak-normalized and aligned by peak position, thus this data illustrates the change in peak-shape but not the possible associated energy shift.

3.7 Other crystal analyzer spectrometer geometries

While the spectrometer of chapter 5 which is the focus of this thesis uses the Rowland circle geometry, there are a number of other geometries which have been used which offer various advantages. Here, we describe the basic setups of the other geometries and refer to publications of instruments based on them which offer more detailed discussions.

3.7.1 Double-crystal

The first crystal analyzer spectrometers to achieve truly high resolution measurements of XES are the double-crystal spectrometers (also known as "two-crystal" spectrometers). Some of the first measurements of XES in the tender x-ray regime were made by Parratt in 1936[55] with a double-crystal spectrometer.[55] Later, Goshi et al.[56] and Taniguchi[57] in Japan also constructed double-crystal spectrometers which were used in a number of measurements of tender XES by Sugiura.[58-60]

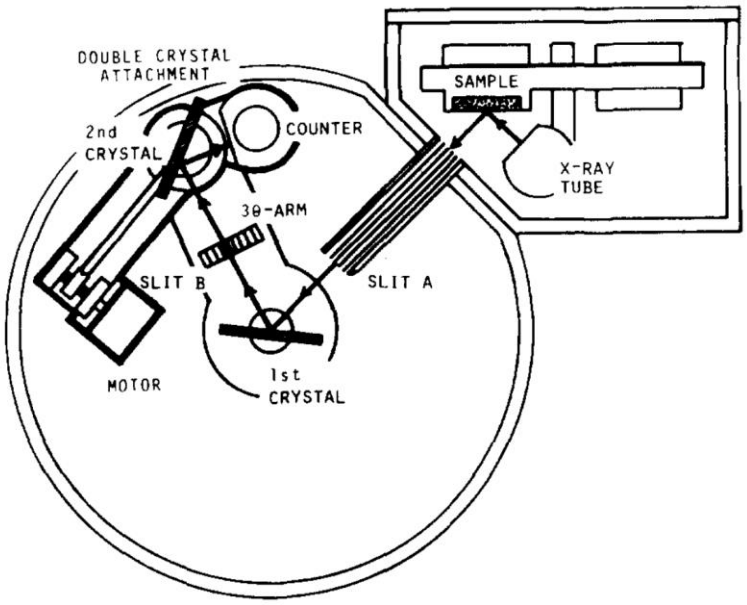

Figure 3.22: Diagram of a double-crystal spectrometer designed by Taniguchi.[57]

The basic principle is the use of Bragg diffraction by the first crystal to sort the x-ray energies by angle, then the use of the second crystal to accept only rays of a certain angle from the first crystal. The advantage of this approach is the very high achievable resolution. A few key disadvantages are the relative mechanical complexity of the alignment for scanning energies, and most importantly the very low efficiency of measurement. As seen in Figure 3.22, multiple slits are needed along the beam path to restrict the accepted angles to improve the resolution at the cost

of counts. In addition, with a flat crystal, only a narrow region of the crystal can participate in diffraction for a given point of the sample. As a consequence of the low efficiency, double crystal spectrometers require very high powered x-ray tubes (1–2 kW and higher) to achieve reasonable count rates. These high powered tubes can also cause radiation damage to the sample.

3.7.2 von Hamos

Similar to the Rowland circle geometry, the von Hamos geometry also utilizes a curved crystal analyzer. In the van Hamos geometry, the source location and detector are displaced axially along the curvature axis of the analyzer. An illustration is shown in Figure 3.23. The basic geometry is shown in the top of the figure, where x-rays coming from a source point on the left travel to the cylindrically bent crystal, and x-rays that reach the crystal at different points along the axis make varying angles with the face of the crystal, and thus varying energies will be diffracted. The resulting pattern on the detector is that energies are dispersed along the cylindrical axis. Thus, the von Hamos is intrinsically a dispersive geometry, and position-sensitive detectors such as CCD cameras are used. This intrinsic dispersive behavior is one of the main advantages of the von Hamos geometry. The main disadvantage of the von Hamos geometry is its relatively low efficiency. Similar to the double-crystal case, only a small region of the crystal can participate at each energy, resulting in a relatively low absolute efficiency. The other main disadvantage is that the achievable resolution depends on the size of the source of the x-rays. To achieve high resolution, a relatively small point source is needed, and for operation in a laboratory instrument, this means that the full output of an x-ray tube cannot be used. Instead, the output of an x-ray tube must be focused to a small point, typically with a polycapillary focusing optic as in the case of Anklamm et al.,[30] which drastically reduces the incident x-ray intensity on a sample. Other authors

making use of laboratory instruments in the von Hamos geometry include Hoszowska et al.,[61] Kayser et al.,[31] Németh et al.,[62] Malzer et al.[28] and Błachucki et al.[29]

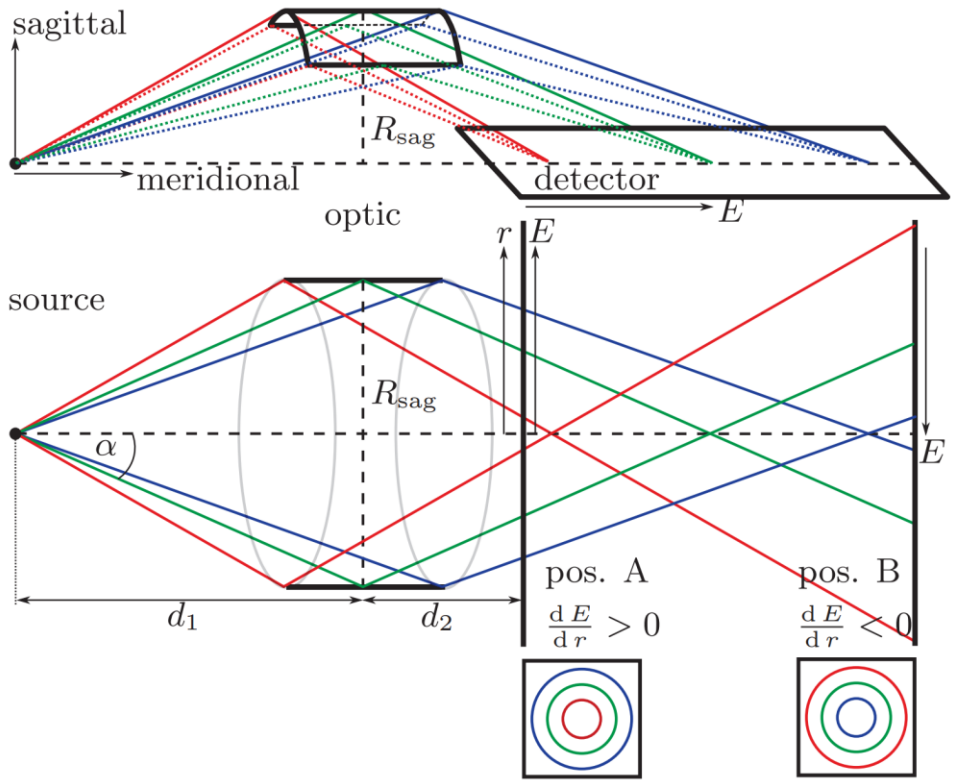

Figure 3.23: Diagram of the von Hamos geometry for an x-ray spectrometer with a curved crystal analyzer. Figure from Anklamm et al.[30]

3.7.3 Laue-type

In contrast to previously discussed geometries that rely on reflection at crystal analyzers by Bragg diffraction, Laue-type spectrometers make use of diffracted beams that are transmitted through the crystal analyzers. A diagram of a Laue-type spectrometer using a curved crystal in the Dumond geometry is shown in Figure 3.24. The Dumond geometry utilizes the same useful properties of the Rowland focusing circle, namely a focusing circle of radius R with a crystal analyzer bent to a radius 2R. Therefore, rays coming from the source (number 3 in Figure 3.24) make nearly equal angles with the surface of the crystal analyzer. In contrast to the Rowland circle

geometry, instead of reflective diffraction, in the Dumond geometry the rays are instead transmitted while undergoing diffraction. The result is that the energies are sorted by angle. With the use of a collimating slit (number 5 in Figure 3.24) to prevent extraneous transmitted rays from going to the detector, the result is energy sorted by position which can be measured by a detector and scanned to different energies at different positions. The Laue-type transmission geometries are primarily useful at higher energies, where absorption by the crystal analyzers is limited. The spectrometer illustrated in Figure 3.24 by Szlachetko et al.[26] demonstrated measurements as high in energy as gold Kα (78 keV).

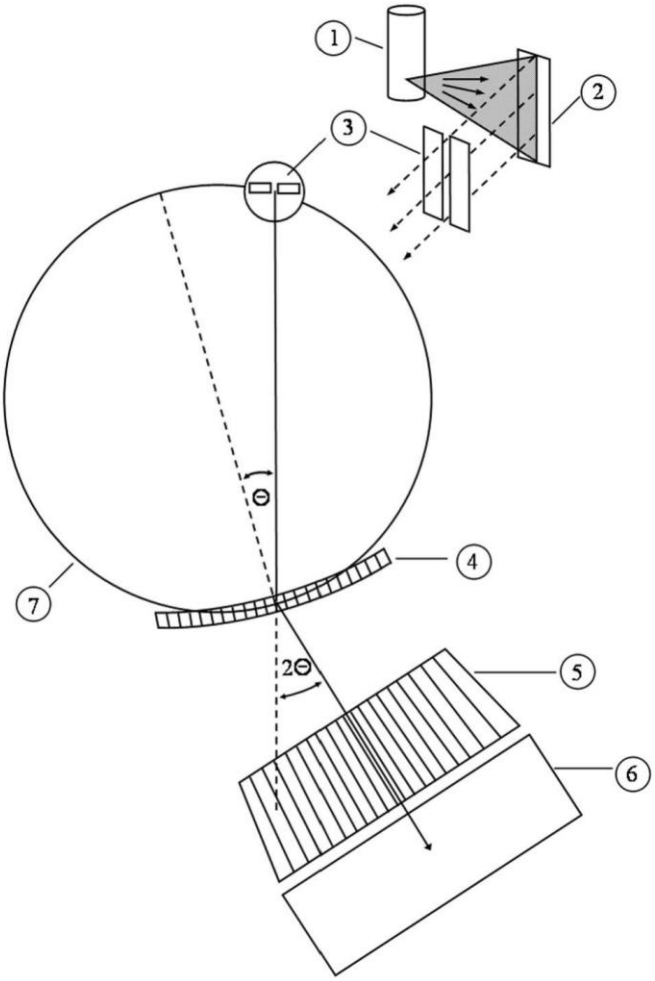

Figure 3.24: Laue-type Dumond curved crystal spectrometer schematic. (1) X-ray tube, (2) target, (3) slit, (4) cylindrically bent crystal analyzer, (5) Soller slit collimator, (6) detector and

(7) focusing circle. Note in particular the orientation of the crystal planes indicated in the crystal analyzer. Figure from Szlachetko et al.[26]

3.8 Sample considerations for tender XES

One of the advantages of XES is the penetrating abilities of x-rays that allow bulk-sensitive measurements as well as *in situ* measurements in various environments, such as batteries or reaction cells. The level of bulk sensitivity and the possibility of special sample environments depend on the x-ray energy being measured. Taking phosphorus and sulfur fluorescence as examples in the tender x-ray range, the penetration depth of signals depends on the nature of the samples being studied. Figure 3.25 shows the attenuation length versus x-ray energy for x-rays in a number of phosphorus and sulfur sample types. Also indicated are the phosphorus and sulfur Kα fluorescence energies. The attenuation lengths vary in magnitude from ~1–10 μm for inorganic matrices, and closer to ~40 μm for organic systems. These examples indicate the order of magnitude of bulk sensitivity and provide some indication of the effort required to design *in-situ* measurement devices.

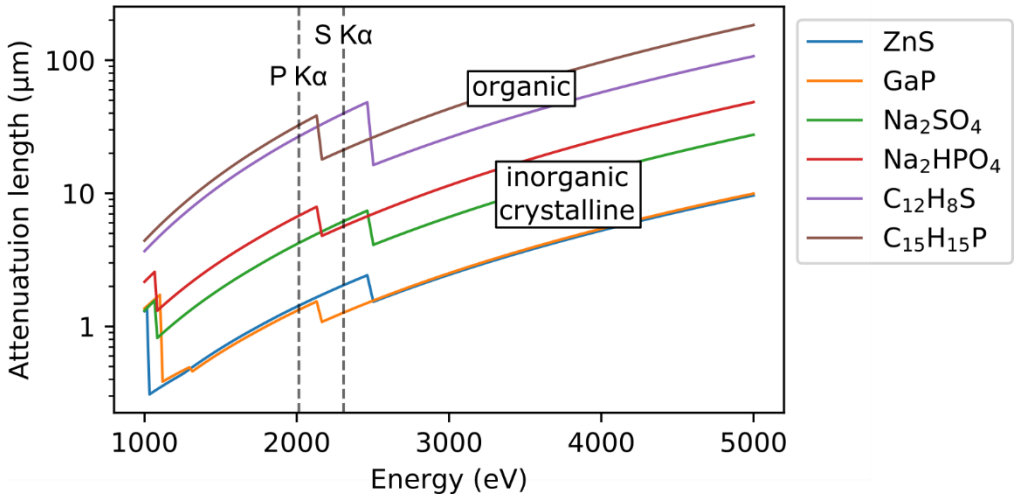

Figure 3.25: Attenuation lengths of x-ray energies in different types of samples for sulfur and phosphorus compounds. Data generated using the CXRO online calculator[1] based on the data compiled by Henke et al.[63]

For mounting samples and designing *in-situ* cells, it's clear from Figure 3.25 that organic materials have significantly lower absorption, and that thicknesses on the order of only a few microns are required. Polyimide thin films (trade name Kapton) with thickness as low as 7.5 micron and thin mylar as thin as 3–5 microns are commonly used. Kavcic et al.[64] have used an *in-situ* battery cell for the study of sulfur in lithium-sulfur batteries using a cell design based on Leriche et al.[65] with the use of a 6 micron mylar window coated with 50 nm of aluminum. Kuzmenko et al.[66] have designed an *in-situ* reaction cell to study sulfur speciation in chemical reactions using a cell design with a 7 micron polyimide window.

3.9 References

1 Gullikson, E. *X-Ray Interactions With Matter*, <http://henke.lbl.gov/optical_constants/> (2019).

2 Rontgen, W. C. On a New Kind of Rays. *Science* **3**, 227-231, doi:10.1126/science.3.59.227 (1896).

3 Agarwal, B. K. *X-ray spectroscopy : an introduction*. 2nd edn, (Springer-Verlag, 1991).

4 Kramers, H. A. XCIII. On the theory of X-ray absorption and of the continuous X-ray spectrum. *The London, Edinburgh, and Dublin Philosophical Magazine and Journal of Science* **46**, 836-871, doi:10.1080/14786442308565244 (2009).
5 Shabalin, A. *Coherent X-ray diffraction studies of mesoscopic materials*, Universitat Hamburg, (2015).
6 Deutsches Elektronen-Synchrotron DESY. *How does a synchrotron radiation source work?*, <http://photon-science.desy.de/sites/site_photonscience/content/e62/e189219/e189248/e189389/e196698/e189414/Spectra_eng.png> (2019).
7 Brookhaven National Laboratory. *X-ray Fluorescence Microprobe (XFM)*, <https://www.bnl.gov/ps/beamlines/beamline.php?r=4-BM> (2019).
8 Bacquart, T., Devès, G. & Ortega, R. Direct speciation analysis of arsenic in sub-cellular compartments using micro-X-ray absorption spectroscopy. *Environmental Research* **110**, 413-416, doi:10.1016/j.envres.2009.09.006 (2010).
9 March, A. M. *et al.* Feasibility of Valence-to-Core X-ray Emission Spectroscopy for Tracking Transient Species. *The Journal of Physical Chemistry C* **119**, 14571-14578, doi:10.1021/jp511838q (2015).
10 Vankó, G. *et al.* Picosecond Time-Resolved X-Ray Emission Spectroscopy: Ultrafast Spin-State Determination in an Iron Complex. *Angewandte Chemie International Edition* **49**, 5910-5912, doi:10.1002/anie.201000844 (2010).
11 Haldrup, K. *et al.* Guest–Host Interactions Investigated by Time-Resolved X-ray Spectroscopies and Scattering at MHz Rates: Solvation Dynamics and Photoinduced Spin Transition in Aqueous Fe(bipy)32+. *The Journal of Physical Chemistry A* **116**, 9878-9887, doi:10.1021/jp306917x (2012).
12 Miaja-Avila, L. *et al.* Ultrafast Time-Resolved Hard X-Ray Emission Spectroscopy on a Tabletop. *Physical Review X* **6**, doi:10.1103/PhysRevX.6.031047 (2016).
13 Mahieu, B. *et al.* Probing warm dense matter using femtosecond X-ray absorption spectroscopy with a laser-produced betatron source. *Nature Communications* **9**, doi:10.1038/s41467-018-05791-4 (2018).
14 Popmintchev, T. *et al.* Bright Coherent Ultrahigh Harmonics in the keV X-ray Regime from Mid-Infrared Femtosecond Lasers. *Science* **336**, 1287-1291, doi:10.1126/science.1218497 (2012).
15 Johnson, A. S. *et al.* Apparatus for soft x-ray table-top high harmonic generation. *Review of Scientific Instruments* **89**, 083110, doi:10.1063/1.5041498 (2018).
16 Sánchez, E., Torres Deluigi, M. & Castellano, G. Binding effects in sulfur Kα and Kβ X-ray emission spectra. *Journal of Analytical Atomic Spectrometry* **34**, 274-283, doi:10.1039/c8ja00345a (2019).
17 Pérez, P. D., Carreras, A. C. & Trincavelli, J. C. Structure of the sulfurKx-ray emission spectrum: influence of the oxidation state. *Journal of Physics B: Atomic, Molecular and Optical Physics* **45**, 025004, doi:10.1088/0953-4075/45/2/025004 (2012).
18 Kavčič, M., Petric, M. & Vogel-Mikuš, K. Chemical speciation using high energy resolution PIXE spectroscopy in the tender X-ray range. *Nuclear Instruments and Methods in Physics Research Section B: Beam Interactions with Materials and Atoms* **417**, 65-69, doi:10.1016/j.nimb.2017.06.009 (2018).
19 Heirwegh, C. M. *et al.* Multiple ionization X-ray satellites of magnesium, aluminum and silicon in alpha particle PIXE. *Nuclear Instruments and Methods in Physics Research*

Section B: Beam Interactions with Materials and Atoms **428**, 9-16, doi:10.1016/j.nimb.2018.05.005 (2018).

20 Tada, T., Fukuda, H., Hasegawa, J. & Oguri, Y. Application of a wavelength-dispersive particle-induced X-ray emission system to chemical speciation of phosphorus and sulfur in lake sediment samples. *Spectrochimica Acta Part B: Atomic Spectroscopy* **65**, 46-50, doi:10.1016/j.sab.2009.11.001 (2010).

21 Maeda, K., Tonomura, A., Hamanaka, H. & Hasegawa, K. Chemical shift measurements of PIXE spectra using a position-sensitive crystal spectrometer. *Nuclear Instruments and Methods in Physics Research Section B: Beam Interactions with Materials and Atoms* **150**, 124-128, doi:10.1016/s0168-583x(98)00927-6 (1999).

22 Maeda, K., Hasegawa, K., Hamanaka, H. & Maeda, M. Chemical state analysis in air by high-resolution PIXE. *Nuclear Instruments and Methods in Physics Research Section B: Beam Interactions with Materials and Atoms* **136-138**, 994-999, doi:10.1016/s0168-583x(97)00820-3 (1998).

23 Kavčič, M., Karydas, A. G. & Zarkadas, C. Chemical state analysis of sulfur in samples of environmental interest using high resolution measurement of Kα diagram line. *Nuclear Instruments and Methods in Physics Research Section B: Beam Interactions with Materials and Atoms* **222**, 601-608, doi:10.1016/j.nimb.2004.04.161 (2004).

24 Kavčič, M. *et al.* Design and performance of a versatile curved-crystal spectrometer for high-resolution spectroscopy in the tender x-ray range. *Review of Scientific Instruments* **83**, 033113, doi:10.1063/1.3697862 (2012).

25 Nikl, M. Scintillation detectors for x-rays. *Measurement Science and Technology* **17**, R37-R54, doi:10.1088/0957-0233/17/4/r01 (2006).

26 Szlachetko, M., Berset, M., Dousse, J. C., Hoszowska, J. & Szlachetko, J. High-resolution Laue-type DuMond curved crystal spectrometer. *Review of Scientific Instruments* **84**, 093104, doi:10.1063/1.4821621 (2013).

27 Jahrman, E. P. *et al.* An improved laboratory-based x-ray absorption fine structure and x-ray emission spectrometer for analytical applications in materials chemistry research. *Review of Scientific Instruments* **90**, 024106, doi:10.1063/1.5049383 (2019).

28 Malzer, W. *et al.* A laboratory spectrometer for high throughput X-ray emission spectroscopy in catalysis research. *Review of Scientific Instruments* **89**, 113111, doi:10.1063/1.5035171 (2018).

29 Błachucki, W., Czapla-Masztafiak, J., Sá, J. & Szlachetko, J. A laboratory-based double X-ray spectrometer for simultaneous X-ray emission and X-ray absorption studies. *Journal of Analytical Atomic Spectrometry* **34**, 1409-1415, doi:10.1039/c9ja00159j (2019).

30 Anklamm, L. *et al.* A novel von Hamos spectrometer for efficient X-ray emission spectroscopy in the laboratory. *Review of Scientific Instruments* **85**, 053110, doi:10.1063/1.4875986 (2014).

31 Kayser, Y. *et al.* Laboratory-based micro-X-ray fluorescence setup using a von Hamos crystal spectrometer and a focused beam X-ray tube. *Review of Scientific Instruments* **85**, 043101, doi:10.1063/1.4869340 (2014).

32 Ullom, J. N. & Bennett, D. A. Review of superconducting transition-edge sensors for x-ray and gamma-ray spectroscopy. *Superconductor Science and Technology* **28**, 084003, doi:10.1088/0953-2048/28/8/084003 (2015).

33 Morgan, K. M. Hot science with cool sensors. *Physics Today* **71**, 28-34, doi:10.1063/pt.3.3995 (2018).

34 Smith, S. J. *et al.* Small Pitch Transition-Edge Sensors with Broadband High Spectral Resolution for Solar Physics. *Journal of Low Temperature Physics* **167**, 168-175, doi:10.1007/s10909-012-0574-y (2012).
35 Jonas, A., Meurer, T., Kanngießer, B. & Mantouvalou, I. Note: Reflection zone plates as highly resolving broadband optics for soft X-ray laboratory spectrometers. *Review of Scientific Instruments* **89**, 026108, doi:10.1063/1.5018910 (2018).
36 Ghiringhelli, G. *et al.* SAXES, a high resolution spectrometer for resonant x-ray emission in the 400–1600eV energy range. *Review of Scientific Instruments* **77**, 113108, doi:10.1063/1.2372731 (2006).
37 Chan, C. D. N. *Braggs Law*, <https://commons.wikimedia.org/w/index.php?curid=14524146> (2011).
38 Als-Nielsen, J. & McMorrow, D. *Elements of modern X-ray physics*. 2nd edn, (Wiley, 2011).
39 Sanchez del Rio, M. & Stepanov, S. A. X-ray server: an online resource for simulations of x-ray diffraction and scattering. **5536**, 16-26, doi:10.1117/12.557549 (2004).
40 Stepanov, S. A. *Sergey Stepanov's X-ray Server*, <https://x-server.gmca.aps.anl.gov> (2019).
41 Hayakawa, S. *et al.* A wavelength dispersive X–ray spectrometer for small area X–ray fluorescence spectroscopy at SPring–8 BL39XU. *Spectrochimica Acta Part B: Atomic Spectroscopy* **54**, 171-177, doi:10.1016/s0584-8547(98)00206-7 (1999).
42 Szlachetko, J. *et al.* Wavelength-dispersive spectrometer for X-ray microfluorescence analysis at the X-ray microscopy beamline ID21 (ESRF). *Journal of Synchrotron Radiation* **17**, 400-408, doi:10.1107/s0909049510010691 (2010).
43 Rowland, H. A. LXI. Preliminary notice of the results accomplished in the manufacture and theory of gratings for optical purposes. *The London, Edinburgh, and Dublin Philosophical Magazine and Journal of Science* **13**, 469-474, doi:10.1080/14786448208627217 (2009).
44 Johann, H. H. Die Erzeugung lichtstarker Röntgenspektren mit Hilfe von Konkavkristallen. *Zeitschrift für Physik* **69**, 185-206, doi:10.1007/bf01798121 (1931).
45 Johansson, T. Über ein neuartiges, genau fokussierendes Röntgenspektrometer. *Zeitschrift für Physik* **82**, 507-528, doi:10.1007/bf01342254 (1933).
46 Saint-Gobain. *Crystals for X-ray Spectrometry*, <https://www.crystals.saint-gobain.com/sites/imdf.crystals.com/files/documents/xray-crystals-spectroscopy.pdf> (2019).
47 Underwood, J. H. *X-Ray Data Booklet Section 4.1: Multilayers and Crystals*. (Lawrence Berkeley National Laboratory, University of California, 2009).
48 Wang, E. *et al.* Calculation of the Johann error for spherically bent x-ray imaging crystal spectrometers. *Review of Scientific Instruments* **81**, 10E329, doi:10.1063/1.3491195 (2010).
49 Lu, K. q. & Stern, E. A. Johann and Johansson focussing arrangements; Analytical analysis. 104-108, doi:10.1063/1.32243 (1980).
50 Bergmann, U. *et al.* High-resolution large-acceptance analyzer for x-ray fluorescence and Raman spectroscopy. **3448**, 198, doi:10.1117/12.332507 (1998).
51 Moretti Sala, M. *et al.* A high-energy-resolution resonant inelastic X-ray scattering spectrometer at ID20 of the European Synchrotron Radiation Facility. *Journal of Synchrotron Radiation* **25**, 580-591, doi:10.1107/s1600577518001200 (2018).

52 Wittry, D. B. & Sun, S. X-ray optics of doubly curved diffractors II. *Journal of Applied Physics* **71**, 564-568, doi:10.1063/1.350406 (1992).
53 Suortti, P., Pattison, P. & Weyrich, W. An X-ray spectrometer for inelastic scattering experiments. II. Spectral flux and resolution. *Journal of Applied Crystallography* **19**, 343-352, doi:10.1107/s0021889886089240 (1986).
54 Klementiev, K. & Chernikov, R. *Powerful scriptable ray tracing package xrt*. Vol. 9209 OPO (SPIE, 2014).
55 Parratt, L. G. Effects of Chemical Binding on the X-RayKα1, 2Doublet Lines of Sulphur Studied with a Two-Crystal Spectrometer. *Physical Review* **49**, 14-16, doi:10.1103/PhysRev.49.14 (1936).
56 Gohshi, Y., Hukao, Y. & Hori, K. A wide-range, single-axis, vacuum two-crystal spectrometer for fluorescent X-ray analysis. *Spectrochimica Acta Part B: Atomic Spectroscopy* **27**, 135-142, doi:10.1016/0584-8547(72)80016-8 (1972).
57 Taniguchi, K. Simple quasi-two-crystal x-ray spectrometer. *Review of Scientific Instruments* **54**, 559-562, doi:10.1063/1.1137437 (1983).
58 Sugiura, C., Gohshi, Y. & Suzuki, I. SulfurKβx-ray emission spectra and electronic structures of some metal sulfides. *Physical Review B* **10**, 338-343, doi:10.1103/PhysRevB.10.338 (1974).
59 Sugiura, C. Kβ X-Ray Emission and K X-Ray Absorption Spectra of Sulfur in Sulfate Compounds. *Japanese Journal of Applied Physics* **32**, 3509-3514, doi:10.1143/jjap.32.3509 (1993).
60 Sugiura, C. Kβ X-Ray Emission Spectra and Chemical Environments of Phosphorus and Sulfur in Various Compounds. *Journal of the Physical Society of Japan* **64**, 3840-3852, doi:10.1143/jpsj.64.3840 (1995).
61 Hoszowska, J., Dousse, J. C., Kern, J. & Rhême, C. High-resolution von Hamos crystal X-ray spectrometer. *Nuclear Instruments and Methods in Physics Research Section A: Accelerators, Spectrometers, Detectors and Associated Equipment* **376**, 129-138, doi:10.1016/0168-9002(96)00262-8 (1996).
62 Németh, Z., Szlachetko, J., Bajnóczi, É. G. & Vankó, G. Laboratory von Hámos X-ray spectroscopy for routine sample characterization. *Review of Scientific Instruments* **87**, 103105, doi:10.1063/1.4964098 (2016).
63 Henke, B. L., Gullikson, E. M. & Davis, J. C. X-Ray Interactions: Photoabsorption, Scattering, Transmission, and Reflection at E = 50-30,000 eV, Z = 1-92. *Atomic Data and Nuclear Data Tables* **54**, 181-342, doi:10.1006/adnd.1993.1013 (1993).
64 Kavčič, M. *et al.* Operando Resonant Inelastic X-ray Scattering: An Appropriate Tool to Characterize Sulfur in Li–S Batteries. *The Journal of Physical Chemistry C* **120**, 24568-24576, doi:10.1021/acs.jpcc.6b06705 (2016).
65 Leriche, J. B. *et al.* An Electrochemical Cell for Operando Study of Lithium Batteries Using Synchrotron Radiation. *Journal of The Electrochemical Society* **157**, A606, doi:10.1149/1.3355977 (2010).
66 Kuzmenko, D. *et al.* A von Hamos spectrometer for in situ sulfur speciation by non-resonant sulfur Kα emission spectroscopy. *Journal of Analytical Atomic Spectrometry* **34**, 2105-2111, doi:10.1039/c9ja00195f (2019).

CHAPTER 4 OVERVIEW OF PUBLISHED RESEARCH

This chapter serves as a brief overview of the layout of the remainder of this thesis, and to explain some of the interconnections in the published research as well as indicate other contributions and outcomes that are a result of the work of this thesis.

4.1 RESEARCH PRESENTED IN CHAPTERS OF THIS THESIS

The core of this thesis is built on the instrumental capability developed in chapter 5, which details the design and implementation of a tender x-ray emission spectrometer.[1] There, the efficiency, resolution, and measurements are discussed and the spectrometer's performance is established. A key component of the instrumental design was the energy resolving x-ray camera that was also developed in our laboratory. The camera was an updated design based on previous efforts led by Oliver R. Hoidn. Chapter 6 is a publication describing this improved camera and its performance characteristics that enable the high performance of the XES spectrometer. [2] With the established capabilities of the spectrometer, chapter 7 describes a study making use of the speciation capabilities of Kα XES for sulfur in biochar materials that were previously investigated using sulfur K-edge XANES, serving as a useful comparison of x-ray techniques.[3] Chapters 8 and 9 form a core analytical application of the XES spectrometer, namely, a study of surface defects of InP quantum dots.[4,5] Making use of Kα XES, we were able to establish the ability to determine bulk speciation of the phosphorus in the quantum dots with two important comparisons to the alternative techniques of XPS and SSNMR. We were also able to utilize Kβ XES to find signatures of the oxygen bonds in the surface defects, or lack thereof in the samples synthesized in an oxygen-free procedure. After the analytical applications of the XES technique demonstrated in chapters 7–9, in Chapter 10 an experimental and theoretical analysis of sulfur Kα and Kβ XES is conducted by making use of computations in a linear-response time-dependent density functional theory

approach. There, measurements with our laboratory instrument are combined with measurements reported elsewhere to compare theoretical predictions with experimental results for dozens of sulfur compounds including organic molecular compounds as well as inorganic solid-state materials. Lastly, chapter 11 stands somewhat apart from the other work in this thesis and details a study of a system for using vacuum pressure to form spherically and toroidally bent crystal analyzers that can be used in x-ray spectrometers.[6] That study also utilizes the x-ray camera described in chapter 6 to perform a finer comparison of the performance of the various approaches to forming the analyzers. Although the study was performed in the context of a different laboratory spectrometer, the temporary vacuum analyzers may find application in future compact dispersive spectrometers such as the one in chapter 5.

4.2 Other outcomes of the efforts in this thesis

With the success of the spectrometer developed in chapter 5, a second identical system was constructed and sent to Los Alamos National Laboratory (LANL) for use in studies of actinide systems. At LANL, in addition to measurements conducted in the laboratory, extensive use has been made of the capability to install the spectrometer at synchrotron beamlines for resonant studies, as demonstrated in chapter 5. This is leading to several publications, including a paper further demonstrating the RIXS capabilities of the spectrometer at SSRL,[7] as well as publications using the RIXS capabilities to study actinide *f*-electron chemistry in uranyl systems. The x-ray camera of chapter 6 is being utilized in a number of instruments under development, including a spectrometer utilizing the vacuum formed analyzers of chapter 11 for small radius-of-curvature spherical analyzers. Building on chapters 7–9, a new instrument is also being commissioned with funding from the UW's MEM-C NSF MRSEC to enable analytical measurements of phosphorus

systems integrated into an inert-air glovebox environment for studies of air-sensitive phosphorus materials, such as InP quantum dots and phosphorene-based materials.

Working with Niri Govind from PNNL, Evan Jahrman and I worked closely together in developing and applying tools for performing the LR-TDDFT calculations of XES that are the subject of chapter 10. Evan Jahrman utilized these tools for a study of vanadium valence-to-core XES in vanadyl phosphate battery materials and has submitted a publication of this work.[8]

4.3 References

1 Holden, W. M. *et al.* A compact dispersive refocusing Rowland circle X-ray emission spectrometer for laboratory, synchrotron, and XFEL applications. *Review of Scientific Instruments* **88**, 073904, doi:10.1063/1.4994739 (2017).

2 Holden, W. M., Hoidn, O. R., Seidler, G. T. & DiChiara, A. D. A color x-ray camera for 2–6 keV using a mass produced back illuminated complementary metal oxide semiconductor sensor. *Review of Scientific Instruments* **89**, 093111, doi:10.1063/1.5047934 (2018).

3 Holden, W. M., Seidler, G. T. & Cheah, S. Sulfur Speciation in Biochars by Very High Resolution Benchtop Kα X-ray Emission Spectroscopy. *The Journal of Physical Chemistry A* **122**, 5153-5161, doi:10.1021/acs.jpca.8b02816 (2018).

4 Stein, J. L. *et al.* Probing Surface Defects of InP Quantum Dots Using Phosphorus Kα and Kβ X-ray Emission Spectroscopy. *Chemistry of Materials* **30**, 6377-6388, doi:10.1021/acs.chemmater.8b02590 (2018).

5 Cossairt, B. M., Stein, J. L., Holden, W. M. & Seidler, G. T. 4-1: Invited Paper: Role of Phosphorus Oxidation in Controlling the Luminescent Properties of Indium Phosphide Quantum Dots. *SID Symposium Digest of Technical Papers* **49**, 21-24, doi:10.1002/sdtp.12481 (2018).

6 Jahrman, E. P. *et al.* Vacuum formed temporary spherically and toroidally bent crystal analyzers for x-ray absorption and x-ray emission spectroscopy. *Review of Scientific Instruments* **90**, 013106, doi:10.1063/1.5057231 (2019).

7 Ditter, A. S. *et al.* Resonant Inelastic X-ray Scattering Using a Miniature Dispersive Rowland Refocusing Spectrometer. *Journal of Synchrotron Radiation* **Submitted** (2019).

8 Jahrman, E. P. *et al.* Valence-to-core X-ray Emission Spectroscopy of Vanadium Oxide and Lithiated Vanadyl Phosphate Materials. *Chemistry of Materials* **Submitted** (2019).

CHAPTER 5 A COMPACT DISPERSIVE REFOCUSING ROWLAND CIRCLE X-RAY EMISSION SPECTROMETER FOR LABORATORY, SYNCHROTRON, AND XFEL APPLICATIONS

Originally published as: Holden, W. M.; Hoidn, O. R.; Ditter, A. S.; Seidler, G. T.; Kas, J.; Stein, J. L.; Cossairt, B. M.; Kozimor, S. A.; Guo, J.; Ye, Y.; et al. A Compact Dispersive Refocusing Rowland Circle X-Ray Emission Spectrometer for Laboratory, Synchrotron, and XFEL Applications. *Review of Scientific Instruments* 2017, 88 (7), 073904. https://doi.org/10.1063/1.4994739.

This chapter represents a significant portion of this dissertation, and I led the effort for this work.

X-ray emission spectroscopy is emerging as an important complement to x-ray absorption fine structure spectroscopy, providing a characterization of the occupied electronic density of states local to the species of interest. Here, we present details of the design and performance of a compact x-ray emission spectrometer that uses a dispersive refocusing Rowland (DRR) circle geometry to achieve excellent performance for the 2 – 2.5 keV range, i.e., especially for the K-edge emission from sulfur and phosphorous. The DRR approach allows high energy resolution even for unfocused x-ray sources. This property enables high count rates in laboratory studies, approaching those of insertion-device beamlines at third-generation synchrotrons, despite use of only a low-powered, conventional x-ray tube. The spectrometer, whose overall scale is set by use of a 10-cm diameter Rowland circle and a new small-pixel CMOS x-ray camera, is easily portable to synchrotron or x-ray free electron laser (XFEL) beamlines. Photometrics from measurements

at the Advanced Light Source show excellent overall instrumental efficiency. In addition, the compact size of this instrument lends itself to future multiplexing to gain large factors in net collection efficiency, or its implementation in controlled gas gloveboxes either in the lab or in an endstation.

5.1 INTRODUCTION

High-resolution x-ray emission spectroscopy (XES) has demonstrated its utility across a wide range of contemporary problems.[1-22] However, the significant restriction of this method to synchrotron light sources has inhibited its broader implementation, especially for industrial and more analytical, rather than fundamental, directions. Recent work in several groups[23-28] has aimed to resolve this issue by developing laboratory-based XES instruments ranging from as low as the C K-edge (284 eV)[27] to as high as the Au K-edge (78 keV).[28] Of particular interest here are high-resolution laboratory measurements of sulfur and phosphorous x-ray emission using double-crystal spectrometers,[29-31] von Hamos geometry instruments,[32,33] and a dispersive Rowland circle geometry.[34-37] These spectrometers were all built in the latter half of the twentieth century, and required multi-kW x-ray tubes to achieve reasonable measurement times. More recent laboratory-based work in this energy range has seen an impressive extension to proton-induced x-ray emission analysis,[38, 39] with the same Rowland-circle instrument also seeing important use at a synchrotron endstation.[17, 18, 40]

Here we present technical details and representative results for a dispersive x-ray emission spectrometer designed to function particularly well in this 2-2.5 keV energy range, and demonstrate measurements on S and P XES both in the laboratory and at a synchrotron endstation. Our results include a representative, laboratory-based analytical application where we determine

the distribution of oxidation states of P in InP quantum dots. In the laboratory setting, this instrument also has the important feature that it can be operated very efficiently with an unfocused x-ray source and consequently a large beamspot on the sample. This greatly decreases cost and increases ease of use. When implemented at the synchrotron, either a focused or unfocused source can be used, with the former giving a modest improvement in energy resolution.

The performance and small size of the instrument reported here results from a synergistic overlap of important technical features of the x-ray analyzer, the position-sensitive detector, and the overall optical configuration itself. High-quality cylindrically-bent crystal analyzers are only recently commercially available with extremely small, i.e., 10-cm, radii of curvature. In general, the overall size of any Rowland-circle x-ray spectrometer scales linearly with the radius of curvature of the optic, so the decrease from the 'standard' 1-m radius of curvature spherically-bent crystal analyzer, as commonly used in synchrotron endstation instrumentations[41-44] and also used in lab-based spectrometers for the hard x-ray range,[23] to the present 10-cm radius optic allows a corresponding factor of 10 change in the linear dimensions of the resulting instrument. The compact size offers advantages in portability and ease of installation for use at synchrotron and x-ray free electron laser XFEL endstations, as well as a unique scientific possibility: it is small enough that it could be readily integrated into controlled-gas glove box systems to enable new directions in analytical chemistry for air-sensitive materials.

Concerning the position-sensitive detector, our recent and ongoing development of complementary metal-oxide-semiconductor (CMOS) x-ray cameras using mass-produced sensors is a critical enabling technology.[45, 46] These sensors, including the back-illuminated sensor used in the present instrument, can have pixels below 3-μm pitch while also having useful spectroscopic capability in the 2-5 keV energy range. At least moderately small pixels are necessary if fine

energy resolution is to be maintained for the tightly curved Bragg optic, and the sensitivity to the energy of each recorded incident photon allows for very high rejection of background signals, minimizing the need for internal shielding. In addition, there is a subtle pragmatic benefit that comes from the fact that CMOS sensors, unlike CCD sensors commonly used in x-ray cameras, have low dark counts even when they are not cooled. Our camera operates at room temperature. Consequently, absorption from any sensor window is avoided and the sensor functions well in air without risk of condensation on the sensor. Direct detection with CCD sensors, on the other hand, would require UHV environment.

Finally, as a central defining concept of the instrument design, we employ a dispersive refocusing Rowland (DRR) geometry, defined in detail in section 5.2 below. In the context of XES, we believe that this geometry was first pointed out by Dolgih and Yarmoshenko *et al*.,[34] who constructed a DRR spectrometer based on a much larger 1.3-m diameter Rowland circle. The DRR optical layout has considerable qualitative similarities to that for Bragg-Brentano diffractometers using position sensitive detectors.[47, 48] The DRR approach is beneficial in three practical matters: (1) its insensitivity to the illumination spot size allows the use of conventional 'x-ray fluorescence (XRF) style' x-ray tubes without any focusing optic; (2) the option of larger illuminated spot size (as much as ~5 mm) on the sample helps to reduce the exposure flux density and consequently serves to lower the likelihood of x-ray induced damage during the measurement; and, (3) the resulting spectrum, if a large beamspot is used, constitutes an average over the illuminated region, giving a decreased sensitivity to spatial inhomogeneities in sample preparation.

We continue as follows. First, in section 5.2, we describe the general ray-tracing and design issues that arise in the DRR geometry. This includes a discussion of the similarities and differences between the DRR geometry and other more common Rowland-circle approaches.

Second, in section 5.3 we give a detailed description of the implementation of the instrument in the laboratory and synchrotron environments, and provide other experimental details. Next, in section 5.4 we present results taken in the laboratory and at the synchrotron, comparing and contrasting energy resolution and count rates in the present study with those previously reported at synchrotron light sources. This includes a representative laboratory-based 'analytical' application where we quantify the fractional oxidation of P in InP nanocrystalline materials. Finally, we conclude and discuss future directions in Section 5.5.

5.2 The Dispersive Refocusing Rowland (DRR) Geometry

To operate a dispersive spectrometer using a Rowland-circle geometry, there are three basic configurations using different source sizes and locations, as shown in Fig. 5.1. In Fig. 5.1a, where the sample is illuminated by a small point-source *off* of the Rowland circle, multiple energies will be diffracted from the crystal. These energies diffract at different angles and ray-tracing back towards the Rowland circle results in a collection of 'virtual' point sources on the source arc of the Rowland circle.[49] The bandwidth diffracted then depends on the distance of the sample from the crystal analyzer.[50] In the limit when the source is significantly off circle, the location of the position-sensitive detector (PSD) is not especially delicate – the ray-tracing is non-focal, and diffracted rays have only a very small divergence. Because of this small divergence, the PSD need not be tangent to the Rowland circle to achieve high-resolution.[49] Each energy diffracts from a very small portion of the crystal, resulting in no appreciable Johann error, even at low Bragg angles. The geometry of Fig. 5.1a is used in the synchrotron results of section 5.3.2.

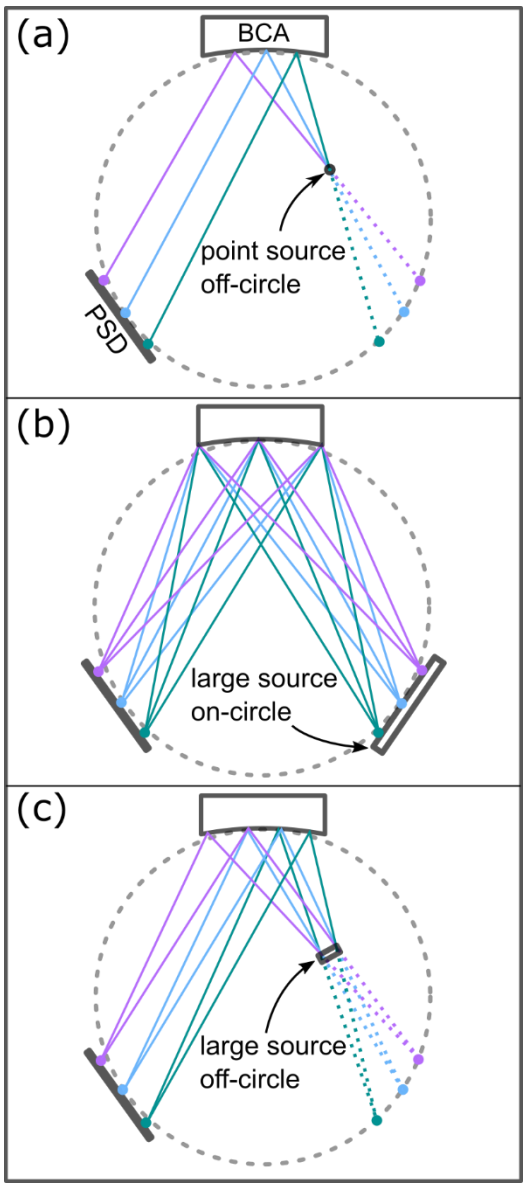

Figure 5.1: Comparison of Rowland circle geometries for different sample illuminations. Each setup has the same basic layout, a source on the lower right arc, a bent crystal analyzer (BCA) at the top of the circle, and a position-sensitive detector (PSD) on the lower left arc. (a) Point source illumination of a sample off of the Rowland circle has 'virtual' rays that can be traced back to intersect the circle. The geometry is dispersive and multiple energies are collected by the PSD. (b) A large source on the Rowland circle has multiple energies that undergo point-to-point focusing and are measured on the PSD. Different regions of the sample contribute at different energies. (c) The dispersive refocusing Rowland (DRR) geometry used in the present work. See the text for discussion.

In Fig. 5.1b, the situation is shown for large-spot illumination of a sample *on* the Rowland circle. In this case, different energies of fluoresced x-rays are collected from different portions of the sample, thus requiring a homogeneous sample to avoid gross systematic error in the dispersed spectrum on the detector arc. For each point of the sample on the source arc of the Rowland circle, x-rays of a particular energy are captured by the *entire* crystal. This increases signal strength at each energy, but at the cost of larger divergence of the rays refocusing onto the detector, as well as an increased potential for Johann error at lower Bragg angles. The large divergence of the refocused, analyzed radiation requires precise placement of the camera for a high energy-resolution signal, i.e., the depth of focus is small. With the incident beam brought in perpendicular to the Rowland plane, this geometry is used for combined imaging and spectroscopic measurements in many plasma physics studies, as well as in some synchrotron applications.[51-53]

Finally, in Fig. 5.1c and of direct relevance here, a large-spot illumination of a sample *off* the Rowland circle has an effective collection of 'virtual' sources at different energies, as in panel (a). However, for a large beamspot, each portion of the sample can contribute at all energies, except when truncated at the boundary of the analyzer. This 'dispersive Rowland refocusing' (DRR) approach removes the need for a focused beam, while also decreasing the sensitivity to sample inhomogeneities by giving a natural averaging of the spectrum over the illuminated region of the sample. Spectrometers making use of this approach have been recently discussed and implemented at some synchrotron endstations,[50] where the relatively large spot size allows for efficient measurements, e.g. for gaseous samples.[40, 54] In the present spectrometer, the large spot size is taken to an even greater extreme, allowing the use of an unfocused x-ray tube on an extremely small 10-cm Rowland circle.

To minimize distortions of the spectrum in the DRR geometry, it is important that each energy in the bandwidth of interest has equal net detection efficiency in the final spectrum. This can be accomplished in either of two extremes: (1) the sample illumination is extremely large such that each energy is usefully captured by the entire crystal analyzer, or (2) the sample illumination is sufficiently small that each energy uses the same fraction of the crystal, i.e. that each illuminated sub-region of the sample can contribute at all energies from some segment of the crystal analyzer. Within either configuration, distance from the crystal to the sample can be varied to trade-off count rates against total energy bandwidth analyzed.

Moving now to the specific implementation of mechanical components, there are numerous possible implementations of any Rowland-circle configuration, with the pragmatically-preferred approach always determined by external criteria. Here, we choose to fix the x-ray source in the lab frame to simplify operation in both the laboratory and the synchrotron. In addition, we choose to let the circle be free to rotate about the source axis so that the camera face can always be kept parallel to the same reference plane, thus minimizing the number of degrees of freedom that require fine-tuning. These characteristics are illustrated in Fig. 5.2. After coarsely adjusting the height of the camera so that the analyzed radiation strikes the sensor, necessary fine-adjustments are made to bring the sensor tangent to the Rowland circle and hence to the refocal position for the analyzed radiation.

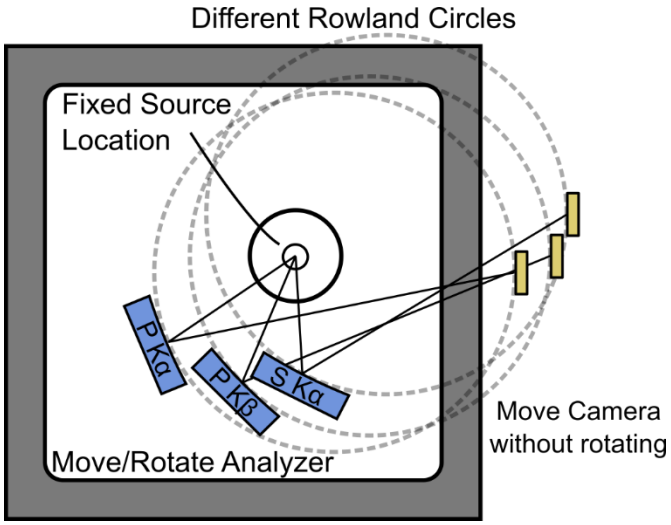

Figure 5.2: Illustration of the implemented DRR design. To fix the source location and maintain camera orientation, the analyzer is moved to different positions yielding different Rowland circles. The sample-analyzer distance is also changed for different Bragg positions to maximize signal from the sample. Maintaining the orientation of the camera reduces the degrees of freedom that need to be optimized to achieve high-resolution.

Returning to Fig. 5.2, when a new Bragg angle is desired, in order to keep the source location fixed and maintain the camera orientation, the Rowland circle must be moved by appropriate modification to the location and rotation of the crystal analyzer. Finally, note that this requires that the distance of the focal point region on the Rowland circle from the spectrometer chamber wall varies for different Bragg angles. We show below, in the detailed instrument design, that this is easily addressed.

5.3 Experimental

5.3.1 Laboratory Environment

Computer-aided design (CAD) renderings and photographs of the spectrometer, as implemented in the laboratory environment, are shown in Figures 5.3 and 5.4. The sample is directly illuminated with x-rays from a conventional, air-cooled tube source (Varian VF-50 with a Pd anode) having a maximum electron beam power of 50W at 25 kV accelerating potential. The

choice of a Pd anode is advantageous due to its strong fluorescence lines at ~2.8 keV that are very effective at stimulating *K*-shell photoionization of P and S. The x-ray tube is driven by a Spellman uX50P50 high voltage power supply. The VF-50 provides an *unfocused* beam of combined bremsstrahlung and characteristic fluorescence radiation from the Pd anode.

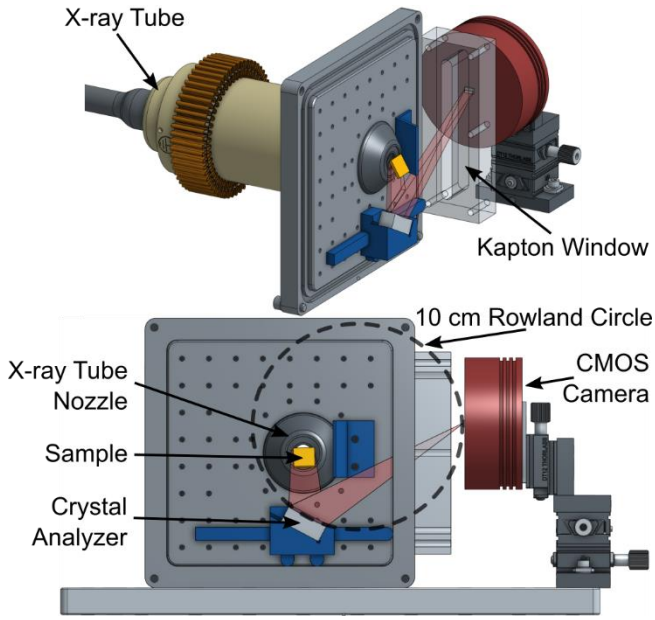

Figure 5.3: Spectrometer CAD renderings illustrating the layout of the components with respect to the Rowland circle. The vacuum chamber has been suppressed for clarity of presentation, see also Fig. 5.4.

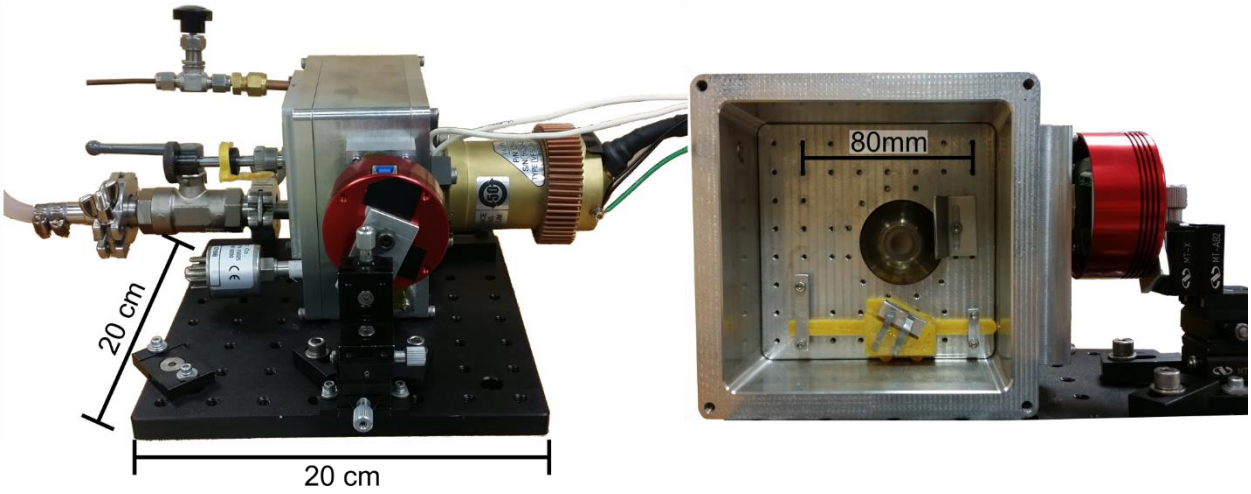

Figure 5.4: Photographs of the spectrometer. Use of a small-radius cylindrically-bent crystal analyzer allows a very small geometry to be utilized. The vacuum chamber houses the nozzle of the x-ray tube, the crystal analyzer, and the sample, which is on a sample turret (not shown) to allow multiple samples to be measured without breaking vacuum or altering the setup.

Fluorescence from the sample is diffracted by a 10-cm radius, cylindrically-bent, Si (111) Johann analyzer (XRS Tech) in the DRR geometry of the corresponding 10-cm diameter Rowland circle. The analyzer dimensions are 20 mm (width) x 8 mm (height, out of the Rowland plane). The Si (111) orientation provides Bragg angles of 79° for P Kα (2014 eV) and 59° for S Kα (2308 eV). For P, the sample is placed in the second configuration described in section 5.2, such that each energy in the resulting spectrum makes use of the same fraction of the crystal. When measuring S K-shell XES, however, the relatively low Bragg angles introduce a large Johann error distorting the spectrum. To compensate, the edges of the crystal analyzer are masked with aluminum foil so that only the central ~4 mm are used. This results in the first configuration described in section 5.2, wherein the fluorescence from the sample now makes use of the entire 4 mm of the crystal for all analyzed energies. Moving to a Johansson-type analyzer would clearly improve efficiency for S XES.

Placement of the crystal analyzer is accomplished using 3-D printed plastic mounting pieces that register with the walls of the spectrometer box to determine the optics position and orientation, as per the discussion in section 5.2. Again, the location of the crystal is chosen such that the camera, oriented vertically outside of the chamber, is tangent to the Rowland circle at the energy of interest. Also, as described in section 5.2, alignment and tuning is achieved by first locating the signal on the camera via manual, vertical translation, and then by fine-focusing adjustments where the camera is moved closer to or further away from the spectrometer chamber.

The refocused rays are detected by a recently developed energy-resolving x-ray camera[46], which uses a back-illuminated CMOS sensor and is similar to a previously-reported instrument.[45] The detector is based on a commercial amateur astronomy camera (ZWO Company) that we have modified by removing the glass from its image sensor (Sony IMX-291), allowing x-rays to directly illuminate the sensor's active region. The camera's CMOS sensor has a pixel pitch of 2.9-μm and a 1936×1096 pixel layout. On a 10-cm radius Rowland circle, the sensor's 2.9-μm pixel size corresponds to an energy broadening of ~0.01 eV at P Kα and ~0.04 eV at S Kα. The charge separation generated by each photon absorbed on each pixel results in a proportional readout value. In the simplest case, wherein the entire charge cloud from an incident x-ray event is concentrated in a single pixel, the detecting pixel has intrinsic sensitivity to the energy of the incident x-ray photon. In the majority of events, however, the charge cloud spreads over a cluster of several adjacent pixels.[45, 46] To include all events while preserving optimal energy resolution we have developed software to identify such clusters and reconstruct corresponding photon energies and positions.[45, 46, 55] With this additional processing, the sensor's quantum efficiency (QE) and energy resolution are 65% and 150 eV, respectively, at the photon energy of P Kα. The quantum

efficiency of the sensor decreases considerably above 4 keV,[46] leading us to focus here on the 2 – 2.5 keV energy range where the Si 111 optic and camera performance are synergistic.

Note that the use of an energy-resolving, single photon counting camera is extremely beneficial in the present application. Performing frame-by-frame rejection of single-photon events that are outside the energy window of interest removes a wide range of backgrounds that would otherwise contaminate an energy-integrating position-sensitive detector. Consequently, only very minimal internal shielding is required.

From the discussion in Section 5.2, the fluorescence x-rays from the sample are dispersed onto the detector, and each pixel acts as an effective slit that only accepts rays in a narrow energy band. For a cylindrical optic, like that used here, the focusing is theoretically exact in the plane of the Rowland circle, but for rays with some out-of-plane divergence, the rays are bent towards the backscatter (low-energy) direction. The results in a curved focal line[40] as the ideal point-source response function. The curvature itself does significantly affect instrumental resolution since the curved focal line can be taken into account to produce a spectrum, as is commonly done in synchrotron implementations.[40, 54, 56] In the present spectrometer in the laboratory setting, however, the curvature of the signal convolved with the large spot illumination results in irreversible blurring of the ideal point-source response function for regions of the sensor far out of the Rowland plane. In order to maintain high resolution for lab-based measurements, this requires that the signal on the detector be cropped around the region centered on the Rowland plane to exclude these blurred regions.

The absorption length in air of, e.g., S Kα fluorescence, is ~1.5 cm. Consequently, the sample, crystal analyzer, and majority of the beam path are inside of a 30 × 30 × 7 cm^3 aluminum chamber which is operated at rough vacuum (~200 mTorr) or else flushed and filled with He at 1

atm. As shown in Figures 5.2, 5.3, and 5.4, the camera is outside of the spectrometer box. The x-rays exit through an 8-μm thick polyimide film and traverse a ~2-3 mm air gap before landing on the camera. The small air-gap is maintained by having different thickness spacers below the polyimide window. The combined absorption from the polyimide exit window and small air path is ~50 – 60% in the targeted 2 – 2.5 keV energy range, leaving room for a two-fold increase in counts if the camera is adapted to mount inside of the spectrometer chamber.

The energy scale of the measurements was determined by ray-tracing considerations, using the 10-cm Rowland circle geometry. Measuring samples on the same energy scale (including one or more reference materials) is made possible by swapping samples while maintaining the analyzer and camera locations. After an ensemble of internally-consistent results is obtained, a single common energy shift is applied all spectra so as to match, e.g., prior published results for one of the reference materials.[18, 57]

5.3.2 Synchrotron Environment

The compact size of the spectrometer allows for easy transport and interface with existing synchrotron and XFEL beamlines. To demonstrate this utility, the spectrometer was taken to beamline 10.3.2 at ALS for demonstration studies. This is a bending-magnet, microfocus beamline, with a beam size of ~12×6 μm and an approximate flux of 10^9/s. Installation was straightforward, requiring less than two hours from the start of setup to the onset of data collection. The spectrometer fit within the existing endstation equipment, and the laboratory x-ray source was replaced by a simple adapter connected to the beampipe using flexible bellows. Helium gas was flowed through the chamber and bellows throughout the measurements. The configuration of the various spectrometer components is otherwise unchanged from the laboratory setup in section

5.3.1, above. This allowed for the spectrometer to be pre-calibrated and pre-focused for a fluorescence line of interest (in this case P Kα) before traveling to the synchrotron.

The incident flux was 3×10^9/s at the selected incident photon energy of 3 keV. This was determined using a gas ionization chamber with an effective path length of 2 cm, filled with a 33% N_2, 67% He mix and also confirmed with a second measurement using only pure N_2, in the ion chamber. The spectrometer was translated downstream from the usual focus of this microfocus beamline to achieve a ~200-μm spot size on the sample. This small source size simplified treatment of the sensor image. Whereas in laboratory operation blurring of the image out of the Rowland plane requires significant cropping of the signal to achieve high-resolution, the small spot size at the beamline resulted in a signal that required minimal cropping. Despite the reduction in count rates due to the low flux of the bending magnet source, background signals were proportionally reduced and good spectra were achieved with longer integration times.

5.3.3 Samples

For testing the spectrometer in the laboratory and at the synchrotron, the following phosphorous- and sulfur-containing reference samples were used: a $10\times10\times0.5$ mm^3 crystalline wafer of GaP (MTI Corporation), a $10\times10\times1$ mm^3 crystalline wafer of ZnS (MTI Corporation), and a pressed powder pellet of $FePO_4$ (Alfa Aesar) mixed with graphite binder. For the pellet, $FePO_4$ powder was mixed with graphite in an approximate 1:3 ratio, then pressed into a 13 mm-diameter pellet.

P Kα emission for three different samples of InP nanocrystals was measured as a pilot study to demonstrate the analytical capabilities of the spectrometer. The InP quantum dots (QDs) were prepared by a procedure from Gary and Cossairt.[58] One sample consisted of the pure as-synthesized InP QDs, while the second sample consisted of Zn-passivated InP QDs, which were

post-synthetically modified with zinc oleate as described in Stein *et al*.[59] The third sample measured was InP magic-sized clusters with the initial carboxylate ligand environment replaced with phosphonates, prepared following a procedure from Gary *et al*.[60]

5.4 Results and Discussion

To begin, a 500 s exposure for P Kα emission of GaP is shown in Fig. 5.5. As mentioned in section 5.3.1, the blurring due to finite sample illumination size requires cropping the image to the central 600 rows to retain high energy resolution. We show measurements of the P Kα emission spectrum for GaP and $FePO_4$ in Fig. 5.6. An energy shift of 1.03 eV is observed due to the difference in oxidation state, P^{3-} in GaP, and P^{5+} in $FePO_4$. The integration time of the measurements was 500 s, although for these concentrated samples the shift is clearly observed after only 60 s of measurement. The energy bandwidth depends on the spectrometer geometry, and at the P Kα Bragg angle of 79° the bandwidth is only 12 eV. The GaP sample gave a useful count rate of 1200/s and the $FePO_4$ pellet, being somewhat less concentrated, gave a useful count rate of 450/s. Although comparisons across different instruments and measurement conditions are difficult, the count rate for GaP is impressive, in that it is ~50% that observed in a prior synchrotron-based study using a third-generation insertion device beamline and a high-resolution spectrometer employing an admittedly less-efficient quartz analyzer optic .[57] The comparison to the synchrotron count rate together with the high net efficiency of the spectrometer (see below) suggests that the 'useful' core hole generation rate[20] is 10^{11}/s - 10^{12}/s for concentrated samples.

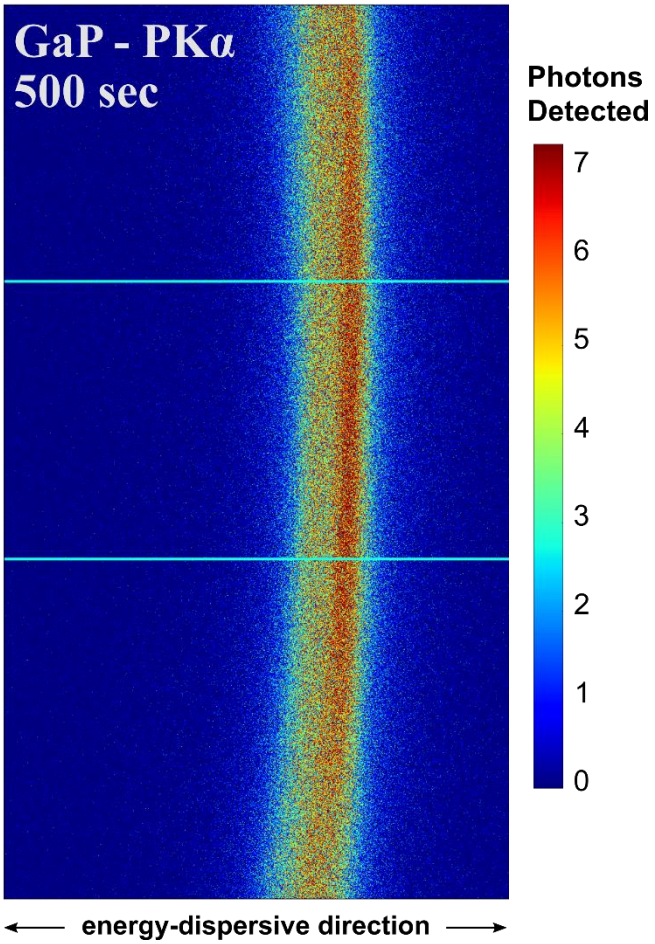

Figure 5.5: Sensor image for data obtained measuring P Kα emission from GaP. The main peak and shoulder of the Kα doublet can be seen. There is an apparent curvature in the data, as well as blurring in the extremes of the curve. For a clean spectrum we process only the cropped, central region indicated by the horizontal lines. The width of the sensor corresponds to a bandwidth of 12 eV at the Bragg angle for P Kα.

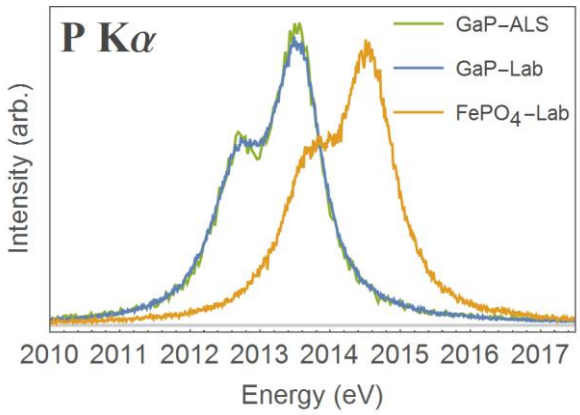

Figure 5.6: Comparison of P Kα emission for samples of GaP and $FePO_4$. The difference in oxidation state (3^- for P in GaP, 5^+ for P in $FePO_4$) leads to an observed energy shift of the $K\alpha_{1,2}$ doublet by 1.03 eV. For GaP, data is shown for measurements taken in the laboratory and at ALS beamline 10.3.2. The measurement times in the lab for these concentrated samples was 500 s, and the measurement time for GaP at ALS was 7200 s.

P Kβ emission was measured on the same samples, and the results are shown in Fig. 5.7 (top). Although the peak Kβ signal is ~40× weaker than that of the Kα, clean spectra are measured in ~600 s. As the Kβ emission constitutes valence-to-core transitions for P and S, it is sensitive to the chemical bonding environment. For example, the presence of the Kβ' peak at 2123 eV in the $FePO_4$ spectrum has been shown by DFT calculations to arise from interaction with oxygen in the phosphate bond.[57] In Fig. 5.7 (bottom), the Kβ emission of GaP is compared to FEFF9 calculations, which uses an *ab initio* multiple-scattering code to calculate the species-specific, local occupied density of states near the Fermi level.[61] After broadening with a Gaussian profile and shifting the energy of the simulated spectrum, there is clear agreement with the measured results.

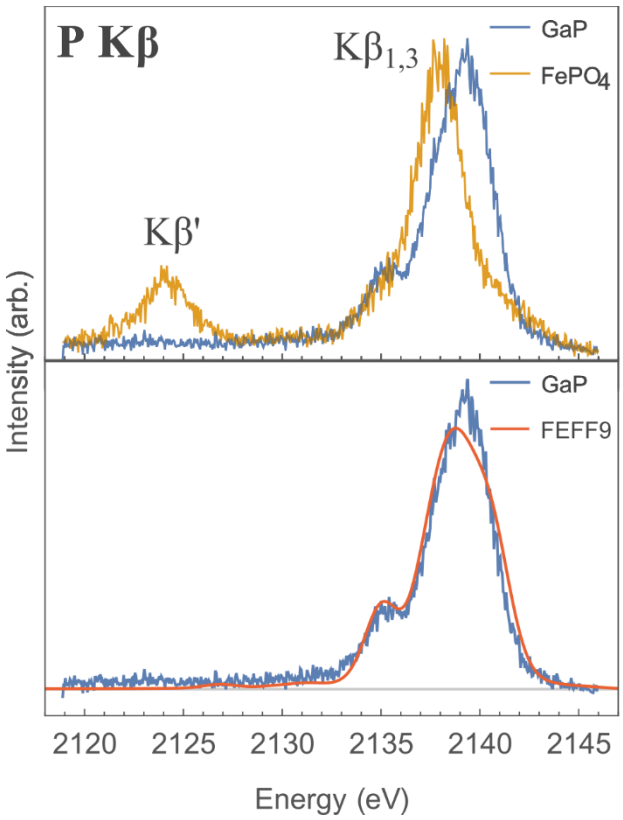

Figure 5.7: Phosphorous Kβ spectrum obtained in the laboratory with a measurement time of 600 seconds. (Top) Comparison of the spectra obtained from samples of GaP and $FePO_4$. The presence and position of the Kβ' peak at 2123 eV in the $FePO_4$ spectrum is a clear indicator of oxygen bonded to the probed P atoms. (Bottom) Comparison of the GaP spectrum to a calculation of the occupied density of states using FEFF9. The output of the FEFF9 calculation was Gaussian broadened and shifted in energy to align with the measured results.

The ability to select a narrow window of photon energies with our detector results in very low background levels. For the strong P Kα emissions, no appreciable background is observed. For the weaker P Kβ emission, taking the $FePO_4$ emission shown in Fig. 5.7 as an example, the total, time-integrated background in one energy bin is 22 counts, compared to the 355 counts of the fluorescence line peak intensity at 2138 eV.

In Fig. 5.8, S Kα measurement results are shown for a ZnS single crystal, using 1300 s measurement time to obtain sufficiently quiet data to also resolve the components of the $K\alpha L^1$

satellite lines[39] on the high-energy tail of the main $K\alpha_{1,2}$ doublet. The Bragg angle for S Kα is much further from back scatter at 59°, and hence a larger bandwidth of 46eV is measured. The extremely small pixels of the CMOS-based x-ray camera ensure negligible smearing to the spectrometer response function, e.g., $\Delta E/E \sim 10^{-5}$ or less. Comparing the S Kα spectral shape obtained here with that of Mori *et al.*,[18] good agreement is seen after convolving their spectra with a 0.5 eV FWHM Gaussian profile. Given the reported resolution of 0.44 eV in the prior work, we find an experimental resolution of approximately 0.7 eV for the present instrument in the laboratory environment. In Fig. 5.9, we show the S Kβ spectrum of ZnS; the comparison to the prior results from ESRF is extremely favorable [17]

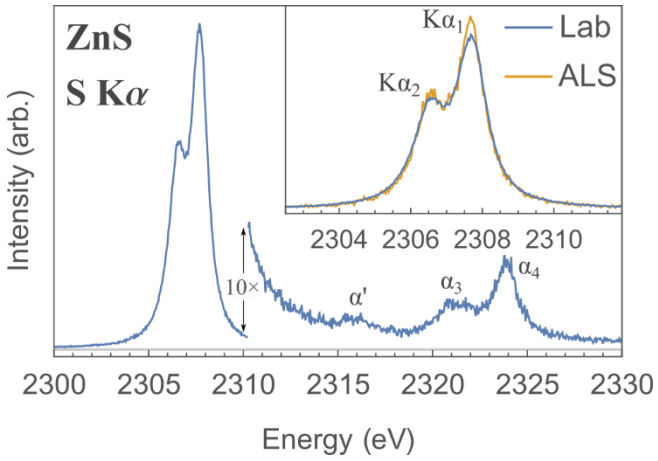

Figure 5.8: Sulfur Kα spectrum of a sample of ZnS, demonstrating the high-resolution capabilities of the spectrometer. Because of the lower Bragg angle, the bandwidth is increased relative to the phosphorous Kα spectrum, and the components of the $K\alpha L^1$ satellite lines on the high-energy tail are clearly resolved. The integration time was 1300 s for the laboratory spectrum, and 9600 s for the spectrum taken at ALS beamline 10.3.2.

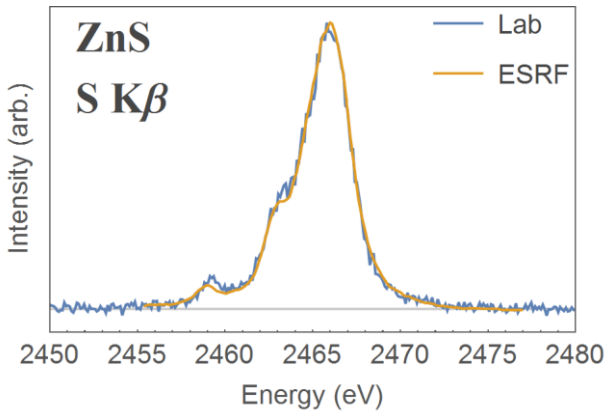

Figure 5.9: Sulfur Kβ emission spectrum of a sample of ZnS taken in the laboratory compared with data taken at beamline ID26 at ESRF.[17] The measurement time in the laboratory was 3600 s, and a background of amplitude approximately 10% of the peak has been subtracted.

A primary purpose of laboratory-based spectrometers is not to compete with synchrotrons, but instead to enable new directions in analytical chemistry. For a pilot study in such a direction, we use several different preparations of InP QD's to demonstrate the ease with which distributions of oxidation state can be extracted from simple linear superposition fits to reference standards. This is enabled by the significant insensitivity of the spectral shape of the $K\alpha_{1,2}$ doublet to oxidation state – despite overall shifts in energy due to changes in the valence electron population.[18] InP is chosen as a useful representative case not only because of its convenient chemistry in the present context, but also because the surface of InP is readily oxidized, requiring rigorously air-free synthetic procedures for desired applications in solid-state lighting, and biomedical imaging.[62, 63] Hence, a bulk-sensitive quantification of the distribution of P oxidation states is of immediate relevance to characterizing and validating the synthesis process.

In Fig. 5.10 (middle), InP QDs have been post-synthetically treated with zinc carboxylates leading to a zinc saturated surface environment that has been shown to improve photoluminescence quantum yields.[59] Compared to the as-synthesized InP core in Fig. 5.10 (top), the amount of oxidized P species increases from 10% to 18% with the addition of zinc. Previous literature has

also reported oxidized P levels of InP cores close to 10% by XPS and NMR, but have shown an increase to approximately 35% after shelling with ZnS.[64] In Fig. 5.10 (bottom), InP magic-sized clusters were prepared with a phosphonate ligand shell, showing the mixed environment of P^{3-} from the inorganic core, and P^{5+} from the organic ligands. While further study, such as cross-comparison to NMR and XPS on the same samples, is needed to fully integrate benchtop XES into this type of analytical approach, the present results strongly support such a campaign. The same approach, if successful, would have even higher impact for analytical chemistry of sulfur-based materials due to the difficulties inherent in applying NMR methods to sulfur.

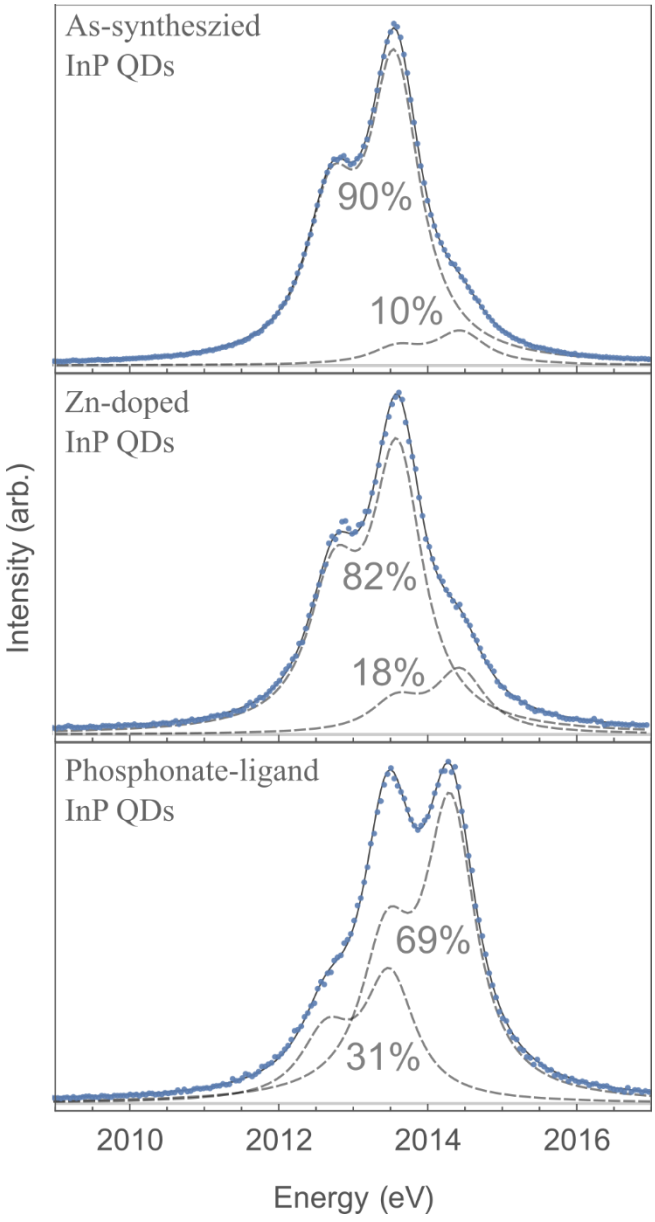

Figure 5.10: Linear combination fits of reference spectra to the P Kα spectra for three different samples of InP nanoparticles showing the relative proportions of oxidation states of phosphorous. The lower energy doublet corresponds to the reduced P^{3-} state of P in InP, while the higher energy doublet represents a highly oxidized state, close in energy to P^{5+} of P in PO_4^{3-}. All measurement times were less than 3600 s.

Finally, the high efficiency and compact size of our DRR spectrometer suggests it can also be easily used at synchrotron and XFEL endstations. At such high-brilliance facilities, there is a

wider potential for fundamental application through microprobe studies, time-resolved experiments, or resonant methods capable of more finely interrogating the local electronic structure. Here, we investigate the performance of the miniature DRR spectrometer at beamline 10.3.2 at the Advanced Light Source (ALS). This comes with the added benefit of a microfocused, monochromatic source, for comparison to the unfocused lab source, and also to determine a well-referenced metric for the instrument's absolute efficiency normalized by unit incident flux, a metric that is difficult to characterize with the laboratory x-ray source. Representative measurements taken at the ALS are included in Figures 5.6 and 5.8. The integration time for the GaP spectrum was 7200 s, and for the ZnS was 9600 s. The long measurement times in the synchrotron studies are due to the small flux, i.e., 3 x 10^9/s, of the bending-magnet beamline. For both P Kα and S Kα emission, the ALS measurements show slightly better resolution of the $K\alpha_{1,2}$ doublet, but otherwise agree well with the laboratory results. Comparison of the ZnS S Kα signal taken at ALS with results of Mori et al.[18] as above, finds a modest improvement in energy resolution compared to the laboratory, from approximately 0.7 to 0.6 eV.

Compared to the 1200/s for GaP measured in the laboratory, the relatively low flux of the microfocused, bending-magnet source gave a count rate of 7.2/s on the same GaP sample. However, the small-spot illumination of the bending-magnet source (~200μm) improved the spectrometer efficiency by a factor of ~3× because blurring of the point-response function on the sensor was greatly decreased. Normalizing the count rate per unit incident flux (3×10^9/s at 3 keV), we calculate an efficiency of 2.4 counts/10^9 incident photons, which scales to very favorable measurement times at a 3rd-generation insertion device beamlines where the incident flux would be increased by a factor of ~10^3. We find good likelihood of long-term impact for this approach at major x-ray facilities, even in the present single-analyzer approach. The extremely compact layout

of the optical elements also strongly suggests future multi-analyzer, multi-camera systems to further gain efficiency through multiplexing.

Before concluding, with an eye to the future it is useful to address three issues. First, improvement of the energy resolution to a few tenths of an eV would greatly improve this instrument's performance for resonant inelastic x-ray scattering at synchrotron light sources. This is a challenging problem to diagnose at the present time due to the novelty of the tightly-curved optic used here. It is tempting to hypothesize that strains from the bending and bonding process dominate. However, a detailed characterization of such effects, and especially how rapidly they decrease with somewhat larger radius of curvature, will require further study. Second, the question of background levels and detection thresholds is important for defining the scope of applications of any x-ray emission spectrometer. This issue is particularly important for dispersive spectrometers as it is often difficult to shield their detectors from stray scatter. A point that should therefore be re-emphasized here is that the x-ray camera is operated in a single-photon detection mode where it achieves a few hundred eV energy resolution for each detected x-ray photon. The dominant background is consequently from stray scattering of the desired fluorescence itself and therefore scales with that intensity. Other backgrounds are very strongly rejected. While we have not determined ultimate detection limits, we have recently completed a study of S chemistry in biochar samples having S concentrations as low as 150 ppm.[65] Third, and finally, in this manuscript we have focused specifically on the narrow energy range from 2 – 2.5 keV where S and P have their diagram lines. This energy range corresponds to a Bragg angle range of ~53 to ~80 degrees from a Si 111 analyzer. Other energies can be probed in this Bragg angle range when using harmonics of the Si 111 or by switching to a different analyzer crystal orientation. The performance of the DRR approach at higher energies is, however, a topic for further work that will

involve a considerable interplay between the detector quantum efficiency, the more deleterious effects of bending strains at higher energies and higher-order Miller indices, possible benefits from changing to doubly-bent (e.g., toroidal) optics at larger radii, and also possible broadening of the analyzer response due to deeper penetration of radiation into the curved optic.

5.5 Conclusions

We report an efficient, inexpensive, high-resolution tender x-ray spectrometer having similar utility in the laboratory with a conventional, low-powered x-ray tube or at synchrotron or XFEL endstations. This instrument is enabled by the recent commercial availability of small-radius crystal analyzers, our development of a small-pixel energy-resolving x-ray camera, and our choice of a dispersive refocusing Rowland (DRR) geometry that removes much sensitivity to the beamspot size on the sample.

Having particular relevance for future laboratory-based analytical applications of advanced XES, a pilot study was conducted in which the distribution of oxidation states of phosphorous was measured in samples of InP quantum dots having different preparation conditions and consequently different amounts of surface-mediated oxidation. The results suggest high utility for this approach in an analytical chemistry perspective, a venue that will accrue significant benefits especially for sulfur-rich materials, due to the challenges involved in sulfur NMR.

Finally, the small size of the present instrument also suggests a unique scientific advantage: it can be readily integrated into controlled-gas glove box systems to enable new directions in analytical chemistry for air-sensitive materials. This would have wide-ranging use not only for S and P compounds, but also for Tc (whose $L\alpha_{1,2}$ fluorescence lines are in the present energy range) and possibly for M-edge emission of several actinides when using different crystal materials and orientations in the x-ray analyzer, if performance in that higher energy range proves sufficient.

5.6 Acknowledgements

This work was supported by the United States Department of Energy, Basic Energy Sciences, under grant DE-SC00008580 and by the Joint Plasma Physics Program of the National Science Foundation and the Department of Energy under grant DE-SC0016251 (WHM, ORH, GTS) and also by the Heavy Element Chemistry Program at LANL by the Division of Chemical Sciences, Geosciences, and Biosciences, Office of Basic Energy Sciences, U.S. Department of Energy (SAK, ASD) and the U.S. Department of Energy. Los Alamos National Laboratory is operated by Los Alamos National Security, LLC, for the National Nuclear Security Administration of U.S. Department of Energy (contract DE-AC52-06NA25396). Additional support also came from the National Science Foundation under grant number CHE-1552164 (JLS, BMC) This research used resources of the Advanced Light Source, which is a DOE Office of Science User Facility under contract no. DE-AC02-05CH11231.

5.7 References

1. P. Glatzel and U. Bergmann, Coordination Chemistry Reviews **249** (1-2), 65-95 (2005).
2. U. Bergmann and P. Glatzel, Photosynthesis Research **102** (2-3), 255-266 (2009).
3. I. Zaharieva, P. Chernev, G. Berggren, M. Anderlund, S. Styring, H. Dau and M. Haumann, Biochemistry **55** (30), 4197-4211 (2016).
4. J. Kowalska and S. DeBeer, Biochimica et Biophysica Acta (BBA) - Molecular Cell Research **1853** (6), 1406-1415 (2015).
5. Y. Ding, D. Haskel, S. G. Ovchinnikov, Y.-C. Tseng, Y. S. Orlov, J. C. Lang and H.-k. Mao, Phys Rev Lett **100** (4), 045508 (2008).
6. K. M. Davis, M. C. Palenik, L. F. Yan, P. F. Smith, G. T. Seidler, G. C. Dismukes and Y. N. Pushkar, J Phys Chem C **120** (6), 3326-3333 (2016).
7. J. Kern, R. Alonso-Mori, R. Tran, J. Hattne, R. J. Gildea, N. Echols, C. Glockner, J. Hellmich, H. Laksmono, R. G. Sierra, B. Lassalle-Kaiser, S. Koroidov, A. Lampe, G. Y. Han, S. Gul, D. DiFiore, D. Milathianaki, A. R. Fry, A. Miahnahri, D. W. Schafer, M. Messerschmidt, M. M. Seibert, J. E. Koglin, D. Sokaras, T. C. Weng, J. Sellberg, M. J. Latimer, R. W. Grosse-Kunstleve, P. H. Zwart, W. E. White, P. Glatzel, P. D. Adams, M. J. Bogan, G. J. Williams, S. Boutet, J. Messinger, A. Zouni, N. K. Sauter, V. K. Yachandra, U. Bergmann and J. Yano, Science **340** (6131), 491-495 (2013).
8. M. J. Lipp, A. P. Sorini, J. Bradley, B. Maddox, K. T. Moore, H. Cynn, T. P. Devereaux, Y. Xiao, P. Chow and W. J. Evans, Phys Rev Lett **109** (19), 195705 (2012).

9. R. Alonso-Mori, J. Kern, R. J. Gildea, D. Sokaras, T. C. Weng, B. Lassalle-Kaiser, R. Tran, J. Hattne, H. Laksmono, J. Hellmich, C. Glockner, N. Echols, R. G. Sierra, D. W. Schafer, J. Sellberg, C. Kenney, R. Herbst, J. Pines, P. Hart, S. Herrmann, R. W. Grosse-Kunstleve, M. J. Latimer, A. R. Fry, M. M. Messerschmidt, A. Miahnahri, M. M. Seibert, P. H. Zwart, W. E. White, P. D. Adams, M. J. Bogan, S. Boutet, G. J. Williams, A. Zouni, J. Messinger, P. Glatzel, N. K. Sauter, V. K. Yachandra, J. Yano and U. Bergmann, Proceedings of the National Academy of Sciences **109** (47), 19103-19107 (2012).
10. N. Lee, T. Petrenko, U. Bergmann, F. Neese and S. DeBeer, J Am Chem Soc **132** (28), 9715-9727 (2010).
11. H. Gretarsson, A. Lupascu, J. Kim, D. Casa, T. Gog, W. Wu, S. R. Julian, Z. J. Xu, J. S. Wen, G. D. Gu, R. H. Yuan, Z. G. Chen, N. L. Wang, S. Khim, K. H. Kim, M. Ishikado, I. Jarrige, S. Shamoto, J. H. Chu, I. R. Fisher and Y. J. Kim, Phys. Rev. B **84** (10), 100509 (2011).
12. G. Vankó, T. Neisius, G. Molnár, F. Renz, S. Kárpáti, A. Shukla and F. M. F. de Groot, The Journal of Physical Chemistry B **110** (24), 11647-11653 (2006).
13. J. F. Lin, G. Vanko, S. D. Jacobsen, V. Iota, V. V. Struzhkin, V. B. Prakapenka, A. Kuznetsov and C. S. Yoo, Science **317** (5845), 1740-1743 (2007).
14. V. Iota, J. H. P. Klepeis, C. S. Yoo, J. Lang, D. Haskel and G. Srajer, Appl Phys Lett **90** (4), 042505 (2007).
15. M. U. Delgado-Jaime, S. DeBeer and M. Bauer, Chemistry - A European Journal **19** (47), 15888-15897 (2013).
16. C. J. Pollock and S. DeBeer, J Am Chem Soc **133** (14), 5594-5601 (2011).
17. R. A. Mori, E. Paris, G. Giuli, S. G. Eeckhout, M. Kavcic, M. Zitnik, K. Bucar, L. G. M. Pettersson and P. Glatzel, Inorganic Chemistry **49** (14), 6468-6473 (2010).
18. R. A. Mori, E. Paris, G. Giuli, S. G. Eeckhout, M. Kavcic, M. Zitnik, K. Bucar, L. G. M. Pettersson and P. Glatzel, Analytical Chemistry **81** (15), 6516-6525 (2009).
19. Y. Pushkar, X. Long, P. Glatzel, G. W. Brudvig, G. C. Dismukes, T. J. Collins, V. K. Yachandra, J. Yano and U. Bergmann, Angew Chem Int Edit **49** (4), 800-803 (2010).
20. D. R. Mortensen, G. T. Seidler, J. A. Bradley, M. J. Lipp, W. J. Evans, P. Chow, Y. M. Xiao, G. Boman and M. E. Bowden, Review of Scientific Instruments **84** (8), 083908 (2013).
21. A. Leon, A. Fiedler, M. Blum, A. Benkert, F. Meyer, W. L. Yang, M. Bar, F. Scheiba, H. Ehrenberg, L. Weinhardt and C. Heske, J Phys Chem C **121** (10), 5460-5466 (2017).
22. L. Zhang, L. W. Ji, P. A. Glans, Y. G. Zhang, J. F. Zhu and J. H. Guo, Phys Chem Chem Phys **14** (39), 13670-13675 (2012).
23. G. T. Seidler, D. R. Mortensen, A. J. Remesnik, J. I. Pacold, N. A. Ball, N. Barry, M. Styczinski and O. R. Hoidn, Review of Scientific Instruments **85** (11), 113906 (2014).
24. Z. Németh, J. Szlachetko, É. G. Bajnóczi and G. Vankó, Review of Scientific Instruments **87** (10), 103105 (2016).
25. Y. Kayser, W. Błachucki, J. C. Dousse, J. Hoszowska, M. Neff and V. Romano, Review of Scientific Instruments **85** (4), 043101 (2014).
26. L. Anklamm, C. Schlesiger, W. Malzer, D. Grötzsch, M. Neitzel and B. Kanngießer, Review of Scientific Instruments **85** (5), 053110 (2014).
27. I. Mantouvalou, K. Witte, D. Grötzsch, M. Neitzel, S. Günther, J. Baumann, R. Jung, H. Stiel, B. Kanngießer and W. Sandner, Review of Scientific Instruments **86** (3), 035116 (2015).

28. M. Szlachetko, M. Berset, J. C. Dousse, J. Hoszowska and J. Szlachetko, Review of Scientific Instruments **84** (9), 093104 (2013).
29. Y. Gohshi, K. Hori and Y. Hukao, Spectrochim Acta B **B 27** (3), 135-142 (1972).
30. C. Sugiura, Y. Gohshi and I. Suzuki, Phys. Rev. B **10** (2), 338-343 (1974).
31. C. Sugiura, Y. Gohshi and I. Suzuki, Jpn J Appl Phys **11** (6), 911-912 (1972).
32. J. Hoszowska, J. C. Dousse, J. Kern and C. Rhême, Nuclear Instruments and Methods in Physics Research Section A: Accelerators, Spectrometers, Detectors and Associated Equipment **376** (1), 129-138 (1996).
33. M. Kavčič, J. C. Dousse, J. Szlachetko and W. Cao, Nuclear Instruments and Methods in Physics Research Section B: Beam Interactions with Materials and Atoms **260** (2), 642-646 (2007).
34. V. E. Dolgih, V. M. Cherkashenko, E. Z. Kurmaev, D. A. Goganov, E. K. Ovchinnikov and Y. M. Yarmoshienko, Nuclear Instruments and Methods in Physics Research **224** (1-2), 117-119 (1984).
35. Y. M. Yarmoshenko, V. A. Trofimova, L. V. Elokhina, E. Z. Kurmaev, S. Butorin, R. Cloots, M. Ausloos, J. A. Aguiar and N. I. Lobatchevskaya, J Phys Chem Solids **54** (10), 1211-1214 (1993).
36. Y. M. Yarmoshenko, V. A. Trofimova, E. Z. Kurmaev, P. R. Slater and C. Greaves, Physica C **224** (3-4), 317-320 (1994).
37. Y. M. Yarmoshenko, V. A. Trofimova, V. E. Dolgih, M. A. Korotin, E. Z. Kurmaev, J. A. Aguiar, J. M. Ferreira and A. C. Pavao, J Phys-Condens Mat **7** (1), 213-218 (1995).
38. M. Kavcic, A. G. Karydas and C. Zarkadas, X-Ray Spectrom **34** (4), 310-314 (2005).
39. M. Kavčič, A. G. Karydas and C. Zarkadas, Nuclear Instruments and Methods in Physics Research Section B: Beam Interactions with Materials and Atoms **222** (3-4), 601-608 (2004).
40. M. Kavcic, M. Budnar, A. Muhleisen, F. Gasser, M. Zitnik, K. Bucar and R. Bohinc, Review of Scientific Instruments **83** (3), 033113 (2012).
41. T. T. Fister, G. T. Seidler, L. Wharton, A. R. Battle, T. B. Ellis, J. O. Cross, A. T. Macrander, W. T. Elam, T. A. Tyson and Q. Qian, Review of Scientific Instruments **77** (6), 063901 (2006).
42. D. Sokaras, D. Nordlund, T. C. Weng, R. A. Mori, P. Velikov, D. Wenger, A. Garachtchenko, M. George, V. Borzenets, B. Johnson, Q. Qian, T. Rabedeau and U. Bergmann, Review of Scientific Instruments **83** (4), 043112 (2012).
43. D. Sokaras, T. C. Weng, D. Nordlund, R. Alonso-Mori, P. Velikov, D. Wenger, A. Garachtchenko, M. George, V. Borzenets, B. Johnson, T. Rabedeau and U. Bergmann, Review of Scientific Instruments **84** (5), 053102 (2013).
44. R. Verbeni, T. Pylkkänen, S. Huotari, L. Simonelli, G. Vankó, K. Martel, C. Henriquet and G. Monaco, Journal of Synchrotron Radiation **16** (4), 469-476 (2009).
45. O. R. Hoidn and G. T. Seidler, Review of Scientific Instruments **86** (8), 086107 (2015).
46. O. R. Hoidn, W. M. Holden and G. T. Seidler, Review of Scientific Instruments **In preparation** (2017).
47. J. Słowik and A. Zięba, Journal of Applied Crystallography **34** (4), 458-464 (2001).
48. R. W. Cheary and A. Coelho, Journal of Applied Crystallography **27**, 673-681 (1994).
49. S. Brennan, P. L. Cowan, R. D. Deslattes, A. Henins, D. W. Lindle and B. A. Karlin, Review of Scientific Instruments **60** (7), 2243-2246 (1989).

50. E. Welter, P. Machek, G. Drager, U. Bruggmann and M. Froba, Journal of Synchrotron Radiation **12**, 448-454 (2005).
51. S. Huotari, G. Vanko, F. Albergamo, C. Ponchut, H. Graafsma, C. Henriquet, R. Verbeni and G. Monaco, J. Synchrot. Radiat. **12**, 467-472 (2005).
52. S. Huotari, T. Pylkkanen, R. Verbeni, G. Monaco and K. Hamalainen, Nat Mater **10** (7), 489-493 (2011).
53. S. Huotari, F. Albergamo, G. Vanko, R. Verbeni and G. Monaco, Review of Scientific Instruments **77** (5), 053102 (2006).
54. A. C. Hudson, W. C. Stolte, D. W. Lindle and R. Guillemin, Review of Scientific Instruments **78** (5), 053101 (2007).
55. O. R. Hoidn, Ph.D. Thesis, University of Washington, 2017.
56. B. Dickinson, G. T. Seidler, Z. W. Webb, J. A. Bradley, K. P. Nagle, S. M. Heald, R. A. Gordon and I. M. Chou, Review of Scientific Instruments **79** (12), 123112 (2008).
57. M. Petric, R. Bohinc, K. Bucar, M. Zitnik, J. Szlachetko and M. Kavcic, Analytical Chemistry **87** (11), 5632-5639 (2015).
58. D. C. Gary and B. M. Cossairt, Chem Mater **25** (12), 2463-2469 (2013).
59. J. L. Stein, E. A. Mader and B. M. Cossairt, J Phys Chem Lett **7** (7), 1315-1320 (2016).
60. D. C. Gary, M. W. Terban, S. J. L. Billinge and B. M. Cossairt, Chem Mater **27** (4), 1432-1441 (2015).
61. J. J. Rehr, J. J. Kas, F. D. Vila, M. P. Prange and K. Jorissen, Phys Chem Chem Phys **12** (21), 5503-5513 (2010).
62. J. McKittrick and L. E. Shea-Rohwer, J Am Ceram Soc **97** (5), 1327-1352 (2014).
63. P. Mushonga, M. O. Onani, A. M. Madiehe and M. Meyer, J Nanomater, 869284 (2012).
64. H. Virieux, M. Le Troedec, A. Cros-Gagneux, W. S. Ojo, F. Delpech, C. Nayral, H. Martinez and B. Chaudret, J Am Chem Soc **134** (48), 19701-19708 (2012).
65. W. M. Holden, G. T. Seidler and S. Cheah, Analytical Chemistry **In Preparation** (2017).

CHAPTER 6 A COLOR X-RAY CAMERA FOR 2 – 6 KEV USING A MASS PRODUCED BACK ILLUMINATED CMOS SENSOR

Originally published as: Holden, W. M.; Hoidn, O. R.; Seidler, G. T.; DiChiara, A. D. A Color X-Ray Camera for 2–6 KeV Using a Mass Produced Back Illuminated Complementary Metal Oxide Semiconductor Sensor. *Review of Scientific Instruments* 2018, 89 (9), 093111. https://doi.org/10.1063/1.5047934.

My contributions to this work include leading the efforts for testing, data acquisition and analysis, as well as supporting efforts of the hardware implementation of the camera. I also assisted Oliver R. Hoidn, who led the development of software. Oliver R. Hoidn and I contributed equally to this work.

There are several reports in the scientific literature of the use of mass-produced charge coupled device (CCD) or complementary metal oxide semiconductor (CMOS) sensors as x-ray detectors that combine high spatial resolution with significant energy resolution. Exploiting a relatively new, especially favorable ambient-temperature back-illuminated CMOS sensor, we report the development of a spectroscopic x-ray camera having particularly impressive performance for 2 – 6 keV photons. This instrument has several beneficial characteristics for advanced x-ray spectroscopy studies in the laboratory, at synchrotron light sources, at x-ray free electron lasers, or when using pulsed x-ray sources such as for laser plasma physics research. These characteristics include fine position and energy resolution for individual photon events; high saturation rates; frame rates above 100 Hz; easy user maintenance for damaged sensors; and software for real-time processing. We evaluate this camera as an alternative to traditional energy-

dispersive solid-state detectors, such as silicon drift detectors, and also illustrate its use in a very high resolution wavelength-dispersive x-ray fluorescence spectrometer (i.e., x-ray emission spectrometer) that has recently been reported elsewhere [W. M. Holden et al., Rev. Sci. Instrum. 88(7), 073904 (2017)].

6.1 INTRODUCTION

The capabilities of a variety of x-ray techniques at synchrotrons, x-ray free electron lasers (XFEL), laser plasma facilities, and university-scale laboratories are heavily dependent on the characteristics of the x-ray detectors with which they are implemented. One technological regime of interest is that of pixel area detectors combining spectroscopic and spatial resolution with features such as high readout rate, large collection solid angle, and hardness to ionizing radiation and electromagnetic pulses (EMPs). The advent of time-resolved spectroscopy at synchrotron and x-ray free electron laser (XFEL) facilities has greatly expanded the need for this class of detectors.[1-16] Similar needs are also present in laser-plasma physics, where entire spectra for fluorescence, x-ray band thermal emission, or inelastic scattering must often be collected in few-pulse or even truly single-pulse experiments.[17-34]

While there is an impressive effort aimed at either improvement of existing state-of-the-art technology or *de novo* development of new ideas for truly advanced high-performance detectors,[1-16, 35, 36] there is another route that requires consideration. Highly mass-produced, commercial multipixel sensors intended for primary use at optical wavelengths are, by the standards of x-ray science, already stunningly advanced sensors. For example, recent advances in the performance of mass-produced complementary metal-oxide-semiconductor (CMOS) image sensors, including readout rates above 200 Mpx/second and optical-wavelength quantum efficiencies exceeding 80%,

significantly increase their potential for scientific applications. The direct application of such sensors to the x-ray regime is limited mainly by the fact that their small pixel thickness leads to greatly decreased quantum efficiency for hard x-rays. That being said, the use of mass-produced CMOS image sensors in the x-ray regime has been explored in prior literature that has established them as viable spectroscopic imaging detectors having a favorable combination of low cost (a consequence of chip-level integration of all sensor functions), high framerates, and improved radiation hardness relative to comparable charge coupled devices (CCDs). [37-41] By 'spectroscopic', we mean that the camera output contains sufficient information for determination of both the energy and position of a photoabsorbed x-ray. Such devices are often referred to as 'color x-ray cameras'. CMOS image sensors can also be operated at room temperature while still having low noise, which is beneficial in multiple ways. Without need for cooling, the cameras can be simpler and have a smaller footprint. Not having cooling also removes the need for shielding over the sensor to protect from condensation, which improves efficiency at lower x-ray photon energies where window material would be more strongly absorbing.

In a prior publication[40] we presented an x-ray camera platform for the 2-6 keV photon energy range based on a legacy CMOS image sensor, the Aptina MT9M001. Here, we introduce a new camera that incorporates a modern back-illuminated CMOS sensor with significantly improved readout rates and finer spectral and spatial resolution. Specifically, we find an energy resolution of ~86 eV at 2 keV with saturation rates above 10^6/s at ~80 Hz frame rate. These spectroscopic benefits are complemented by a spatial resolution of 2.9 μm and real-time processing of all results, but are constrained by a ~50% quantum efficiency at 2 keV that decreases to below 20% at 5 keV.

This manuscript continues as follows. First, in section 6.2, we describe experimental details including the commercial hardware and its modification used in the present instruments, as well as the new software package that has been developed to support real-time spectral analysis and real-time energy-windowed imaging. A key point here is that it is not only the sensor, but also the entire camera read-out system that is commercially available because of the high demand for extreme low-light sensitivity imaging for, e.g., amateur astronomy. Next, in section 6.3, we present results and discussion, demonstrating the cluster-binning methods and also both energy-dispersive and photon-counting modes for the camera. This includes representative data from a wavelength-dispersive spectrometer whose design has recently been described elsewhere[42] and also data from single-shot x-ray fluorescence measurements at a synchrotron light source. Finally, in section 6.4 we conclude and provide future directions.

6.2 Experimental

6.2.1 Hardware

The hardware consists of a commercial amateur astronomy camera (ZWO Company) based on the Sony IMX291, a back-illuminated CMOS image sensor with a rolling shutter, pixel pitch of 2.9-µm, pixel grid of 1936×1096, and maximum framerate of 170 fps. The sensor features high sensitivity and dynamic range, with a 12-bit A/D converter and readout noise of 1e- at maximum analog gain. The choice of vendor and model was driven by the manufacturer's provision of a software application programming interface (API) allowing straightforward configuration and access to the sensor's uncompressed video stream; we note that other manufacturers offer products with similar feature sets.

We have modified the camera in two ways. First, the main camera board has been reworked by removing the IMX291 sensor and replacing it with a custom IC socket (Andon

Electronics). This was done to more easily allow sensor replacement if radiation damage occurred. Second, the sensor itself has been modified by removal of the glass cover (Pacific X-Ray). A photo of the resulting camera is shown in Fig. 6.1. The blue 3-D printed plastic part is a simple clamp used to press the sensor against the socket contact pads.

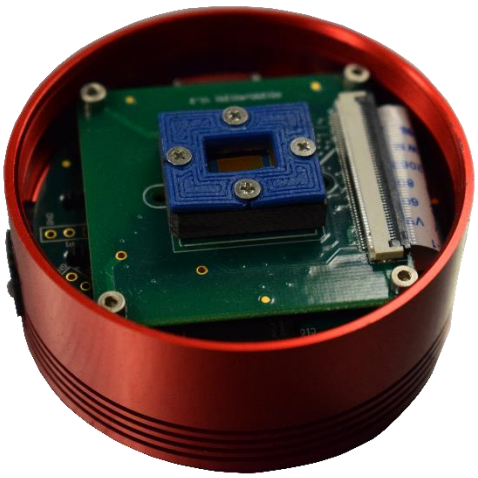

Figure 6.1: Photograph of the modified camera. The original commercial product has been reworked to install an IC socket for the sensor and to remove the glass cover of the sensor. For scale, the outer diameter of the cylindrical package is 62 mm.

6.2.2 Software

After the necessary hardware modifications, additional software was developed to process the sensor's output to optimize its performance with x-rays. First, a software package written in C was developed to efficiently parse the acquired frames, and second, a real-time processing pipeline was implemented to communicate with the camera, process the data, and allow for real-time data analysis.

When an x-ray photon is absorbed in the active layer of a sensor pixel, the charge separation results in a signal with expectation value proportional to the photon's energy. In the simplest case, wherein the entire charge cloud from an x-ray absorption event is concentrated in a single pixel, the detecting pixel has intrinsic sensitivity to the energy of the incident x-ray photon.[39, 40, 43] In the

majority of events, however, the charge cloud spreads over a cluster of several adjacent pixels.[39, 40, 43] To optimize the camera's quantum efficiency (QE) and spectroscopic sensitivity, it is essential to use this prior information to recover the energy and position of each detected photon on an event-by-event basis. To do this we perform a "breadth-first" search[44] of every frame to identify sets of connected pixels with analog-to-digital converter (ADC) values above a user-specified signal threshold. For each cluster thus identified, the signal is summed over all member pixels and the event's position is inferred from the cluster's center of mass. This technique is similar to event-reconstruction algorithms used for the same purpose in prior literature, with the difference that we place no constraint on the size and shape of signal clusters.[39] The sensor's manufacturer-specified low noise floor (under 1 e^- per pixel) allows the use of an aggressively low threshold level, resulting in a high level of signal.

To implement the above analysis, we developed a real-time data processing pipeline. It consists of a collection of several software components communicating with one another over ZeroMQ sockets. First, a customized version of the open source image capture program `oaCapture` controls the camera's readout, allowing the user to configure the camera's gain and per-frame exposure time. Event reconstruction, which requires the computational throughput of multiple CPU cores for intense signals, is done by a pool of worker processes collecting frames from the capture application in round-robin fashion. The resulting filtered frames from this parallel pipeline are aggregated on a sink node, which users can access with high-level functions for acquiring and visualizing the pre-processed camera data.

6.2.3 X-ray Measurements

X-ray measurements for direct characterization of the camera performance used a low-powered Rh-anode x-ray tube (Moxtek MAGPRO 12W). For quantum efficiency (QE)

determination at different energies, the x-ray tube illuminated appropriate reference targets that generated elemental fluorescence at desired energies. The camera and a commercial SDD (Amptek X-123SDD) were alternately placed behind a pinhole that ensured equal illumination on each sensor. The ratio of detection rates, corrected for the SDD's QE, then allows determination of the camera QE. Saturation rate measurements involved direct illumination of the camera by the full broadband output of the x-ray tube, displaced several tens of cm away from the sensor to allow for a useful tube-current range before saturation.

In addition to the above tests, the camera is also used as a position-sensitive detector in a miniature wavelength-dispersive spectrometer, as described in Holden, et al.[42] This application makes heavy use of the camera's energy-resolving capability. By applying an energy window to the photon absorption events detected in each camera frame, stray scatter and fluorescence from the x-ray chamber are rejected and only the desired signal photons are summed into the final frame, allowing a low-noise spectrum to be obtained even for dilute samples with weak signal, such as in a recent study of S speciation in biochars by some of the present authors.[45]

Finally, as a demonstration of the camera's ability to perform single-shot spectroscopy, measurements were also taken at BioCARS beamline 14-ID-B at the Advanced Photon Source. The beamline was set to pink-beam mode, with the peak energy set to 13 keV, which provided pulses with energy 13 μJ. The small size of the camera allowed installation close to the sample, even amongst the existing beamline equipment, at a distance of ~ 8 cm from the sample. A 7.5-μm thick Fe foil was exposed to the unattenuated beam in single-shot mode, and x-ray fluorescence spectra of the Fe foil for individual synchrotron pulses were recorded by the camera. The majority of exposures were captured in single frames, but due to the rolling-shutter operation of the camera, shots were occasionally measured over two subsequent frames.

6.3 Results and Discussion

In this section we address four aspects of the camera operation and performance: the cluster algorithm, energy dispersive operation, quantum efficiency, and finally single-photon counting mode for spectroscopically-constrained imaging. First, a magnified view of a small region of a captured image is presented in Fig. 6.2, where single-photon signal clusters are readily identifiable. The distribution of cluster sizes is strongly skewed; the largest clusters contain more than 10 pixels, while the mean number is 2.1.

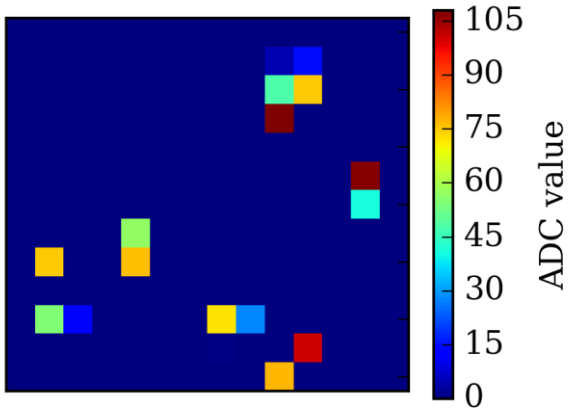

Figure 6.2: Representative cropped region of a camera frame during direct illumination by a Rh anode x-ray tube source operating at 6 kV bias voltage. The total illumination results in detection of 2×10^6 photons/s at an 80 Hz frame rate.

Second, when operated as a spectroscopic sensor, the camera's user-visible output is a histogram of number of events binned by per-event signal. This is demonstrated in Fig. 6.3a, which shows the direct-illumination spectrum of a laboratory x-ray tube source. The ADC values have been converted to an energy scale using the identified spectral features. Note that the energy scale and the energy range detectable within the limit of the ADC depend on the user-selected gain value. The read noise of the sensor is lower with higher gain, so in practice the gain is chosen to be as high as possible while avoiding signals in the region of interest saturating the sensor. The

dominant components of the signal are the tube's continuous bremsstrahlung spectrum and Rh L-shell emission from the anode. Two detector artifacts are also visible. First, a peak at the energy of Si Kα is generated by Si fluorescence photons emitted in the sensor that propagate far enough from their originating interaction sites to be registered as separate events. Second, the escape of Si fluorescence from the absorption sites of Rh L-shell fluorescence photons creates so-called escape peak echoes of the Rh L peaks that are downshifted by 1.74 keV, the energy of Si Kα. We find that the camera's energy resolution at the energy of P Kα is 86 eV (Fig. 6.3b), close to the limit imposed by statistical fluctuations in the charge generated by an absorbed x-ray (i.e. Fano noise) of ~68 eV (calculated according to Lumb[46] assuming no readout noise).

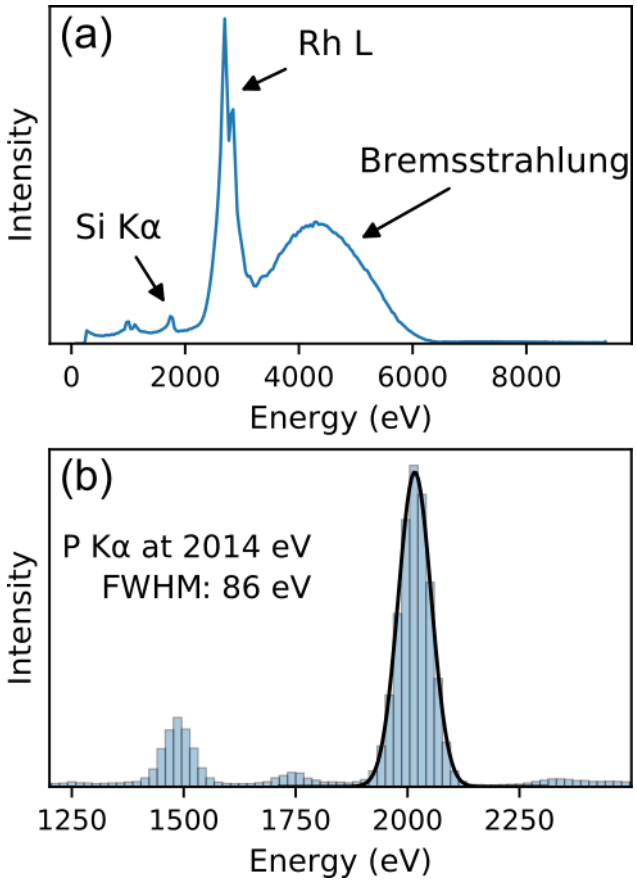

Figure 6.3: (a) Energy dispersive spectrum from direct illumination of the camera by a Rh anode x-ray tube source operating at 6 kV bias voltage. The ADC channel at the peak of the Rh L

emission contains 3.2 $\times 10^4$ counts. (b) Energy dispersive spectrum of monochromatized P Kα photons, showing a resolution of 86 eV full-width at half-maximum.

Third, the quantum efficiency (QE) of the detector is presented in Fig. 6.4. We note a maximum QE of 51% at the energy of P Kα, a more than two-fold improvement over our previous camera and software.[40] Under x-ray uniform illumination at 6 kV accelerating potential, the observed count rates have only minimal deviations from linearity at 2×10^6 photons per second for a 80 Hz frame rate (see Fig. 6.5) – an impressive performance that is higher than the typical saturation rate of commercial silicon drift detectors. The exposure sub-region shown in Fig. 6.2 was captured at this count rate. Note that the photon clusters are still largely disconnected, so that pile-up from cluster overlap is infrequent. The lower count rates for the CMOS camera compared to the SDD are a consequence of the camera's lower quantum efficiency at higher photon energies. The camera should retain the observed high saturation rate performance when illuminated with more monochromatic, lower-energy sources where its QE is higher.

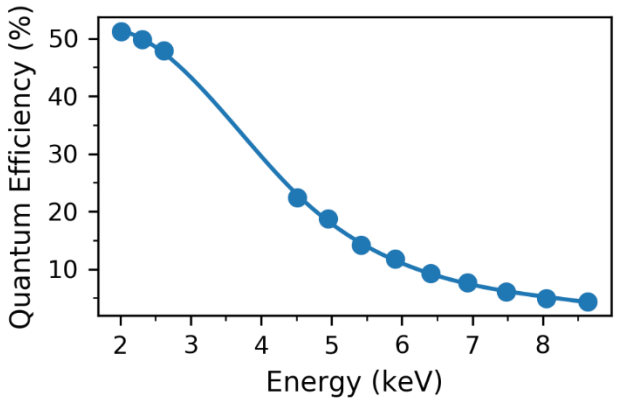

Figure 6.4: The camera's quantum efficiency as a function of x-ray photon energy, established by comparison with a commercial Si drift detector.

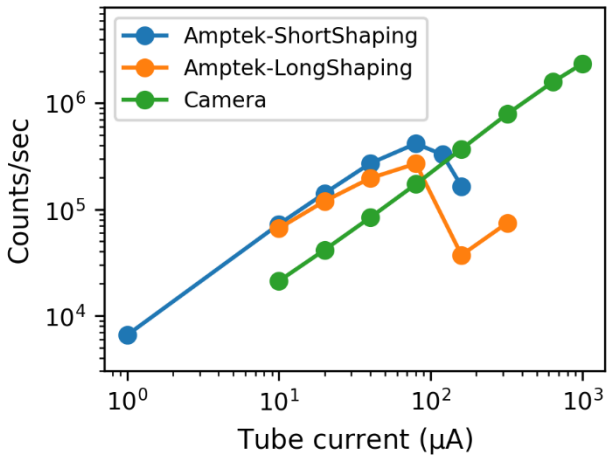

Figure 6.5: Camera count rate as a function of incident photon intensity, controlled via current provided to an x-ray tube source directly illuminating the camera with a broadband spectrum (see Fig. 6.3a). We compare to the same curves for a commercial SDD and digital pulse processing hardware having pulse shaping times optimized for count rate (short shaping time) or for energy resolution (long shaping time). The low efficiency of the camera is due to the large flux at higher photon energies where its QE is poor, see Figures 6.3a and 6.4. Illumination at lower photon energies will retain the high saturation rates but give the improved QE of Fig. 6.4.

The energy-dispersive mode of operation combined with the ability to measure high count rates with minimal saturation is appealing for single-shot studies at intense beamlines at synchrotrons and XFEL sources, where the extremely short pulse durations are a poor fit with SDD's, i.e., single-pixel detectors that can only detect one photon per incident pulse lest they suffer from pile-up. A synchrotron single-shot spectra for a pulse energy of 13 μJ in pink-beam mode centered at 13 keV is shown in Fig. 6.6 for an Fe foil. With this intensity, about 4,000 x-ray events were recorded in a single-shot frame, from which the Kα/Kβ ratio can be determined to an accuracy of ~10%. Higher count rates at, e.g., the Linac Coherent Light Source and/or parallelizing detection with the use of multiple x-ray cameras should will allow much finer determination of branch ratios, or other quantitative aspects of x-ray fluorescence spectra in single-shot studies. In

Fig 6.6. one other detector artifact can be seen: a weak low energy tail that results from events in which an incomplete fraction of the total charge created during x-ray absorption is recorded. This effect has been previously reported,[39] and although relatively weak, it could be accounted for through further characterization if required for, e.g., fine determination of Kα/Kβ ratios.

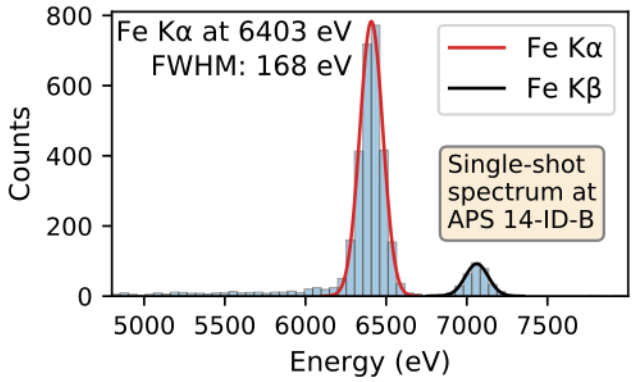

Figure 6.6: Single shot energy-dispersive spectrum from an Fe foil at APS beamline 14-ID-B.

Finally, the camera's combination of high saturation count rates and small pixel dimension makes it a strong fit as a position-sensitive detector in dispersive x-ray emission spectrometer designs. The camera's spectroscopic sensitivity may be employed for background rejection (i.e., for rejection of photons with energies outside a pre-specified range), thus minimizing the need for shielding from stray scatter. Holden et al.[42] have demonstrated this advantage in a novel compact wavelength-dispersive spectrometer design that incorporates the camera as its position-sensitive detector. In Fig. 6.7, we show a representative accumulation of camera exposures and the resulting spectrum. An energy region-of-interest (ROI) was set around the nominal S Kα photon energy, so that as each frame was captured, the detected x-ray events having energy outside of the ROI were filtered out and the resulting frames were added to the accumulation. The spectrometer's small dimensions, which are enabled in part by the camera's fine spatial resolution, give it a large collection efficiency which results in count rates in laboratory studies (using low-power x-ray tube

sources) comparable to those at a third-generation synchrotron insertion device beamline. The instrument has thus far been demonstrated in the university-scale laboratory and at the synchrotron.

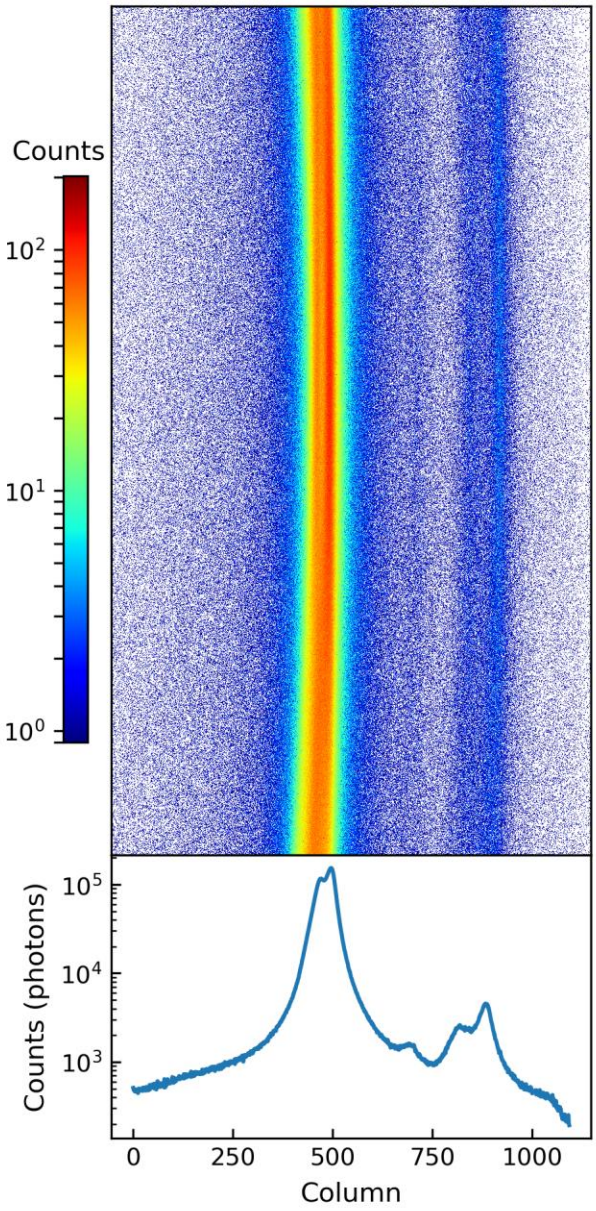

Figure 6.7: Image of the sensor's output when serving as the position-sensitive area detector of a miniature wavelength-dispersive spectrometer (Holden, et al., 2017).[42] The signal shown is a S Kα spectrum. In order to reduce the background level, the camera was configured to reject all events with photon energies outside of a spectral region of interest centered at S Kα.

Before concluding, it is interesting to consider future directions for this instrument development project. First, while the present sensor manifests several benefits when compared to CCD detectors commonly used for spectroscopic imaging, the poor quantum efficiency at higher energies is a substantial drawback. Specialized production of CMOS sensors with thicker pixel active regions could be created to improve the QE, if supported by the obvious cost-benefit analysis. Second, the inherent modularity of the sensor strongly suggests future work to tile many such sensors to increase the net collection solid angle. This could be particularly useful at high-flux synchrotron beamlines at tender x-ray energies. There, the fluorescence intensities quite typically saturate conventional SDD, with common mitigations being to simply back up the detector to decrease its solid angle and/or to multiplex across several such detectors. Given that these detection schemes are already effectively low efficiency (low solid angle), a high-solid angle multi-CMOS array with inherently lower quantum efficiency holds high potential to be competitive. This would obviously be aided by back-illuminated CMOS sensors with larger number of pixels, such as are indeed presently reaching the market, or sensors with much larger pixels (to decrease cluster size, thus enhancing count rates prior to pile-up). Third, whether for lower energy operation, where we have not yet tested the sensor, or for more convenient use at laser plasma facilities or some 2-3 keV endstations at synchrotrons, it will be important to package this type of camera in a high-vacuum or even ultra-high-vacuum compatible small chamber with a silicon nitride window. We have begun such an effort.

6.4 Conclusions

In conclusion, we have reported the development of a spectroscopic x-ray camera based on a mass-produced consumer product. The observed performance suggests a range of potential applications as a spectroscopic detector capable of operating at ~100 Hz with fine spatial resolution

and adequate quantum efficiency in the 2 - 6 keV photon energy range. Among these applications, we have demonstrated effective use of the camera as an energy-selective position-sensitive detector in a high-performance compact dispersive spectrometer. We see significant potential for use of this detector in the lab, at synchrotrons, at XFELs, and at laser plasma facilities.

6.5 Acknowledgements

This work (W.M.H. and G.T.S) was supported by the Joint Plasma Physics Program of the National Science Foundation and the Department of Energy under Grant No. DE-SC0016251. This research used resources of the Advanced Photon Source, a U.S. Department of Energy (DOE) Office of Science User Facility operated for the DOE Office of Science by Argonne National Laboratory under Contract No. DE-AC02-06CH11357. Use of BioCARS was also supported by the National Institute of General Medical Sciences of the National Institutes of Health under grant number R24GM111072. The content is solely the responsibility of the authors and does not necessarily represent the official views of the National Institutes of Health.

6.6 References

1. S. Aschauer, P. Majewski, G. Lutz, H. Soltau, P. Holl, R. Hartmann, D. Schlosser, U. Paschen, S. Weyers, S. Dreiner, M. Klusmann, J. Hauser, D. Kalok, A. Bechteler, K. Heinzinger, M. Porro, B. Titze and L. Struder, Journal of Instrumentation **12**, P11013 (2017).
2. R. Ballabriga, M. Campbell, E. H. M. Heijne, X. Llopart and L. Tlustos, Ieee Transactions on Nuclear Science **54** (5), 1824-1829 (2007).
3. E. N. Gimenez, R. Ballabriga, G. Blaj, M. Campbell, I. Dolbnya, E. Frodjh, I. Horswell, X. Llopart, J. Marchal, J. McGrath, D. Omar, R. Plackett, K. Sawhney and N. Tartoni, Ieee Transactions on Nuclear Science **62** (3), 1413-1421 (2015).
4. A. Grande, C. Fiorini, F. Erdinger, P. Fischer and M. Porro, Journal of Instrumentation **12**, T12008 (2017).
5. D. Greiffenberg and A. Collaboration, Journal of Instrumentation **7**, C01103 (2012).
6. A. Koch, M. Hart, T. Nicholls, C. Angelsen, J. Coughlan, M. French, S. Hauf, M. Kuster, J. Sztuk-Dambietz, M. Turcato, G. A. Carini, M. Chollet, S. C. Herrmann, H. T. Lemke, S. Nelson, S. Song, M. Weaver, D. Zhu, A. Meents and P. Fischer, Journal of Instrumentation **8**, C11001 (2013).

7. P. Kraft, A. Bergamaschi, C. Broennimann, R. Dinapoli, E. F. Eikenberry, B. Henrich, I. Johnson, A. Mozzanica, C. M. Schleputz, P. R. Willmott and B. Schmitt, Journal of Synchrotron Radiation **16**, 368-375 (2009).
8. A. Mozzanica, A. Bergamaschi, S. Cartier, R. Dinapoli, D. Greiffenberg, I. Johnson, J. Jungmann, D. Maliakal, D. Mezza, C. Ruder, L. Schaedler, B. Schmitt, X. Shi and G. Tinti, Journal of Instrumentation **9**, C05010 (2014).
9. A. Mozzanica, A. Bergamaschi, R. Dinapoli, H. Graafsma, D. Greiffenberg, B. Henrich, I. Johnson, M. Lohmann, R. Valeria, B. Schmitt and S. Xintian, Journal of Instrumentation **7**, C01019 (2012).
10. M. Porro, L. Andricek, S. Aschauer, M. Bayer, J. Becker, L. Bombelli, A. Castoldi, G. De Vita, I. Diehl, F. Erdinger, S. Facchinetti, C. Fiorini, P. Fischer, T. Gerlach, H. Graafsma, C. Guazzoni, K. Hansen, P. Kalavakuru, H. Klar, A. Kugel, P. Lechner, M. Lemke, G. Lutz, M. Manghisoni, D. Mezza, D. Muntefering, U. Pietsch, E. Quartieri, M. Randall, V. Re, C. Reckleben, C. Sandow, J. Soldat, L. Struder, J. Szymanski, G. Weidenspointner and C. B. Wunderer, Ieee Transactions on Nuclear Science **59** (6), 3339-3351 (2012).
11. S. Redford, M. Andra, R. Barten, A. Bergamaschi, M. Bruckner, R. Dinapoli, E. Frojdh, D. Greiffenberg, C. Lopez-Cuenca, D. Mezza, A. Mozzanica, M. Ramilli, M. Ruat, C. Ruder, B. Schmitt, X. Shi, D. Thattil, G. Tinti, S. Vetter and J. Zhang, Journal of Instrumentation **13**, C01027 (2018).
12. D. P. Siddons, R. Kirkham, C. G. Ryan, G. deGeronimo, A. Dragone, A. J. Kuczewski, Z. Y. Li, G. A. Carini, D. Pinelli, R. Beuttenmuller, D. Elliot, M. Pfeffer, t. A. Tyson, G. F. Moorhead and P. A. Dunn, Journal of Physics: Conference Series **499**, 012001 (2014).
13. B. Thomas, M. C. Veale, M. D. Wilson, P. Seller, A. Schneider and K. Iniewski, Journal of Instrumentation **12**, C12045 (2017).
14. M. C. Veale, P. Adkin, P. Booker, J. Coughlan, M. J. French, M. Hart, T. Nicholls, A. Schneider, P. Seller, I. Pape, K. Sawhney, G. A. Carini and P. A. Hart, Journal of Instrumentation **12**, P12003 (2017).
15. J. Zhang, M. Andra, R. Barten, A. Bergamaschi, M. Bruckner, R. Dinapoli, E. Frojdh, D. Greiffenberg, C. Lopez-Cuenca, D. Mezza, A. Mozzanica, M. Ramilli, S. Redford, M. Ruat, C. Ruder, B. Schmitt, X. Shi, D. Thattil, G. Tinti, M. Turcato and S. Vetter, Journal of Instrumentation **13**, P01025 (2018).
16. I. Ordavo, S. Ihle, V. Arkadiev, O. Scharf, H. Soltau, A. Bjeoumikhov, S. Bjeoumikhova, G. Buzanich, R. Gubzhokov, A. Gunther, R. Hartmann, P. Holl, N. Kimmel, M. Kuhbacher, M. Lang, N. Langhoff, A. Liebel, M. Radtke, U. Reinholz, H. Riesemeier, G. Schaller, F. Schopper, L. Struder, C. Thamm and R. Wedell, Nuclear Instruments & Methods in Physics Research Section a-Accelerators Spectrometers Detectors and Associated Equipment **654** (1), 250-257 (2011).
17. R. Fazeli, Optics Letters **41** (22), 5250-5253 (2016).
18. E. J. Gamboa, C. M. Huntington, M. R. Trantham, P. A. Keiter, R. P. Drake, D. S. Montgomery, J. F. Benage and S. A. Letzring, Review of Scientific Instruments **83** (10), 10e108 (2012).
19. J. Hawreliak, H. E. Lorenzana, B. A. Remington, S. Lukezic and J. S. Wark, Review of Scientific Instruments **78** (8), 083908 (2007).
20. O. R. Hoidn and G. T. Seidler, Physics of Plasmas **21** (1), 012707 (2014).

21. L. T. Hudson, A. Henins, R. D. Deslattes, J. F. Seely, G. E. Holland, R. Atkin, L. Marlin, D. D. Meyerhofer and C. Stoeckl, Review of Scientific Instruments **73** (6), 2270-2275 (2002).
22. S. Kojima, T. Ikenouchi, Y. Arikawa, S. Sakata, Z. Zhang, Y. Abe, M. Nakai, H. Nishimura, H. Shiraga, T. Ozaki, S. Miyamoto, M. Yamaguchi, A. Takemoto, S. Fujioka and H. Azechi, Review of Scientific Instruments **87** (4), 043502 (2016).
23. A. L. Kritcher, T. Doppner, C. Fortmann, O. L. Landen, R. Wallace and S. H. Glenzer, High Energy Density Physics **7** (4), 271-276 (2011).
24. L. Labate, P. Koster, T. Levato and L. A. Gizzi, Review of Scientific Instruments **83** (10), 103504 (2012).
25. J. Y. Mao, L. M. Chen, L. T. Hudson, J. F. Seely, L. Zhang, Y. Q. Sun, X. X. Lin and J. Zhang, Review of Scientific Instruments **83** (4), 043104 (2012).
26. N. H. Matlis, S. Reed, S. S. Bulanov, V. Chvykov, G. Kalintchenko, T. Matsuoka, P. Rousseau, V. Yanovsky, A. Maksimchuk, S. Kalmykov, G. Shvets and M. C. Downer, Nature Physics **2** (11), 749-753 (2006).
27. S. R. Nagel, T. J. Hilsabeck, P. M. Bell, D. K. Bradley, M. J. Ayers, M. A. Barrios, B. Felker, R. F. Smith, G. W. Collins, O. S. Jones, J. D. Kilkenny, T. Chung, K. Piston, K. S. Raman, B. Sammuli, J. D. Hares and A. K. L. Dymoke-Bradshaw, Review of Scientific Instruments **83** (10), 10e116 (2012).
28. G. R. Plateau, C. G. R. Geddes, D. B. Thorn, M. Chen, C. Benedetti, E. Esarey, A. J. Gonsalves, N. H. Matlis, K. Nakamura, C. B. Schroeder, S. Shiraishi, T. Sokollik, J. van Tilborg, C. Toth, S. Trotsenko, T. S. Kim, M. Battaglia, T. Stohlker and W. P. Leemans, Physical Review Letters **109** (6), 064802 (2012).
29. M. Suggit, G. Kimminau, J. Hawreliak, B. Remington, N. Park and J. Wark, Review of Scientific Instruments **81** (8), 083902 (2010).
30. M. P. Valdivia, D. Stutman and M. Finkenthal, Applied Optics **54** (10), 2577-2583 (2015).
31. M. P. Valdivia, D. Stutman, C. Stoeckl, C. Mileham, I. A. Begishev, J. Bromage and S. P. Regan, Applied Optics **57** (2), 138-145 (2018).
32. N. C. Woolsey, R. J. Clarke, D. Doria, L. A. Gizzi, G. Gregori, P. Hakel, S. B. Hansen, P. Koester, L. Labate, T. Levato, B. Li, M. Makita, R. C. Mancini, J. Pasley, P. P. Rajeev, A. P. L. Robinson, E. Wagenaars, J. N. Waugh and N. Booth, High Energy Density Physics **7** (2), 105-109 (2011).
33. S. Glenzer and R. Redmer, Review of Modern Physics **81**, 1625-1663 (2009).
34. S. H. Glenzer, G. Gregori, R. W. Lee, F. J. Rogers, S. W. Pollaine and O. L. Landen, Physical Review Letters **90** (17), 175002 (2003).
35. J. N. Ullom and D. A. Bennett, Superconductor Science and Technology **28** (8), 084003 (2015).
36. C. G. Ryan, D. P. Siddons, R. Kirkham, Z. Y. Li, M. D. de Jonge, D. J. Paterson, A. Kuczewski, D. L. Howard, P. A. Dunn, G. Falkenberg, U. Boesenberg, G. De Geronimo, L. A. Fisher, A. Halfpenny, M. J. Lintern, E. Lombi, K. A. Dyl, M. Jensen, G. F. Moorhead, J. S. Cleverley, R. M. Hough, B. Godel, S. J. Barnes, S. A. James, K. M. Spiers, M. Alfeld, G. Wellenreuther, Z. Vukmanovic and S. Borg, Journal of Physics: Conference Series **499**, 012002 (2014).
37. D. W. Lane, Nuclear Instruments and Methods in Physics Research Section B: Beam Interactions with Materials and Atoms **284**, 29-32 (2012).

38. F. Nachtrab, T. Hofmann, M. Firsching, N. Uhlmann and R. Hanke, presented at the Nuclear Science Symposium Conference Record (NSS/MIC), 2009 IEEE, 2009 (unpublished).
39. L. Servoli, D. Biagetti, D. Passeri and E. S. Gattuso, Journal of Instrumentation **5** (07), P07003 (2010).
40. O. R. Hoidn and G. T. Seidler, Review of Scientific Instruments **86** (8), 086107 (2015).
41. M. Perez, J. Lipovetzky, M. S. Haro, I. Sidelnik, J. J. Blostein, F. A. Bessia and M. G. Berisso, Nuclear Instruments & Methods in Physics Research Section a-Accelerators Spectrometers Detectors and Associated Equipment **827**, 171-180 (2016).
42. W. M. Holden, O. R. Hoidn, A. S. Ditter, G. T. Seidler, J. Kas, J. L. Stein, B. M. Cossairt, S. A. Kozimor, J. Guo, Y. Ye, M. A. Marcus and S. Fakra, Review of Scientific Instruments **88** (7), 073904 (2017).
43. W. Fullagar, J. Uhlig, M. Walczak, S. Canton and V. Sundström, Review of Scientific Instruments **79** (10), 103302 (2008).
44. C. Y. Lee, IRE Transactions on Electronic Computers **EC-10** (3), 346-365 (1961).
45. W. M. Holden, G. T. Seidler and S. Cheah, The Journal of Physical Chemistry A **122** (23), 5153-5161 (2018).
46. D. H. Lumb, Nuclear Instruments and Methods in Physics Research Section A: Accelerators, Spectrometers, Detectors and Associated Equipment **290** (2-3), 559-564 (1990).

CHAPTER 7 SULFUR SPECIATION IN BIOCHARS BY VERY HIGH RESOLUTION BENCHTOP KA X-RAY EMISSION SPECTROSCOPY

Originally published as: Holden, W. M.; Seidler, G. T.; Cheah, S. Sulfur Speciation in Biochars by Very High Resolution Benchtop Kα X-Ray Emission Spectroscopy. *The Journal of Physical Chemistry A* 2018, 122 (23), 5153–5161. https://doi.org/10.1021/acs.jpca.8b02816.

This chapter represents a significant portion of this dissertation, and I led the effort for this work.

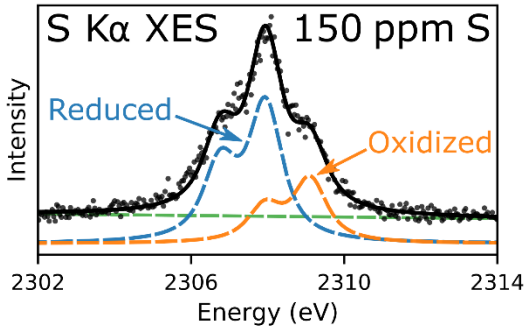

Figure 7.0: Table of contents graphic.

The analytical chemistry of sulfur-containing materials poses substantial technical challenges, especially due to the limitations of ^{33}S NMR and the time-intensive preparations required for wet-chemistry analyses. A number of prior studies have found that synchrotron-based x-ray absorption near edge structure (XANES) measurements can give detailed speciation of sulfur chemistry in such cases. However, due to the obvious access limitations, synchrotron XANES of sulfur cannot be part of routine analytical practice across the chemical sciences community. Here, in a study of the sulfur chemistry in biochars, we compare and contrast the chemical inferences available from synchrotron XANES with that given by benchtop, extremely high resolution wavelength-dispersive x-ray fluorescence (WD-XRF) spectroscopy, also often called x-ray emission spectroscopy (XES). While the XANES spectra have higher total information content, often giving differentiation between different moieties having the same oxidation state, the lower sensitivity of

the S Kα XES to coordination and local structure provides pragmatic benefit for the more limited goal of quantifying the S oxidation state distribution. Within that constrained metric, we find good agreement between the two methods. As the sulfur concentrations were as low as 150ppm, these measurements provide proof-of-principle for characterization of the sulfur chemistry of biochars and potential applications to other areas such as soils, batteries, catalysts, and fossil fuels and their combustion products.

7.1 INTRODUCTION

Recent interest in the use of lignocellulosic biomass as a source of renewable liquid fuels has spurred interest in studying one of the major byproducts, biochar, for its possible use in soil augmentation.[1-3] In this context, the S content in biochars may be used to increase the sulfur bioavailability in soils. However, a study of plant residues and corn stover biochar by Blum et al.[4] found that the speciation of sulfur added to soil, rather than simply the total sulfur concentration, played a major role in the final bioavailability of sulfur. For example, it was found that in early stages of incubation, more oxidized S species played an important role in sulfur mineralization.

From an analytical perspective, the question of S speciation in biochars shares strong commonalities with ongoing efforts to improve knowledge of the chemistry of S in other carbonaceous solids, e.g., soil, oil shale,[5] and coal, [6-7] which also have limited response to liquid-extraction methods. Nuclear magnetic resonance of sulfur is challenging mainly for two reasons: (1) the NMR-active nucleus, ^{33}S, is a quadrupole (spin 3/2) with broad lines, and (2) the natural abundance of ^{33}S is only 0.76 %, resulting in very low sensitivity of the S NMR method. Several traditional wet chemistry methods have been developed for analysis of sulfur in coal[8-9] but are time-consuming and the organic sulfur content has to be calculated as the difference between the total and the sum of pyrite and sulfate. The American Society for Testing and Materials (ASTM)

wet chemical method for determination of sulfate and pyrite forms of sulfur in coal[9] has been used to measure sulfur in biochar.[10] However, this method also has low sensitivity, with differing applicable ranges for pyrite (>1,000 ppm) and sulfate (>200 ppm).[9] Recently an electrothermal vaporization inductively coupled plasma optical emission spectrometry method was developed,[11] but it is not yet clear whether this method would work well for non-coal samples or samples with low total sulfur (< 600 ppm).

Given the above challenges, some studies have instead looked to x-ray absorption near edge structure (XANES) methods available at synchrotron light sources when seeking to better understand S in a wide range of matrices.[12-14] XANES at the K-edge (1*s* binding energy) of S gives a rich spectrum with features that can be used to fingerprint different oxidation states and S local moieties.[15] In the context of biochar, work by Cheah, et al.,[10] found XANES to be valuable for quantifying the relative abundance of sulfide, organosulfur, and sulfate in the same biochar samples that we study here.

While synchrotron XANES provides the fine detail needed for a robust discrimination of S local chemistry, the limited access of synchrotron x-ray facilities poses some barrier to progress, in addition to excluding their possible use for 'routine' analytical testing of large numbers of samples needed in both academic research and industrial process control applications. This raises the question of applying laboratory-based x-ray spectroscopy techniques having similar sensitivities but much higher access. While several groups are pursuing different modernizations of lab-based XANES,[16-22] the low photon energy of the S K-edge provides substantial challenges for efficient photon generation using conventional x-ray tubes. This has been discussed in Taguchi, et al.,[21] where the use of a multi-kW x-ray tube still resulted in a system that functioned only for transmission-mode studies, i.e., that required very concentrated samples.

Consequently, we move away from the question of absorption and instead discuss the merits of high-resolution studies of the resulting x-ray fluorescence; this method is far more amenable to benchtop development. High resolution x-ray fluorescence analysis, which in typical implementations is referred to as 'wavelength-dispersive x-ray fluorescence' (WD-XRF) analysis,[23] has a long history for use in fine determination of elemental composition.[24-25] That being said, there have been several WD-XRF studies of S oxidation state, exactly due to the access limitations of synchrotron XANES. For example there are reports of nonzero, but limited, sensitivity to S speciation using commercial WD-XRF instrumentation having ~4-eV or poorer energy resolution,[26-28] i.e., broader than the intrinsic broadening in S Kα spectra combined with the full energy shift upon going from oxidation state of 2- to 6+.

Such commercial systems have high access but would greatly benefit from improved energy resolution. In the synchrotron community, the term 'x-ray emission spectroscopy' (XES) is used when the energy resolution of WD-XRF becomes comparable to the intrinsic broadening from quantum-mechanical lifetime effects.[29-31] There is steadily increasing use of XES at synchrotron beamlines,[32-35] especially for applications in organometallic chemistry and catalysis.[36-39] However, the important issue here is benchtop, high-access use.

In this sense, four studies should be discussed. First, Li et al.,[40] achieved higher resolution S Kα XRF, very reasonably called XES, in the laboratory using a classic, commercial double flat-crystal spectrometer. Those authors were able to distinguish mixtures of reference compounds using a Kalman filtering algorithm, though this approach does not appear to have seen further development, possibly in part due to the inefficiency of the spectrometer optical design which required a very high powered x-ray source to obtain useful count rates on concentrated samples. Second, Petric and Kavčič[41] made use of a spectrometer based on a cylindrically-curved analyzer

to obtain sub-eV energy resolution with much improved efficiency for S Kα. This instrument was used both at a synchrotron light source and also with a focused incident proton beam and showed significant advantaged from the higher energy resolution, with a clear improvement in the information content of the spectra *vis a vis* the ability to fit the $K\alpha_1$ and $K\alpha_2$ contributions. An initial discussion of the benefits of such higher energy resolution for possible analytical applications is given in two prior studies.[41-42] Third, another proton-induced x-ray emission spectrometer, based on the von-Hamos geometry, was used by Tada et al.[43] to measure speciation of sulfur in activated carbon. Lastly, and of most relevance for the present study, Holden, et al.[44] presented the most promising benchtop approach to date for S Kα XES. The tiny spectrometer described in that work uses a low-powered conventional x-ray tube and a cylindrically-curved analyzer in a novel wavelength-dispersive optical configuration to obtain sub-eV energy resolution with nearly synchrotron-level count rates.

Here, we use exactly this new benchtop S Kα XES capability of Holden, et al.[44] to investigate the speciation of S in biochar samples that have previously been studied with S K-edge XANES.[10] Our study validates the accuracy and effectiveness of the new benchtop instrumentation and methods for characterization of S speciation. Several other outcomes are also discussed in detail, including a pragmatic perspective of the relative merits and potential systematic errors in XES and XANES linear-decomposition analysis, and a view to the future where the considerable limitations of ^{33}S NMR and alternative chemical extraction methods may be ameliorated with S XES for a wide range of sulfur-containing materials.

7.2 METHODS

The samples studied here are a subset of four samples from the S K-edge XANES study of Cheah, et al.[10], selected to encompass a wide range of relevant S chemistry in biochar. These

samples were chosen to span a large range in sulfur oxidation state and to push the limits of sensitivity of the benchtop instrument. The oak and corn stover derived biochars were produced at 500 and/or 600 °C under pyrolysis conditions, i.e., in nitrogen, in a 20.3-cm diameter pilot-scale entrained flow reactor at the National Renewable Energy Laboratory. These samples are labelled according to the biomass they originate from and the temperature in which they were produced, e.g. CS500 is corn stover derived biochar from pyrolysis at 500 °C. Additionally, a separate oak derived biochar was also produced at 850 °C using a two-stage pyrolysis-gasification process. Details of the biochar preparation process can be found in Cheah et al.[10]

For measurements in the laboratory XES spectrometer, biochar powder was mixed with hexagonal boron nitride (BN, which serves as a binder), in a 3:1 ratio, i.e., approximately 120 mg biochar : 40 mg BN. The mixture was lightly ground with a mortar and pestle, and then pressed into a 13-mm diameter pellet using a hydraulic press. The concentration of S in the biochar samples prior to dilution with the BN binder varied from 150-800 ppm.

S Kα XES measurements were performed using a recently reported laboratory S XES spectrometer. This extremely compact, benchtop instrument uses a 'dispersive refocusing Rowland' (DRR) geometry to remove sensitivity to the x-ray spot size on the sample.[44] All XES spectra were measured using an unfocused, commercial x-ray tube (model VF-50 with Pd anode, from Varex, Inc.) operating at 2 mA electron beam current and 25 kV accelerating potential, i.e., only 50 W total electron beam power. For S Kα, we use a cylindrical Si (111) analyzer at an average Bragg angle of 58.9°. The analyzed x-rays were measured using an energy-resolving x-ray camera, as described in Hoidn, et al.[45-46] Prior work with this spectrometer configuration demonstrates energy resolution of approximately 0.7eV.[44] All samples were measured in ~100

mTorr vacuum. The energy of the spectrometer was calibrated with reference to a sample of crystalline ZnS (MTI Corporation), which has an S $K\alpha_1$ emission at 2307.69 eV.[42]

The use of defocused incident radiation helps to reduce the potential for radiation damage. That being said, it is still important to compare the time-sequence of collected spectra during integration to look for evidence of systematic sample degradation. Only the Oak850 sample shows even weak evidence for radiation damage. In particular, there was a mild monotonic trend from 3% oxidized S in spectra collected near the beginning of integration to 8% oxidized sulfur in spectra collected near the end of integration. This is slightly outside of expected statistical errors, and has only a weak potential effect on our results, as discussed in Section 7.3, below.

While the shape of the S Kα doublet has been shown to have only modest dependence on oxidation state (discussed below), the dominant effect is instead that the doublet itself experiences an overall energy shift towards higher energy for increasingly positive oxidation state.[42] This fact permits the calculation of S speciation based on simple linear superposition fits using the combination of multiple Kα doublet line-shapes together with a linear background to allow for instrumental stray signal. This technique has been validated for mixtures of reference compounds by several studies,[41-42, 47] and has also been used for measurements of S in aerosols[47] and in biological tissues.[48]

The non-linear least-squares fitting Python package LMFIT[49] was used. Several variations in the fitting procedure were tested to investigate possible systematic errors of the technique. In the first method, the Kα doublet shape was modelled using two Voigt profiles, which were fixed based on the spectrum of the measured ZnS reference, i.e. fixed $K\alpha_{1,2}$ ratio, peak widths, and splitting. The energy position and relative amplitude of the two superposed fixed doublet line-shapes were allowed to vary, and the best fit was optimized by the least-squares algorithm of the

LMFIT package. In the second method, the biochar spectra were fit to a linear combination of two interpolation functions of the measured ZnS lineshape, which captures slight deviations of the lineshape from Voigt fits due to the instrumental response function.

Lastly, as shown in Mori et al.,[42] there is a ~30% variation in the $K\alpha_1/K\alpha_2$ integral intensity ratios for sulfur in different oxidation states. To investigate the dependence of the fitting procedure on these ratios, the Voigt profile width parameters were kept fixed, while the peak ratios were varied among all combinations in the range 1.7-2.3. In all cases, the speciation is then calculated based on the relative integrated intensities of the doublet line-shapes of each sulfur species. The uncertainty introduced by varying the peak ratios varies from ±1% in Oak850 to about ±4% in CS500. It is emphasized that this uncertainty is a systematic error and could be improved by further study of sulfur peak shapes in organic compounds similar to biochar. The statistical error of the technique is smaller, on the order of 1%, based on the estimation of the standard error from the estimated covariance matrix. We note that deep shell XES, such as studied here, does not suffer from self-absorption effects because the fluorescence photon energy is below the relevant binding energy.

We also report a reanalysis of the S K-edge XANES measurements from Cheah, et al.[10] The XANES fitting was performed using SIXPACK,[50] which builds on the iFEFFIT engine.[51] The measured spectra are fit to a linear combination of reference compounds: gypsum ($CaSO_4 \cdot 2H_2O$) representing sulfate, dibenzothiophene representing organic sulfur, and pyrite (FeS_2) representing sulfidic sulfur. Compared to analysis in the earlier report, we make one change in the fit procedure. In the earlier publication, linear combination fitting of S XANES was conducted using the option of restricting the sum of all components to unity. However, we find that omitting this constraint better adapts to the realistic errors and differences between the normalization of the reference

standards and samples. Normalization of S XANES spectra can be challenging due to the self-absorption problem, particularly for standard compounds that are in pure, bulk forms. In addition, two of the reference spectra used came from the public ID-21 database,[52] where slightly different sample preparation or normalization criteria could have been used relative to those for our samples. Since we do not restrict the sum of all components to unity during the current least-squares fitting, the contribution of each component is calculated manually by dividing the fraction of each component by the actual sum of all components. With this method, the goodness of fit parameters (R and reduced χ^2) are smaller and visual comparison of the fit to the data show better agreement than when the sum of all components is restricted to unity. Numerically, all new results differ from those reported earlier by less than 16 % (most are within 10%).

7.3 Results and Discussion

We proceed in three steps in this section. First, we present and discuss the S Kα XES results. Second, we present and discuss the S K-edge XANES results and their re-analysis after Cheah, et al.[10] Finally we compare and contrast the XES and XANES results, both from the standpoint of their agreement in the present study and also about how this informs possible future developments.

The S Kα XES spectra of the four biochar samples and the ZnS reference are shown in Fig. 7.1. The integration time for the two extremes of S concentration were 50 minutes for the CS500 sample (800 ppm S) and 6 hours for the Oak600 sample (150 ppm S). Such measurement times are of course fairly common across other benchtop analytical methods, broadly defined. For comparison, after necessary delays for general user application and scheduling, the synchrotron XANES data collection was 24 minutes for the 800 ppm CS500 sample and 144 minutes for the 150 ppm Oak600 sample. As seen in Figure 7.1, a pure component such as ZnS has a doublet in

its emission spectrum with two components resulting from transitions from the spin-orbit split $2p_{1/2}$ and $2p_{3/2}$ states to the unoccupied 1*s* hole. These two overlapping fluorescence lines are referred to as $K\alpha_1$ (~2307.7 eV) and $K\alpha_2$ (~2306.5 eV) respectively. The measured spectra for biochar in Fig. 7.1 clearly show an admixture of $K\alpha_{1,2}$ doublets with different central energies, indicating some range of oxidation states for S in the biochar samples.

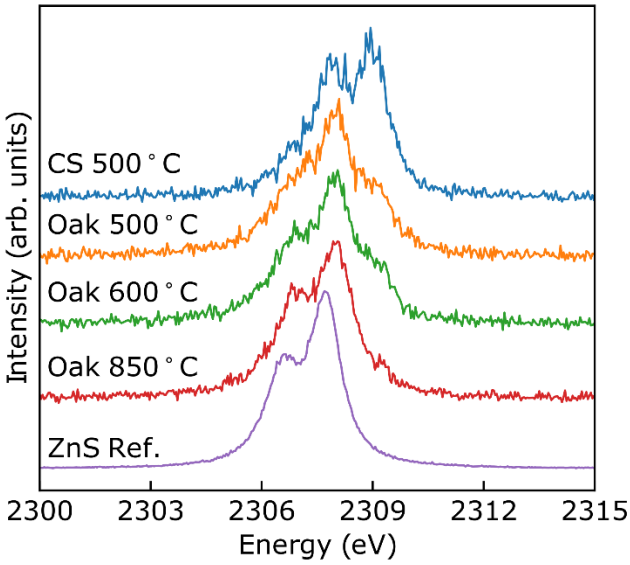

Figure 7.1: S Kα XES spectrum obtained from four different biochar samples processed under different conditions. The decrease of the shoulder near 2309.15 eV with increasing temperature shows a decrease in the amount of oxidized sulfur species.

Following the first technique described in detail in the Methods section, i.e., a fixed $K\alpha_1/K\alpha_2$ ratio and linewidths set by the ZnS reference material, fits to a reduced and an oxidized component are shown in Fig. 7.2. The XES spectra are fit well using two such Kα doublet components representing two oxidation states, one with $K\alpha_1$ near 2309.15 eV representing sulfate and another with $K\alpha_1$ near 2307.97 which is lower in oxidation state. The oxidation state distributions determined from these fits are presented in the 'Laboratory XES' column of Table 1.

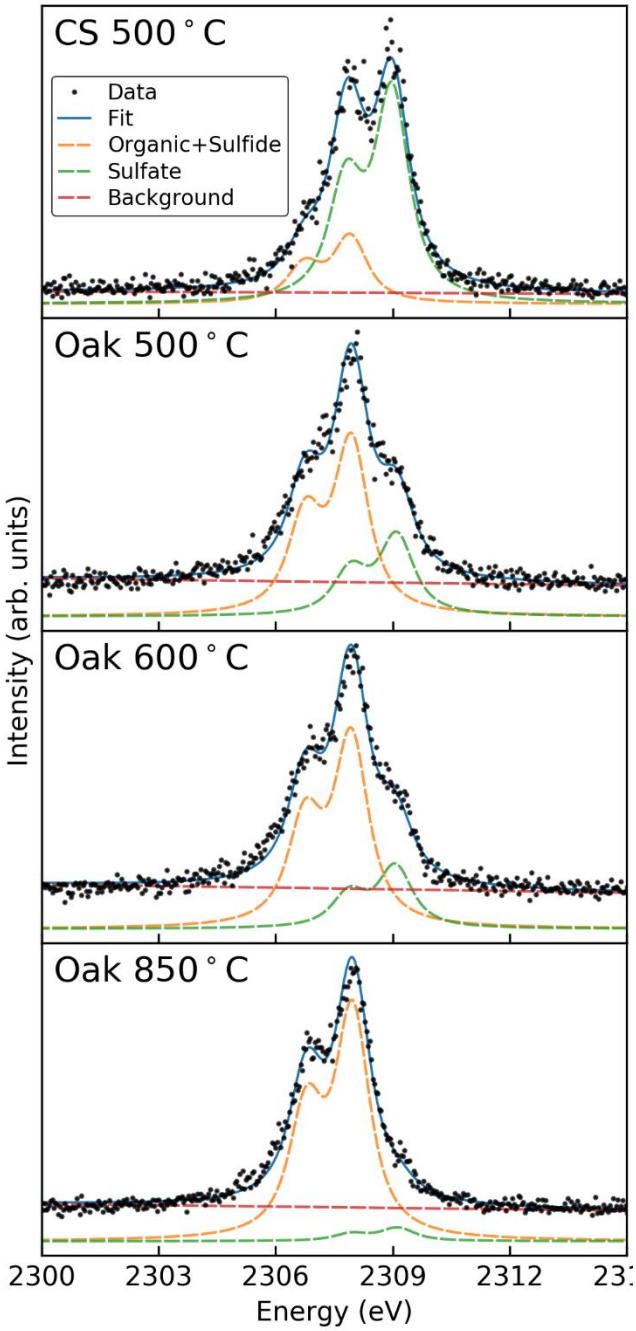

Figure 7.2: Linear combination fits to S Kα XES spectra used to determine speciation for the biochar samples. The lower energy doublet represents sulfur in an organic + sulfidic oxidation state, while the higher energy doublet represents sulfate.

Table 7.1: Comparison of sulfur speciation determined by laboratory S Kα XES, S K-edge XANES performed at a synchrotron facility, and sulfate determination from ASTM method D2492-02. For XANES of sample CS500, to address the inhomogeneity of the biochar, four samples were measured from different portions taken from the sample batch, and the results are reported as ranges. For the Laboratory XES, the reduced-chi-squared metric is reported to indicate the goodness-of-fit of the linear combination fitting results. For the Synchrotron XANES, the commonly used goodness-of-fit "R-Factor," defined as R = Sum(|data - fit|^2) / Sum(|data|^2) is reported. Errors for both XES and XANES are discussed in detail in the text.

Method	Laboratory XES			Synchrotron XANES				D2492-02
Sample	Sulfate	Organic + Sulfide	Reduced-χ^2	Sulfate	Organosulfur	Sulfide	R-Factor	Sulfate
CS 500°C	76	24	1.16	55-77	23-34	0-11	0.0038	63
Oak 500°C	32	68	1.25	40	52	8	0.0084	
Oak 600°C	24	76	1.50	20	52	28	0.018	
Oak 850°C	5	95	1.20	1	87	12	0.031	

The lower oxidation state component of the fitting procedure may contain separate organic and sulfidic contributions. Further work is needed to determine if the distinction between organic and sulfidic species can be made via S Kα spectroscopy by itself or whether this requires augmentation by the more chemically-sensitive Kβ spectrum. Laboratory measurements of S Kβ fluorescence as a means to determine speciation of S in coal were made by Martins and Urch,[53] and have also been considered more broadly by Perino et al.,[54] though the ~25× weaker Kβ signal would be difficult with the present apparatus for samples with much lower S concentration than coal, such as the biochars studied here. That being said, in the present study we focus on the much stronger Kα signal, with the idea of providing proof-of-principle for a wide range of applications including those where only the distinction between highly oxidized and non-oxidized sulfur species is needed and not finer distinction such as between organosulfur and sulfides.

To investigate possible uncertainties of the fitting procedure, other constrained fit combinations were explored as described in the Methods. If the fitting to reduced and oxidized model spectra is done using the second technique in the Methods, i.e., using two shifted

interpolation functions of the ZnS lineshape as opposed to Voigt profiles based on the ZnS lineshape, the speciation of all samples is shifted by 1% in the oxidized direction. To account for possible systematic error resulting from changes in peak shape with oxidation, peak ratios of the synthetic $K\alpha_{1,2}$ doublet were varied over the range of 1.7-2.3 seen in Mori, et al.[42], which resulted in shifts in speciation of up to ±4%. As a conservative estimate, allowing that the errors may be correlated, the combined statistical and systematic errors therefore result in a ~5% error for the determination of oxidation state by S Kα XES.

To summarize the XES results (taken in isolation from the other conclusions in Table 1), we find that the S Kα XES provides excellent sensitivity to S speciation fractions in the biochars, even for concentrations as low as 150 ppm. The resulting spectra are easily analyzed as a linear combination of shifted lineshapes, with ~5% resulting combined uncertainty in the speciation from statistical and systematic effects. Sample preparation is simple, and there are no 'self-absorption' effects in XES – the raw spectra suffices for analysis with no further processing except for subtraction of a linear background.

We now move on to the analysis of the XANES results from Cheah, et al. Those XANES spectra and associated fits are shown in Fig. 7.3. In comparison to the Kα XES spectra, the XANES spectra have a more complicated structure, containing far more information about the coordination chemistry and other local atomic structure near the S atoms. Consequently, in many cases XANES is used for fingerprinting purposes, i.e., to determine the relative composition of different coordinations, oxidation states, and other aspects of the local environment. As described in the Methods section, gypsum, pyrite, and dibenzothiophene were used to determine the contributions from sulfate, sulfide, and organosulfur. The results of the fits of the XANES structure to these reference standards, summarized as sulfide, organosulfur, and sulfate, are presented in the

‘Synchrotron XANES’ columns in Table 1. For the CS500 sample, the XANES results are reported as the ranges of values measured on four different sub-portions of the CS500 batch from the reactor, showing fluctuations due to inhomogeneity of the produced biochar. The XES result reported for CS500 was measured on one of those sub-portions. For the Oak samples, the same portions were measured for both the laboratory XES and synchrotron XANES results.

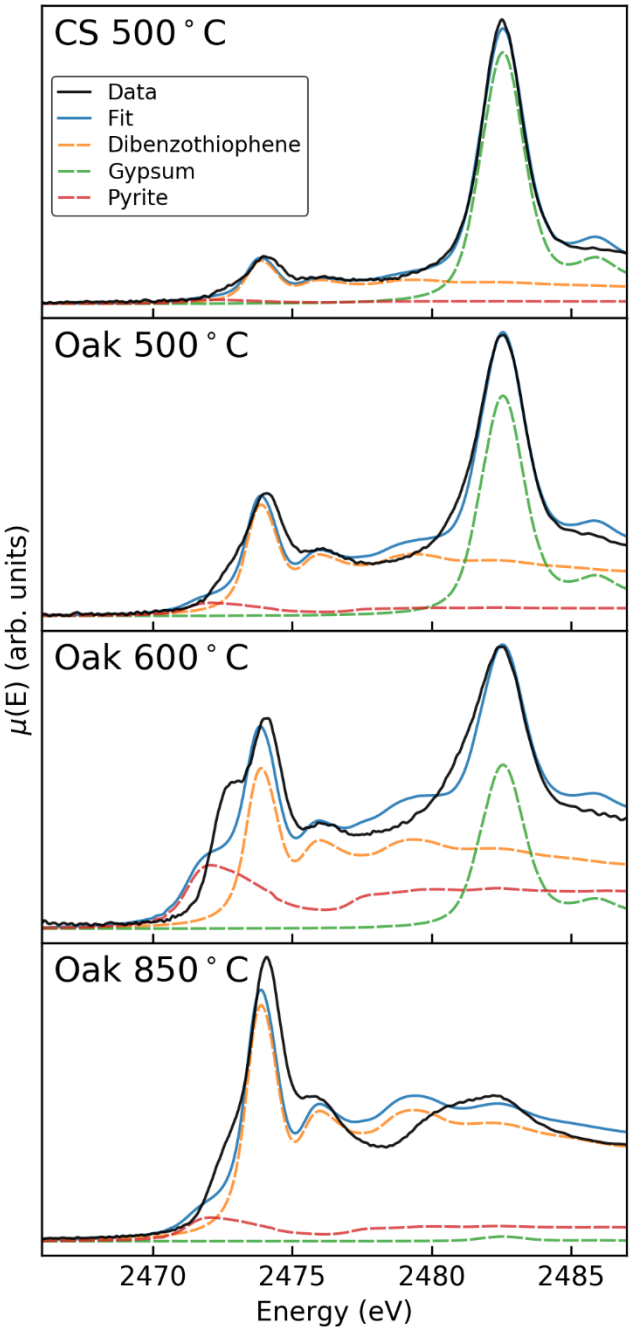

Figure 7.3: S K-edge XANES spectra from Cheah et al.,[10] showing the linear combination fitting to reference standards representing sulfidic (pyrite), organic (dibenzothiophene), and sulfate (gypsum) sulfur. For the CS 500°C sample, one of the four measured sub-portions is shown, having 3% sulfidic, 30% organic, and 67% sulfate components.

Before further discussion however, some discussion of the methods and results for the differentiation of the sulfide from the organosulfur is appropriate. Five different types of organosulfur standards were tested in initial fitting. Ultimately dibenzothiophene, consisting of a single sulfur atom in a polycyclic structure, was found to represent the structure of organosulfur in biochar much better than S in a small molecule such as cysteine. However, there is some interesting information and differentiation among the different samples.

The oak and corn stover samples pyrolized at 500 °C show generally good fits to the three reference standards with dominant contributions easily attributable to sulfate (gypsum) and a more reduced fraction (dibenzothiophene). The Oak 600 °C sample sees significant disagreement between the observed first, large shoulder at the edge and fit contribution from pyrite; this peak can be better fitted with the introduction of an organosulfide, dibenzyldisulfide (shown in Fig. S1 in the SI of Cheah et al.[10]). Chemically, the appearance of the dibenzyldisulfide at 600 °C is consistent with a potential mechanism where the inorganic sulfide is converted to organosulfide. However, quantitatively, the introduction of the dibenzyldisulfide only changed the inferred fraction of sulfate by 3% (sulfate content 23%, inorganic sulfide 1%, total organosulfur 76%).

The Oak 850 °C sample shows edge energy that is slightly higher than that of dibenzothiophene, and closer to that of thianthrene (2474.38 eV, see SI section of Cheah et al.[10]), which has two sulfurs per molecule and is thus a more sulfur-enriched heterocyclic chemical compound than dibenzothiophene. However, including thianthrene in the fit only change the inferred organosulfur fraction by 4%. The appearance of a more thianthrene-like structure is consistent with the hypothesis of the biochar reacting with gas phase sulfur species resulting in local enrichment of the sulfur. The qualitative information from XANES illustrates the power and information content of XANES to differentiate chemical moieties even within a single oxidation

state. With more samples, e.g., biochar produced from different temperatures and residence times, the changes can be tracked and used for determination of the chemical reaction mechanism. However, for the more limited present purpose of determining how the different fractions of sulfur change with temperature of biochar preparation, and especially in the context of comparison to XES, it is simpler to be consistent in the fitting and thus only dibenzothiophene was used to fit the organic fraction in all four of the biochar samples.

In summary, for the Oak 850 C biochar, there is reasonable good fit of the XANES from 2466 to 2475 eV. However, whether with the inclusion of dibenzothiophene or thianthrene, there is poor agreement between experimental data and the post-edge features from approximately 2475 to 2482 eV. There are two likely explanations for the poor fit in this energy range. One is that this post-edge region in XANES is typically associated with multiple scattering effects due to the substantial range of the lower-energy photoelectron in this near-edge regime.[15, 55] Even if the molecular species is perfectly identified, the XANES spectrum for the pure, crystalline reference material does not represent the intermediate range structure of isolated molecules adsorbed under multiple coordinations on a post-pyrolysis carbonaceous soot. Such carbonaceous soot tends to grow as temperature of pyrolysis and gasification increases. It is therefore not surprising that the fit in the multiple scattering area is particularly poor for the 850 °C biochar. A second potential explanation is that there is additional organosulfone species which typically have white lines at approximately 2480 eV, higher than the white line of other organosulfurs, which are generally in the vicinity of 2473 eV. The original study of Cheah, et al., did measure a single sulfone reference compound, dibenzothiophene sulfone, which did not improve the fit though there are many more potential sulfone structures that may be relevant but were not measured.

It is also worth asking about the overall reliability of linear combination fitting (LCF) for XANES data, given a broader range of common systematic errors, such as from self-absorption effects. This has been studied by Prietzel, et al, for the problem of S K-edge XANES.[14] They found, for mixtures of reference compounds, that the fraction of different S species as calculated by LCF differed on average by ±5-10% from the real percentage of the mixtures, when fit using suitably diluted reference compounds to avoid self-absorption errors.

To summarize the above discussion of the detailed of XANES fitting to a superposition of reference standards: as with many other cases where XANES decomposition is regularly used, the overall char structure is poorly defined and this complicates the comparison to reference standards and the assessment of possible errors. This is due to the significant photoelectron range and high multiple scattering effects for photoelectrons in the near-edge region, where extrinsic losses from, e.g., plasmon creation, are not relevant. Such comparisons can be further complicated by self-absorption effects and other errors that can skew the relative amplitudes of pre-edge features relative to atomic backgrounds. We emphasize these issues not because they are new observations, but instead by means of contrast with XES.

Moving again to Table 1, the comparison across different methods can now be discussed. To begin, the CS500 sample is also the only sample that has high enough sulfur concentration for sulfate measurement using ASTM D2492-02, which yields a sulfate concentration of 63% for this sample. The XANES results reported for the CS500 sample represent the range of results measured on four different sub-portions, showing variability in the homogeneity of the biochar (55-77% sulfate). The XES and the XANES result agree with the ASTM result within this variability, which dominates the small expected error of the ASTM result. For the other samples with lower concentrations, the speciation fractions inferred from XES and synchrotron XANES

compare well, with deviations between the two methods on the scale of the expected mutual error budget. As mentioned in the methods section, there was weak evidence for beam damage in the Oak850 sample. That may account for some of the modest over-estimate by XES of the oxidized fraction, but the difference is still essentially within statistical error.

Hence, the central result of this paper is that our work strongly supports a future analytical role for benchtop S Kα XES for determination of oxidation state distributions. With that established, it is interesting to consider three observations that could guide future work. First, as we have motivated above, there is an interesting, broad complementarity between S K-edge XANES and S Kα XES. Whereas XANES has very high information content allowing for chemical analysis well beyond oxidation state distributions, its great sensitivity to the exact S moiety, including possible defective structures, places high priority on the correct selection of reference standards in terms of both their chemistry and their short-range and intermediate-range order. On the other hand, nonresonant S Kα XES is a purely deep core process due to the absence of interference effects involving the primary photoelectron. By having such a strongly intra-atomic character, Kα XES is sensitive to changes of 1s screening by valence electrons (i.e., changing oxidation state) but has only much weaker signatures of differing covalency or other inter-atomic effects. This simplifies the problem of oxidation-state analysis, but comes at the cost of less total information content and final scientific scope of application.

Second, this raises the questions of whether one might bridge the gap between the capabilities and access modes of sulfur K-edge XANES and XES. Considerable recent effort has gone into the measurement and interpretation of so-called valence-to-core (VTC) XES.[31, 56-58] The VTC XES occurs when bonding electrons undergo a radiative transition to fill the deep, photoexcited core hole. This gives a natural complement to XANES, wherein the VTC XES

reflects the occupied local density of states near the Fermi level while XANES of course interrogates only the unoccupied states. For sulfur, the VTC is folded within the Kβ spectrum because S 3p electrons are valence-level and directly involved in chemical bonding. As mentioned earlier, several studies of more sulfur-rich materials have found that the Kβ region is directly useful for more detailed speciation beyond oxidation state.[53-54, 59-61] While the very low concentration of the present samples prohibited S Kβ XES with our low powered (50 W) x-ray source, this could be accessed in the future with upgrades to the benchtop spectrometer design (higher power tube, larger solid-angle optics, etc.) that would also accelerate the Kα measurements on dilute materials. With the current configuration, the instrument has similar efficiency and resolution at S Kα and Kβ. Since the Kβ fluorescence is approximately 20× weaker than the Kα, we estimate a lower concentration limit around 3000ppm S to measure useful Kβ spectra in samples similar to the biochars measured here.

Third, there is the question of the broader analytical application of S Kα XES to other systems. Some aspects of this have been discussed in Mori et al.[42] and Petric and Kavčič[41], but it merits a more complete consideration here where a new analytical application has in fact been demonstrated. The limitations of ^{33}S NMR, chemical extraction methods, and the high surface sensitivity and vacuum requirements of x-ray photoelectron spectroscopy each complicate the routine analysis of sulfur in many materials. This includes the characterization of sulfur speciation in soils and soil augmenters, air-borne particulate matter, vulcanized rubber materials, and fossil fuel solids and their combustion products. The technical range of this approach would also clearly be expanded by the integration of such spectrometers with controlled-atmosphere glove boxes so as to enable the easy characterization of air-sensitive chemical systems, such as for Li-S battery research or catalyst development. In addition, if care was taken to develop sample cells having

only thin, weakly-absorbing mylar or polyimide windows, then liquid samples become viable, allowing measurements of sulfur compounds in aquatic systems,[62] contaminated water, sewage sludge,[63] and fossil fuel liquids.

7.4 CONCLUSIONS

Measurements of S Kα x-ray emission spectra from low-concentration biochar samples have been performed using a laboratory-based x-ray emission spectrometer having better than 1-eV resolution. Oxidation state distributions for S are determined by linear-combination fitting to two shifted $K\alpha_{1,2}$ doublet shapes, and the results agree within errors with those determined by a synchrotron XANES study at the S K-edge. Both XES and XANES show that as the temperature of biomass pyrolysis and/or gasification increases, the biochar produced from oak contains increasing amount of organosulfur at the expense of inorganic sulfur. Although the XES spectra contains less information than XANES, the relative simplicity of changes in the XES spectra with changing oxidation state suggests that desktop XES could be an efficient, robust, and economical technique for limited questions of oxidation state distribution.

The ability to perform these measurements in a laboratory instrument, in contrast to a synchrotron facility, demonstrates a new direction for analytical chemistry of sulfur-containing materials, where many inquiries are presently constrained by the limitations of ^{33}S NMR and of chemical extraction methods. The benchtop XES measurement requires only small amounts of sample and involves minimal sample preparation. Consequently, this method is readily applicable to many industrial, environmental and organic samples. We believe that benchtop S Kα XES therefore holds high potential for a wide range of future efforts.

7.5 Acknowledgements

The work at the University of Washington was supported by a subcontract from the Heavy Element Chemistry Program at LANL that is funded by the Division of Chemical Sciences, Geosciences, and Biosciences, Office of Basic Energy Sciences, U.S. Department of Energy and also by the Joint Plasma Physics Program of the National Science Foundation and the Department of Energy under grant DE-SC0016251. The work conducted at NREL was supported by the U.S. Department of Energy, Bioenergy Technologies Office (BETO), under Contract No. DE-AC36-08GO28308. We thank Calvin Feik and Shealyn Malone for providing and riffling the biochars.

7.6 References

1. Lehmann, J.; Rillig, M. C.; Thies, J.; Masiello, C. A.; Hockaday, W. C.; Crowley, D., Biochar effects on soil biota – A review. *Soil Biol. Biochem.* **2011,** *43* (9), 1812–1836.
2. Biederman, L. A.; Harpole, W. S., Biochar and its effects on plant productivity and nutrient cycling: a meta-analysis. *GCB Bioenergy* **2013,** *5* (2), 202–214.
3. Kuppusamy, S.; Thavamani, P.; Megharaj, M.; Venkateswarlu, K.; Naidu, R., Agronomic and remedial benefits and risks of applying biochar to soil: Current knowledge and future research directions. *Environment International* **2016,** *87*, 1–12.
4. Blum, S. C.; Lehmann, J.; Solomon, D.; Caires, E. F.; Alleoni, L. R. F., Sulfur forms in organic substrates affecting S mineralization in soil. *Geoderma* **2013,** *200*, 156-164.
5. Smith, J. W.; Young, N. B.; Lawlor, D. L., Direct determination of sulfur forms in Green River oil shale. *Anal. Chem.* **1964,** *36* (3), 618–622.
6. Gryglewicz, G.; Jasieńko, S., The behaviour of sulphur forms during pyrolysis of low-rank coal. *Fuel* **1992,** *71* (11), 1225–1229.
7. Telfer, M. A.; Zhang, D. K., Investigation of sulfur retention and the effect of inorganic matter during pyrolysis of South Australian low-rank coals. *Energy & Fuels* **1998,** *12* (6), 1135–1141.
8. Coal -- Determination of forms of sulfur. International Organization for Standardization: 1996; Vol. ISO 157:1996, p 15.
9. Standard test method for forms of sulfur in coal. ASTM International: Reapproved 2012; Vol. D2492–02, p 5.
10. Cheah, S.; Malone, S. C.; Feik, C. J., Speciation of sulfur in biochar produced from pyrolysis and gasification of oak and corn stover. *Environ. Sci. Technol.* **2014,** *48* (15), 8474-8480.
11. Bauer, D.; Vogt, T.; Klinger, M.; Masset, P. J.; Otto, M., Direct determination of sulfur species in coals from the Argonne Premium Sample Program by solid sampling

electrothermal vaporization inductively coupled plasma optical emission spectrometry. *Anal. Chem.* **2014,** *86* (20), 10380–10388.
12. George, G. N.; Gorbaty, M. L., Sulfur K-edge x-ray absorption spectroscopy of petroleum asphaltenes and model compounds. *J. Am. Chem. Soc.* **1989,** *111* (9), 3182–3186.
13. Kelly, S. D.; Hesterberg, D.; Ravel, B., Analysis of soils and minerals using x-ray absorption spectroscopy. In *Methods of Soil Analysis. Part 5. Mineralogical Methods*, Ulery, A. L.; Drees, L. R., Eds. Soil Science Society of America: Madison, WI, USA, 2008; pp 387–464.
14. Prietzel, J.; Botzaki, A.; Tyufekchieva, N.; Brettholle, M.; Thieme, J.; Klysubun, W., Sulfur speciation in soil by S K-edge XANES spectroscopy: comparison of spectral deconvolution and linear combination fitting. *Environ. Sci. Technol.* **2011,** *45* (7), 2878–2886.
15. Bunker, G., *Introduction to XAFS*. Cambridge University Press: 2010.
16. Legall, H.; Stiel, H.; Schnürer, M.; Pagels, M.; Kanngießer, B.; Müller, M.; Beckhoff, B.; Grigorieva, I.; Antonov, A.; Arkadiev, V., et al., An efficient X-ray spectrometer based on thin mosaic crystal films and its application in various fields of X-ray spectroscopy. *J. Appl. Crystallogr.* **2009,** *42* (4), 572-579.
17. Németh, Z.; Szlachetko, J.; Bajnóczi, É. G.; Vankó, G., Laboratory von Hámos X-ray spectroscopy for routine sample characterization. *Rev. Sci. Instrum.* **2016,** *87* (10), 103105.
18. Seidler, G. T.; Mortensen, D. R.; Remesnik, A. J.; Pacold, J. I.; Ball, N. A.; Barry, N.; Styczinski, M.; Hoidn, O. R., A laboratory-based hard x-ray monochromator for high-resolution x-ray emission spectroscopy and x-ray absorption near edge structure measurements. *Rev. Sci. Instrum.* **2014,** *85* (11), 113906.
19. Szlachetko, M.; Berset, M.; Dousse, J. C.; Hoszowska, J.; Szlachetko, J., High-resolution Laue-type DuMond curved crystal spectrometer. *Rev. Sci. Instrum.* **2013,** *84* (9), 093104.
20. Taguchi, T.; Harada, J.; Kiku, A.; Tohji, K.; Shinoda, K., Development of a new in-laboratory XAFS apparatus based on new concept. *J. Synchrotron Rad.* **2001,** *8* (2), 363-365.
21. Taguchi, T.; Shinoda, K.; Tohji, K., Customization of an inhouse XAFS spectrometer for sulfur measurement. *Phys. Scr.* **2005**, 1017.
22. Yuryev, Y. N.; Lee, H.-J.; Park, H.-M.; Cho, Y.-K.; Lee, M.-K.; Pogrebitsky, K. J., Variable Rowland radius laboratory vacuum surface-sensitive x-ray absorption fine structure spectrometer. *Rev. Sci. Instrum.* **2007,** *78* (2), 025108.
23. West, M.; Ellis, A. T.; Streli, C.; Vanhoof, C.; Wobrauschek, P., 2017 atomic spectrometry update – a review of advances in X-ray fluorescence spectrometry and its special applications. *J. Anal. At. Spectrom.* **2017,** *32* (9), 1629-1649.
24. Jenkins, R.; Gould, R. W.; Gedcke, D., *Quantitative X-ray Spectrometry*. M. Dekker: 1995.
25. Willis, J. P.; Feather, C. E.; Turner, K., *Guidelines for XRF Analysis*. James Willis Consultants: 2014.
26. Uhlig, S.; Mockel, R.; Plessow, A., Quantitative analysis of sulphides and sulphates by WD-XRF: Capability and constraints. *X-Ray Spectrom.* **2016,** *45* (3), 133-137.
27. Chubarov, V.; Amosova, A.; Finkelshtein, A., X-ray fluorescence determination of sulfur chemical state in sulfide ores. *X-Ray Spectrom.* **2016,** *45* (6), 352-356.
28. Pinkerton, A.; Norrish, K.; Randall, P. J., Determination of forms of sulphur in plant material by x-ray fluorescence spectrometry. *X-Ray Spectrom.* **1990,** *19* (2), 63-65.

29. Bergmann, U.; Glatzel, P., X-ray emission spectroscopy. *Photosynth. Res.* **2009,** *102* (2-3), 255-266.
30. Groot, F. d.; Kotani, A., *Core level spectroscopy of solids*. CRC Press: Boca Raton, 2008.
31. Glatzel, P.; Bergmann, U., High resolution 1s core hole X-ray spectroscopy in 3d transition metal complexes - electronic and structural information. *Coord. Chem. Rev.* **2005,** *249* (1-2), 65-95.
32. Kleymenov, E.; van Bokhoven, J. A.; David, C.; Glatzel, P.; Janousch, M.; Alonso-Mori, R.; Studer, M.; Willimann, M.; Bergamaschi, A.; Henrich, B., et al., Five-element Johann-type x-ray emission spectrometer with a single-photon-counting pixel detector. *Rev. Sci. Instrum.* **2011,** *82* (6), 065107.
33. Sokaras, D.; Weng, T. C.; Nordlund, D.; Alonso-Mori, R.; Velikov, P.; Wenger, D.; Garachtchenko, A.; George, M.; Borzenets, V.; Johnson, B., et al., A seven-crystal Johann-type hard x-ray spectrometer at the Stanford Synchrotron Radiation Lightsource. *Rev. Sci. Instrum.* **2013,** *84* (5), 053102.
34. Alonso-Mori, R.; Kern, J.; Gildea, R. J.; Sokaras, D.; Weng, T. C.; Lassalle-Kaiser, B.; Tran, R.; Hattne, J.; Laksmono, H.; Hellmich, J., et al., Energy-dispersive X-ray emission spectroscopy using an X-ray free-electron laser in a shot-by-shot mode. *Proc. Natl. Acad. Sci. U.S.A.* **2012,** *109* (47), 19103-19107.
35. Kavčič, M.; Budnar, M.; Muhleisen, A.; Gasser, F.; Zitnik, M.; Bucar, K.; Bohinc, R., Design and performance of a versatile curved-crystal spectrometer for high-resolution spectroscopy in the tender x-ray range. *Rev. Sci. Instrum.* **2012,** *83* (3), 033113.
36. Pollock, C. J.; DeBeer, S., Insights into the geometric and electronic structure of transition metal centers from valence-to-core x-ray emission spectroscopy. *Acc. Chem. Res.* **2015,** *48* (11), 2967-2975.
37. Kowalska, J.; DeBeer, S., The role of X-ray spectroscopy in understanding the geometric and electronic structure of nitrogenase. *Biochim. Biophys. Acta, Mol. Cell Res.* **2015,** *1853* (6), 1406-1415.
38. Delgado-Jaime, M. U.; DeBeer , S.; Bauer, M., Valence-to-core x-ray emission spectroscopy of iron-carbonyl complexes: implications for the examination of catalytic intermediates. *Chem. Eur. J.* **2013,** *19* (47), 15888-15897.
39. Lancaster, K. M.; Roemelt, M.; Ettenhuber, P.; Hu, Y. L.; Ribbe, M. W.; Neese, F.; Bergmann, U.; DeBeer, S., X-ray emission spectroscopy evidences a central carbon in the nitrogenase iron-molybdenum cofactor. *Science* **2011,** *334* (6058), 974-977.
40. Li, Z. L.; Yu, R. Q.; Shi, L. M.; Jun, X.; Zhang, M.; Wang, Q. G., Valence-state speciation of sulfur by x-ray fluorescence spectometry and Kalman filtering. *Anal. Chim. Acta* **1991,** *248* (1), 257-261.
41. Petric, M.; Kavčič, M., Chemical speciation via X-ray emission spectroscopy in the tender X-ray range. *J. Anal. At. Spectrom.* **2016,** *31* (2), 450-457.
42. Mori, R. A.; Paris, E.; Giuli, G.; Eeckhout, S. G.; Kavčič, M.; Zitnik, M.; Bucar, K.; Pettersson, L. G. M.; Glatzel, P., Electronic structure of sulfur studied by x-ray absorption and emission spectroscopy. *Anal. Chem.* **2009,** *81* (15), 6516-6525.
43. Tada, T.; Fukuda, H.; Hasegawa, J.; Oguri, Y.; Tsuji, M., Chemical speciation of sulfur in activated carbon by wavelength-dispersive PIXE technique. *X-Ray Spectrom.* **2009,** *38* (3), 239-243.
44. Holden, W. M.; Hoidn, O. R.; Ditter, A. S.; Seidler, G. T.; Kas, J.; Stein, J. L.; Cossairt, B. M.; Kozimor, S. A.; Guo, J.; Ye, Y., et al., A compact dispersive refocusing Rowland circle

X-ray emission spectrometer for laboratory, synchrotron, and XFEL applications. *Rev. Sci. Instrum.* **2017,** *88* (7), 073904.
45. Hoidn, O. R.; Seidler, G. T., Note: A disposable x-ray camera based on mass produced complementary metal-oxide-semiconductor sensors and single-board computers. *Rev. Sci. Instrum.* **2015,** *86* (8), 086107.
46. Holden, W. M.; Hoidn, O. R.; Seidler, G. T., A color x-ray camera for 2 – 6 keV using a back-illuminated mass-produced CMOS sensor. *Rev. Sci. Instrum.* **2018,** *In preparation*.
47. Kavčič, M.; Karydas, A. G.; Zarkadas, C., Chemical state analysis of sulfur in samples of environmental interest using high resolution measurement of K alpha diagram line. *Nucl. Instrum. Methods Phys. Res., Sect. B* **2004,** *222* (3-4), 601-608.
48. Kavčič, M.; Petric, M.; Vogel-Mikuš, K., Chemical speciation using high energy resolution PIXE spectroscopy in the tender X-ray range. *Nucl. Instrum. Methods Phys. Res., Sect. B* **2018,** *417*, 65-69.
49. Newville, M.; Stensitzki, T.; Allen, D. B.; Ingargiola, A., LMFIT: Non-linear least-square minimization and curve-fitting for Python. **2014**.
50. Webb, S. M., SIXpack: a graphical user interface for XAS analysis using IFEFFIT. *Phys. Scr.* **2005,** *T115*, 1011–1014.
51. Newville, M., IFEFFIT: interactive XAFS analysis and FEFF fitting. *Journal of Synchrotron Radiation* **2001,** *8*, 322–324.
52. ID21 Sulfur XANES spectra database. European Synchrotron Radiation Facility: http://www.esrf.eu/UsersAndScience/Experiments/Imaging/ID21/php, 2013.
53. Martins, E.; Urch, D. S., Progress towards an x-ray emission method for the speciation of sulphur in coal using S Kβ emission. *Anal. Chim. Acta* **1994,** *286* (3), 411–421.
54. Perino, E.; Deluigi, M. a. T.; Olsina, R.; Riveros, J. A., Determination of oxidation states of aluminium, silicon and sulfur. *X-Ray Spectrom.* **2002,** *31* (2), 115-119.
55. Rehr, J. J.; Albers, R. C., Theoretical approaches to x-ray absorption fine structure. *Rev. Mod. Phys.* **2000,** *72* (3), 621-654.
56. Petric, M.; Bohinc, R.; Bučar, K.; Nowak, S. H.; Žitnik, M.; Kavčič, M., Electronic structure of third-row elements in different local symmetries studied by valence-to-core x-ray emission spectroscopy. *Inorg. Chem.* **2016,** *55* (11), 5328-5336.
57. Lee, N.; Petrenko, T.; Bergmann, U.; Neese, F.; DeBeer, S., Probing valence orbital composition with iron Kβ x-ray emission spectroscopy. *J. Am. Chem. Soc.* **2010,** *132* (28), 9715-9727.
58. Pollock, C. J.; DeBeer, S., Valence-to-core x-ray emission spectroscopy: a sensitive probe of the nature of a bound ligand. *J. Am. Chem. Soc.* **2011,** *133* (14), 5594-5601.
59. Maeda, K.; Hasegawa, K.; Maeda, M.; Ogiwara, K.; Hamanaka, H., Rapid chemical state analysis in air by highly sensitive high-resolution PIXE using a v. Hamos crystal spectrometer. *X-Ray Spectrom.* **2005,** *34* (4), 389-392.
60. Mori, R. A.; Paris, E.; Giuli, G.; Eeckhout, S. G.; Kavčič, M.; Žitnik, M.; Bučar, K.; Pettersson, L. G. M.; Glatzel, P., Sulfur-metal orbital hybridization in sulfur-bearing compounds studied by x-ray emission spectroscopy. *Inorg. Chem.* **2010,** *49* (14), 6468-6473.
61. Niskanen, J.; Sahle, C. J.; Ruotsalainen, K. O.; Müller, H.; Kavčič, M.; Žitnik, M.; Bučar, K.; Petric, M.; Hakala, M.; Huotari, S., Sulphur Kβ emission spectra reveal protonation states of aqueous sulfuric acid. *Scientific Reports* **2016,** *6* (1).

62. O'Reilly, J. W.; Dicinoski, G. W.; Shaw, M. J.; Haddad, P. R., Chromatographic and electrophoretic separation of inorganic sulfur and sulfur–oxygen species. *Anal. Chim. Acta* **2001,** *432* (2), 165–192.
63. Zhang, J.; Zuo, W.; Tian, Y.; Chen, L.; Yin, L.; Zhang, J., Sulfur transformation during microwave and conventional pyrolysis of sewage sludge. *Environ. Sci. Technol.* **2017,** *51* (1), 709–717.

CHAPTER 8 ROLE OF PHOSPHORUS OXIDATION IN CONTROLLING THE LUMINESCENT PROPERTIES OF INDIUM PHOSPHIDE QUANTUM DOTS

Originally published as: Cossairt, B. M.; Stein, J. L.; Holden, W. M.; Seidler, G. T. 4-1: Invited Paper: Role of Phosphorus Oxidation in Controlling the Luminescent Properties of Indium Phosphide Quantum Dots. *SID Symposium Digest of Technical Papers* 2018, 49 (1), 21–24. https://doi.org/10.1002/sdtp.12481.

My contributions to this work include performing the XES measurements and data analysis, and assisting with the interpretation and discussion of those results.

Indium phosphide (InP) is the leading Cd-free quantum dot material for application in photoluminescence downconversion display and lighting technologies. To date the performance of InP quantum dots (QDs) has lagged behind cadmium selenide in terms of both luminescence line width and quantum yield. Extensive studies in our lab have implicated kinetically persistent magic-sized cluster intermediates as a leading contributor to polydispersity in these samples, providing new opportunities for achieving high color purity. Now, using a combination of solid-state NMR spectroscopy and recently developed benchtop X-ray emission spectroscopy, we have studied the evolution of oxidized phosphorus species during both synthesis and shell growth.

8.1 INTRODUCTION

InP quantum dots are leading emissive materials for luminescence downconversion applications, such as LED-backlit displays.[1–3] Display manufacturers including Samsung, Sony, LG, and Apple have devoted significant resources to investigating methods to narrow the size

distributions of InP QD samples and increase the photoluminescence quantum yields up to 100%. Despite these efforts, state of the art syntheses produce QD ensembles that are characterized by luminescence linewidths in the green and red that range between 40-80 nm and quantum yields that max out at 85% in the most sophisticated shelled samples.[4–7] We hypothesize that surface phosphorus oxidation plays a leading role in limiting our ability to access higher quality samples.

Even under synthetic conditions in which extreme care is taken to exclude oxygen and water, surface phosphorous oxidation often arises as the result of undesired side-reactions that occur during the nucleation, growth and shelling of InP QDs.[8,9] Although there has been debate concerning the potential benefits of an amorphous oxidized interface between an InP core and its shell material with respect to reducing lattice strain between materials,[10,11] the detrimental impact water has on particle nucleation and growth has directed efforts towards removing any source of surface oxidation.[9,12,13] Additionally, oxidized phosphorus that is present at the core-shell interface may serve as an electronic trap site or prevent conformal deposition of shell material, both of which have the effect of reducing quantum yield. In this study, we aim to probe the degree of phosphorus oxidation that arises across a series of common, but chemically distinct synthetic methods.

X-ray photoelectron (XPS) and solid-state NMR (SS-NMR) spectroscopy have been the traditional options to measure the degree of oxidized phosphorus present in quantum dots.[8,14] These measurements can be challenging due to the low sensitivity of SS-NMR, requiring large amounts of sample and long acquisition times, or the surface-sensitive nature of XPS. X-ray emission spectroscopy (XES) is an appealing alternative method for characterizing the oxidation of phosphorus in a bulk sample because it does not face these obstacles. Recent progress in benchtop XES spectrometry at the University of Washington holds the potential to develop XES of sulfur and phosphorus into an accessible and powerful technique for probing oxidation state and

bonding electronic structure for those elements, achieving synchrotron-level energy resolution and count rates with a spectrometer illuminated by only a conventional x-ray tube.[15] The use of XES as an analytical tool to probe electronic structure has previously been limited in the field of nanoscience.[16,17]

8.2 Results and Discussion

With this tool in hand, we used SS-NMR and XES to examine a series of InP QDs prepared under air-free conditions with fatty acids, metal carboxylates and silylphosphines – including as-synthesized cores, cores passivated by Zn^{2+} and InP/ZnS core-shell particles.[18,19] Our results, shown in Table 8.1, strongly support the equivalence of oxidation state measurements by ^{31}P SS-NMR and P Kα XES. A representative XES spectrum for InP QDs is shown in Figure 8.1.[15]

Table 8.1. Comparison of SS-NMR and P Kα XES for determination of phosphorus oxidation state in InP QDs.

Sample	SS-NMR (% red)	SS-NMR (% ox)	P Kα XES (% red)	P Kα XES (% ox)
InP	93	7	89	11
InP/Zn	87	13	83	17
InP/ZnS	54	46	51	49

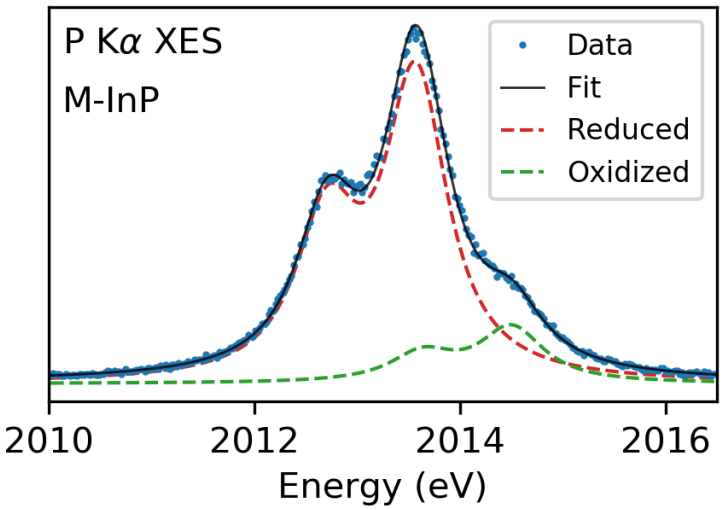

Figure 8.1: The phosphorus Kα emission from InP produced using InP magic-sized clusters as single-source precursors (M-InP). Measurement time was 50 minutes. The simple linear superposition fit gives 84% reduced fraction.

As can be seen from this data, the proportion of oxidized P in as-synthesized InP and InP/Zn QDs is non-negligible. It is widely accepted that during the synthesis of InP QDs in which silylphosphines are injected into a hot solution of indium carboxylates, an excess of acid present will lead to decarboxylative coupling, thus producing water *in-situ*.[14] As expected, after purification and thermal treatment with zinc carboxylates, the proportion of oxidized P did not significantly increase due to the lack of free acid to undergo ketonization.[20] The marked increase in the proportion of oxidized P in the ZnS shelled sample has been well-documented by Virieux *et al.* as a mixed oxide surface phase that forms during ZnS shell growth.[8] Elemental sulfur can form hydrogen sulfide through activation by the non-coordinating solvent, 1-octadecene.[21] H_2S then reacts with zinc carboxylate to form carboxylic acids, which initiate ketonization and the production of water.

The aforementioned measurements demonstrate that unintended oxidation is a characteristic of InP syntheses and shelling procedures due to adventitious side reactions.

Furthermore, these measurements demonstrate that P Kα XES is a reliable tool for measuring phosphorus oxidation with significant advantages over SS-NMR spectroscopy. Each XES measurement required <5 mg of material with most measurement times under an hour, while the SS-NMR measurements required samples on the scale of 100 mg with multiple days of collection time required for reliable integration.

Based on this promising data, we proceeded with measuring the extent of phosphorus oxidation as a function of synthetic method using XES with the motivation to examine the correlation between surface oxidation and luminescence properties. In this study, we chose 3 different synthetic methods to produce unshelled InP QDs with an expected range of minimal to no oxidation present. Furthermore, each InP QD was shelled with either ZnS or ZnSe with the prediction that samples that are initially more oxidized or introduce processes to oxidize the surface will result in particles with lower photoluminescence quantum yields.

First, InP was synthesized via the traditional approach in which $P(SiMe_3)_3$ is injected into a hot solution of indium carboxylate and excess acid, thus inherently introducing a ~10% oxidized P component through ketonization. Second, our group has recently developed the chemistry of InP magic-sized clusters (MSCs) as a single source precursor for InP QDs.[22,23] The MSCs can be purified to remove any excess acid, ensuring that the reaction solution is a homogeneous mixture of only the MSC $In_{37}P_{20}(O_2CR)_{51}$. A hot injection of MSCs into non-coordinating solvent induces particle dissolution and nucleation to give monodisperse InP QDs. Lastly, aminophosphines have been introduced as reliable phosphorus precursors for the synthesis of size-tunable InP QDs when paired with indium halides.[24,25] The reaction between metal halides and aminophosphines is driven by redox chemistry and more importantly, does not involve any oxygen-containing reagents, eliminating the possibility of oxidation via reagent decomposition products.[26] In future reference

and plots, InP QDs will be referred to as **C** (indium carboxylates + $P(SiMe_3)_3$), **M** (MSC single-source precursors), or **A** (aminophosphines and metal halides).

Figure 8.2 shows a stack plot of the P Kα spectra for **C/M/A** InP samples with bulk GaP and Na_2HPO_4 as P(3-) and P(5+) references, respectively. Based on linear superposition fitting of the reference standard spectra, the content of reduced and oxidized phsophorus and corresponding peak positions are summarized in Table 8.2. Measuring any oxidized phosphorus component in **M** (15%) and **A** (17%), was unexpected due to either the acid-free or oxygen-containing ligand-free nature of each synthesis. Shifts in the emission energy of the oxidized component lead us to consider the possibility of molecular impurities that skew the represented populations. To this end, the utilization of phosphorus Kβ XES can be telling of the surrounding phosphorus environment by probing the valence to core transitions; we will continue to explore this as a powerful tool to distinguish specific phosphorus coordination environments in future work.

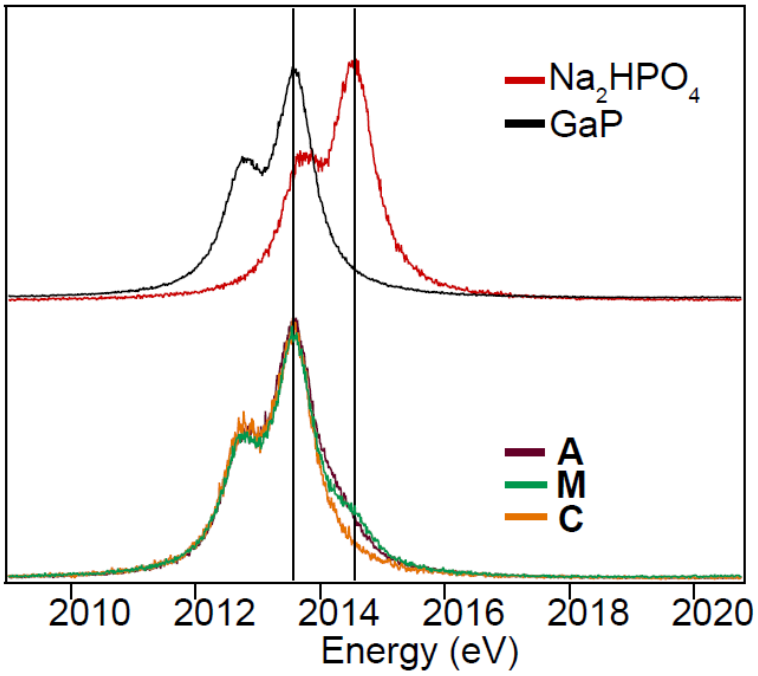

Figure 8.2: P Kα emission from unshelled InP QDs (**C**/**M**/**A**) with GaP and Na_2HPO_4 references to guide the eye to expected P^{3-} (2013.57 eV) and P^{5+} (2014.55 eV) peak positions.

Table 8.2. Oxidized and reduced phosphorus components based on linear superposition fits for InP QDs and respective Kα peak positions.

Sample	Ox (%)	Red (%)	Ox $K\alpha_1$ (eV)	Red $K\alpha_1$ (eV)
C-InP	11	89	2014.41	2013.54
M-InP	16	84	2014.50	2013.57
A-InP	17	83	2014.29	2013.59

To address the intrinsically low PL QY of as-synthesized InP QDs, we shelled each of the samples (**C**, **M**, and **A**) with either ZnS or ZnSe. ZnS shell growth was performed using conventional successive ionic layer adsorption and reaction (SILAR) addition of zinc carboxylate and elemental sulfur. This approach was selected because it would provide a baseline for shelled QDs that have a known mechanism for oxidation during shell growth.[8,19] To compare to this, we

also targeted shell growth with ZnSe that has demonstrated upwards of 60% PL QY in the literature and produced nearly blinking-free samples. [7,25] ZnSe shell growth was performed in a similar fashion with SILAR addition of zinc carboxylates and trioctylphosphine-selenide (TOPSe).

Shell growth reactions were not optimized for each subset of InP QDs in this study so the reported PL QYs are not representative of the highest achieved in other literature examples utilizing these methods. Rather, we targeted consistency across shelling the various InP starting materials. We achieved this by ensuring that concentrations of InP QD solutions were matched across all shelling reactions to maintain similar concentrations of added Zn/E precursors (E=S/Se).

The P Kα spectra for ZnS and ZnSe shelled **C/M/A** InP QDs are shown in Figure 8.3 with corresponding data in Table 8.3. As expected, the degree to which the ZnS shell further oxidizes surface P, 40-50%, is observed regardless of starting material. Although the trend follows our prediction in which higher QYs are achieved in samples with less oxidized phosphorus present, we recognize that these values need to be deconvoluted further from the initial InP QD measurements via P Kβ analysis. Likewise, the InP/ZnSe results present an issue with anomalously high oxidized phosphorus content, in the range of 50-80%. Emission peak energy shifts are much more significant across the InP/ZnSe samples, thus Kβ analysis will aid in clarifying these results by enabling the deconvolution of oxidized phosphorus from different sources.

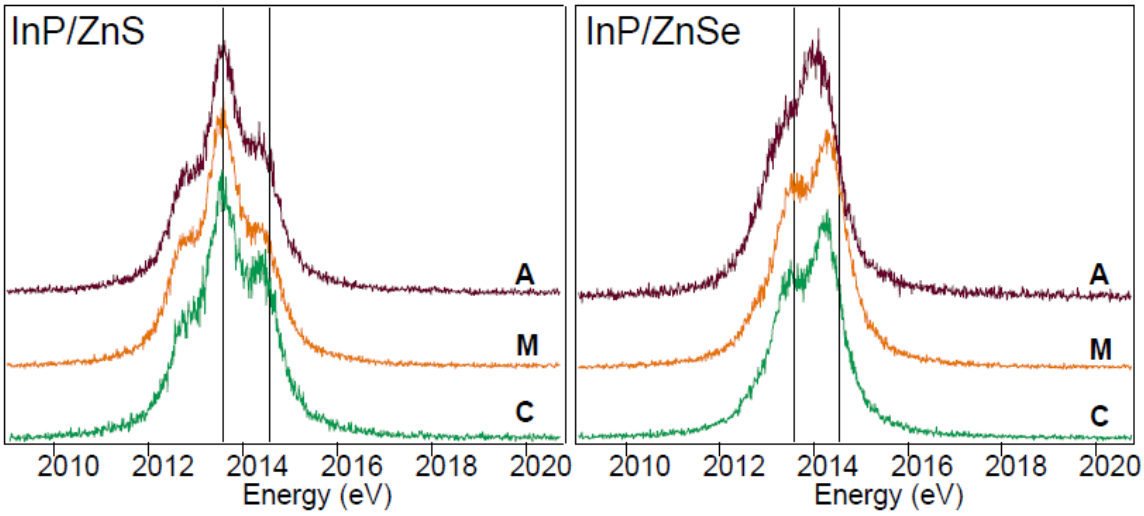

Figure 8.3: P Kα spectra of InP/ZnS (left) and InP/ZnSe (right). Black lines designate the reference positions of GaP(P^{3-}) at 2013.57 eV and Na_2HPO_4(P^{5+}) at 2014.55 eV.

Table 8.3. Oxidized and reduced phosphorus components based on linear superposition fits for InP/ZnE, respective Kα peak positions, and corresponding quantum yields.

Sample	Ox (%)	Red (%)	Ox $K\alpha_1$ (eV)	Red $K\alpha_1$ (eV)	PL QY
C/ZnS	49	52	2014.43	2013.56	7%
M/ZnS	38	62	2014.44	2013.55	28%
A/ZnS	43	57	2014.42	2013.58	25%
C/ZnSe	85	15	2014.27	2013.67	10%
M/ZnSe	80	20	2014.35	2013.71	44%
A/ZnSe	56	44	2014.25	2013.85	30%

8.3 Conclusions

We have demonstrated the viability of phosphorus XES measurements as a tool to characterize the extent of oxidation in InP quantum dots through a comparative analysis with SS-NMR spectroscopy. Utilizing the convenience of benchtop XES, we examined the role of phosphorus oxidation on quantum yield by measuring surface phosphorus oxidation as a function of synthetic method and shelling strategy. This work provides strong motivation to systematically examine phosphorus oxidation as a metric for rationalizing lower-than-expected PL QY. It also provides impetus to evaluate the more sensitive valence-to-core XES Kβ transitions to fully assign the nature of the chemical environment of phosphorus. In future work, intentional stoichiometric oxidation of the InP surface will verify our results and offer opportunities for developing new chemistry to reverse surface oxidation post-synthetically.

8.4 Acknowledgements

The authors gratefully acknowledge the aid of Prof. Aaron Rossini and Amrit Venkatesh at Iowa State University with collection of solid-state NMR data. JLS and BMC acknowledge support from the University of Washington Molecular Engineering Materials Center under grant MRSEC DMR 1719797. GTS and WMH acknowledge support by the Joint Plasma Physics Program of the National Science Foundation and the Department of Energy under grant DE-SC0016251.

8.5 References

1. Shirasaki, Y., Supran, G. J., Bawendi, M. G. & Bulović, V. Emergence of Colloidal Quantum-Dot Light-Emitting Technologies. *Nat. Photonics* **7,** 13–23 (2013).
2. Supran, G. J. *et al.* QLEDs for displays and solid-state lighting. *MRS Bull.* **38,** 703–711 (2013).

3. Coe-Sullivan, S., Liu, W., Allen, P. M. & Steckel, J. S. Quantum Dots for LED Downconversion in Display Applications. *ECS J. Solid State Sci. Technol.* **2,** R3026–R3030 (2013).
4. Li, L. & Reiss, P. One-pot Synthesis of Highly Luminescent InP/ZnS Nanocrystals without Precursor Injection. *J. Am. Chem. Soc.* **130,** 11588–11589 (2008).
5. Kim, S. *et al.* Highly Luminescent InP/GaP/ZnS Nanocrystals and Their Application to White Light-Emitting Diodes. *J. Am. Chem. Soc.* **134,** 3804–3809 (2012).
6. Lim, J. *et al.* InP@ZnSeS, Core@Composition Gradient Shell Quantum Dots with Enhanced Stability. *Chem. Mater.* **23,** 4459–4463 (2011).
7. Chandrasekaran, V. *et al.* Nearly Blinking-Free, High-Purity Single-Photon Emission by Colloidal InP/ZnSe Quantum Dots. *Nano Lett.* **17,** 6104–6109 (2017).
8. Virieux, H. *et al.* InP/ZnS Nanocrystals: Coupling NMR and XPS for Fine Surface and Interface Description. *J. Am. Chem. Soc.* **134,** 19701–19708 (2012).
9. Baquero, E. A. *et al.* Synthesis of Oxide-Free InP Quantum Dots: Surface Control and H_2-Assisted Growth. *Chem. Mater.* **29,** 9623–9627 (2017).
10. Ramasamy, P., Kim, B., Lee, M.-S. & Lee, J.-S. Beneficial effects of water in the colloidal synthesis of InP/ZnS core–shell quantum dots for optoelectronic applications. *Nanoscale* **8,** 17159–17168 (2016).
11. Kim, K. *et al.* Halide–Amine Co-Passivated Indium Phosphide Colloidal Quantum Dots in Tetrahedral Shape. *Angew. Chem. Int. Ed.* **55,** 3714–3718 (2016).
12. Gary, D. C. & Cossairt, B. M. Role of Acid in Precursor Conversion During InP Quantum Dot Synthesis. *Chem. Mater.* **25,** 2463–2469 (2013).
13. Xie, L., Harris, D. K., Bawendi, M. G. & Jensen, K. F. Effect of Trace Water on the Growth of Indium Phosphide Quantum Dots. *Chem. Mater.* **27,** 5058–5063 (2015).
14. Cros-Gagneux, A. *et al.* Surface Chemistry of InP Quantum Dots: A Comprehensive Study. *J. Am. Chem. Soc.* **132,** 18147–18157 (2010).
15. Holden, W. M. *et al.* A compact dispersive refocusing Rowland circle X-ray emission spectrometer for laboratory, synchrotron, and XFEL applications. *Rev. Sci. Instrum.* **88,** 073904 (2017).
16. Petric, M. *et al.* Chemical State Analysis of Phosphorus Performed by X-ray Emission Spectroscopy. *Anal. Chem.* **87,** 5632–5639 (2015).
17. Sugiura, C. X-Ray Emission Spectra and Electronic Structures of Red Phosphorus, 3d Transition-Metal Phosphides and III–V Compounds. *J. Phys. Soc. Jpn.* **64,** 2510–2523 (1995).
18. Stein, J. L., Mader, E. A. & Cossairt, B. M. Luminescent InP Quantum Dots with Tunable Emission by Post-Synthetic Modification with Lewis Acids. *J. Phys. Chem. Lett.* **7,** 1315–1320 (2016).
19. Xie, R., Battaglia, D. & Peng, X. Colloidal InP Nanocrystals as Efficient Emitters Covering Blue to Near-Infrared. *J. Am. Chem. Soc.* **129,** 15432–15433 (2007).
20. Stein, J. L., Mader, E. A. & Cossairt, B. M. Luminescent InP Quantum Dots with Tunable Emission by Post-Synthetic Modification with Lewis Acids. *J. Phys. Chem. Lett.* **7,** 1315–1320 (2016).
21. Li, Z., Ji, Y., Xie, R., Grisham, S. Y. & Peng, X. Correlation of CdS Nanocrystal Formation with Elemental Sulfur Activation and Its Implication in Synthetic Development. *J. Am. Chem. Soc.* **133,** 17248–17256 (2011).

22. Gary, D. C., Terban, M. W., Billinge, S. J. L. & Cossairt, B. M. Two-Step Nucleation and Growth of InP Quantum Dots via Magic-Sized Cluster Intermediates. *Chem. Mater.* **27,** 1432–1441 (2015).
23. Gary, D. C. *et al.* Single-Crystal and Electronic Structure of a 1.3 nm Indium Phosphide Nanocluster. *J. Am. Chem. Soc.* **138,** 1510–1513 (2016).
24. Song, W.-S. *et al.* Amine-derived synthetic approach to color-tunable InP/ZnS quantum dots with high fluorescent qualities. *J. Nanoparticle Res.* **15,** 1750 (2013).
25. Tessier, M. D., Dupont, D., De Nolf, K., De Roo, J. & Hens, Z. Economic and Size-Tunable Synthesis of InP/ZnE (E = S, Se) Colloidal Quantum Dots. *Chem. Mater.* **27,** 4893–4898 (2015).
26. Tessier, M. D. *et al.* Aminophosphines: A Double Role in the Synthesis of Colloidal Indium Phosphide Quantum Dots. *J. Am. Chem. Soc.* **138,** 5923–5929 (2016).

CHAPTER 9 PROBING SURFACE DEFECTS OF INP QUANTUM DOTS USING PHOSPHORUS KA AND KB X-RAY EMISSION SPECTROSCOPY

Originally published as: Stein, J. L.; Holden, W. M.; Venkatesh, A.; Mundy, M. E.; Rossini, A. J.; Seidler, G. T.; Cossairt, B. M. Probing Surface Defects of InP Quantum Dots Using Phosphorus Kα and Kβ X-Ray Emission Spectroscopy. *Chemistry of Materials* 2018, 30 (18), 6377–6388. https://doi.org/10.1021/acs.chemmater.8b02590.

This chapter represents a significant portion of this dissertation. My main contributions to this work include performing the Kα and Kβ XES measurements, data analysis, and discussion of those results. I also assisted Jennifer L. Stein on the interpretation and discussion of those results in the context of the other measurements and across the series of InP quantum dot systems being studied. Jennifer L. Stein and I contributed equally on this work.

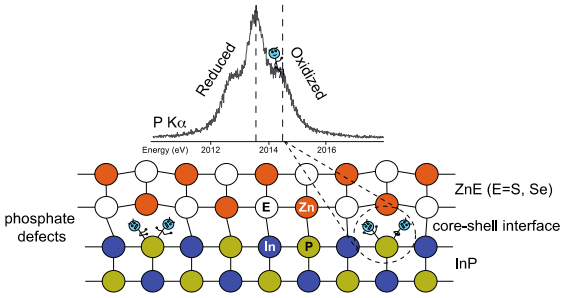

Figure 9.0: Table of contents graphic.

Synthetic efforts to prepare indium phosphide (InP) quantum dots (QDs) have historically generated emissive materials with lower than unity quantum yields. This property has been

attributed to structural and electronic defects associated with the InP core as well as the chemistry of the shell materials used to overcoat and passivate the InP surface. Consequently, the uniformity of the core-shell interface plays a critical role. Using X-ray emission spectroscopy (XES) performed with a recently developed benchtop spectrometer, we studied the evolution of oxidized phosphorus species arising across a series of common, but chemically distinct, synthetic methods for InP QD particle growth and subsequent ZnE (E=S, Se) shell deposition. XES afforded us the ability to measure the speciation of phosphorus reliably, quantitatively, and more efficiently (with respect to both quantity of material required and speed of the measurement) than traditional techniques, i.e. X-ray photoelectron spectroscopy and magic angle spinning solid-state NMR spectroscopy. Our findings indicate that even with deliberate care to prevent phosphorus oxidation during InP core synthesis, typical shelling approaches unintentionally introduce oxidative defects at the core-shell interface, limiting the attainable photoluminescence quantum yields.

9.1 Introduction

Indium phosphide (InP) quantum dots (QDs) are the leading cadmium-free emissive material for luminescence downconversion applications, such as LED-backlit displays, and lighting technologies.[1–5] Display manufacturers including Samsung, Sony, Vizio, LG, and Apple have devoted significant resources to investigating methods to narrow the size distributions of InP QD samples and increase the photoluminescence quantum yields (PL QYs) up to 100%.[6] Despite these efforts, state of the art syntheses produce QD ensembles that are characterized by luminescence linewidths in the green and red region that range between 40-80 nm and quantum yields that max out at 85% in the most sophisticated shelled samples.[7–9] While minimizing defects

in the core and shell materials is necessary, perhaps the most crucial aspect of design is at the core-shell interface. InP QDs have been shown to be incredibly susceptible to surface oxidation from *in-situ* and *ex-situ* sources during both core and shell syntheses, resulting in oxidized phosphorus species that likely perturb conformal shell growth.[10–12] We hypothesize that surface phosphorus oxidation plays a leading role in limiting our ability to access higher quality samples.

Even under synthetic conditions in which extreme care is taken to exclude oxygen and water, surface phosphorus oxidation often arises as the result of undesired side-reactions that occur during the nucleation, growth, and shelling of InP QDs. Although there has been debate concerning the potential benefits of an amorphous oxidized interface between an InP core and its shell material with respect to reducing lattice strain between materials,[13,14] the detrimental impact of water on particle nucleation and growth has directed efforts towards removing any source of surface oxidation.[15–17] Furthermore, oxidized phosphorus that is present at the core-shell interface may serve as an electronic trap site or prevent conformal deposition of shell material, both of which have the effect of reducing PL QYs. In this study, we chose three different synthetic methods that are expected to produce InP QDs with minimal or no oxidation. Furthermore, each InP QD was shelled with either ZnS or ZnSe with the hypothesis that samples that are initially more oxidized or that are subjected to processes that oxidize the surface will result in particles with lower PL QYs.

X-ray photoelectron spectroscopy (XPS) and magic angle spinning solid-state NMR (MAS SSNMR) spectroscopy have been the traditional routes to measure the degree of oxidized phosphorus present in InP quantum dots.[11–13,17–19] These measurements can be challenging due to the low sensitivity of SSNMR spectroscopy which traditionally require large amounts of sample and long acquisition times. XPS analysis is generally impeded by its surface-sensitive nature and

the presence of common long-chain surface ligands that further limit the escape depth of the photogenerated electrons and reduce the signal resolution.[20] Extremely high energy resolution wavelength dispersive X-ray fluorescence spectroscopy, more commonly called X-ray emission spectroscopy (XES), is an appealing alternative method for characterizing the oxidation of phosphorus in a bulk sample because it does not face these obstacles. Recent progress in benchtop XES instrumentation holds the potential to develop XES of sulfur and phosphorus into an accessible and powerful technique for probing oxidation state and bonding electronic structure, achieving synchrotron-level energy resolution and count rates with a spectrometer illuminated by only a conventional X-ray tube.[21] The same instrument was used in a recent study of sulfur speciation in biochars as a first analytical application,[22] and the present study reinforces and, in many ways, exceeds the message of that earlier work in emphasizing new potential for XES for routine application in analytical chemistry.

A number of recent studies have demonstrated the capability of synchrotron and laboratory-based XES to measure speciation in phosphorus, sulfur, and chlorine compounds.[22–27] In particular, P Kα XES has been used to quantitatively determine the fraction of phosphorus species with different local charge densities (i.e. oxidation states). The Kα emission line corresponds to a transition of an electron between the deep, atomic-like 2p and 1s orbitals. In the simplest treatment, the sensitivity of this transition to changes in the valence electron population comes from the different changes in the screening of the nuclear charge as observed from the 2p and 1s orbitals. As these effects are only weakly perturbative for phosphorus (but can be much more complex for, e.g., 3d transition metals) the Kα emission spectra typically show only a shift of the peak position from lower to higher energy with increasing oxidation state, while the spectral shape remains unchanged (Figure 9.1). For a compound containing phosphorus in multiple

oxidation states, the proportion of each oxidation state can be determined quantitatively by simple linear-combination fitting to multiple line shapes, although this benefits from prior knowledge of a suitable reference spectrum set.

For information beyond oxidation state determination by the P Kα emission, P Kβ XES enables a more detailed interrogation of the electronic structure. The Kβ emission line results from electronic transitions from the 3p shell, suitably hybridized with valence and semi-core ligand electrons, to the 1s core hole. Due to the direct relevance of such a characterization of the bonding electronic density of states for chemistry, this type of valence to core (VTC) XES is seeing growing use, such as in studies of organometallic systems.[28–31] Thus the Kβ emission has increased chemical sensitivity, and can provide information about bonding, symmetry, and ligand type.[24] A full interpretation of the various spectral features requires quantum chemistry calculations.[24,28,32,33] Here, we focus on the ligand fingerprinting capability of the Kβ spectral features, specifically the Kβ' satellite feature near 2123.5 eV in the phosphate spectrum. This feature results from mixing of P valence states with an O 2s orbital,[24,34] and thus serves as a clear indicator of the presence of phosphate. P Kβ spectra are shown for reference compounds in Figure 9.1.

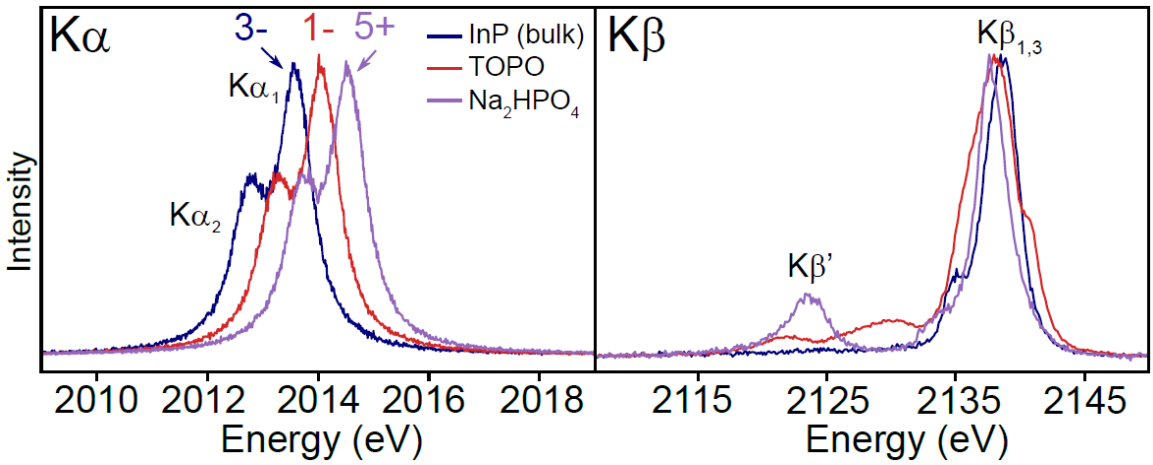

Figure 9.1: P Kα and Kβ X-ray emission spectra of reference compounds. The Kα spectra of the three compounds are nearly identical, with shifts in energy towards higher energy with increasing

oxidation state. Nominal oxidation states of the reference compounds are indicated above the given spectra. The Kβ spectra is a valence to core transition, and a number of different spectral features are observed. Of particular importance is the strong Kβ' peak at 2123.5 eV in the Na_2HPO_4 spectra, which is due to mixing of the P 3p and O 2s orbitals, and thus serves as a fingerprint of P–O bonds from the phosphate.

9.2 Experimental

9.2.1 X-ray emission spectroscopy

P Kα and Kβ XES measurements were performed on a recently developed laboratory spectrometer, reported in detail in Holden *et al.*[21] The spectrometer uses a low-powered, unfocused X-ray tube (Varex VF50, 50W) to illuminate the sample, whose emitted X-rays are analyzed by a 10 cm radius of curvature cylindrical crystal analyzer and detected using a new home-made CMOS direct-exposure color X-ray camera.[21,35] The spectrometer makes use of the dispersive refocusing Rowland (DRR) geometry, in which the sample is placed within the Rowland circle and illuminated with an unfocused beam of incident radiation while a position-sensitive detector is placed tangential to the circle at the location of the refocused fluorescence. This method of illumination allows efficient collection of signal from the sample, and the entire energy region of interest is measured simultaneously by the CMOS camera functioning as a position-sensitive detector with sufficient single-photon energy resolution to reject background scatter and chamber-wall fluorescence. The wavelength dispersing component is a Si(111) cylindrically-bent Johann analyzer having a 10 cm radius of curvature (XRSTech). The Si(111) analyzer provides Bragg angles of 79° for P Kα (~2014eV) and 67.6° for P Kβ (~2138eV). To prevent air contamination during XES measurements, the sample and crystal are inside a small vacuum chamber which was pumped to <100 mTorr pressure during the measurements. For improved resolution at P Kα, the crystal analyzer was masked using aluminum foil to a 10×2 mm^2

region (along Rowland plane × out of Rowland plane). For the weaker P Kβ signal the crystal was unmasked in order to improve count rates at the expense of increased Johann error. The Johann error causes weak tails on the high-energy side of the spectrum. These distortions do not significantly affect the analysis of the P Kβ spectra used here. The energy scale of P Kα and Kβ measurements is calculated based on the instrumental geometry with Na_2HPO_4 as a reference standard having $K\alpha_1$ and $K\beta_{1,3}$ energy positions at 2014.55 eV and 2137.80 eV, respectively.[24]

The InP QD samples were prepared for XES measurements by drop-casting onto silicon wafers with a spot size ~3-4 mm in diameter with <5 mg of material. The drop-cast samples were stored in an inert nitrogen atmosphere and were briefly exposed to air during loading into the instrument. The wafers were mounted in the instrument and the drop-cast spot exposed directly to the incident beam. With the current instrumental configuration, switching between Kα and Kβ measurements requires manually repositioning the crystal analyzer and re-tuning, thus the measurements were done in batches to separately measure Kα and Kβ. Fresh InP QD samples were drop-cast for each measurement.

The P Kα emission spectra were analyzed using linear-combination fitting with the non-linear least-squares fitting Python package LMFIT.[36] With a few exceptions discussed below, spectra were fit with two oxidation state components, each consisting of two Voigt profiles representing the spin-split $K\alpha_1/K\alpha_2$ peaks. The widths and height ratios of these peak shapes were constrained to the values obtained from fitting the bulk InP and Na_2HPO_4 reference compounds, and the energy position of the two peak shapes were allowed to vary. The fits were weighted assuming Poisson statistics. The speciation was calculated from the relative intensity of the fit components.

The primary source of systematic uncertainty in this approach is due to limited prior knowledge of the number of distinct oxidation states in the sample. For the InP QDs, our primary expectation is a superposition of a low-energy $K\alpha_{1,2}$ spin-orbit split doublet representing the reduced phosphorus in the InP cores and a higher-energy $K\alpha_{1,2}$ doublet due to surface oxidized phosphorus species. If an appreciable amount of a third phosphorus species exists in an oxidation state between these two extremes, the energy positions and results of the phosphide-vs-phosphate speciation based on the erroneous two component fit will be skewed. As discussed in the Results, this effect was observed for samples where TOP-Se was used as a precursor, producing TOPO as a byproduct. To analyze the spectra for those samples, linear combination fitting was performed with three components, where the energy positions of the reduced and oxidized components were allowed to vary, but the TOPO component was fixed to be at 2014.07 eV, as determined by measurement of a pure reference TOPO sample.

Another source of systematic uncertainty is variations in the detailed shape of the $K\alpha_{1,2}$ doublet for the components of the fitting procedure. Though these variations have not been reported in detail for phosphorus, variations in the $K\alpha_{1,2}$ intensity ratio in the range of 1.7-2.3 have been reported for a variety of sulfur compounds.[25] In addition, variations in the Voigt widths of the line shapes on the order of 2% are observed for the reference compounds measured here. The effect of these variations on the systematic uncertainty were estimated by performing the fitting procedure over a range of intensity ratios and widths, and the results are given in Table S1 and S2 in the Supporting Information.

During the P Kα measurements, changes in speciation due to possible radiation damage were checked by performing the speciation calculations on subsets of the accumulated data. The results are shown in Figures S1 and S2. The majority of the samples changed speciation by less

than ± 2% during the measurements and vary non-monotonically. For the three samples which show large monotonic changes, **C**-InP, **C**/ZnS, and InP/Zn, it is believed that a vacuum leak may have contributed. For those samples, only the first scan was kept for the final results. The vacuum leak was addressed before the remaining samples were measured.

To obtain a final estimate of the uncertainty from the XES fitting results, the uncertainty from signal variation over time was combined with the uncertainties estimated by varying the $K\alpha_{1,2}$ intensity ratio and Voigt widths and added to the statistical uncertainty. The full details are given in Table S1 and S2, and the final uncertainty estimates are given in Table 9.1.

9.2.2 ^{31}P MAS solid state NMR spectroscopy

All quantum dot samples were prepared for SSNMR analysis from concentrated colloidal solutions (ca. 50 mg of dried quantum dots in 1 mL anhydrous toluene) by impregnating 150-450 µL of the colloidal solutions in 8-12 mg of boron nitride, in 50 µL aliquots. The mixture was allowed to dry on a watch glass for an hour before packing into a 1.3 mm rotor. In order to confirm that there is a minimal increase in oxidation induced by this procedure, ^{31}P SSNMR spectra were obtained from InP QDs after 10 days of air exposure (Figure S3). These tests indicated that there should be minimal oxidation over the course of several hours that are required to prepare the samples for SSNMR experiments.

MAS ^{31}P SSNMR spectra were recorded using a Bruker Avance III HD console on a wide-bore 9.4 T magnet ($\nu_0(^{31}P)$ = 162.1 MHz). All experiments were performed using a 1.3 mm fast MAS broadband HX SSNMR probe and the rotors were spun with nitrogen gas to prevent additional oxidation of the QDs during the course of the measurements. ^{31}P MAS NMR spectra were obtained using a rotor synchronized Hahn echo (90°-τ-180°-τ-acquire) pulse sequence with continuous wave ^{1}H heteronuclear decoupling applied during acquisition. The pulse widths for 90°

and 180° pulses were 1.3 μs and 2.6μs, respectively (192 kHz RF field) and the rotor synchronized τ periods were set such that the total echo delay was 2 rotor cycles. The MAS frequency was 50 kHz in all cases. Fast MAS helps to provide quantitative NMR spectra by eliminating spinning sidebands and focusing signal into the isotropic peaks. The ^{1}H RF power for continuous wave heteronuclear decoupling was set to the HORROR condition [$\nu_1(^{1}H)$ = 25 kHz]. All ^{31}P SSNMR spectra were acquired with 500 s recycle delay to ensure there was adequate relaxation delay ≥ $3\times T_1$ to give quantitative SSNMR spectra. This was confirmed by acquiring a ^{31}P SSNMR spectrum of **C**-InP QDs with a 750 s recycle delay, which showed a comparable intensity for the phosphide signal. The spectral width was set to 200 kHz and the number of digitized points to 8 k, corresponding to a total acquisition time of 20.48 ms. ^{31}P spectra were acquired in steps of 32 scans (4.4 hour experiment time), and multiple spectra were acquired until the sum of all spectra provided a spectrum with reasonable signal to noise ratio. Each spectrum was processed by zero filling up to 8k real data points and by adding a simple exponential window function with 1000 Hz line broadening. All data processing was performed on Topspin 3.5.

9.2.3 X-ray photoelectron spectroscopy

All XPS spectra were taken on a Surface Science Instruments S-Probe photoelectron spectrometer. This instrument has a monochromatized Al Kα X-ray source which was operated at 20 mA and 10 kV and a low-energy electron flood gun for charge neutralization. X-ray analysis area for these acquisitions was approximately 800 μm across. Pressure in the analytical chamber during spectral acquisition was less than 5×10^{-9} Torr. All included figures are high-resolution spectra. The pass energy for high-resolution spectra was 50 eV, and data point spacing was 0.065 eV/step. The takeoff angle (the angle between the sample normal and the input axis of the energy analyzer) was 0°. Service Physics Hawk version 7 data analysis software was used to fit high-

resolution spectra. The binding energy scale was calibrated from hydrocarbon ligands using the C 1s peak at 284.6 eV. P_{2p} peaks were analyzed using a linear background and fits were constrained with a 0.84 eV splitting value.

All InP samples were drop-cast solutions on a Si wafer while solids were brushed onto a strip of double-sided tape on a Si wafer. Sample preparation was performed in a nitrogen glovebox and transported in sealed containers to the instrument but transfer into the instrument chamber did require a minor degree of exposure to air/moisture.

9.2.4 General Nanoparticle Characterization

UV-vis spectra were collected on a Cary 5000 spectrophotometer from Agilent. Fluorescence and absolute quantum yield measurements were taken on a Horiba Jobin Yvon FluoroMax-4 fluorescence spectrophotometer with the QuantaPhi integrating sphere accessory. Quantum dot solids were digested in 67% nitric acid overnight and diluted in 18 MΩ water in order to collect ICP-OES compositional data using a PerkinElmer Optima 8300. Powder X-ray diffraction data was collected on solid films drop-cast onto a Si wafer using a Bruker D8 Discover diffractometer. TEM images were collected on a FEI Tecnai G2 F20 microscope. Samples for TEM imaging were prepared by spotting a 50/50 toluene/pentane solution of nanoparticles onto an ultrathin carbon on holey carbon support film purchased from Ted Pella. Solution NMR spectra were recorded on a 700 MHz Bruker Avance III spectrometer.

9.3 Synthetic Details: General Considerations

All glassware was dried in a 160 °C oven overnight prior to use. All reactions, unless otherwise noted, were run under an inert atmosphere of nitrogen using a glovebox or using standard Schlenk techniques. Myristic acid (≥99%), indium acetate (99.99%), anhydrous acetonitrile (99.8%), trioctylphosphine (97%), tris(diethylamino)phosphine (97%), indium chloride

(99.999%), zinc chloride (99.999%), trioctylphosphine oxide (90%), InP (mesh pieces, 99.998%), sulfur powder (99.5% sublimed), and selenium powder (99.99%) were purchased from Sigma-Aldrich Chemical Co. and used without further purification. Diethyl zinc (95%) was purchased from Strem Chemicals and stored in a nitrogen atmosphere glovebox. Toluene purchased from Sigma Aldrich Chemical Co. was collected from a solvent still and stored over activated 3 Å molecular sieves in a glovebox. 1-octadecene (90%), oleylamine (70%), and squalane (96%) were purchased from Sigma Aldrich Chemical Co. and were dried by stirring overnight with CaH_2, distilled, and stored over activated 3 Å molecular sieves in a glovebox. C_6D_6 was purchased from Cambridge Isotope Labs and similarly dried and stored. Bio-Beads S-X1 were purchased from Bio-Rad Laboratories and were dried under vacuum before storage in a glovebox. Omni Trace nitric acid was purchased from EMD Millipore. 18.2 MΩ water was collected from an EMD Millipore water purification system. Tris(trimethylsilyl)phosphine was prepared by modifying a literature procedure in which Na-napthalene was used in place of Na/K alloy.[15] Zinc myristate was prepared from diethyl zinc and myristic acid using a modified literature procedure.[37]

*9.3.1 Synthesis of **C**-InP QDs*

C-InP QDs were prepared following a literature procedure[15] in which indium acetate (1. 167 g, 4 mmol) and myristic acid (3.31 g, 14.5 mmol) were heated to 100 °C overnight under reduced pressure in 12 mL of ODE. *$P(SiMe_3)_3$ is a very reactive and pyrophoric source of phosphorus and should be handled with care.* $P(SiMe_3)_3$ (590 μL, 2 mmol) was measured into ODE (5 mL) and injected into the indium myristate solution at 315 °C. Particle growth was maintained at 285 °C and monitored by UV-vis spectroscopy. The reaction was halted by cooling down to room temperature after ca. 20 minutes of growth and the ODE was removed through distillation under reduced pressure. The resulting QD paste was transferred into a glovebox for

purification by re-dissolving in a minimal amount of toluene, centrifuging to remove insoluble products, then precipitating the particles with acetonitrile. The flocculated solution was centrifuged at 7,000 rpm and the clear supernatant was discarded. After a single precipitation to remove residual ODE, the particles were dissolved in toluene and purified by gel permeation chromatography (GPC), which has been demonstrated as an effective purification technique for these types of materials.[38,39] For all following quantum dot samples, standard purification entails the removal of high-boiling point solvents through distillation and a combination of precipitation cycles and GPC.

9.3.2 Synthesis of InP/Zn QDs

InP/Zn QDs were prepared following a literature procedure using **C**-InP QDs.[40] Briefly, zinc myristate (335 mg, 0.64 mmol) was heated to 80 °C in 5 mL of ODE until the solution was a cloudy white suspension. InP QDs (0.42 mmol of In) suspended in 5 mL of ODE were added to the suspension and heated to 200 °C for 3 hours. Particles were purified by the standard procedure.

*9.3.3 Synthesis of **M**-InP QDs*

First, InP magic-sized clusters (MSCs) were synthesized following a modified preparation from our lab.[41] Indium acetate (5.605 g, 19.2 mmol) and myristic acid (15.9 g, 69.6 mmol) were heated neat at 100 °C under reduced pressure overnight. Dry toluene (50 mL) was added to the reaction flask at room temperature under N_2 the following day, after which $P(SiMe_3)_3$ (2.8 mL, 9.6 mmol) was measured into 10 mL of toluene and injected into the indium myristate solution at 100 °C. Cluster growth was complete within 1 hour as indicated by the characteristic absorbance peak at 386 nm. The particles were concentrated down to a minimal volume of toluene, centrifuged to remove insoluble products, and purified by GPC. Following purification, the absence of free acid was confirmed by ^{1}H NMR spectroscopy and the MSCs were stored as a solid.

M-InP QDs were synthesized from InP MSCs through a modified procedure.[41] Myristate-capped InP MSCs (60 mg) were dissolved in 3 mL of ODE and transferred to a syringe. In a 3-neck flask under N_2 on a Schlenk line, 12 mL of ODE was heated to 300 °C at which point the MSCs were rapidly injected. Particle growth was held at 285 °C until complete (15-20 minutes) and then cooled down to room temperature. Particles were purified by the standard procedure.

*9.3.4 Synthesis of **A**-InP QDs*

A-InP QDs were synthesized following a modified procedure as described by Brainis *et al*.[42] Indium chloride (50 mg, 0.23 mmol) and zinc chloride (150 mg, 1.1 mmol) were stirred in oleylamine (2.5 mL, 7.5 mmol) under reduced pressure at 120 °C for an hour. The reaction was placed under N_2 and at 180 °C, tris(diethylamino)phosphine (0.23 mL, 0.8 mmol) was injected and particle growth was complete within approximately 20 minutes. After cooling down to room temperature, particles were removed from oleylamine by precipitation with ethanol. GPC purification was performed once particles were re-dissolved in toluene.

*9.3.5 ZnS shelling of **C**, **M**, and **A**-InP QDs*

ZnS shelling of InP QDs was performed following a modified procedure as described by Peng *et al*.[43] A purified solution of InP QDs (0.04 mmol indium) was dissolved in 7 mL of ODE and heated to 150 °C under inert atmosphere. Initial solutions of InP QDs (**C**, **M**, and **A**) were standardized to each other by matching absorption at 310 nm. Stock solutions of zinc myristate (28.8 mg in 10 mL ODE, 5.6 mM) and sulfur (22.4 mg in 10 mL ODE, 0.07 M) were prepared and heated to 100 °C in Schlenk flasks in an oil bath. For the first monolayer, a 2.17 mL aliquot of the zinc myristate stock (0.012 mmol) was added to the InP particles at 150 °C. After 10 minutes, 170 µL (0.012 mmol) of the sulfur stock solution was added, then the reaction was heated at 220 °C for 30 minutes. The second monolayer was added in the same fashion with 2.89 mL (0.016 mmol)

of zinc myristate and 230 µL (0.016 mmol) of sulfur. After 30 minutes at 220 °C, the reaction was cooled down and purified through the standard procedure.

*9.3.6 ZnSe shelling of **C**, **M**, and **A**-InP QDs*

ZnSe shelling was performed following a modified procedure as described by Brainis *et al.*[42] A purified solution of InP QDs (0.04 mmol indium) was dissolved in 10 mL of squalane and heated to 180 °C. Zinc myristate (100 mg, 0.192 mmol) suspended in squalane was injected and held at 180 °C for 20 minutes. Then, a stoichiometric TOP-Se solution was prepared by sonicating 1.755 g (22.2 mmol) of selenium in 10 mL of TOP (2.23 M) and 87 µL (0.192 mmol) of this stock was slowly injected into the reaction flask. After 140 minutes, a second addition of zinc myristate was added (300 mg, 0.576 mmol). At this point, the reaction was set to 320 °C and during heat-up, the second injection of TOP-Se was added drop-wise (262 µL, 0.576 mmol). Particle luminescence was monitored at 320 °C and the reaction was cooled when the PL ceased to change (ca. 1 hour). Particles were purified using the standard procedure.

9.4 Results and Discussion

To validate the use of Kα XES as a method to determine P speciation in InP QDs, a series of three samples was used in a head-to-head comparison of oxidation state distributions inferred from P Kα XES and from ^{31}P MAS SSNMR. Notably the InP and InP/ZnS samples have in part been previously characterized by Chaudret et al. via XPS and SSNMR spectroscopies with the primary conclusion that oxidation occurs during both synthesis and shell growth.[12] Here, samples including InP QDs, InP QDs that have been post-synthetically treated with zinc (InP/Zn), and InP QDs that have been shelled with ZnS (InP/ZnS) were studied. The results for all samples are presented in Table 9.1 and a comparison of the quantification of phosphorus oxidation state by both ^{31}P SSNMR and P Kα X-ray emission spectroscopy for the InP/ZnS sample is shown in Figure

9.2. Additional spectra are presented in Figure S4. Excellent agreement is found between the two techniques, and the results fall within the range of values reported by Chaudret et al.[12] The ^{31}P SSNMR spectra generally show resonances centered at ca. 0 ppm, assigned to oxidized phosphate species, and –200 ppm, assigned to the core phosphide species. Cross polarization magic angle spinning (CP-MAS) and direct excitation ^{31}P SSNMR experiments have previously demonstrated that the oxidized phosphorus species are located at the surface of the nanocrystals.[44,45] Using the fitting procedure described in the Experimental section, the P Kα XES signal for each of the three samples is fit well using two oxidation state components, one with an average $K\alpha_1$ energy position of 2013.56 eV identified as InP and one higher in energy with an average position of 2014.41 eV. Although the SSNMR identifies the oxidized species as phosphate-like, the $K\alpha_1$ energy position is somewhat lower in energy than that of the disodium phosphate reference standard used (2014.55 eV). Though phosphides and sulfides are known to have small shifts in the $K\alpha_1$ energy position due to differing degrees of covalency,[24,25] this hasn't previously been observed in phosphates or sulfates and could be worthy of future investigation. With the identification of phosphate from the SSNMR resonance at ca. 0 ppm and the agreement between the SSNMR and XES results, this confirms the oxidized component at 2014.41 eV corresponds to phosphate.

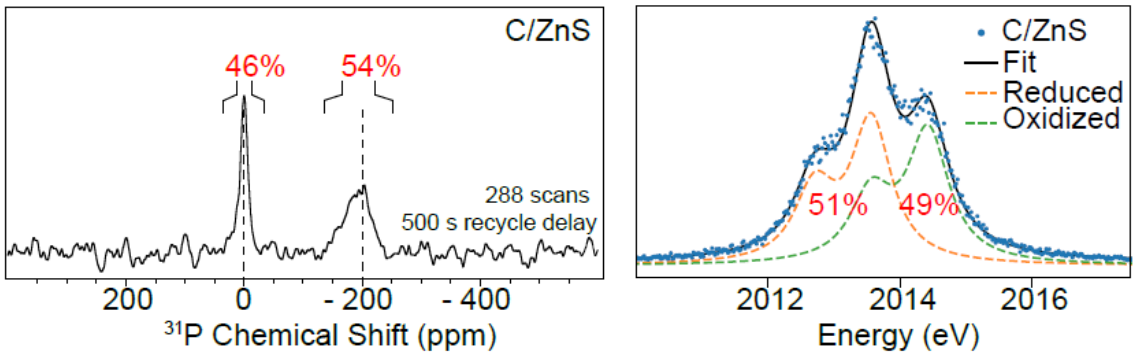

Figure 9.2: Comparison of ^{31}P SSNMR spectrum (left) and P Kα XES (right) of the same batch of InP/ZnS QDs. The SSNMR signal near 0 ppm corresponds to surface phosphate, and this component shows up at a Kα1 energy position of ~2014.41 eV. The relative peak areas in both types of spectra are indicated as percentages.

Table 9.1. Comparison of SSNMR and P Kα XES for Determination of Phosphorus Oxidation State in InP QDs.

Sample	SSNMR (% red)	SSNMR (% ox)	P Kα XES (% red)	P Kα XES (% ox)
InP	93	7	89 ± 3	11 ± 3
InP/Zn	87	13	83 ± 4	17 ± 4
InP/ZnS	54	46	51 ± 5	49 ± 5

These measurements demonstrate that P Kα XES is a reliable tool for measuring phosphorus oxidation having significant advantages over ^{31}P SSNMR spectroscopy. Each XES measurement required <5 mg of material and speciation could be determined within the first 30 minutes, though the measurements were extended to improve the resulting spectra and monitor for possible radiation damage (Figures S1 and S2). The SSNMR measurements required ca. 10-20 mg of material to prepare the samples for measurements (although within the 1.3 mm rotor there is likely less than 1 mg of material). Regardless, the SSNMR spectra typically required multiple days of collection time to obtain spectra that can be reliably integrated. Based on this promising data, we proceeded by measuring the extent of phosphorus oxidation as a function of synthetic method

using XES for rapid feedback, augmented by SSNMR and other methods when appropriate. Our goal is to obtain a uniquely detailed picture of the existence and origin of synthesis-specific adventitious phosphorus oxidation and its correlation with QD QY. A detailed understanding of phosphorus speciation and the degree of oxidation induced by different synthetic procedures is a critical first step to devising new synthetic routes to high performance InP QDs.

9.4.1 Surface oxidation as a function of initial InP synthesis

Here, we evaluate the extent of oxidation that can occur in a core synthesis by studying InP quantum dots synthesized via three different routes. All reactions were performed under air-free conditions in a nitrogen-atmosphere glovebox or on a Schlenk line. All reagents and glassware were rigorously dried as described in the experimental section. A summary of particle characterization for this series of InP QDs including optical peak positions, composition, particle size, and powder diffraction patterns, can be found in Table S3 and Figure S5.

The first synthesis is the most common approach to produce crystalline InP QDs through the reaction between indium carboxylates, excess carboxylic acid, and tris(trimethylsilyl)phosphine, $P(SiMe_3)_3$, at elevated temperatures.[9,43,46] In future reference and plots, InP QDs prepared by this route (indium carboxylates + $P(SiMe_3)_3$) will be referred to as **C**-InP. Although this approach is well-established, water is generated as a by-product from carboxylic acid ketonization at elevated temperatures and thus, the InP QDs are detrimentally impacted through surface oxidation. This oxidation has previously been implicated in the inability to grow InP QDs to large diameters.[14,47] Thus far, water has been identified as the most likely primary source of oxygen atoms involved in phosphate formation.[44,48] Chaudret and co-workers characterized the amorphous surface oxide layer that is produced by the concurrent oxidation through a combination of XPS, IR, and SSNMR spectroscopy.[11]

C-InP was synthesized following a literature procedure in which $P(SiMe_3)_3$ was injected into a 300 ºC 1-octadecene (ODE) bath of indium myristate and excess myristic acid.[49] The resulting particles have a lowest energy electronic transition (LEET) at 530 nm and weak emission features comprised of a peak at 579 nm and a broad red-shifted shoulder that corresponds to band edge and radiative surface defect emission, respectively. The normalized PL spectrum is shown in Figure S6 and corresponds to a PL QY <1%.

In the second synthesis, atomically-precise $In_{37}P_{20}(O_2CR)_{51}$ magic-sized clusters (MSCs) were used as single-source precursors.[41,50] Carboxylate-capped InP MSCs can be purified to remove any freely diffusing carboxylic acid, ensuring that the reaction solution is a homogeneous mixture of only the MSC. We found this an appealing choice for this study since the removal of acidic protons would ideally prevent decarboxylative coupling and aqueous by-products. In future reference, the quantum dots derived from InP MSCs are referred to as **M**-InP.

The production of **M**-InP requires two steps, with the first step being the synthesis and isolation of $In_{37}P_{20}(O_2CR)_{51}$. This can be done by following the conditions to make **C**-InP QDs as described above but dropping the injection/growth temperature to 100 ºC and running the reaction in toluene.[41] The MSCs were purified through gel permeation chromatography (GPC) and analyzed by ^{1}H NMR spectroscopy to ensure the removal of excess acid (Figure S7). At this point, a portion of MSCs, which exist in the form of a waxy solid, can be dissolved in ODE and injected into a 300 ºC solution of ODE. Depending on the concentration of MSCs in the growth solution, particle size can be modified.[41] In this instance, a 60 mg injection of MSC produced particles with a LEET at 555 nm and emission features similar to **C**-InP with the band edge emission at 591 nm (Figure 9.3 and Figure S6). The advantages to using this 2-step route over traditional indium/phosphorus monomer nucleation are two-fold in that the synthesis can be performed more

reproducibly with a homogeneous precursor and the monodispersity of the resulting sample ensemble is improved. TEM images of **M**-InP QDs show this with more ordered packing due to the more uniform particle morphologies.

In the final synthesis method, we examined InP QDs prepared from indium halides and aminophosphines in primary amine solvent. Aminophosphines have been introduced as reliable phosphorus precursors for the synthesis of size-tunable InP QDs when paired with indium halides.[51] The reaction between metal halides and aminophosphines is driven by the dual role of aminophosphines as a phosphorus source and as a reducing agent.[19,52] More importantly for the present work, the aminophosphine synthesis does not involve any oxygen-containing reagents, eliminating the possibility of oxidation via reagent decomposition products. In future reference and plots, InP QDs synthesized with an aminophosphine P-source will be referred to as **A**-InP.

The aminophosphine-based InP QD synthesis diverges from indium carboxylate/silylphosphine chemistry in that the solvent, a primary amine, is coordinating and so acts as a solvent, ligand, and even plays a role in the precursor conversion reactions. Furthermore, Zn(II) was added to the precursor mixture prior to particle nucleation and has been observed to improve the resulting particle crystallinity and monodispersity. Further details can be found in the Experimental section but briefly, zinc chloride and indium chloride were heated to 180 ºC in oleylamine followed by injection of tris(diethylamino)phosphine. The final **A**-InP particles have a LEET at 573 nm and an emission peak at 618 nm (3% PL QY) shown in Figure 9.3 and Figure S6. Replacing carboxylates as surface ligands with chlorides and amines also impacts particle morphology by preferentially binding to the (111) face as seen by the tetrahedral shape of the resulting particles.[14]

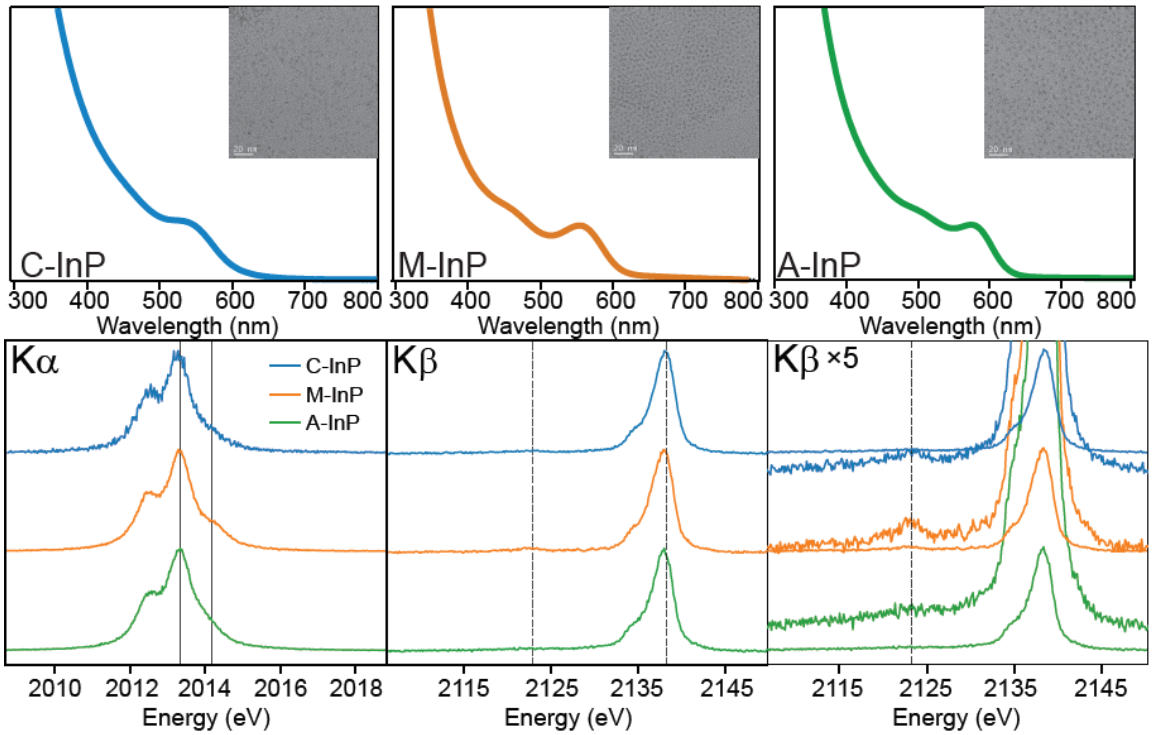

Figure 9.3: The final absorbance trace (top) of C-InP, M-InP, and A-InP with TEM image insets (20 nm scale bar) of purified material. P Kα and Kβ XES spectra (bottom) for the InP QD samples where solid vertical lines in the Kα spectra indicate the InP component (2013.59 eV) and the identified phosphate component (2014.41 eV). In the Kβ spectra, dashed lines indicate the Kβ' peak of phosphate (2123.5 eV), and the $K\beta_{1,3}$ peak of bulk InP (2138.6 eV).

Kα XES measurements were used to measure phosphorus speciation as described in the Experimental section. The P Kα emission spectra of **C**, **M**, and **A**-InP QDs are shown in Figure 9.3 with corresponding peak positions and speciation percentages summarized in Table 9.2. The lower energy component is described as 'reduced' and the higher energy component is described as 'oxidized'. We attribute the 11% oxidized component measured in **C**-InP to the previously characterized ketonization reaction that occurs during particle growth, which is supported by the two phosphorus resonances in the ^{31}P SSNMR spectrum (Figure 9.4a). At elevated temperatures, the excess acid undergoes decarboxylative coupling in which a ketone, carbon dioxide, and water are products. Our initial expectation from the **M**-InP was to circumvent water formation through

the removal of acid (^{1}H NMR, Figure S7). As can be seen from the 16% oxidized component of **M**-InP, this process was difficult to avoid. A solution ^{13}C NMR spectrum of the **M**-InP QDs before purification shows an apparent peak in the expected region for a ketone carbon at 210 ppm (Figure S8); formation of ketone in the synthesis would be accompanied by the formation of water. There is a notable lack of an acidic proton in the ^{1}H NMR spectrum of the initial MSCs, suggesting no free carboxylic acid is present prior to synthesis. Furthermore, the P Kα emission spectrum of the stock MSCs shows that the starting material was not oxidized, which agrees with the single-crystal structure that is fully saturated with surface indium carboxylates (Figure S9).[50] However, we hypothesize that in the case of long-chain carboxylate ligands, carboxylic acid is difficult to remove due to hydrogen bonding interactions and entanglement of the aliphatic side-chains with the carboxylate ligand shell.

Unexpectedly, we measured a 17% oxidized component in the **A**-InP QDs, a synthesis lacking any oxygen-containing precursors. The $K\alpha_1$ energy position of the oxidized population was notably lower in energy than the component near 2014.41 eV identified above as phosphate, which led us to investigate further. P Kβ XES can be used for exactly this question of ligand identity. The strong Kβ' satellite feature at 2123.5 in the phosphate reference standard serves as a fingerprint of the presence of P–O bonds. P Kβ spectra of **C**, **M**, and **A**-InP QDs are shown in Figure 9.3. The **C**-InP and **M**-InP show clear peaks at the phosphate energy position, in qualitative agreement with their relative proportion of oxidized component (11% vs 16% respectively). In contrast, the absence of the Kβ' feature in the **A**-InP spectrum implies that the 17% oxidized component is not due to phosphate.

Table 9.2. Phosphorus Speciation as Determined by Linear Combination Fitting to Kα XES Spectra. For the InP and ZnS-shelled samples, the Kα1 energy positions from two-component fitting are reported. For the ZnSe shelled samples, the Kα1 energy positions of the reduced and oxidized components are reported from three-component fitting.

Sample	Reduced (%)	Oxidized (%)	Estimated Uncertainty (%)	Reduced $K\alpha_1$ energy (eV)	Oxidized $K\alpha_1$ energy (eV)	Reduced-χ^2
C-InP	89	11	± 3	2013.54	2014.40	1.15
M-InP	84	16	± 2	2013.57	2014.50	1.17
A-InP	83	17	± 4	2013.59	2014.29	1.32
C/ZnS	51	49	± 5	2013.57	2014.42	1.32
M/ZnS	62	38	± 4	2013.55	2014.44	1.18
A/ZnS	57	43	± 5	2013.58	2014.42	1.12
C/ZnSe	14	86	± 9	2013.55	2014.32	1.02
M/ZnSe	16	84	± 5	2013.53	2014.41	1.24
A/ZnSe	51	49	± 5	2013.58	2014.45	1.06

To investigate the identity of this component, we utilized XPS and solution ^{31}P NMR spectroscopy to aid in the detection of potential reaction by-products. Following multiple rounds of precipitation and GPC purification, we initially found that the solution ^{31}P NMR spectrum of the stock solution contained no detectable resonances. Over the period of several weeks of storage in a nitrogen atmosphere glovebox however, the solution ^{31}P NMR spectrum revealed P-containing impurities at 80 and 30 ppm (Fig S12). The peak at 80 ppm lies in the region of transaminated species produced during this reaction that likely exist in equilibrium with phosphonium salt byproducts.[19,52] Phosphonium salts, $P(NHR)_4Cl$ in which R is an oleyl group, is the dominant reaction byproduct, forming 3 equivalents for every InP unit formed, and has been previously identified in the ^{31}P NMR spectrum to have a peak at 29 ppm. Although alternative routes to remove P-containing impurities exist, of which ligand exchange with thiols has met with success, subjecting the InP particle surface to further modification was not an ideal pathway with the goal

of probing the surface defects intrinsic to the synthesis. The direct excitation ^{31}P SSNMR spectrum identified that there was a mixed environment of core InP, 91%, centered at –200 ppm and phosphonium salt, 9%, at 30 ppm with a notable absence of signal at 0 ppm that would correspond to surface phosphate species (Fig 4b). The P_{2p} XPS spectrum shown in Figure S11 further supports the identification of a mixed phosphide/phosphonium environment when compared to the peak position of a commercial phosphonium salt (aminotris(dimethylamino)phosphonium chloride). Lastly, we measured the P Kα XES spectrum of the commercial phosphonium salt, and observed a $K\alpha_1$ energy position at 2014.35 eV, which agrees well with the shift of $K\alpha_1$ position to lower energy for the A-InP sample. Taken together, this evidence supports the conclusion that the 17% oxidized component is a result of electrostatically interacting phosphonium impurities and the A-InP particle surface can be considered unsullied P^{3-}.

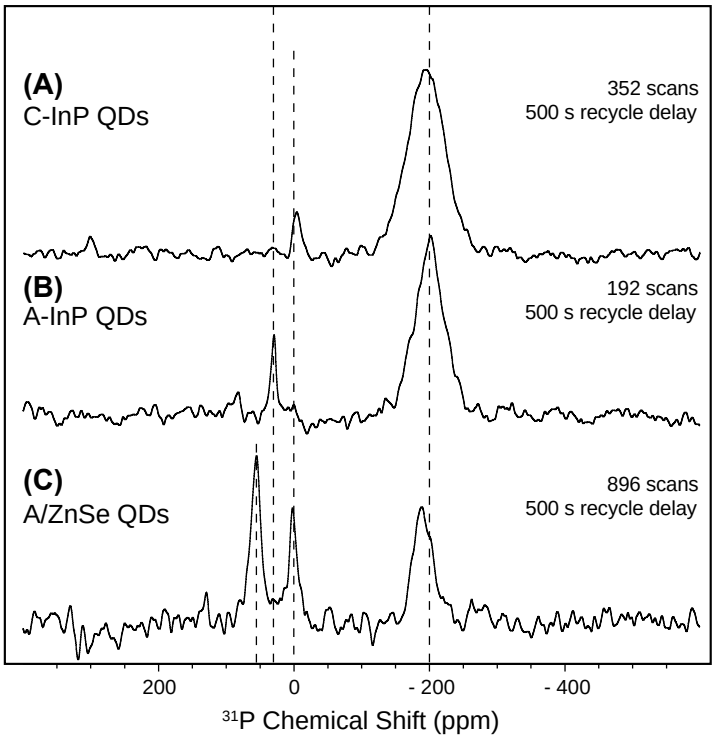

Figure 9.4: ^{31}P SSNMR spectra of (A) C-InP QDs (B) A-InP QDs and (C) A/ZnSe QDs. Dashed lines are to guide the eye to -200 ppm (phosphide resonance), 0 ppm (phosphate resonance), 30 ppm (phosphonium salt resonance), and 55 ppm (TOPO resonance).

As demonstrated by the P Kα emission spectra of InP QDs formed in the presence of carboxylate groups (**C** and **M** samples), ketonization is difficult to prevent, even following attempts to remove excess acid in the case of MSC precursors. Alternatively, utilizing aminophosphines effectively reduces *in-situ* oxidation while also minimizing the cost and hazard of the phosphorus precursor. Progress has been made toward other oxide-free syntheses in which InP is formed by heating indium carboxylates and $P(SiMe_3)_3$ in a 1.8 bar H_2 atmosphere.[17] The authors conclude that H_2 molecules are activated at the QD surface and yield P–H bonds which protect the surface through the concurrent water-forming condensation reactions. At this point, oxidative-defect-free surfaces are accessible if running a synthesis under H_2 or utilizing

aminophosphines with indium halides, while offering different options for surface chemistry or particle morphologies. The general consensus in the field of InP QD chemistry is that the presence of surface phosphorus-oxygen bonds will detrimentally impact subsequent shell growth. We extend the characterization of InP QD oxidation through the addition of ZnE (E=S, Se) shells to gauge the effect further chemical transformations may have on the optical properties and oxidized populations of the InP samples.

9.4.2 Impact of oxidative surface species on optical properties

We chose to examine the resulting properties of the **C**/**M**/**A**-InP series shelled with either a thin ZnS shell or a thick ZnSe shell. With regard to the ZnS shell, we refer back to the work Chaudret and co-workers performed in characterizing the InP/ZnS interface.[12] ZnS was grown by the successive ion layer adsorption and reaction (SILAR) approach in which zinc carboxylate and sulfur powder were added separately at elevated temperatures in order to drive reaction with the InP surface and prevent nucleation of ZnS nanoparticles.[43] Through extensive optimization, thin ZnS shells (<2 nm) have been able to enhance the QY's of InP QDs up to 60-70%. The Chaudret group found that InP is even further oxidized during shell growth due to a series of side reactions. First, elemental sulfur has been observed to form hydrogen sulfide through activation by the solvent, ODE.[53] H_2S then reacts with zinc carboxylate to form carboxylic acids which promote ketonization and water production as seen in the initial InP core syntheses (**C**-InP). They found that the oxidized percentage of phosphorus in the core InP increased from 8% to 21% following shell growth. This approach to ZnS shell growth was selected to compare the impact of an established oxidation chemistry across the series of InP QDs.

The second comparison we focus on is the growth of a thick (>5 nm) ZnSe shell. In addition to minimizing the surface defects to improve the core-shell interface, selecting materials with

similar lattice constants aids in reducing strain. ZnSe has a 3.4% lattice mismatch with InP, which is smaller than that for ZnS at 7.7%, and thus may improve InP optical properties. Recently, thicker ZnSe shells have been reported in the literature to suppress the single-dot PL intermittency of InP QDs associated with nonradiative Auger processes, with QYs reaching 60%.[42,54] While the thick shell effectively cuts off carrier interaction with the environment, the compressive strain induced upon the core nanoparticle can often lead to further lattice strain-related defects.[55] Some of the detrimental effects of thick shells have been offset by alloying, particularly at the interface, or by stacking materials with a gradient lattice, as observed in chalcogenide-based materials.[56–58]

Following purification by GPC, solutions of **C**, **M**, and **A**-InP were dissolved in either ODE or squalane for shell growth. Rather than optimize conditions for maximum QY, we emphasized the comparison across initial InP syntheses by matching the concentration of the InP samples by standardizing the absorption at 310 nm across pre-shelled solutions to add the same amount of Zn and chalcogenide precursors. It should be noted that the particles are not precisely the same size (TEM and λ_{max}), in addition to particle polydispersity, which may contribute to differences among the observed shell thicknesses. A summary of particle characterization for this series of InP/ZnE QDs including optical peak positions, composition, particle size, and powder diffraction patterns, can be found in Table S3 and Figure S5.

ZnS shells were grown following a literature procedure in which zinc myristate and sulfur powder were added individually over 10-minute intervals to InP QDs at elevated temperatures. This layer by layer approach was performed a second time for an intended 2 monolayer ZnS shell. The resulting InP/ZnS particles exhibit a minor blue-shift in their features which we attribute to etching by H_2S produced in the synthesis (Figure 9.5). The measured PL QYs and emission linewidths for **C**/ZnS, **M**/ZnS, and **A**/ZnS were 7% (66 nm), 28% (56 nm), and 25% (69 nm),

respectively. Comparatively, the emission linewidths of highly optimized core-shell InP syntheses are 40-60 nm.[9]

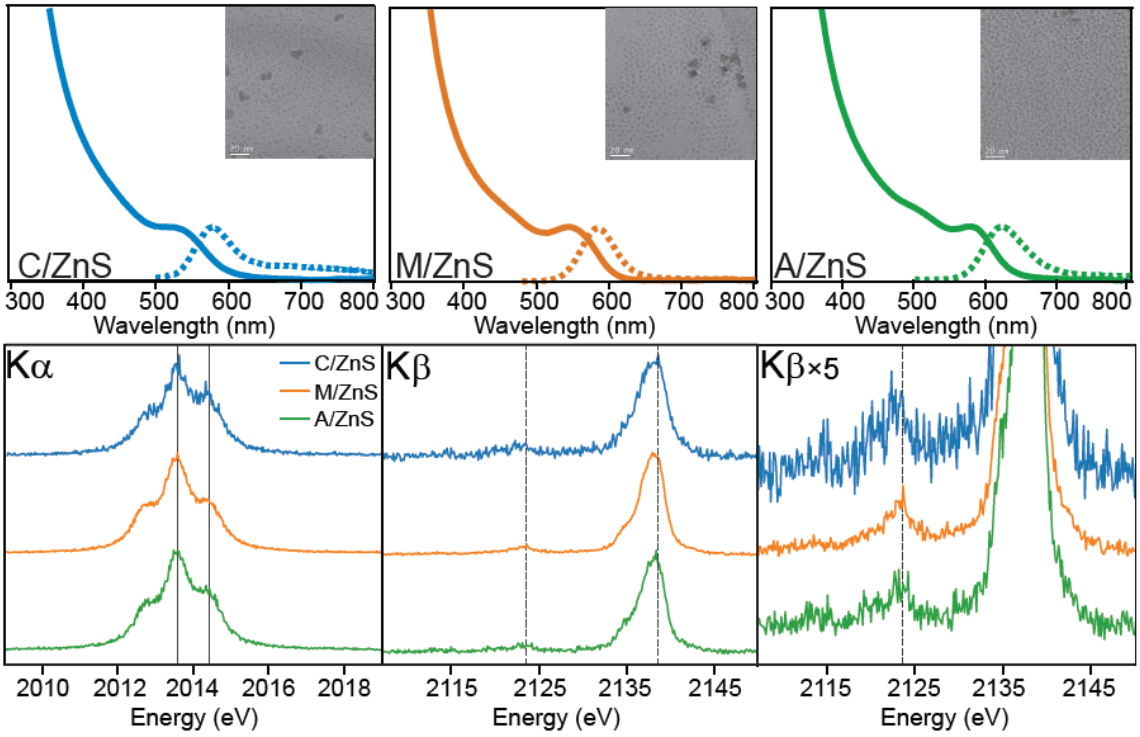

Figure 9.5: The final absorbance (solid) and PL (dashed) trace C/ZnS, M/ZnS, and A/ZnS with TEM image insets (20 nm scale bar) of purified material (top). P Kα and Kβ XES spectra (bottom) for the InP/ZnS samples where solid vertical lines in the Kα spectra indicate the InP component (2013.59 eV) and the identified phosphate component (2014.41 eV). In the Kβ spectra, dashed lines indicate the Kβ' peak of phosphate (2123.5 eV), and the $K\beta_{1,3}$ peak of bulk InP (2138.6 eV).

The P Kα emission spectra of the InP/ZnS samples demonstrate that each InP core was significantly oxidized (Figure 9.5). Peak positions, given in Table 2, are in line with our identified phosphate and phosphide components and show that the phosphate population for all samples increased to a range of 38-49%. The P Kβ spectrum supports the identification of the oxidized component as phosphate, with strong Kβ' peaks at 2123.5 eV (Figure 9.5). From previous reports of a shell growth-coupled oxidation event, we expected a substantial increase in phosphorus

oxidation. Surprisingly, the extent of phosphorus oxidation is apparently not dependent on the initial InP surface environment. Along those lines, it is difficult to correlate the extent of phosphorus oxidation with the optical properties since in each case a majority of the surface phosphorus were converted to phosphates. The important conclusion from this series of samples is that even when starting with an ideally oxidative defect-free surface, adventitious side reactions during shell growth will still significantly impact the InP surface and thus the core-shell interface.

With regard to InP/ZnSe, chemists have postulated that incomplete blinking suppression and low quantum yields (40-60%) originate from point defects at the core-shell interface, which was a motivating aspect of studying these samples. Similarly, to the ZnS shell growth, InP QD solutions were matched in concentration across **C**, **M**, and **A** in order to reliably compare across the three. Again, utilizing a SILAR approach, zinc myristate and trioctylphosphine-selenide (TOP-Se) were added to InP QDs at elevated temperatures at varying time intervals (see Experimental section for specific details). Two distinct features arise in the absorbance spectra, one of which is a significant increase in higher energy absorbance due to the thick ZnSe shell. Secondly, the LEET experiences a red-shift due to the near overlap of the InP and ZnSe conduction band edges (Figure 9.6). The emission linewidths range from 59 to 84 nm with the **M**-InP giving the narrowest linewidth (59 nm) likely due to the improved monodispersity of the starting InP cores.

Compared to the InP/ZnS samples, the PL QY of these un-optimized syntheses were slightly greater with a maximum of 44% from the **M**/ZnSe and 10% and 30% for **C**/ZnSe and **A**/ZnSe, respectively. At least in the case of the **C**/ZnSe, there was a mixture of thick-shelled particles and what could be partially shelled or unshelled InP QDs that limit the measured quantum yield (Figure 9.6). For a majority of the **C** and **M**/ZnSe, the morphology of the shelled particles was tetrahedral while the **A**/ZnSe appeared to shell less uniformly and typically looked bulbous,

suggesting shell nucleation occurred separately at each vertex of the InP tetrahedron as opposed to conformal shell deposition on the more spherical cores observed in **C** and **M**. Shell uniformity will also play a role in optimizing emissive properties due to the detrimental impact of structural defects. Furthermore, because of the substantial shell thickness, XPS analysis of the InP/ZnSe only revealed the phosphate peak, most likely because photoelectrons generated in the core phosphide have a lower probability of escaping (Figure S12). In this context, XPS becomes an imprecise and unreliable technique.

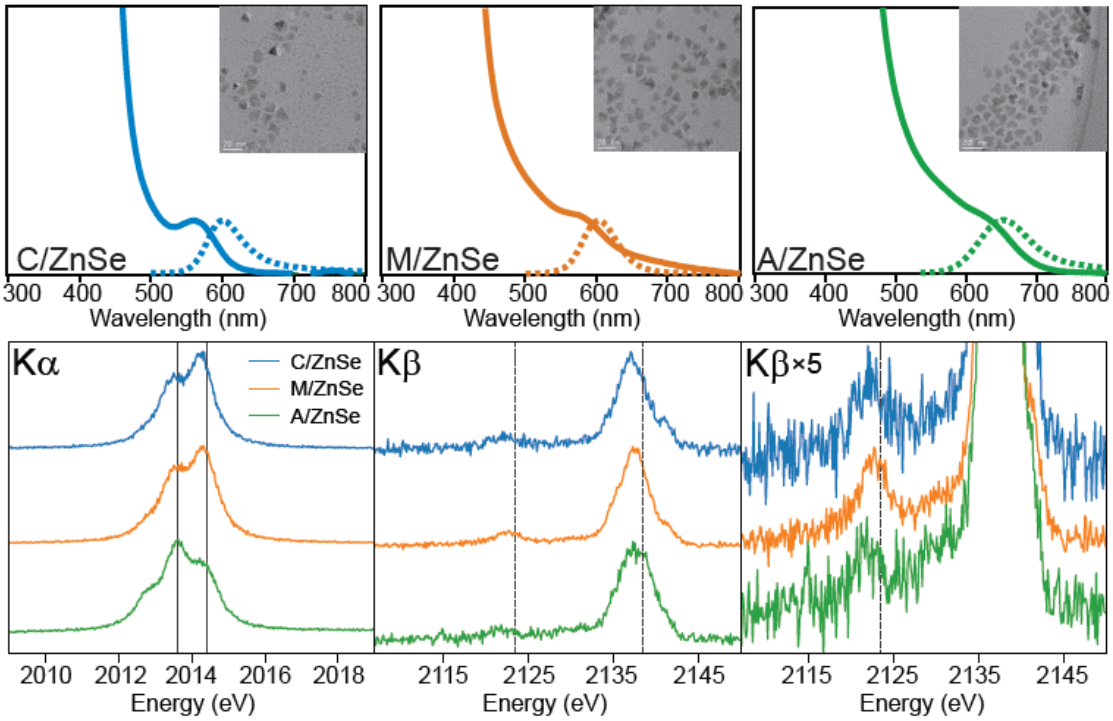

Figure 9.6: The final absorbance (solid) and PL (dashed) trace of C/ZnSe, M/ZnSe, and A/ZnSe with TEM image insets (20 nm scale bar) of purified material (top). P Kα and Kβ XES spectra (bottom) for the InP/ZnSe samples where solid vertical lines in the Kα spectra indicate the InP component (2013.59 eV) and the identified phosphate component (2014.41 eV). In the Kβ spectra, dashed lines indicate the Kβ' peak of phosphate (2123.5 eV), and the $K\beta_{1,3}$ peak of bulk InP (2138.6 eV).

The P Kα emission spectra of the InP/ZnSe, shown in Figure 9.6, were distinctive in that the peak positions from two-component fitting did not overlap with our identified phosphide and phosphate components. The oxidized $K\alpha_1$ were shifted lower in energy and the reduced $K\alpha_1$ were shifted to higher energy (Table S4). These shifts, combined with the higher reduced-χ squared statistic of the **A**/ZnSe and **M**/ZnSe fits, suggests that the two-component fitting procedure does not sufficiently explain the observed spectra. Furthermore, we observed several differences in the Kβ emission spectra from typical InP such as the shift of the $K\beta_{1,3}$ peak to lower energies and a pronounced shoulder at 2140.5 eV (Figure 9.6).

To reconcile these clear changes in the Kα and Kβ spectra for the ZnSe-shelled samples, we considered the possibility of a third significant phosphorus species present in the sample. Fortunately, the main decomposition product of TOP-Se has been previously identified as trioctylphosphine oxide (TOPO) through precursor evolution studies of cadmium chalcogenide nanocrystals.[59,60] The Kβ emission spectrum of TOPO (shown in Figure 9.1) qualitatively matched the distinctive features observed in the InP/ZnSe samples. Although sample purification focused on the removal of excess ligands and by-products, complete removal is often complicated because of entanglement of long chain hydrocarbons, and in this case by weak binding of the TOPO to the particle surface. Thus, in order to evaluate the reduced and oxidized populations excluding the TOPO component, the Kα spectra were fit with three P $K\alpha_{1,2}$ doublets as described in the Experimental section. This procedure results in improved fits for the **A**/ZnSe and **M**/ZnSe samples (Figure S13) and improved $K\alpha_1$ energy positions for all three samples (Table S5). Our analysis was further supported by the ^{31}P SSNMR spectrum of the **A**/ZnSe sample in which three populations of phosphorus are measured; phosphide at –200 ppm, phosphate at 0 ppm, and TOPO at 55 ppm, of which the integrated areas agree qualitatively with the three-component fitting results

(F6). The presence of a significant phosphate species in each of these samples also agrees qualitatively with the Kβ spectra, each of which has a significant phosphate Kβ' peak near 2123.5 eV, much stronger in proportion than the spectral features exhibited in the TOPO spectrum.

X-ray emission spectra of InP/ZnSe samples shows very high oxidized components. In the case of the **A**/ZnSe, roughly 51% of the phosphorus remain as phosphide while a mere ~15% of the phosphide component in the **C**/ZnSe or **M**/ZnSe was retained. We estimated that the core InP particles would have roughly 55-70% of the total phosphorus exposed to the surface, thus while the pathway of oxidation during ZnSe shell growth is unknown, it is reasonable that nearly all surface sites are oxidized. Additionally, we would not expect oxidative defects to penetrate beyond the surface of the InP core so we suggest that anion diffusion occurs during shell growth (in the case of thick shells) that allows core phosphides to migrate to the surface of the shell. Evidence supporting this proposed anion diffusion mechanism was presented by Rosenthal *et al.* in which the energy dispersive X-ray chemical maps of InP/ZnSe particles demonstrate alloying of In/P atoms into the Zn/Se shell.[54] They hypothesized that alloying helps mitigate the increasing strain induced by the growth of a thick shell.

Our goal to examine the correlation between surface oxidation and luminescence properties in the InP/ZnSe samples was similarly obstructed by excessive oxidation that prevented a careful analysis of these key factors. As with the InP/ZnS particles, the core-shell interface is thoroughly oxidized regardless of the defect-free surface of the starting materials (i.e. **A**-InP). These results emphasize the importance of critically examining the chemistry occurring after the InP core growth phase, especially when rigorous care is taken to improve the quality of the core particles. There has been a growing awareness to address the issue of introducing oxidative defects during shell growth. For example, Jeong *et al.* targeted the growth of a ZnS shell in the absence of acid-

containing precursors and reported a phosphate-free interface, but the PL QYs of these samples still plateaued at 60%.[14] If indeed the particles experienced no oxidation through core/shell growth, which was assessed with XPS, non-radiative recombination defect sites likely still formed as a combined result of compressive strain because of the growth of a >5 nm shell and the lattice mismatch between InP and ZnS.

9.5 Conclusions

Using a recently developed benchtop X-ray emission spectrometer, we have demonstrated the viability of phosphorus Kα XES measurements as a quantitative analytical tool to characterize the extent of oxidation in InP quantum dots through a comparative analysis with ^{31}P SSNMR spectroscopy. Complemented by measurements of the valence-to-core P Kβ emission using the same spectrometer, we were able to identify the presence of phosphate species and phosphine/phosphonium salt by-products, which were also confirmed by ^{31}P SSNMR. XES measurements gave us the capability to rapidly measure a high volume of samples with excellent resolution from only a few milligrams of deposited material. This demonstration strongly suggests a future in which benchtop XES serves a role in the routine analysis of phosphorus compounds and materials.

We examined the impact of phosphorus oxidation on InP optical properties by measuring surface phosphorus oxidation as a function of synthetic method and shelling strategy. The high degree of oxidation in the shelled compounds limit a careful interpretation of the correlation between QY and oxidized P, while being further complicated by various other synthetic factors. In this regard, the use of ultrafast spectroscopy and high-resolution electron microscopy may aid in elucidating a more apparent relationship. While there are routes to achieving a phosphate-free surface, these result in the specific ligation environment and particle morphology associated with

indium halides and aminophosphine precursors. To expand upon the available options, it may serve the field to develop a deeper understanding of the mechanism involving fluoride etching to address surface defects on QD surfaces,[61,62] and develop new chemical methods to remove phosphate defects. Side reactions occurring during shell growth further oxidize the interface to the extent that the initial condition of the core surface is inconsequential. Current industry patents cite the usage of the same precursors examined in this study, implicating the presence of oxidized surfaces and rationalizing the lower than expected PL QYs.[6] This strongly motivates a push towards designing shelling syntheses involving innocent precursors in an effort to minimize interfacial defect sites and optimizing conditions to prevent significant diffusion of phosphorus from the QD core.

9.6 Associated Content

Supporting Information

Additional details regarding X-ray emission spectra fitting and QD characterization can be found in the supporting in-formation PDF. The Supporting Information is available free of charge on the ACS Publications website.

9.7 Acknowledgement

This research (B.M.C. and J.L.S) was partially supported by the U.S. National Science Foundation through the University of Washington Molecular Engineering Materials Center, a Materials Research Science and Engineering Center (grant no. DMR-1719797). This work (W.M.H. and G.T.S) was par-tially supported by the Joint Plasma Physics Program of the National Science Foundation and the Department of Energy under Grant No. DE-SC0016251. A.J.R and A.V. were sup-ported by the U.S. Department of Energy (DOE), Office of Science, Basic Energy Sciences, Materials Science and Engi-neering Division. The Ames Laboratory is operated for the U.S. DOE by Iowa State University under contract # DE-AC02-07CH11358. Part of this work was

conducted at the Molecu-lar Analysis Facility, a National Nanotechnology Coordinated Infrastructure site at the University of Washington, which is supported in part by the National Science Foundation (grant ECC-1542101), the University of Washington, the Molecular Engineering & Sciences Institute, the Clean Energy Institute, and the National Institutes of Health.

9.8 ABBREVIATIONS

QD, quantum dot; PL, photoluminescence; QY, quantum yield; MAS, magic angle spinning; SSNMR, solid state nuclear magnetic resonance; XES, X-ray emission spectroscopy; XPS, X-ray photoelectron spectroscopy; ICP-OES, inductively coupled plasma optical emission spectroscopy; LEET, lowest energy electronic transition; XRD, X-ray diffraction; TEM, transmission electron microscopy; MSC, magic-sized cluster; ODE, 1-octadecene; GPC, gel permeation chromatography.

9.9 REFERENCES

(1) Chopra, S. S.; Theis, T. L. Comparative Cradle-to-Gate Energy Assessment of Indium Phosphide and Cadmium Selenide Quantum Dot Displays. *Environ. Sci. Nano* **2017**, *4* , 244–254.

(2) Shirasaki, Y.; Supran, G. J.; Bawendi, M. G.; Bulovic, V. Emergence of Colloidal Quantum-Dot Light-Emitting Technologies. *Nature Photon.* **2013**, *7*, 13–23.

(3) Supran, G. J.; Shirasaki, Y.; Song, K. W.; Caruge, J.-M.; Kazlas, P. T.; Coe-Sullivan, S.; Andrew, T. L.; Bawendi, M. G.; Bulović, V. QLEDs for Displays and Solid-State Lighting. *MRS Bull.* **2013**, *38*, 703–711.

(4) Steckel, J. S.; Ho, J.; Hamilton, C.; Xi, J.; Breen, C.; Liu, W.; Allen, P.; Coe-Sullivan, S. Quantum Dots: The Ultimate down-Conversion Material for LCD Displays. *J. Soc. Inf. Disp.* **2015**, *23*, 294–305.

(5) Anc, M. J.; Pickett, N. L.; Gresty, N. C.; Harris, J. A.; Mishra, K. C. Progress in Non-Cd Quantum Dot Development for Lighting Applications. *ECS J. Solid State Sci. Technol.* **2013**, *2*, 3071–3082.

(6) Jun, S. A.; Jang, E. J.; Kwon, S. K.; Kim, T. H.; Lee, W. J. Semiconductor Nanocrystal, and Method of Preparing the Same. US20140117292A1, May 1, 2014.

(7) Kim, S.; Kim, T.; Kang, M.; Kwak, S. K.; Yoo, T. W.; Park, L. S.; Yang, I.; Hwang, S.; Lee, J. E.; Kim, S. K.; et al. Highly Luminescent InP/GaP/ZnS Nanocrystals and Their Application to White Light-Emitting Diodes. *J. Am. Chem. Soc.* **2012**, *134*, 3804–3809.

(8) Lim, J.; Bae, W. K.; Lee, D.; Nam, M. K.; Jung, J.; Lee, C.; Char, K.; Lee, S. InP@ZnSeS, Core@Composition Gradient Shell Quantum Dots with Enhanced Stability. *Chem. Mater.* **2011**, *23*, 4459–4463.
(9) Tamang, S.; Lincheneau, C.; Hermans, Y.; Jeong, S.; Reiss, P. Chemistry of InP Nanocrystal Syntheses. *Chem. Mater.* **2016**, *28*, 2491–2506.
(10) Jasinski, J.; Leppert, V. J.; Lam, S.-T.; Gibson, G. A.; Nauka, K.; Yang, C. C.; Zhou, Z.-L. Rapid Oxidation of InP Nanoparticles in Air. *Solid State Commun.* **2007**, *141*, 624–627.
(11) Cros-Gagneux, A.; Delpech, F.; Nayral, C.; Cornejo, A.; Coppel, Y.; Chaudret, B. Surface Chemistry of InP Quantum Dots: A Comprehensive Study. *J. Am. Chem. Soc.* **2010**, *132*, 18147–18157.
(12) Virieux, H.; Le Troedec, M.; Cros-Gagneux, A.; Ojo, W.-S.; Delpech, F.; Nayral, C.; Martinez, H.; Chaudret, B. InP/ZnS Nanocrystals: Coupling NMR and XPS for Fine Surface and Interface Description. *J. Am. Chem. Soc.* **2012**, *134*, 19701–19708.
(13) Ramasamy, P.; Kim, B.; Lee, M.-S.; Lee, J.-S. Beneficial Effects of Water in the Colloidal Synthesis of InP/ZnS Core–Shell Quantum Dots for Optoelectronic Applications. *Nanoscale* **2016**, *8*, 17159–17168.
(14) Kim, K.; Yoo, D.; Choi, H.; Tamang, S.; Ko, J.-H.; Kim, S.; Kim, Y.-H.; Jeong, S. Halide–Amine Co-Passivated Indium Phosphide Colloidal Quantum Dots in Tetrahedral Shape. *Angew. Chem. Int. Ed.* **2016**, *55*, 3714–3718.
(15) Gary, D. C.; Cossairt, B. M. Role of Acid in Precursor Conversion During InP Quantum Dot Synthesis. *Chem. Mater.* **2013**, *25*, 2463–2469.
(16) Xie, L.; Harris, D. K.; Bawendi, M. G.; Jensen, K. F. Effect of Trace Water on the Growth of Indium Phosphide Quantum Dots. *Chem. Mater.* **2015**, *27*, 5058–5063.
(17) Baquero, E. A.; Virieux, H.; Swain, R. A.; Gillet, A.; Cros-Gagneux, A.; Coppel, Y.; Chaudret, B.; Nayral, C.; Delpech, F. Synthesis of Oxide-Free InP Quantum Dots: Surface Control and H_2-Assisted Growth. *Chem. Mater.* **2017**, *29*, 9623–9627.
(18) Xi, L.; Cho, D.-Y.; Besmehn, A.; Duchamp, M.; Grützmacher, D.; Lam, Y. M.; Kardynał, B. E. Effect of Zinc Incorporation on the Performance of Red Light Emitting InP Core Nanocrystals. *Inorg. Chem.* **2016**, *55*, 8381–8386.
(19) Buffard, A.; Dreyfuss, S.; Nadal, B.; Heuclin, H.; Xu, X.; Patriarche, G.; Mézailles, N.; Dubertret, B. Mechanistic Insight and Optimization of InP Nanocrystals Synthesized with Aminophosphines. *Chem. Mater.* **2016**, *28*, 5925–5934.
(20) Berends, A. C.; van der Stam, W.; Hofmann, J. P.; Bladt, E.; Meeldijk, J. D.; Bals, S.; de Mello Donega, C. Interplay between Surface Chemistry, Precursor Reactivity, and Temperature Determines Outcome of ZnS Shelling Reactions on $CuInS_2$ Nanocrystals. *Chem. Mater.* **2018**, *30*, 2400–2413.
(21) Holden, W. M.; Hoidn, O. R.; Ditter, A. S.; Seidler, G. T.; Kas, J.; Stein, J. L.; Cossairt, B. M.; Kozimor, S. A.; Guo, J.; Ye, Y.; et al. A Compact Dispersive Refocusing Rowland Circle X-Ray Emission Spectrometer for Laboratory, Synchrotron, and XFEL Applications. *Rev. Sci. Instrum.* **2017**, *88*, 073904.
(22) Holden, W.; Seidler, G. T.; Cheah, S. Sulfur Speciation in Biochars by Very High Resolution Benchtop Kα X-Ray Emission Spectroscopy. *J. Phys. Chem. A* **2018**, *122*, 5153–5161.
(23) Petric, M.; Kavčič, M. Chemical Speciation via X-Ray Emission Spectroscopy in the Tender X-Ray Range. *J. Anal. At. Spectrom.* **2016**, *31*, 450–457.

(24) Petric, M.; Bohinc, R.; Bučar, K.; Žitnik, M.; Szlachetko, J.; Kavčič, M. Chemical State Analysis of Phosphorus Performed by X-Ray Emission Spectroscopy. *Anal. Chem.* **2015**, *87*, 5632–5639.
(25) Alonso Mori, R.; Paris, E.; Giuli, G.; Eeckhout, S. G.; Kavčič, M.; Žitnik, M.; Bučar, K.; Pettersson, L. G. M.; Glatzel, P. Electronic Structure of Sulfur Studied by X-Ray Absorption and Emission Spectroscopy. *Anal. Chem.* **2009**, *81*, 6516–6525.
(26) Kavčič, M.; Petric, M.; Vogel-Mikuš, K. Chemical Speciation Using High Energy Resolution PIXE Spectroscopy in the Tender X-Ray Range. *Nucl. Instrum. Methods Phys. Res. Sect. B Beam Interact. Mater. At.* **2018**, *417*, 65–69.
(27) Kavčič, M.; Karydas, A. .; Zarkadas, C. Chemical State Analysis of Sulfur in Samples of Environmental Interest Using High Resolution Measurement of Kα Diagram Line. *Nucl. Instrum. Methods Phys. Res. Sect. B Beam Interact. Mater. At.* **2004**, *222*, 601–608.
(28) Pollock, C. J.; DeBeer, S. Insights into the Geometric and Electronic Structure of Transition Metal Centers from Valence-to-Core X-Ray Emission Spectroscopy. *Acc. Chem. Res.* **2015**, *48*, 2967–2975.
(29) Kowalska, J.; DeBeer, S. The Role of X-Ray Spectroscopy in Understanding the Geometric and Electronic Structure of Nitrogenase. *Biochim. Biophys. Acta BBA - Mol. Cell Res.* **2015**, *1853*, 1406–1415.
(30) Pollock, C. J.; DeBeer, S. Valence-to-Core X-Ray Emission Spectroscopy: A Sensitive Probe of the Nature of a Bound Ligand. *J. Am. Chem. Soc.* **2011**, *133*, 5594–5601.
(31) Lancaster, K. M.; Roemelt, M.; Ettenhuber, P.; Hu, Y.; Ribbe, M. W.; Neese, F.; Bergmann, U.; DeBeer, S. X-Ray Emission Spectroscopy Evidences a Central Carbon in the Nitrogenase Iron-Molybdenum Cofactor. *Science* **2011**, *334*, 974–977.
(32) Mori, R. A.; Paris, E.; Giuli, G.; Eeckhout, S. G.; Kavčič, M.; Žitnik, M.; Bučar, K.; Pettersson, L. G. M.; Glatzel, P. Sulfur-Metal Orbital Hybridization in Sulfur-Bearing Compounds Studied by X-Ray Emission Spectroscopy. *Inorg. Chem.* **2010**, *49*, 6468–6473.
(33) Lee, N.; Petrenko, T.; Bergmann, U.; Neese, F.; DeBeer, S. Probing Valence Orbital Composition with Iron Kβ X-Ray Emission Spectroscopy. *J. Am. Chem. Soc.* **2010**, *132*, 9715–9727.
(34) Bergmann, U.; Horne, C. R.; Collins, T. J.; Workman, J. M.; Cramer, S. P. Chemical Dependence of Interatomic X-Ray Transition Energies and Intensities – a Study of Mn Kβ″ and Kβ2,5 Spectra. *Chem. Phys. Lett.* **1999**, *302*, 119–124.
(35) Holden, W. M.; Hoidn, O. R.; Seidler, G. T. A Color X-Ray Camera for 2 – 6 KeV Using a Back-Illuminated Mass-Produced CMOS Sensor. *J. Instrum.* **2018**, *In preparation*.
(36) Newville, M.; Stensitzki, T.; Allen, D. B.; Ingargiola, A. Lmfit: Non-Linear Least-Square Minimization And Curve-Fitting For Python. Zenodo September 21, 2014.
(37) Glassy, B. A.; Cossairt, B. M. Ternary Synthesis of Colloidal Zn3P2 Quantum Dots. *Chem. Commun.* **2015**, *51*, 5283–5286.
(38) Shen, Y.; Gee, M. Y.; Tan, R.; Pellechia, P. J.; Greytak, A. B. Purification of Quantum Dots by Gel Permeation Chromatography and the Effect of Excess Ligands on Shell Growth and Ligand Exchange. *Chem. Mater.* **2013**, *25*, 2838–2848.
(39) Roberge, A.; Stein, J. L.; Shen, Y.; Cossairt, B. M.; Greytak, A. B. Purification and In Situ Ligand Exchange of Metal-Carboxylate-Treated Fluorescent InP Quantum Dots via Gel Permeation Chromatography. *J. Phys. Chem. Lett.* **2017**, *8*, 4055–4060.

(40) Stein, J. L.; Mader, E. A.; Cossairt, B. M. Luminescent InP Quantum Dots with Tunable Emission by Post-Synthetic Modification with Lewis Acids. *J. Phys. Chem. Lett.* **2016**, *7*, 1315–1320.
(41) Gary, D. C.; Terban, M. W.; Billinge, S. J. L.; Cossairt, B. M. Two-Step Nucleation and Growth of InP Quantum Dots via Magic-Sized Cluster Intermediates. *Chem. Mater.* **2015**, *27*, 1432–1441.
(42) Chandrasekaran, V.; Tessier, M. D.; Dupont, D.; Geiregat, P.; Hens, Z.; Brainis, E. Nearly Blinking-Free, High-Purity Single-Photon Emission by Colloidal InP/ZnSe Quantum Dots. *Nano Lett.* **2017**, *17*, 6104–6109.
(43) Xie, R.; Battaglia, D.; Peng, X. Colloidal InP Nanocrystals as Efficient Emitters Covering Blue to Near-Infrared. *J. Am. Chem. Soc.* **2007**, *129*, 15432–15433.
(44) Baquero, E. A.; Ojo, W.-S.; Coppel, Y.; Chaudret, B.; Urbaszek, B.; Nayral, C.; Delpech, F. Identifying Short Surface Ligands on Metal Phosphide Quantum Dots. *Phys. Chem. Chem. Phys.* **2016**, *18*, 17330–17334.
(45) Tomaselli, M.; Yarger, J. L.; Bruchez, M.; Havlin, R. H.; deGraw, D.; Pines, A.; Alivisatos, A. P. NMR Study of InP Quantum Dots: Surface Structure and Size Effects. *J. Chem. Phys.* **1999**, *110*, 8861–8864.
(46) Battaglia, D.; Peng, X. Formation of High Quality InP and InAs Nanocrystals in a Noncoordinating Solvent. *Nano Lett.* **2002**, *2*, 1027–1030.
(47) Ramasamy, P.; Ko, K.-J.; Kang, J.-W.; Lee, J.-S. Two-Step "Seed-Mediated" Synthetic Approach to Colloidal Indium Phosphide Quantum Dots with High-Purity Photo- and Electroluminescence. *Chem. Mater.* **2018**, *30*, 3643–3647.
(48) Cervilla, A.; Pérez-Pla, F.; Llopis, E.; Piles, M. Unusual Oxidation of Phosphines Employing Water as the Oxygen Atom Source and Tris(Benzene-1,2-Dithiolate)Molybdenum(VI) as the Oxidant. A Functional Molybdenum Hydroxylase Analogue System. *Inorg. Chem.* **2006**, *45*, 7357–7366.
(49) Gary, D. C.; Glassy, B. A.; Cossairt, B. M. Investigation of Indium Phosphide Quantum Dot Nucleation and Growth Utilizing Triarylsilylphosphine Precursors. *Chem. Mater.* **2014**, *26*, 1734–1744.
(50) Gary, D. C.; Flowers, S. E.; Kaminsky, W.; Petrone, A.; Li, X.; Cossairt, B. M. Single-Crystal and Electronic Structure of a 1.3 Nm Indium Phosphide Nanocluster. *J. Am. Chem. Soc.* **2016**, *138*, 1510–1513.
(51) Tessier, M. D.; Dupont, D.; Nolf, K. D.; Roo, J. D.; Hens, Z. Economic and Size-Tunable Synthesis of InP/ZnE (E = S, Se) Colloidal Quantum Dots. *Chem. Mater.* **2015**, *27*, 4893-4898.
(52) Tessier, M. D.; De Nolf, K.; Dupont, D.; Sinnaeve, D.; De Roo, J.; Hens, Z. Aminophosphines: A Double Role in the Synthesis of Colloidal Indium Phosphide Quantum Dots. *J. Am. Chem. Soc.* **2016**, *138*, 5923–5929.
(53) Li, Z.; Ji, Y.; Xie, R.; Grisham, S. Y.; Peng, X. Correlation of CdS Nanocrystal Formation with Elemental Sulfur Activation and Its Implication in Synthetic Development. *J. Am. Chem. Soc.* **2011**, *133*, 17248–17256.
(54) Reid, K. R.; McBride, J. R.; Freymeyer, N. J.; Thal, L. B.; Rosenthal, S. J. Chemical Structure, Ensemble and Single-Particle Spectroscopy of Thick-Shell InP–ZnSe Quantum Dots. *Nano Lett.* **2018**, *18*, 709–716.
(55) Gong, K.; Kelley, D. F. Lattice Strain Limit for Uniform Shell Deposition in Zincblende CdSe/CdS Quantum Dots. *J. Phys. Chem. Lett.* **2015**, *6*, 1559–1562.

(56) Nasilowski, M.; Spinicelli, P.; Patriarche, G.; Dubertret, B. Gradient CdSe/CdS Quantum Dots with Room Temperature Biexciton Unity Quantum Yield. *Nano Lett.* **2015**, *15*, 3953–3958.
(57) Jeong, B. G.; Park, Y.-S.; Chang, J. H.; Cho, I.; Kim, J. K.; Kim, H.; Char, K.; Cho, J.; Klimov, V. I.; Park, P.; et al. Colloidal Spherical Quantum Wells with Near-Unity Photoluminescence Quantum Yield and Suppressed Blinking. *ACS Nano* **2016**, *10*, 9297–9305.
(58) Bae, W. K.; Padilha, L. A.; Park, Y.-S.; McDaniel, H.; Robel, I.; Pietryga, J. M.; Klimov, V. I. Controlled Alloying of the Core–Shell Interface in CdSe/CdS Quantum Dots for Suppression of Auger Recombination. *ACS Nano* **2013**, *7*, 3411–3419.
(59) Frenette, L. C.; Krauss, T. D. Uncovering Active Precursors in Colloidal Quantum Dot Synthesis. *Nat. Commun.* **2017**, *8*, 2082.
(60) Liu, H.; Owen, J. S.; Alivisatos, A. P. Mechanistic Study of Precursor Evolution in Colloidal Group II−VI Semiconductor Nanocrystal Synthesis. *J. Am. Chem. Soc.* **2007**, *129*, 305–312.
(61) Lovingood, D. D.; Strouse, G. F. Microwave Induced In-Situ Active Ion Etching of Growing InP Nanocrystals. *Nano Lett.* **2008**, *8*, 3394–3397.
(62) Siramdas, R.; McLaurin, E. J. InP Nanocrystals with Color-Tunable Luminescence by Microwave-Assisted Ionic-Liquid Etching. *Chem. Mater.* **2017**, *29*, 2101–2109.

CHAPTER 10 PROBING SULFUR CHEMICAL AND ELECTRONIC STRUCTURE WITH EXPERIMENTAL OBSERVATION AND QUANTITATIVE THEORETICAL PREDICTION OF KA AND VALENCE-TO-CORE KB X-RAY EMISSION SPECTROSCOPY

Submitted for publication: Holden, W. M.; Jahrman, E. P.; Govind, N.; Seidler, G. T. Probing Sulfur Chemical and Electronic Structure with Experimental Observation and Quantitative Theoretical Prediction of Kα and Valence-to-Core Kβ X-Ray Emission Spectroscopy.

This chapter represents a significant portion of this dissertation, and I led the effort for this work.

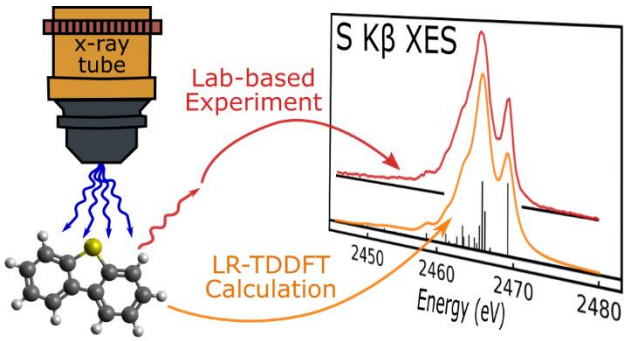

Figure 10.0: Table of contents graphic.

An extensive experimental and theoretical study of the Kα and Kβ high-resolution x-ray emission spectroscopy (XES) of sulfur-bearing systems is presented. This study encompasses a wide range of organic and inorganic compounds, including numerous experimental spectra from both prior published work and new measurements. Employing a linear-response time-dependent density functional theory (LR-TDDFT) approach, strong quantitative agreement is found in the calculation of energy shifts of the core-to-core Kα as well as the full range of spectral features in

the valence-to-core Kβ spectrum. The ability to accurately calculate the sulfur Kα energy shift supports the use of sulfur Kα XES as a bulk-sensitive tool for assessing sulfur speciation. Fine structure of the sulfur Kβ spectrum, in conjunction with the theoretical results, is shown to be sensitive to the local electronic structure including effects of symmetry, ligand type and number, and, in the case of organosulfur compounds, to the nature of the bonded organic moiety. This agreement between theory and experiment, augmented by the potential for high-access XES measurements with the latest generation of laboratory-based spectrometers, demonstrates the possibility of broad analytical use of XES for sulfur and nearby third-row elements. The effective solution of the forward problem, i.e., successful prediction of detailed spectra from known molecular structure, also suggests future use of supervised machine learning approaches to experimental inference, as has seen recent interest for interpretation of x-ray absorption near edge structure (XANES).

10.1 INTRODUCTION

Sulfur has ubiquitous roles in chemistry, from energy storage[1-3] to biochemistry,[4] catalysis,[5-6] and environmental science.[7-8] Understanding the chemical interactions and electronic structure of sulfur is of critical importance towards making advances in many of these fields. While numerous analytical techniques have been used to characterize sulfur containing compounds, element-specific techniques that are capable of interrogating the sulfur directly regardless of the surrounding matrix are of particular importance. Nuclear magnetic resonance (NMR) of sulfur is possible, but suffers from a low natural abundance of active nuclei and broad signals. X-ray spectroscopic techniques fulfill this role and much research has been conducted with synchrotron x-ray absorption near-edge spectroscopy (XANES) as well as x-ray photoelectron

spectroscopy (XPS). These techniques have some drawbacks, in particular the difficulty of access to synchrotron XANES measurements and the surface-sensitivity and typical vacuum-compatibility requirements of XPS.

The last several years have seen growing interest in x-ray emission spectroscopy (XES), and especially valence-to-core XES,[9-16] as an important complement to XANES. In the context of sulfur, the synchrotron-based study of Alonso-Mori et al.[15] for inorganic compounds and the older laboratory-based work of Yasuda and Kakiyama[17] for organic compounds show a considerable richness of spectral features and sensitivity to chemically-relevant information. However, such studies have been quite sparse because of, again, limited synchrotron access and also because of the formerly low efficiency of laboratory-based x-ray emission spectrometers. That being said, there is a growing trend wherein the latest generation of x-ray analyzer optics, often having been developed for use at synchrotron light sources, are successfully repurposed for laboratory x-ray spectroscopies.[12, 18-35] In such cases, the laboratory-based instruments using synchrotron-grade optics typically achieve the same energy resolution as the synchrotron light source facilities and, often surprisingly, achieve similar count rates and sensitivities for nonresonant XES. The key point, as emphasized by Seidler et al.,[19] is that while x-ray tubes lack the monochromaticity of synchrotron beamlines, they do not lack for flux. Core-hole generation rates for samples illuminated by suitably chosen conventional x-ray tubes are often quite comparable to those for monochromatic illumination at 3rd-generation insertion device beamlines. The modest, but growing rebirth of laboratory-based x-ray absorption and emission spectroscopies has included recent development and application of a particularly simple XES spectrometer for sulfur and other nearby light elements.[21, 33, 35-36] Given that it is now technically feasible that sulfur XES could

become a high-access method, it becomes important to more fully explore the actual chemical and electronic sensitivities of sulfur XES, from both an experimental and theoretical perspective.

Hence, in the present work, a comprehensive set of experimental results for S Kα and Kβ XES, collected from extensive prior work in the literature and augmented with new measurements, are compared to theoretical calculations using linear-response time-dependent density functional theory (LR-TDDFT). Strong quantitative agreement is found between theory and experiment, both for Kα XES energy shifts that occur with changes in oxidation state, as well as the full range of spectral features in the valence-to-core (VtC) Kβ XES spectrum. From the analysis of the LR-TDDFT predictions, spectral features of S Kβ are observed to have possible strong polarization effects, suggesting a relatively unexplored avenue to investigate electronic structure through observations of anisotropic XES measurements from single crystals or preferentially oriented compounds. Lastly, the strong agreement between theoretical and experimental Kβ spectra suggest the possibility that supervised machine learning techniques, trained with theoretically generated spectra, could be used in the analysis of experimental measurements. Such machine learning approaches have seen recent progress in the analysis and classification of XANES spectra,[37-38] which share many similarities with VtC-XES in terms of the information content available.

First, a summary is given addressing in detail the prior work in sulfur Kα experiments, sulfur Kβ experiments, XES instrumentation, and XES theory. The general definition of Kα and Kβ fluorescence for sulfur and representative spectra are given in Figure 10.1. The energy position of the core-to-core Kα emission feature has been known to shift with changes in sulfur bonding and oxidation state since at least 1936 when measured by Parratt using a double-crystal spectrometer.[39] Additional measurements before the modern era of synchrotron capabilities were

made infrequently,[17, 40-44] but again indicated the sensitivity of the S Kα energy position to S oxidation state. More recently, Alonso-Mori et al. measured S Kα XES using synchrotron radiation facilities and found good agreement between Kα energy shifts and valence electron configurations calculated using density functional theory (DFT) and *ab initio* multiple scattering based (FEFF) simulations.[45] This effect is qualitatively understood by considering the different degrees of screening of the nuclear charge on the 1*s* and 2*p* binding energies. These same effects are also used by x-ray photoelectron spectroscopy (XPS) to assess oxidation state, though with an important distinction that XPS measures the photoelectrons generated by incident x-rays, and is thus limited by their penetration length which is typically on the order of nanometers. In contrast, S Kα XES captures the emitted x-ray photons which have penetration length on the order of micrometers, making the technique instead bulk sensitive. However, while XPS determines the 2*p* binding energy shifts directly, Kα XES is sensitive to the difference in shifts of the 2*p* and *1*s levels, with the result that the energy shift with oxidation state is smaller in XES than in XPS. Hence, with the advantage of relative bulk sensitivity of S Kα XES, the cost is the requirement of especially high instrumental energy resolution.

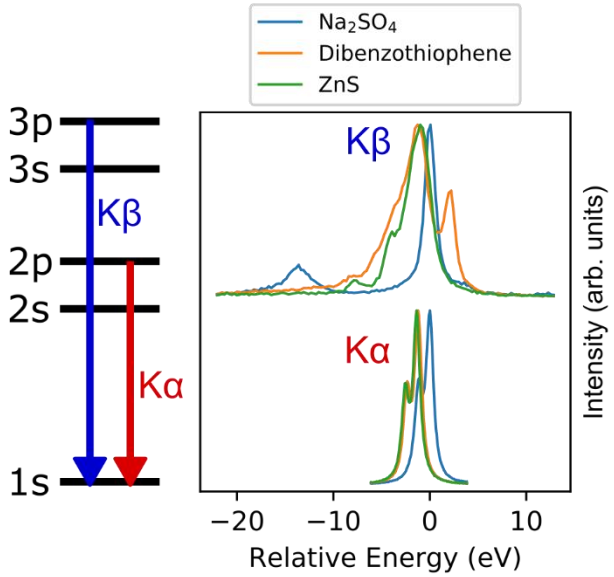

Figure 10.1: Level schematic and S Kα and Kβ XES spectra of selected S compounds on an energy scale relative to the peak position of signal for Na2SO4, highlighting the relative magnitudes of changes in spectral features between the core-to-core Kα emission and the valence-to-core Kβ emission.

Similarly, there are several noteworthy comparisons to be made between S Kα XES and S K-edge x-ray absorption near edge structure (XANES), which has also been used to characterize S speciation and oxidation state.[45-49] In a recent study, Holden et al.[33] showed that S speciation in biochars determined by S Kα XES was in good quantitative agreement with inferred oxidation states from previous S K-edge XANES measurements. In that work, Holden et al.[33] also made pertinent observations regarding systematic effects that can affect K-edge XANES spectra yet, in contrast, do not affect Kα XES. The standard approach for analysis of S speciation by XANES is to use linear-combination fitting, but as pointed out by many authors,[33, 50-51] this is subject to several difficulties including the proper choice of reference compounds, possible differences in crystallinity between references and samples of interest, as well as self-absorption effects. In contrast, non-resonant XES does not have a self-absorption effect that distorts features, and the simple shift of the significantly invariant spectral shape of sulfur Kα XES thus permits higher

confidence linear-combination fitting with no dependence of results on the concentrations and environments of sample and reference compounds.

Next, the Kβ XES of sulfur arises from valence-to-core transitions, where "valence" encompasses all occupied density of states derived from the S 3*p* shell in addition to any orbitals from the ligand atoms which hybridize with the S 3*p* during the formation of molecular orbitals. Consequently, the S Kβ XES carries information about the electronic structure of the bonding environment around S atoms, including effects from hybridization, symmetry, and ligand identities. These sensitivities are similar to those of sulfur K-edge XANES, which has seen extensive use in applications as a tool for fingerprinting sulfur chemistry by comparison to reference compounds[46-49] as well as in the study of sulfur electronic structure by comparison with theoretical computations.[52-54] However, much as with S Kα XES, there is far less prior study of the S Kβ XES than S K-edge XANES. Notable prior work includes the broad surveys of organic S compounds by Yasuda and Kakiyama[17] and inorganic compounds by Alonso-Mori et al.[45] Yasuda and Kakiyama were able to categorize their observed spectra according to a small number of classes of similar spectra and found that each such class possessed substantial chemical similarity. Alonso-Mori et al. were able to interpret several of their measurements of inorganic sulfur in terms of symmetry and molecular orbitals using a density functional theory (DFT) approach. Other remarkable surveys of S Kβ XES measurements include efforts by Takahashi and Yabe,[55] Yarmoshenko at el.,[42, 56-57] and Sugiura et al.[58-62]

The experimental literature summarized above clearly establishes strong sensitivity of S XES to many analytical questions often asked of the coordination chemistry and electronic structure of sulfur. The question then arises as to why S XES has remained rare, especially given the shortcomings of NMR as well as the surface sensitivity and typically high-vacuum

requirements of XPS. This is partly due to limitations of synchrotron access compounded by the small number of beamlines operating in this intermediate, "tender" x-ray range (1–5 keV) and the even smaller number of such beamlines equipped with a high-resolution XES spectrometer. However, it is also due to the previously low efficiency of laboratory-based x-ray emission spectrometers in this energy range[40, 63-65] where the classic double flat-crystal spectrometer provided outstanding energy resolution, but with such small effective collection solid angles that long integration times were required even with very high-powered x-ray tubes.

The recent development of an efficient laboratory-based spectrometer based on the Dispersive Refocusing Rowland (DRR) design mitigates many of these limitations.[21] The DRR-based instrument is an example of the ongoing renaissance of laboratory-based advanced x-ray spectroscopies,[18-32] where XES is proving to be especially powerful because of the core level ionization rates that are possible with conventional x-ray tubes.[12, 33-35] The DRR-based instrument, which was used for the new experimental results presented in this study, is capable of Kα XES measurements on concentrated samples in a matter of minutes, and dilute samples (~150 ppm) within a few hours. Kβ XES measurement times are similarly minutes or hours for concentrated samples. The design allows efficient use of a large spot size, which serves to increase the efficiency when operating with a conventional unfocused laboratory x-ray tube and decreases the damage done to radiation-sensitive samples. These capabilities have already been demonstrated and utilized in a recent study on the speciation of sulfur in biochars[33] and for the problem of the speciation and local electronic structure of phosphorus in InP quantum dots.[35-36] These studies demonstrate synchrotron-quality energy resolution in often-comparable measurement times. In addition, for the narrow problem of determination of the P oxidation state, lab-based XES agreed

with results from ^{31}P magic-angle spinning NMR but required much shorter measurement time and far less sample mass.[35]

The above overview validates that S Kα and Kβ XES have significant analytical sensitivity and that high access to S XES is technically viable. This brings us to the question of a predictive theoretical approach. To date, though theoretical investigations of S XES have been carried out for inorganic sulfur compounds, to our knowledge this is the first report of extensive theoretical calculations of XES for sulfur organic compounds. Previous approaches to modeling sulfur XES spectra include molecular orbital methods,[66-67] discrete variational Xα cluster calculations (DV-Xα),[68-70] and more recently, DFT methods.[15-16, 45, 71] The single-particle density functional theory (DFT) approach represents the initial core-hole and final valence-hole states with Kohn–Sham (KS) orbitals from ground state DFT calculations. Within this approximation, the emission intensities are proportional to the transition dipole matrix elements between the two aforementioned KS orbitals, and the emission energies are just the energy differences between those orbitals. However, this neglects orbital relaxation during the emission process, and multichannel effects involving many orbital pairs with significant contributions to the excited state cannot be described within a single-particle framework. Here, we expand on prior work by using a LR-TDDFT based protocol[72-73] which naturally includes multideterminant character in the excited state to simulate sulfur VtC-XES spectra. We find quantitative agreement between theory and experiment across the full range of molecular and condensed phase systems considered here for both Kα energy shifts and for the overall Kβ spectra. Our results expand on the growing body of work establishing theoretical treatments of XES and VtC-XES of various elements, most commonly transition metals, which often achieve qualitative agreement that aids in interpretation, but also which is increasingly achieving quantitative agreement similar to that seen here.[10-16, 73-89]

Hence, taken *en masse*, the combination of prior work and the present study establish the viability of S Kα and Kβ XES as standard diagnostic methods, strongly supported by a predictive theoretical treatment. The manuscript proceeds with descriptions of both theoretical and experimental methods. The results and related discussions follow, with a comparison of theory to experiment including several new insights about the relationship between electronic structure and possible directional effects in future direction-dependent VtC-XES studies. Two high-impact future directions are highlighted. First, while this work demonstrates the performance of theory and spectrometer in the case of sulfur, similar sensitives of Kα and Kβ XES have been demonstrated for Al, Si, P, and Cl,[16, 67, 71, 90-92] suggesting that many of the methods and conclusions in the present paper might be extended to these elements as well. Second, the strong quantitative agreement between theory and the S Kβ XES strongly suggests that the forward problem (given a structure, predict the spectrum) is sufficiently solved that supervised machine learning of, e.g., a neural network can be used in the future for inference of structural or chemical descriptors from S Kβ XES results.

10.2 Experimental Methods

A number of spectra reported here have been recorded by our group using a recently developed laboratory-based tender x-ray emission spectrometer, described in detail by Holden et al.[21] Briefly, the spectrometer uses an x-ray tube (Varex VF50, Pd-Anode) operated at an electron beam power of 50 W to stimulate fluorescence in the sample. The spectrometer makes use of the dispersive refocusing Rowland (DRR) geometry with a 10-cm radius of curvature, Si (111) cylindrical crystal analyzer (XRS TECH LLC). The refocused fluorescence is detected using an energy-resolving CMOS-based color x-ray camera,[93] where individual photon detection events are

energy-windowed to reject background signals. The majority of the beam path of the spectrometer is within a chamber which is either flushed with helium or evacuated with a roughing pump to low vacuum (<100 mTorr) to reduce air scatter and absorption. Using Na_2SO_4 as reference, energy scales for $K\alpha_1$ measurements were aligned using Alonso-Mori et al.'s reported value of 2309.12 eV,[45] and Kβ measurements were aligned to Alonso-Mori et al.'s using a two-point calibration with the Na_2SO_4 $K\beta_{1,3}$ energy position of 2467.15 eV and Kβ' energy position of 2452.91 eV.[15] Kβ measurements of blanks were used to assess backgrounds, which were observed to be approximately linear, and the resulting linear trend was subtracted from each spectrum. Samples measured include a ZnS crystalline wafer (MTI Corporation); dibenzothiophene, benzyl sulfide, 2-mercaptopyridine, 4-mercaptopyridine, 2-mercaptopyrimidine, and 2-(2-Hydroxyphenyl)benzothiazole (Sigma Aldrich); Na_2SO_4 (Fisher Chemical); and dimethyl sulfone (Frontier Scientific).

Additional Kβ spectra were gathered from Yasuda and Kakiyama[17] and Alonso-Mori et al.[15] Spectra were reproduced from the published figures using the online tool WebPlotDigitizer.[94] Since not all data points were recovered from the digitization, the noise of the spectra is only approximately reproduced. Spectra from Alonso-Mori et al. were used as reported. Spectra from Yasuda and Kakiyama were converted from an angular scale to energy scale using 2d=6.5327 Å for the Ge(111) spacing, and were then shifted by 3.15 eV to better match the energy alignment of Alonso-Mori et al. For presentation in the figures below, the spectra were shifted vertically such that the minimum of the spectra coincides with zero, corresponding to subtraction of a constant background.

10.3 THEORETICAL METHODS

Linear-response time-dependent density functional theory, LR-TDDFT,[95-97] has been used in theoretical calculations for various x-ray spectroscopies, including XANES of sulfur[53, 98-100] and other elements,[101-115] as well as VtC-XES.[12, 72-73] Here, we make use of LR-TDDFT within the Tamm-Dancoff approximation (TDA)[116] to simulate XES of a variety of sulfur compounds. In the present work, in addition to the VtC-XES spectra, energies of the Kα core-core transitions are also obtained from the LR-TDDFT calculation. All calculations were performed with the `NWChem`[117] package (version 6.8.1).

The XES simulation protocol[12, 72-73] is as follows: first a neutral ground state calculation is performed; next, a full core-hole (FCH) ionized state is obtained self-consistently in which an electron is removed from the 1s core orbital while using the maximum overlap constraint[118-119] to prevent core hole collapse; lastly, a LR-TDDFT calculation within the TDA is performed with the FCH ionized state as the reference. The XES features appear as negative eigenvalues of the LR-TDDFT matrix equations, and the energies of the final spectra are obtained by taking absolute values. For VtC-XES calculated spectra, the same energy shift (-18.6 eV) was applied to all systems considered here to match experimental spectra. It is possible to use a constant energy shift in this approach because of the explicit and consistent treatment of the core potential of the emitting center. Kα energy shifts are reported relative to S_8, which was calculated by the LR-TDDFT procedure as 2316.86 eV and has an experimental value of 2307.89 eV,[120] corresponding to a -8.97 eV shift.

To obtain relative spectral intensities from the oscillator strengths, we use the following equation, as discussed by Lee at al.[11]:

$$I_{IF}^{R} = \frac{\omega_{IF}^{2} f_{IF}}{\sum_{F'} \omega_{IF'}^{2} f_{IF'}}$$

where I_{IF}^{R} is the relative radiative decay intensity from initial state I to final state F, f_{IF} is the emission oscillator strength, and $\omega_{IF} = (E_F\text{-}E_I)/\hbar$ is the emission frequency. To produce the theoretical spectra, the spectral transitions were broadened with a Lorentzian profile with a full-width half-maximum of 2 eV to include natural lifetime and experimental resolution effects.

In addition to the VtC-XES spectra, our calculations also yield de-excitations at lower energy and with much stronger oscillator strengths. These de-excitations correspond to the Kα core-to-core 2p→1s transitions. Without inclusion of spin-orbit or multiplet effects, these Kα transitions are nearly degenerate in energy, and the average is taken to represent the average Kα energy position.

In the case of the molecular compounds, single molecules were used to calculate VtC-XES spectra. Optimized geometries were calculated prior to the VtC-XES calculation procedure. Pre-optimized structures were downloaded through MolView.org,[121] which relies primarily on the PubChem[122] database. Geometry optimization calculations were performed with the B3LYP exchange correlation functional[123] and with 6-31G* basis sets[124-127] without symmetry constraints. For the LR-TDDFT procedure, the 6-311G** basis sets[128-129] was used for all atoms other than sulfur, for which the Sapporo QZP-2012[130] basis was used along with the PBE0[131] exchange correlation functional (25% Hartree-Fock).

The solid-state compounds (pyrite, FeS_2; orpiment, As_2S_3; sphalerite, ZnS) were represented with finite clusters constructed from experimentally determined crystal structures.[132-134] To account for the surface states, the clusters were terminated using a set of suitably chosen pseudo-hydrogen saturators whose charges are calculated using the formal charges of the surface

atoms and bonding environment.[12, 135-136] For FeS_2 and As_2S_3, the Los Alamos effective core potential (LANL2DZ[137-138]) and associated basis sets were used on S, Fe, and As atoms. For ZnS, the Stuttgart RSC 1997 ECP[139-140] basis set was used for Zn atoms and Stuttgart RLC ECP[141] was used for S. For all solid-state calculations, the emitting S center was represented with the Sapporo TZP-2012[130] basis. As in the molecular calculations, the PBE0 exchange-correlation functional was used for all solid-state systems.

10.4 Results and Discussion

Combining measurements made with our laboratory spectrometer with the measurements of Yasuda and Kakiyama[17] and Alonso-Mori et al.,[15, 45] experimental sulfur Kα energy shifts have been compared to theoretical calculations for 43 sulfur compounds, and sulfur Kβ experimental and theoretical spectra have been compared for 29 sulfur compounds.

For the following discussion, the compounds are divided into molecular and solid-state (SS) compounds. Using the classifications of Yasuda and Kakiyama, the molecular compounds are further subdivided into types: sulfur-oxygen (SO) and divalent compounds consisting of type A, type B, and type C. Though Yasuda and Kakiyama made these assignments based on sulfur Kβ spectral features, the groupings are well separated by bonding characteristics. The type A compounds are aryl sulfides and thiols in which the sulfur is adjacent to benzene rings, as well as heterocyclic sulfur compounds. Type B compounds are identified as aliphatic sulfides and thiols and benzyl sulfides in which the sulfur atom is separated from the benzene rings by CH_2. Type C compounds consist of thioketones.

10.4.1 Sulfur Kα

For context, some representative S Kα spectra are shown in Figure 10.2. For the variety of compounds shown in the figure, despite varying oxidation states and chemical environments, the Kα doublet lineshape is observed to be essentially constant, with the spectra of different compounds shifted towards higher energy with increasing oxidation state. These observations are in line with well-established findings from prior works that the Kα lineshapes for S are only weakly dependent on the local chemical environment.[45, 71] In all cases, the spectra are largely characterized by the energy position of the stronger, $K\alpha_1$ line, or equivalently, by the energy shift of that line with respect to its position for elemental sulfur. As recent studies have also demonstrated,[33, 45, 71] one consequence of this is that samples of mixed sulfur oxidation states can be analyzed by linear combination fitting of sulfur Kα doublets at different energy shifts.

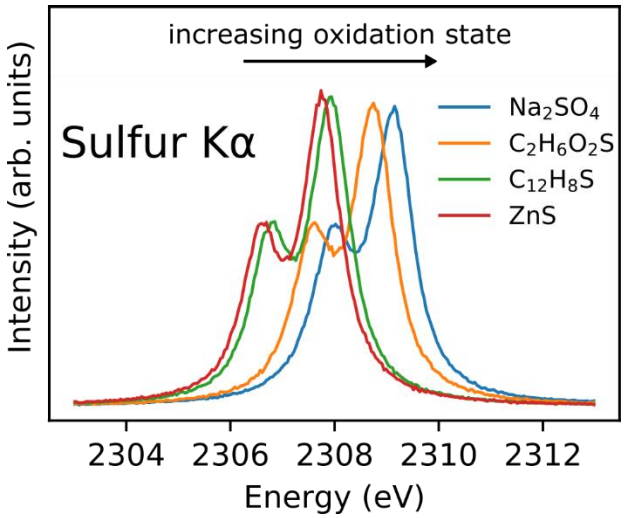

Figure 10.2: Sulfur Kα XES measurements of compounds with a variety of oxidation states taken on our laboratory spectrometer. Common names for compounds in the legend are dibenzothiophene ($C_{12}H_8S$) and dimethyl sulfone ($C_2H_6O_2S$).

Calculated Kα energy shifts are reported and compared to experimental data from present and prior work in Table 1. Excellent agreement is found between our calculations and the

measurements reported by Yasuda and Kakiyama, with an average deviation between the theory and experiment of 0.02 eV, which is comparable to their reported energy uncertainty of ± 0.01 eV. With the exception of ZnS, which appears to be an outlier, we also find good agreement with our own measurements ("present work") and those of Alonso-Mori et al., with average deviations (excluding ZnS) of 0.05 eV and 0.03 eV, respectively. It is also clear from Table 1 that the type of compound is strongly correlated with the Kα energy position. All sulfur-oxygen compounds are highest in energy, and the divalent sulfur compounds show some clear trends, with type C being consistently lowest in energy, and type A and B being intermixed, with B skewed lower in energy and A skewed higher. The solid state compounds, containing reduced sulfur, are also grouped lower in energy, all having negative shifts with respect to S_8.

Table 10.1: Sulfur Kα energy shifts relative to S8 as predicted with the LR-TDDFT protocol compared to experimentally determined values. Shifts of data from Alonso-Mori et al. and the present work were aligned to have the same shift as Yasuda and Kakiyama for sodium sulfate, the only compound measured in all three studies. Counter-ions of experimental compounds which were not included in the LR-TDDFT calculation are indicated in parentheses. (SO = sulfur-oxygen, SS = solid-state)

Type	Compound	Present Work		Yasuda and Kakiyama[17] (exp.)	Alonso-Mori et al.[45] (exp.)
		LR-TDDFT (theory)	Measured (exp.)		
SO	**(Sodium) sulfate**	1.20	1.21	1.21	1.21
SO	**(Sodium) lauryl sulfate**	1.14		1.15	
SO	**(Ammonium) sulfamate**	1.12		1.12	
SO	**(Sodium) p-dodecylbenzenesulfonate**	1.06		1.03	
SO	**Benzenesulfonic acid**	1.06		1.06	
SO	**(Potassium) methanesulfonate**	1.06		1.04	
SO	**(Sodium) hydroxymethanesulfonate**	1.05		1.00	
SO	**(Sodium) methallyl sulfonate**	1.03		1.00	
SO	**Sulfanilic acid**	0.99		1.07	
SO	**P-Toluenesulfonic acid**	0.98		1.04	
SO	**Benzenesulfonamide**	0.94		0.94	
SO	**O-Sulfobenzimide**	0.94		0.95	
SO	**Diphenyl sulfone**	0.84		0.85	
SO	**Dimethyl sulfone**	0.83	0.83	0.80	
SO	**Sulfolene**	0.78		0.76	
SO	**Thiourea dioxide**	0.49		0.42	
SO	**Diphenyl sulfoxide**	0.35		0.35	
SO	**Dibenzyl sulfoxide**	0.28		0.25	
B	**4,4'-Dithiodimorpholine**	0.04		0.05	
B	**Sulfur (S_8)**	0.00		0.00	-0.02
A	**Thenoic acid**	0.00		0.01	
A	**2-Benzoylthiophene**	0.00		0.00	
A	**4,4'-Thiodianiline**	-0.01		0.00	
A	**4,4'-Thiodiphenol**	-0.01		0.01	
B	**Dibenzyl disulfide**	-0.02		-0.02	
A	**Thianthrene**	-0.02		0.00	
A	**2-Aminothiazole**	-0.03		-0.01	
A	**2-(2-Hydroxyphenyl)benzothiazole**	-0.04	0.02		
A	**Dibenzothiophene**	-0.04	0.02	-0.01	
B	**Thiodipropionic acid**	-0.05		-0.04	
B	**1,3,5-Trithiane**	-0.06		-0.03	
B	**Octadecyl sulfide**	-0.06		-0.04	
B	**Dibenzyl sulfide**	-0.07	-0.02	-0.05	
SS	**FeS_2 (Pyrite)**	-0.09			-0.05
C	**2-Mercaptobenzimidazole**	-0.11		-0.11	
C	**Thiourea**	-0.11		-0.13	
C	**Thioacetamide**	-0.11		-0.13	
C	**2-Mercaptopyrimidine**	-0.12	-0.08		
C	**2-Mercaptopyridine**	-0.12	-0.06		
C	**Thiobenzamide**	-0.12		-0.13	
C	**4-Mercaptopyridine**	-0.12	-0.03		
SS	**As_2S_3 (Orpiment)**	-0.14			-0.18
SS	**ZnS (Sphalerite)**	-0.43	-0.15		-0.22

The Kα energy shift is explained at lowest order as a change in the amount of screening of the nuclear charge due to changes in the valence electron population, i.e., oxidation state. Figure 10.3 shows a comparison of the Kα energy shifts predicted using ground-state Kohn-Sham molecular orbital energy differences and energy shifts calculated by the LR-TDDFT procedure. While both approaches produce linear fits with comparably small residuals and capture the energy shift with oxidation state, the response treatment approach of LR-TDDFT produces a slope closer to one, i.e., in systematically better agreement with experiment and illustrating the need to include orbital relaxation.

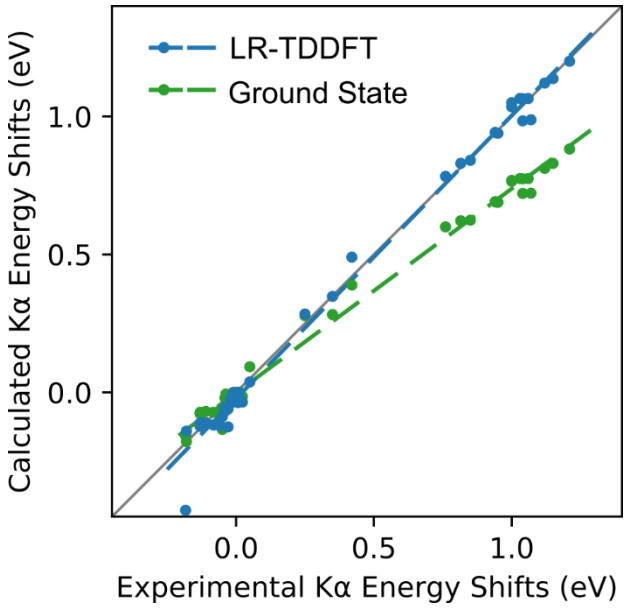

Figure 10.3: Comparison of experimental Sulfur Kα energy shifts (relative to S_8) with theoretical shifts at two different computational levels: ground state DFT sulfur 2*p* – 1*s* molecular orbital energy differences (slope = 0.73, R^2 = 0.993) and LR-TDDFT transition energies (slope = 1.02, R^2 = 0.994). For compounds with multiple experimental values (see Table 1), the average experimental shift was taken.

The last feature of the Kα XES spectrum is the peak ratio of the two main $K\alpha_1/K\alpha_2$ transitions. As reported in Alonso-Mori et al.,[15] there is some modest variation in peak ratio from the ideal 2:1 ratio expected from the relative degeneracies of the $2p_{1/2}$ and $2p_{3/2}$ shells. An understanding of the material-dependence of the variation of this ratio remains an unexplained feature of the spectrum within these calculations. When Kα XES is used for speciation by linear combination fitting, this minor variation introduces a possible systematic uncertainty, as explored in detail in the supporting information of Stein et al.[35] where the same overall approach to determination of oxidation state is used for phosphorus speciation.

10.4.2 Sulfur Kβ

Molecular Compounds

The sulfur Kβ XES spectrum is richer than the Kα in spectral detail and information content. We frame the discussion in four steps. First, we broadly compare the observed Kβ experimental spectra from multiple sources with LR-TDDFT predictions. Second, we investigate the results of analyzing the spectra by the underlying theoretical character of select spectral features, with an emphasis on the transitions dominated by the highest occupied molecular orbital (HOMO) or the cluster of transitions that are highest in energy. Third, we analyze the transition dipole moment directions of spectral features. While directional-dependent non-resonant valence-to-core XES has been occasionally considered,[88, 142-147] our results show that such studies may allow a rich interrogation of theory and molecular electronic structure for many of the compounds considered here. Fourth, we investigate the quantitative agreement between theory and experiment and use that as a stepping stone to discuss possible future use of supervised machine learning based on LR-TDDFT training sets as applied to experimental results.

First, a variety of spectral features are observed among the many molecular compounds shown in Figures 10.4 and 10.5. The agreement between theory and experiment is, at this first qualitative level, impressively strong. All major features in the experimental spectra are reproduced in the theory, and vice versa. While specific features of each spectrum depend on the detailed nature of the bonding environment, a few general trends among the types of compounds emerge. Type A compounds have a dominant peak near 2465.5 eV with a pronounced shoulder 3-4 eV higher in energy, and a weaker, broader shoulder on the low energy side. As seen in the transitions of the calculations (indicated by the black sticks in Figure 10.4), one or two dominant transitions contribute to the high energy shoulder, while the main peak and low energy shoulder consist of a series of transitions. For type B compounds, the dominant feature is the highest in energy, near 2468 eV. This is slightly lower in energy than the highest energy feature of type A compounds, as noted by Yasuda and Kakiyama. With slightly less intensity, type B compounds show a secondary strong feature near 2465.5 eV (nearly coincident with the type A dominant feature). A feature on the low energy side is also observed near 2463 eV, which in some compounds appears as an additional peak, or otherwise as a weaker shoulder. Type C compounds show the least variation between compounds, with two main peaks, the dominant peak near 2467 eV, and a peak near 2463 eV around three times less intense. For sulfur-oxygen compounds, with the exception of diphenyl sulfoxide, the spectra show a main peak near 2467 eV (referred to as $K\beta_{1,3}$) and another peak around 14 eV lower in energy (referred to as Kβ'), the latter being the well-known sulfur-oxygen bonding peak.[15-17, 90] The intensity of the lower energy peak is observed to vary, with a positive correlation between intensity and the number of oxygens. For diphenyl sulfoxide with a single S-O bond, a small peak is predicted by the calculation but not observed in the experimental data of Yasuda and Kakiyama. In addition to the two main peaks, shoulders are

observed on both the low and high energy sides of the main feature, and in the cases of dimethyl sulfone and diphenyl sulfone, isolated peaks are seen near 2458 eV.

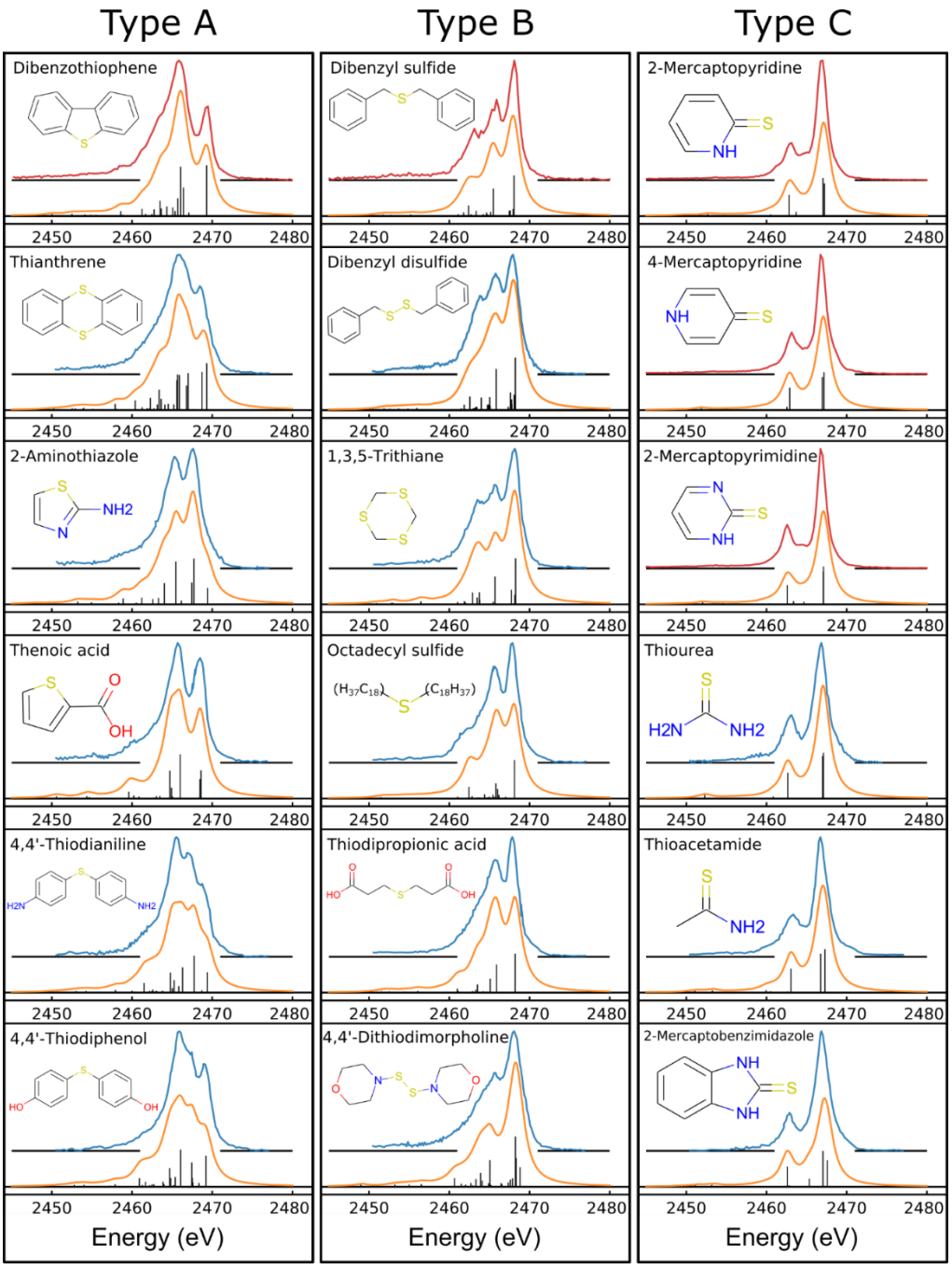

Figure 10.4: Comparison of sulfur Kβ VtC-XES experimental results (red & blue) to LR-TDDFT calculations (black sticks: transitions, orange line: Lorentzian-broadened) for divalent sulfur compounds. The red experimental data was taken on our laboratory-based instrument[21] and the blue data is from Yasuda and Kakiyama.[17]

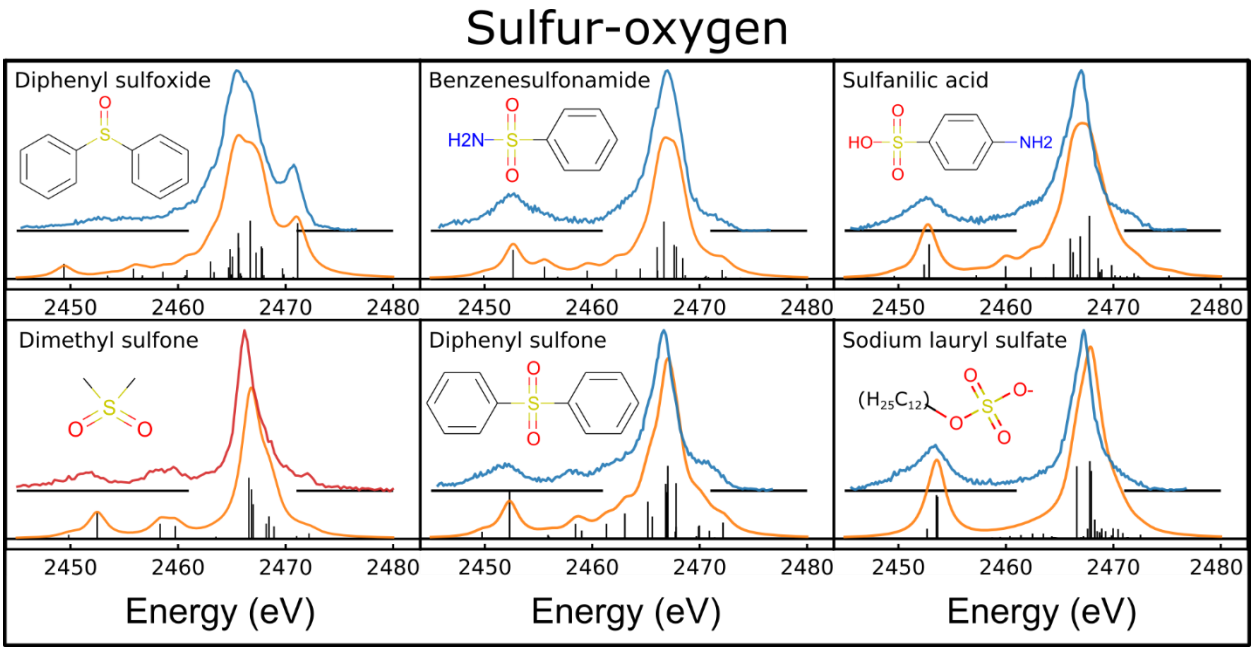

Figure 10.5: Comparison of sulfur Kβ VtC-XES experimental results (red & blue) to LR-TDDFT calculations (black sticks: transitions, orange line: Lorentzian-broadened) for sulfur-oxygen compounds. The red experimental data was taken on our laboratory instrument[21] and the blue data is from Yasuda and Kakiyama.[17]

Second, we consider the underlying character of spectral features. To analyze the character of spectral features, a weighting scheme is used to decompose the contributions from the different configurations into weighted sums of atomic basis orbitals; the details of this procedure are given in the SI. The results of select compounds are shown in Figures 10.6 and 10.7, while the equivalent figures for the remaining compounds are included in the SI.

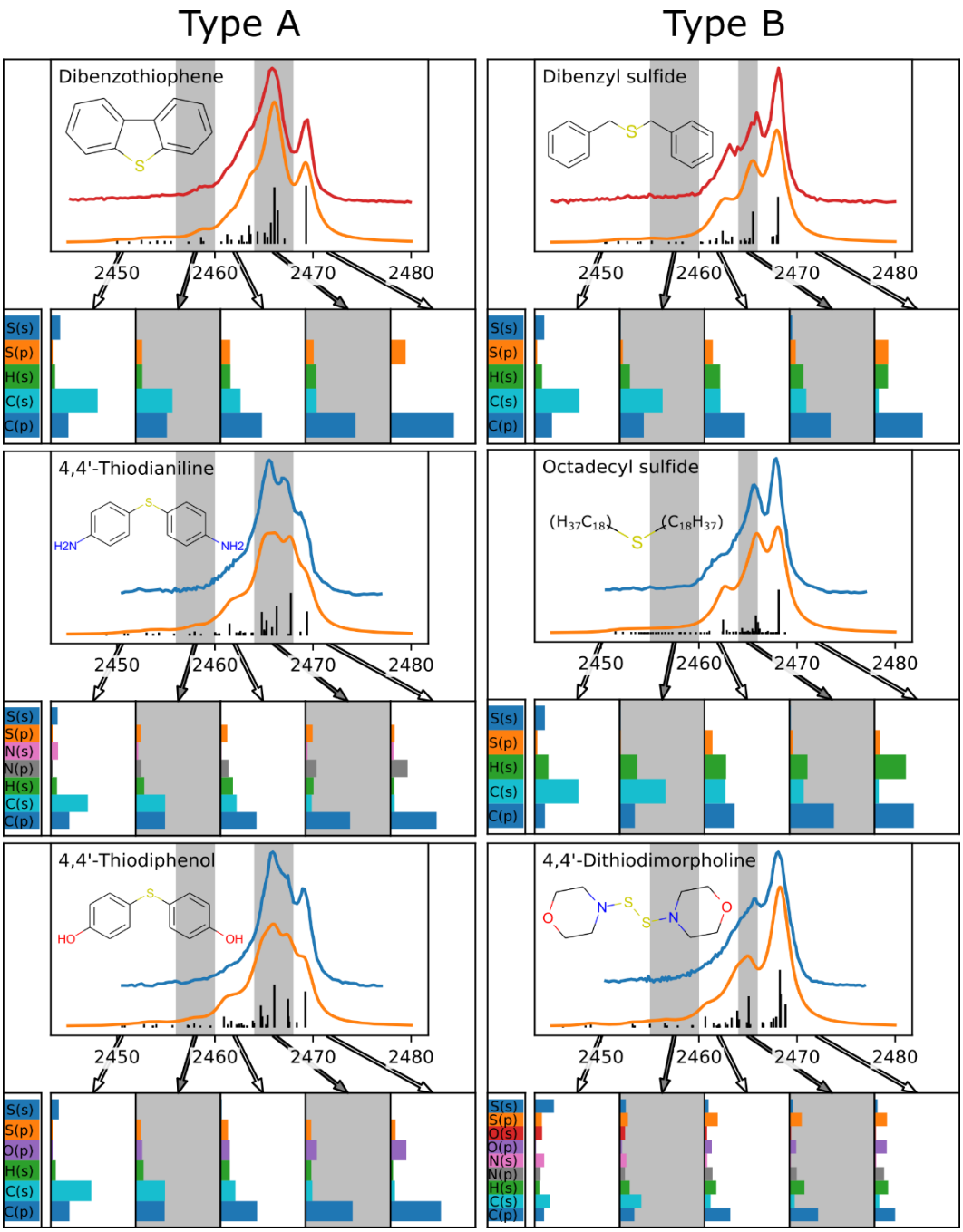

Figure 10.6: Sulfur Kβ experimental and theoretical spectra, with bar plots of atomic orbital contributions of spectral features in different energy ranges for type A (left) and type B (right) compounds. Contributions were calculated according to the weighting scheme as explained in detail in the SI. LR-TDDFT calculated transitions are shown as black sticks and the Lorentzian-broadened spectra as orange lines. The red experimental data was taken on our laboratory-based instrument[21] and the blue data is from Yasuda and Kakiyama.[17] The bar plot x-scale is normalized to one and, for clarity, weighted contributions from orbitals with less than 0.05 contribution are omitted. The x-scale of the spectra represents energy in eV.

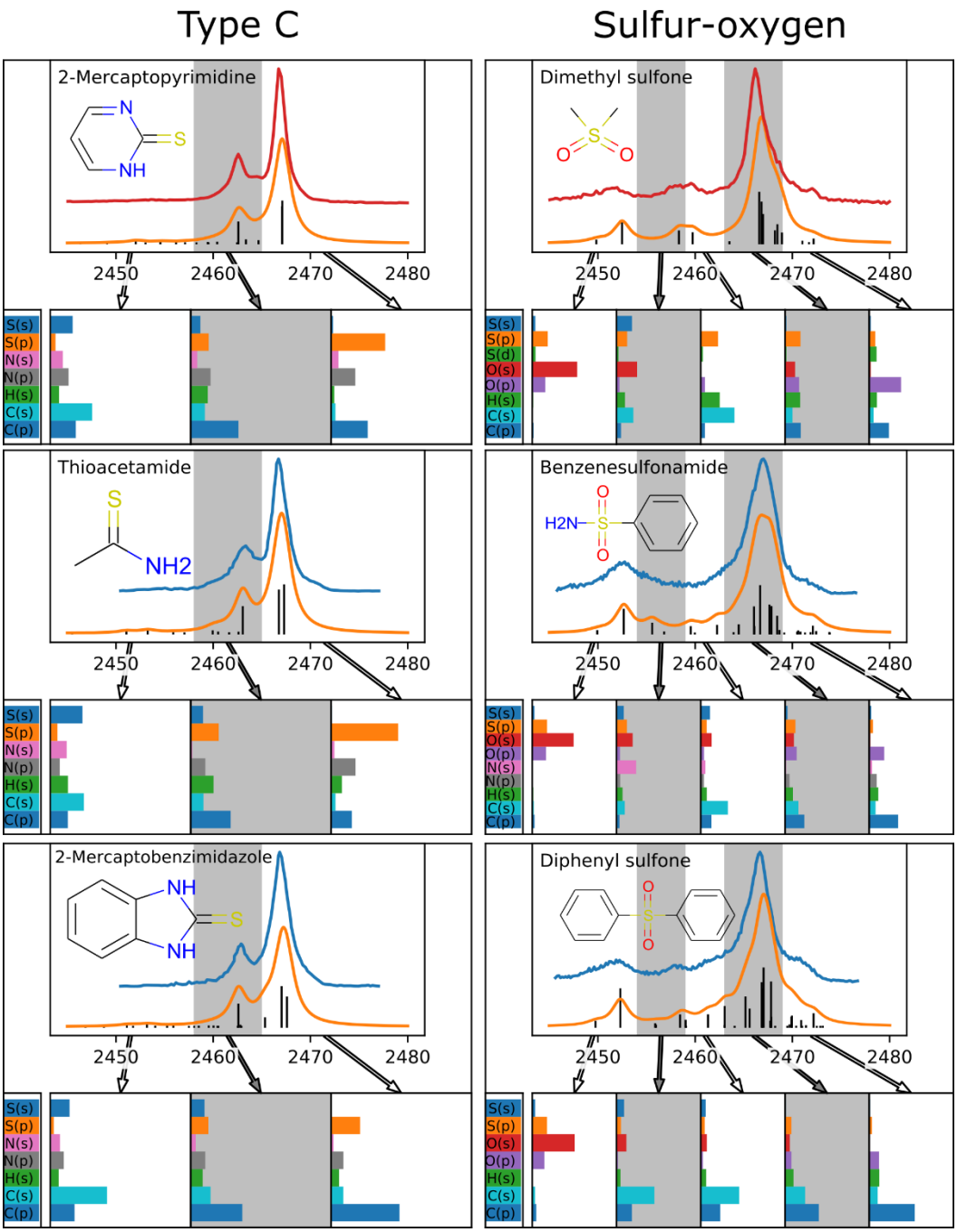

Figure 10.7: Sulfur Kβ experimental and theoretical spectra, with bar plots of atomic orbital contributions of spectral features in different energy ranges for type C (left) and sulfur-oxygen (right) divalent compounds. Contributions were calculated according to the weighting scheme as explained in detail in the SI. LR-TDDFT calculated transitions are shown as black sticks and the Lorentzian-broadened spectra as orange lines. The red experimental data was taken on our laboratory-based instrument[21] and the blue data is from Yasuda and Kakiyama.[17] The bar plot x-scale is normalized to one and, for clarity, weighted contributions from orbitals with less than 0.05 contribution are omitted. The x-scale of the spectra represents energy in eV.

Spectra of type A compounds and their resulting decompositions into atomic character are shown in Figure 10.6 (left) and Figure S1. The higher energy features are seen to be dominated by atomic *p*-character orbitals, mostly from carbon and sulfur, as well as oxygen and nitrogen for compounds with those elements. As features decrease in energy, they contain decreasing contributions from *p*-character orbitals and increasingly consist of *s*-character, predominantly from carbon, but also with contributions from nitrogen, oxygen, and some minor contributions from sulfur. As the highest energy features result from transitions that are largely (or wholly) dominated by the HOMO, the character of these features reflects information about the composition of the HOMO. The large contributions of carbon and sulfur *p*-type orbitals relate to the sulfur participation in the delocalized molecular orbitals of the ring structures. This is highlighted by the strong contributions of nitrogen-*p* and oxygen-*p* to the high energy features of 4,4'-thiodianiline and 4,4'-thiodphenol, respectively. In those compounds, despite the spatial distance from the sulfur atom and the relatively local nature of the sulfur VtC-XES measurement, the nitrogen and oxygen groups opposite the sulfur on the benzene rings are seen to contribute significantly to the high-energy spectral features. Comparing the spectra of those two compounds, this change in character also coincides with a change in predicted intensity, with the highest energy transition for 4,4'-thiodiphenol being more intense than 4,4'-thiodianiline. This relatively small predicted change is indeed observed in the experimental spectra, demonstrating the sensitivity of the spectra in this region as well as the high quality of agreement between the theory and experiment.

Type B compounds (Figure 10.6 right and Figure S2) show similar general trends in the atomic characters as type A compounds, with the highest energy features being dominated by carbon-*p* with a smaller contribution of sulfur-*p* and oxygen/nitrogen-*p* (for compounds with O and N). For decreasing energy of features, again *p*-character contributions of these elements are

reduced and *s*-character contributions increase. One exception is the presence of hydrogen-*s* character, which has a relatively constant contribution throughout, and is also present in the highest energy features, reflecting the fact that the HOMOs are no longer the delocalized ring structure orbitals of type A, but rather involve the aliphatic chain containing the sulfur. Notably, 1,3,5-trithiane (Figure S2) lies somewhat outside of the above trends and has highest energy features dominated by sulfur-*p* and containing significant sulfur-*s* contributions as well. Sulfur-*d* orbitals are also observed to have minor contributions.

For type C compounds (Figure 10.7 left and Figure S3), in contrast to type A and type B, the highest energy features have much stronger (or dominant) contributions from sulfur-*p* character orbitals, likely reflecting the role of the sulfur-carbon double-bond in the HOMO. Similar to type A and B, the lower energy feature contains more carbon and sulfur *s*-character and less sulfur-*p*.

Spectral decompositions for sulfur-oxygen compounds are shown in Figure 10.7 (right) and Figure S4. Starting with the lowest energy feature, it is evident that the Kβ' peak near 2453 eV is dominated by oxygen-*s* character and is thus a signature of S-O bonds. This is consistent with the observed increase in Kβ' intensity with increasing oxygen coordination of the sulfur and is in close analogy to the better-known Kβ'' ligand or 'cross-over' peaks seen in transition metal VtC-XES.[147] Taking that as a guide, we recall that in the case of Mn, isolated ligand peaks are seen in order of increasing energy separation for Mn-N, Mn-O, and Mn-F bonds. Calculating the theoretical spectrum for SF_6 (Figure S5), a Kβ' peak is predicted ~3 eV lower than the Kβ' peak in sulfate compounds, in reasonable agreement with measurements of SF_6 made by Takahashi.[90] Although not observed as an isolated peak, analogous behavior for nitrogen is observed in the character of benzenesulfonamide spectral features around 2455.6 eV (Figure 10.7 right), where nitrogen-*s* character is dominant. Similarly, in the energy region around 2460 eV, the spectral

transitions are dominated by carbon-*s* character. In the case of dimethyl sulfone, an isolated intermediate feature is observed in this spectral region coming from two nearby transitions, the higher energy one dominated by carbon-*s* and the lower energy one with similar contributions of carbon-, oxygen-, and sulfur-*s*. For all sulfur-oxygen compounds, the main Kβ feature around 2467 eV is split among many atomic orbitals. For the spectral region highest in energy, closest to the HOMO, transitions are dominated by carbon-*p* and oxygen-*p*, though notably, sulfur-*d* has an appreciable contribution to the HOMO for dimethyl sulfone.

Third, we discuss the transition dipole moment directions for select spectral features. The X, Y, and Z components of the transition dipole moments contain information related to polarization. In oriented samples, these polarizations are observed as anisotropies in the directions of fluorescence emission. Though the directionality of XES has been discussed by some authors in the past,[77, 88, 142-147] measurements of polarized XES are relatively uncommon. The connection between molecular orientation and anisotropic emission has significant similarity to the polarization dependence of XAFS[148] or the momentum-transfer dependence of non-resonant inelastic x-ray scattering.[149-150] However, while in those cases the polarization or directional dependence is associated with the excitation, here it is instead related to the de-excitation. That is, in polarization XAFS, the directionality is related to the symmetry of unoccupied states, whereas in directional VtC-XES, the polarizations reveal information about the symmetry of the valence electronic configuration.

The directionality of the transition dipole moments are analyzed using cosine-projections of the transition dipole moment vectors onto the X, Y, and Z axes of the molecule (i.e., the contribution of a single transition is proportional to $\cos^2\theta$, where θ is the angle between the vector and the coordinate axis). Plots with spectral decompositions onto orthogonal directions with

molecular depictions illustrating the orientation of the axes for several compounds are shown in Figures 10.8 and 10.9 (and in Figures S6-S9 for remaining compounds). As a demonstration of information that may be obtainable by such an anisotropic VtC-XES measurement, we analyze the case of dibenzothiophene in detail. In Figure 10.8, the transition dipole moment direction of the highest energy transition is calculated to be perpendicular to the plane of the molecule. For the C_{2v} symmetric dibenzothiophene molecule, the dipole operator perpendicular to the plane of the molecule (along the x-axis) is of b_1 symmetry. For a dipole allowed transition, the product of the irreducible representations of the initial and final state with the dipole operator must contain the totally symmetric irreducible representation. Therefore, in order to have a dipole-allowed transition to the a_1 symmetric core-hole, the electron must leave a state of b_1 symmetry, indicating that this high-energy feature originates from states of b_1 symmetry. Indeed, from the calculations, this high-energy feature is dominated by contribution from the HOMO, which is observed to have b_1 symmetry. This information about the symmetry of the HOMO is similar in principle to what can be obtained by linear dichroism spectroscopy, which has also been performed on dibenzothiophene[151-152] and identified the HOMO as b_1. In contrast to linear dichroism spectroscopy, however, for the case of dibenzothiophene where the 1s core-hole belongs to the totally symmetric irreducible representation, valence states of many symmetries are probed by VtC-XES and contribute to the spectrum, whereas only $\pi \rightarrow \pi^*$ transitions are observed in the linear dichroism spectroscopy measurements.

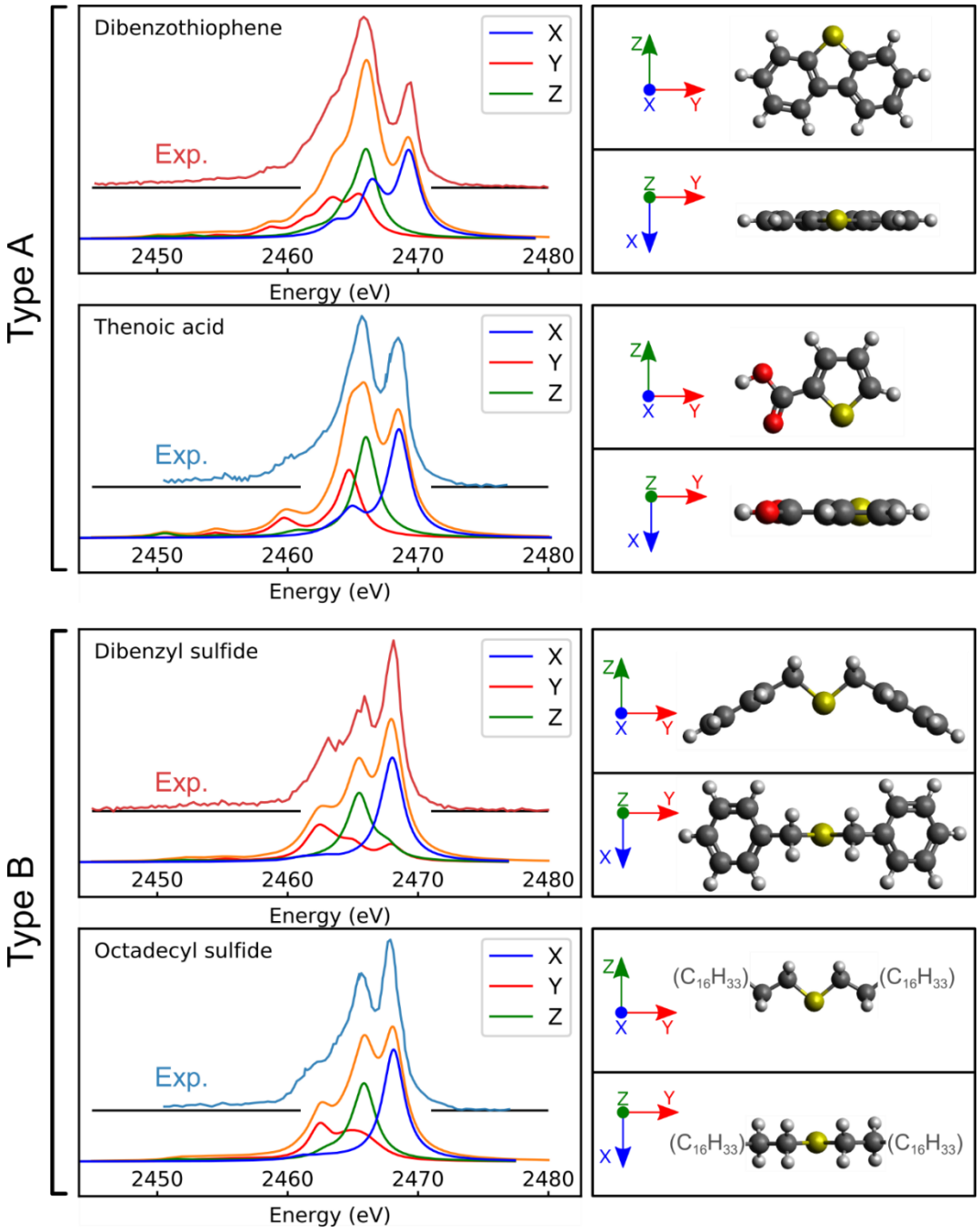

Figure 10.8: (left) Sulfur Kβ experimental (labelled "Exp.", red & blue) and theoretical (orange) spectra of type A and type B compounds, along with decomposition of the theoretical spectra into components of the transition dipole moment vectors along the X, Y, and Z axes. The red experimental data was taken on our laboratory-based instrument[21] and the blue data is from Yasuda and Kakiyama.[17] (right) Molecular geometries showing the orientation of the coordinate axes.

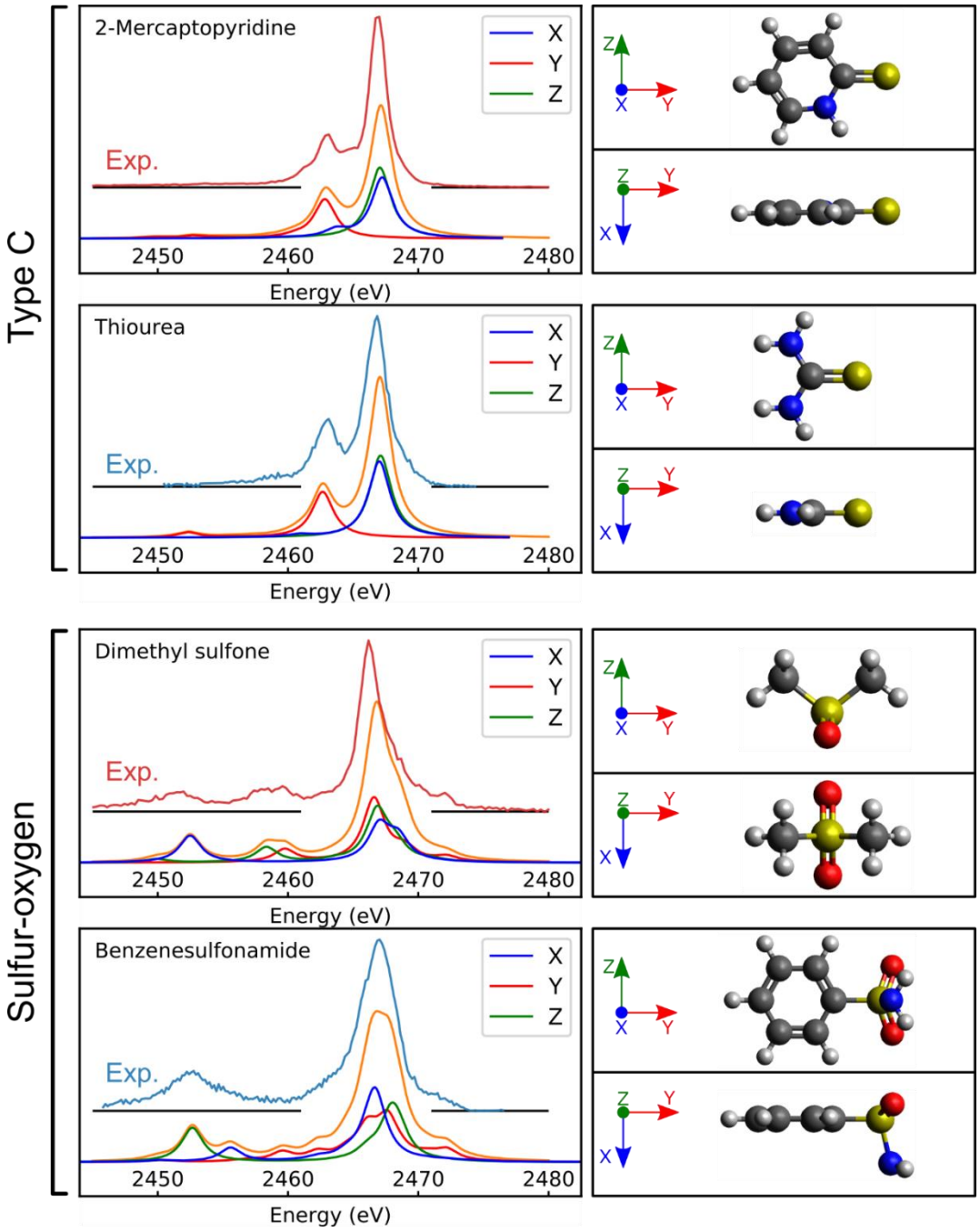

Figure 10.9: (left) Sulfur Kβ experimental (labelled "Exp.", red & blue) and theoretical (orange) spectra of type C and sulfur-oxygen compounds, along with decomposition of the theoretical spectra into components of the transition dipole moment vectors along the X, Y, and Z axes. The red experimental data was taken on our laboratory-based instrument[21] and the blue data is from Yasuda and Kakiyama.[17] (right) Molecular geometries showing the orientation of the coordinate axes.

Looking more broadly, we notice several trends in the transition dipole moment directions among the classes of compounds shown in Figures 10.8 and 10.9 (and Figures S6-S9). For type

A compounds in which the sulfur is bonded to a planar ring structure, the highest energy feature is observed to be entirely perpendicular to the plane of the ring. The other main feature and low energy shoulder are split among Y and Z components, with the main feature predominantly in the direction pointing from the center of the ring structure towards the sulfur, and with the low energy shoulder predominantly along the average C-S-C bond direction. For type B compounds, a similar pattern is observed, now with the highest energy feature dominantly perpendicular to the C-S-C bonding plane. The central spectral feature is dominantly perpendicular to the aliphatic chain in the C-S-C bonding plane, while the low energy feature/shoulder is, similar to type A, along the average C-S-C bond direction. Type C compounds also show consistent directional behavior, with the higher energy feature equally split among the two directions perpendicular to the C=S bond, and the lower energy feature entirely along the C=S bond direction. For sulfur-oxygen compounds, the main $K\beta_{1,3}$ feature does not have strong directionality, however the lower energy shoulder and Kβ' peaks are preferentially oriented. For the compounds in Figure 10.9, the Kβ' feature is along the average O-S-O bond direction. For dimethyl sulfone, the two transitions which are near in energy around 2460 eV are seen to diverge in their behavior. The higher-energy transition (calculated 2459.7 eV) which was calculated to be dominated by carbon-*s* character (vide supra) is preferentially aligned along the C-S-C average bond direction, while the lower-energy transition (calculated 2458.3 eV) which was predominantly a mixture of carbon-*s* and oxygen-*s* is instead aligned along the symmetry axis of the molecule. Similarly, for benzenesulfonamide, the Kβ' feature is again along the average O-S-O bond direction, while the calculated feature near 2455.6 eV, which had a significant nitrogen-*s* character contribution, is directed most strongly near the S-N bond direction, and lastly the low energy shoulder around

2460-2462 eV which had strong carbon-*s* character is aligned most strongly along the S-C bond direction.

To conclude this subsection on directional XES, it should be noted that this approach assumes each spectral transition acts as a linearly polarized dipole oscillating along the transition dipole moment vector direction. The extent to which this would hold in an experiment and the question of whether some spectral features may be circularly polarized (thus having a different angular dependence) is unclear. That being said, with the strong directional dependence discussed below and the previous reports of observed polarization effects in XES, it is likely that some experimental signatures of the effects will be observable, and that directional-dependent non-resonant VtC-XES may be a rich testing ground for this aspect of the theoretical results. We propose this as a valuable future direction, using experiments on single crystals of sufficiently commonly oriented small molecules.

Returning to the overall framework of the manuscript, fourth, as made clear from these results, the ability to predict S VtC-XES spectra from the molecular structure with *ab initio* computational techniques is well demonstrated. The inverse problem, however, of inferring details of molecular structures or local electronic properties from the measured spectra, is seen to be more challenging. On general grounds and on the basis of prior work on VtC-XES for 3d transition metals,[82] we expect that the broadest form of this inverse problem is ill-posed and requires prior information to direct and constrain inferences. For example, some spectral fingerprints are observed, such as the existence of the Kβ' for S-O bond-containing molecules, or the similarity of type C (thiocarbonyl) spectra across the range of compounds. However, the spectra of type A and type B compounds, as well as features other than the Kβ' in sulfur-oxygen compounds, are considerably more varied, without clear systematic trends or isolated features.

This situation is similar to XANES spectroscopy, in which the spectral features encode information about coordination, symmetry, oxidation state, and local chemical environments, but accessing this information in non-model systems still significantly relies on qualitative or semiquantitative approaches using empirical fingerprints. Recent work,[37-38] however, has shown interesting progress by employing supervised machine learning techniques. Illustrating the importance of prior information to better condition the inverse problem, Timoshenko et al.[38] have used ab initio predictions of XANES spectra of platinum nanoparticle structures to train a supervised machine learning system to extract information about coordination environments from the XANES spectra alone. For the applicability of such a machine learning approach to experimental results, it is important that the computationally predicted spectra sufficiently represent the measurements. In the work by Carbone et al.[37] on XANES spectra of 3d transition metals, although machine learning classifiers were able to reliably interpret synthetic spectra, they were not able to reliably classify experimental data due to differences in predicted and experimental features.

As a first step to understand the information content of VtC-XES for sulfur-rich organics, and hence to get some feel for the lower-bound of possible inferences from a future machine-learning approach, R^2 values have been calculated comparing the experimental and theoretically predicted spectra and are presented in Table 2 and shown graphically in the matrix comparison of Figure 10.10. The R^2 values were calculated directly between integral normalized experimental and theoretically broadened spectra as shown in Figures 10.4 and 10.5. The R^2 values show good agreement, with the majority of compounds having R^2 values greater than 0.9, and more than half having R^2 values above 0.95. Also shown in Table 2 is the theoretically predicted spectrum with the highest R^2 value compared to the experiment, showing that for 13 out of the 26 comparisons

made between theory and experiment, the best matching theoretical spectrum is for the same compound as the measured spectrum. For those compounds that do not best match, there are two main sources of disagreement: possible energy shifts between the theory and experiment, and the overall similarity of all type C compounds.

Table 10.2: Comparison of agreement between experimentally measured spectra and theoretically predicted spectra in terms of R^2 values. The theoretical spectrum with the highest R^2 value is also shown, along with the number of compounds whose theoretical spectra had higher R^2 values.

			Theoretical best match		
	Compound	**R^2 value Experiment vs. Theory**	**Compound**	**R^2 value**	**Number of compounds with better R^2**
Type A	**2-Benzoylthiophene**	0.96	2-Benzoylthiophene	0.96	0
	4,4'-Thiodiphenol	0.93	4,4'-Thiodiphenol	0.93	0
	4,4'-Thiodianiline	0.95	4,4'-Thiodiphenol	0.95	1
	2-Aminothiazole	0.96	2-Aminothiazole	0.96	0
	Thianthrene	0.98	Thianthrene	0.98	0
	Thenoic acid	0.97	2-Benzoylthiophene	0.98	1
	Dibenzothiophene	0.96	Dibenzothiophene	0.96	0
	2-(2-Hydroxyphenyl)benzothiazole	0.92	2-(2-Hydroxyphenyl)benzothiazole	0.92	0
Type B	**1,3,5-Trithiane**	0.97	1,3,5-Trithiane	0.97	0
	4,4'-Dithiodimorpholine	0.95	Dibenzyl disulfide	0.98	3
	Dibenzyl sulfide	0.97	Dibenzyl sulfide	0.97	0
	Dibenzyl disulfide	0.97	Dibenzyl disulfide	0.97	0
	Thiodipropionic acid	0.95	Dibenzyl disulfide	0.96	3
	Octadecyl sulfide	0.95	Dibenzyl sulfide	0.96	2
Type C	**Thioacetamide**	0.96	Thioacetamide	0.96	0
	Thiourea	0.94	Thioacetamide	0.94	1
	4-Mercaptopyridine	0.94	Thioacetamide	0.94	2
	2-Mercaptopyrimidine	0.92	Thiourea	0.93	2
	2-Mercaptopyridine	0.93	Thiourea	0.95	4
	2-Mercaptobenzimidazole	0.90	Thiourea	0.97	5
Sulfur-oxygen	**Diphenyl sulfoxide**	0.96	Diphenyl sulfoxide	0.96	0
	(Sodium) lauryl sulfate	0.61	Sulfanilic acid	0.78	4
	Sulfanilic acid	0.82	Diphenyl sulfone	0.88	2
	Benzenesulfonamide	0.95	Benzenesulfonamide	0.95	0
	Dimethyl sulfone	0.81	Diphenyl sulfone	0.82	3
	Diphenyl sulfone	0.85	Diphenyl sulfone	0.85	0

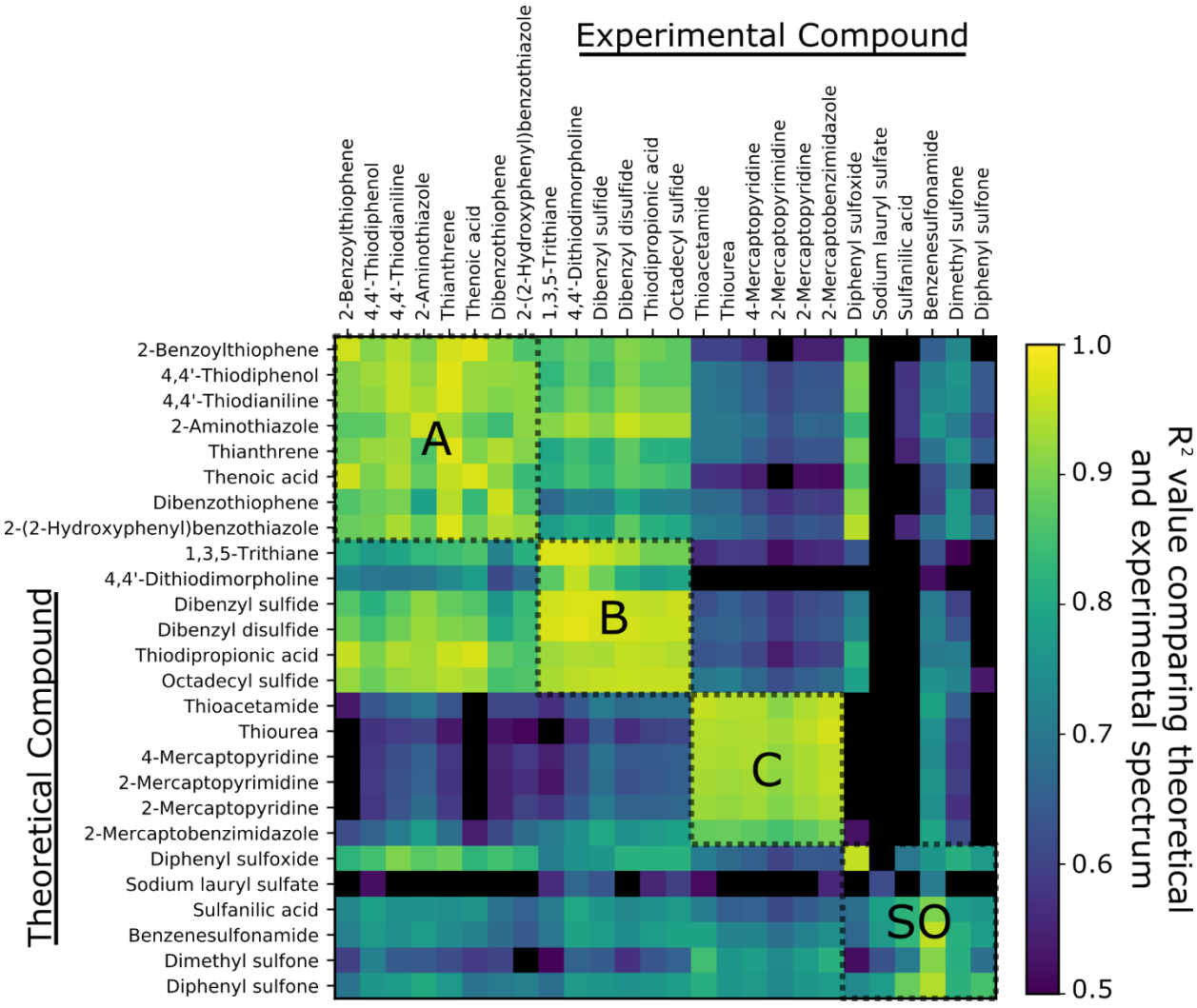

Figure 10.10: Visualization of R^2 calculated between theoretically predicted and experimentally measured spectra. The compounds are sorted in the order: type A, B, C, sulfur-oxygen (SO). These are also shown by the labelled squares, which indicate comparisons within the same type. For increased contrast, the minimum of the colorscale is set to 0.5, therefore comparisons below this value have been set to black.

The more detailed grid comparison in Figure 10.10 again supports the high agreement between theory and experiment but also makes more clear some limitations in the information content of the VtC-XES, i.e., it has significant sensitivity to the general class of local environment, just as with pre-edge and very near-edge features in XANES, but in some cases (e.g., type C compounds) lacks more detailed characterization of the molecular host. That being said,

information about coordination environment is often chemically critical, and this high level of agreement between theory and experiment together with the considerable (albeit incomplete) information content in VtC-XES suggests that machine learning approaches trained on theoretically predicted spectra could indeed allow useful interpretation of experimentally measured spectral features. The question of the richest descriptors showing, e.g., the strongest orthogonality in the vector space of VtC-XES is a promising direction for future investigation for S and likely also for many other elements.

Solid-State Compounds

For the solid-state systems, the theoretical spectra again show good agreement with the experimental spectra, as shown in Figure 10.11. In particular, the calculations for ZnS (sphalerite) accurately reproduce the main peak and shoulder relative intensities, as well as the low-energy peak near 2459 eV. In agreement with the previous results of Alonso-Mori et al.,[15] we find that this low-energy peak is due primarily to transitions involving Zn 3d-character atomic orbitals. Reasonable agreement is also seen for the As_2S_3 (orpiment), where the calculation correctly predicts a shift of the main peak to ~1 eV higher energy than ZnS, though the intensity of the low energy shoulder is weaker than what is observed in experiment. In contrast to the isolated low energy peak of ZnS, the As_2S_3 calculation correctly identifies a low energy tail below the main features, which is also seen to be present in the experimental spectrum. In the case of FeS_2 (pyrite), there is qualitative agreement, but it is somewhat poorer than the other two compounds. The calculation correctly reproduces that the main peak (near 2466 eV) is close in energy to ZnS and at lower energy than the main peak of As_2S_3. The low energy shoulder (near 2462 eV) is correctly identified to shift to lower energy than the ZnS shoulder, though the intensity is not accurately

reproduced. The largest deficit in the FeS_2 calculation is in the position of the high energy shoulder. The calculation does predict a relatively intense feature ~1.5 eV higher in energy than the main feature, a feature that does not show up in either ZnS or As_2S_3, but the calculation underestimates the splitting, which is closer to ~3 eV in the experiment. Briefly, this may be attributed to the choice of the PBE0 exchange-correlation functional, which overestimates the optical gap (~3.3 eV) compared with experiment (~0.95 eV). It is also known that FeS_2-pyrite is a challenging system from a band structure point of view.[153] Since we have utilized the PBE0 functional for all systems so that they are on the same footing, we have not analyzed the sensitivity of this specific system in detail with choice of functional.

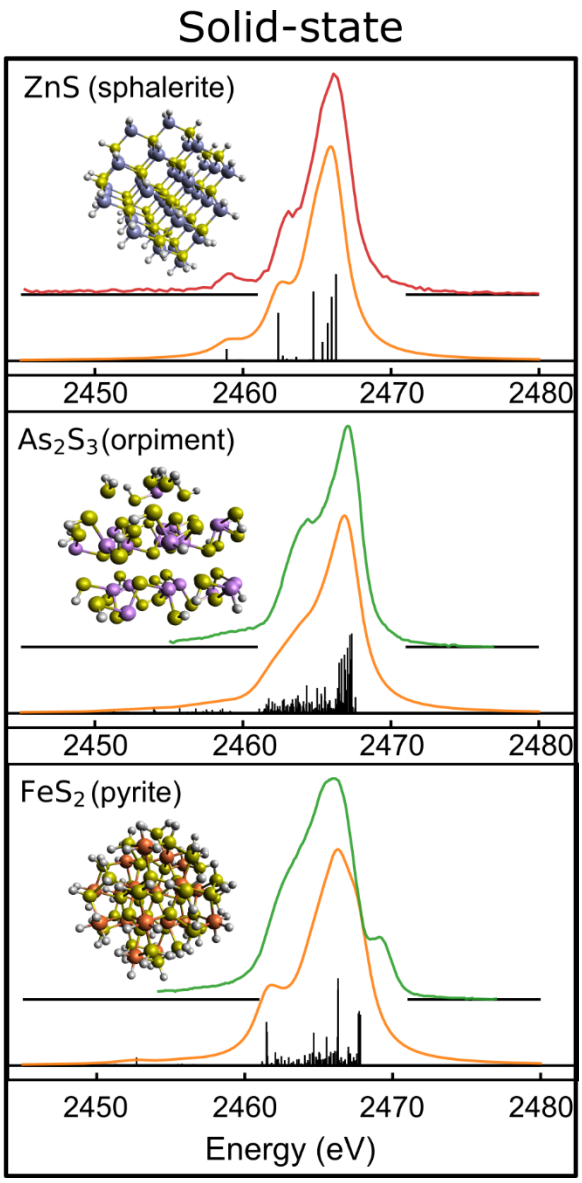

Figure 10.11: Comparison of sulfur Kβ VtC-XES experimental results (red & green) to LR-TDDFT calculations (black sticks: transitions, orange line: Lorentzian-broadened) for solid-state sulfur compounds. The red experimental data was taken on our laboratory-based instrument[21] and the green data is from Alonso-Mori et al.[15]

10.5 Conclusions

Experimental and theoretical comparisons using a LR-TDDFT procedure have been made for a wide range of sulfur compounds, spanning organic sulfur compounds with myriad different bonding structures, as well as inorganic solid-state sulfur compounds. The theoretical approach

accurately reproduces both the core-to-core Kα XES energy shifts, as well as the full variety of observed spectral features in the valence-to-core Kβ XES. Experimental spectra from the literature were augmented with newly acquired spectra using a modern laboratory-based XES spectrometer, demonstrating the possibility of growth of applicability of these techniques as laboratory instruments become more widely available. The theoretical results highlight a relatively unexplored avenue of direction-dependent XES measurements of single crystal compounds as a possible future direction for more rigorous investigation of theory and electronic structure. Following recent effort in the analysis of x-ray absorption near edge structure (XANES), we propose that the apparent solution of the forward problem of predicting S XES from known structures enables the future use of machine learning methods, but that the richest descriptors that can be thus inferred remains an open question.

10.6 Acknowledgements

This research and was partially supported by the National Science Foundation (NSF) through the UW Molecular Engineering Materials Center, a Materials Research Science and Engineering Center (DMR-1719797). EPJ was supported in part by the Joint Center for Energy Storage Research (JCESR), an Energy Innovation Hub funded by the U.S. Department of Energy, Office of Science, and Basic Energy Sciences. EPJ was also supported in part by a subcontract from the National Institute of Standards and Technology. Opinions, recommendations, findings, and conclusions presented in this manuscript and associated materials does not necessarily reflect the views or policies of NIST or the United States Government. N.G. acknowledges support from the U.S. Department of Energy, Office of Science, Office of Basic Energy Sciences through Award No. KC030105172685. This research benefited from computational resources provided by the

Environmental Molecular Sciences Laboratory (EMSL), a DOE Office of Science User Facility sponsored by the Office of Biological and Environmental Research and located at PNNL. PNNL is operated by Battelle Memorial Institute for the United States Department of Energy under DOE Contract No. DE-AC05- 76RL1830. We thank Professor Brandi Cossairt and Professor Munira Khalil of the University of Washington for useful discussions. We thank Dr. Drew Pomerantz for providing some of the sulfur compounds considered in this paper.

10.7 REFERENCES

1. Manthiram, A.; Chung, S.-H.; Zu, C., Lithium-Sulfur Batteries: Progress and Prospects. *Advanced Materials* **2015,** *27* (12), 1980-2006.
2. Manthiram, A.; Fu, Y.; Chung, S.-H.; Zu, C.; Su, Y.-S., Rechargeable Lithium–Sulfur Batteries. *Chemical Reviews* **2014,** *114* (23), 11751-11787.
3. Bruce, P. G.; Freunberger, S. A.; Hardwick, L. J.; Tarascon, J.-M., Li–O2 and Li–S batteries with high energy storage. *Nature Materials* **2011,** *11* (1), 19-29.
4. Beinert, H., Iron-Sulfur Clusters: Nature's Modular, Multipurpose Structures. *Science* **1997,** *277* (5326), 653-659.
5. Rodriguez, J. A.; Hrbek, J., Interaction of Sulfur with Well-Defined Metal and Oxide Surfaces: Unraveling the Mysteries behind Catalyst Poisoning and Desulfurization. *Accounts of Chemical Research* **1999,** *32* (9), 719-728.
6. McCue, A. J.; Anderson, J. A., Sulfur as a catalyst promoter or selectivity modifier in heterogeneous catalysis. *Catal. Sci. Technol.* **2014,** *4* (2), 272-294.
7. Wilhelm Scherer, H., Sulfur in soils. *Journal of Plant Nutrition and Soil Science* **2009,** *172* (3), 326-335.
8. Aas, W.; Mortier, A.; Bowersox, V.; Cherian, R.; Faluvegi, G.; Fagerli, H.; Hand, J.; Klimont, Z.; Galy-Lacaux, C.; Lehmann, C. M. B.; Myhre, C. L.; Myhre, G.; Olivié, D.; Sato, K.; Quaas, J.; Rao, P. S. P.; Schulz, M.; Shindell, D.; Skeie, R. B.; Stein, A.; Takemura, T.; Tsyro, S.; Vet, R.; Xu, X., Global and regional trends of atmospheric sulfur. *Scientific Reports* **2019,** *9* (1).
9. Lancaster, K. M.; Roemelt, M.; Ettenhuber, P.; Hu, Y.; Ribbe, M. W.; Neese, F.; Bergmann, U.; DeBeer, S., X-ray Emission Spectroscopy Evidences a Central Carbon in the Nitrogenase Iron-Molybdenum Cofactor. *Science* **2011,** *334* (6058), 974-977.
10. Pollock, C. J.; DeBeer, S., Valence-to-Core X-ray Emission Spectroscopy: A Sensitive Probe of the Nature of a Bound Ligand. *Journal of the American Chemical Society* **2011,** *133* (14), 5594-5601.
11. Lee, N.; Petrenko, T.; Bergmann, U.; Neese, F.; DeBeer, S., Probing Valence Orbital Composition with Iron Kβ X-ray Emission Spectroscopy. *Journal of the American Chemical Society* **2010,** *132* (28), 9715-9727.
12. Mortensen, D. R.; Seidler, G. T.; Kas, J. J.; Govind, N.; Schwartz, C. P.; Pemmaraju, S.; Prendergast, D. G., Benchmark results and theoretical treatments for valence-to-core x-ray emission spectroscopy in transition metal compounds. *Physical Review B* **2017,** *96* (12).
13. Pollock, C. J.; DeBeer, S., Insights into the Geometric and Electronic Structure of Transition Metal Centers from Valence-to-Core X-ray Emission Spectroscopy. *Accounts of Chemical Research* **2015,** *48* (11), 2967-2975.
14. Gallo, E.; Glatzel, P., Valence to Core X-ray Emission Spectroscopy. *Advanced Materials* **2014,** *26* (46), 7730-7746.
15. Mori, R. A.; Paris, E.; Giuli, G.; Eeckhout, S. G.; Kavčič, M.; Žitnik, M.; Bučar, K.; Pettersson, L. G. M.; Glatzel, P., Sulfur-Metal Orbital Hybridization in Sulfur-Bearing Compounds Studied by X-ray Emission Spectroscopy. *Inorganic Chemistry* **2010,** *49* (14), 6468-6473.
16. Petric, M.; Bohinc, R.; Bučar, K.; Nowak, S. H.; Žitnik, M.; Kavčič, M., Electronic Structure of Third-Row Elements in Different Local Symmetries Studied by Valence-to-Core X-ray Emission Spectroscopy. *Inorganic Chemistry* **2016,** *55* (11), 5328-5336.

17. Yasuda, S.; Kakiyama, H., Chemical effects in X-ray Kα and Kβ emission spectra of sulfur in organic compounds. *Spectrochimica Acta Part A: Molecular Spectroscopy* **1979,** *35* (5), 485-493.
18. Seidler, G. T.; Mortensen, D. R.; Ditter, A. S.; Ball, N. A.; Remesnik, A. J., A Modern Laboratory XAFS Cookbook. *Journal of Physics: Conference Series* **2016,** *712*, 012015.
19. Seidler, G. T.; Mortensen, D. R.; Remesnik, A. J.; Pacold, J. I.; Ball, N. A.; Barry, N.; Styczinski, M.; Hoidn, O. R., A laboratory-based hard x-ray monochromator for high-resolution x-ray emission spectroscopy and x-ray absorption near edge structure measurements. *Review of Scientific Instruments* **2014,** *85* (11), 113906.
20. Mortensen, D. R.; Seidler, G. T.; Ditter, A. S.; Glatzel, P., Benchtop Nonresonant X-ray Emission Spectroscopy: Coming Soon to Laboratories and XAS Beamlines Near You? *Journal of Physics: Conference Series* **2016,** *712*, 012036.
21. Holden, W. M.; Hoidn, O. R.; Ditter, A. S.; Seidler, G. T.; Kas, J.; Stein, J. L.; Cossairt, B. M.; Kozimor, S. A.; Guo, J.; Ye, Y.; Marcus, M. A.; Fakra, S., A compact dispersive refocusing Rowland circle X-ray emission spectrometer for laboratory, synchrotron, and XFEL applications. *Review of Scientific Instruments* **2017,** *88* (7), 073904.
22. Jahrman, E. P.; Holden, W. M.; Ditter, A. S.; Mortensen, D. R.; Seidler, G. T.; Fister, T. T.; Kozimor, S. A.; Piper, L. F. J.; Rana, J.; Hyatt, N. C.; Stennett, M. C., An improved laboratory-based x-ray absorption fine structure and x-ray emission spectrometer for analytical applications in materials chemistry research. *Review of Scientific Instruments* **2019,** *90* (2), 024106.
23. Anklamm, L.; Schlesiger, C.; Malzer, W.; Grötzsch, D.; Neitzel, M.; Kanngießer, B., A novel von Hamos spectrometer for efficient X-ray emission spectroscopy in the laboratory. *Review of Scientific Instruments* **2014,** *85* (5), 053110.
24. Bès, R.; Ahopelto, T.; Honkanen, A. P.; Huotari, S.; Leinders, G.; Pakarinen, J.; Kvashnina, K., Laboratory-scale X-ray absorption spectroscopy approach for actinide research: Experiment at the uranium L3-edge. *Journal of Nuclear Materials* **2018,** *507*, 50-53.
25. Kayser, Y.; Błachucki, W.; Dousse, J. C.; Hoszowska, J.; Neff, M.; Romano, V., Laboratory-based micro-X-ray fluorescence setup using a von Hamos crystal spectrometer and a focused beam X-ray tube. *Review of Scientific Instruments* **2014,** *85* (4), 043101.
26. Németh, Z.; Szlachetko, J.; Bajnóczi, É. G.; Vankó, G., Laboratory von Hámos X-ray spectroscopy for routine sample characterization. *Review of Scientific Instruments* **2016,** *87* (10), 103105.
27. Szlachetko, M.; Berset, M.; Dousse, J. C.; Hoszowska, J.; Szlachetko, J., High-resolution Laue-type DuMond curved crystal spectrometer. *Review of Scientific Instruments* **2013,** *84* (9), 093104.
28. Honkanen, A.-P.; Ollikkala, S.; Ahopelto, T.; Kallio, A.-J.; Blomberg, M.; Huotari, S., Johann-type laboratory-scale x-ray absorption spectrometer with versatile detection modes. *Review of Scientific Instruments* **2019,** *90* (3), 033107.
29. Zeeshan, F.; Hoszowska, J.; Loperetti-Tornay, L.; Dousse, J. C., In-house setup for laboratory-based x-ray absorption fine structure spectroscopy measurements. *Review of Scientific Instruments* **2019,** *90* (7), 073105.
30. Błachucki, W.; Czapla-Masztafiak, J.; Sá, J.; Szlachetko, J., A laboratory-based double X-ray spectrometer for simultaneous X-ray emission and X-ray absorption studies. *Journal of Analytical Atomic Spectrometry* **2019,** *34* (7), 1409-1415.

31. Malzer, W.; Grötzsch, D.; Gnewkow, R.; Schlesiger, C.; Kowalewski, F.; Van Kuiken, B.; DeBeer, S.; Kanngießer, B., A laboratory spectrometer for high throughput X-ray emission spectroscopy in catalysis research. *Review of Scientific Instruments* **2018,** *89* (11), 113111.
32. Yuryev, Y. N.; Lee, H.-J.; Park, H.-M.; Cho, Y.-K.; Lee, M.-K.; Pogrebitsky, K. J., Variable Rowland radius laboratory vacuum surface-sensitive x-ray absorption fine structure spectrometer. *Review of Scientific Instruments* **2007,** *78* (2), 025108.
33. Holden, W. M.; Seidler, G. T.; Cheah, S., Sulfur Speciation in Biochars by Very High Resolution Benchtop Kα X-ray Emission Spectroscopy. *The Journal of Physical Chemistry A* **2018,** *122* (23), 5153-5161.
34. Jahrman, E. P.; Seidler, G. T.; Sieber, J. R., Determination of Hexavalent Chromium Fractions in Plastics Using Laboratory-Based, High-Resolution X-ray Emission Spectroscopy. *Analytical Chemistry* **2018,** *90* (11), 6587-6593.
35. Stein, J. L.; Holden, W. M.; Venkatesh, A.; Mundy, M. E.; Rossini, A. J.; Seidler, G. T.; Cossairt, B. M., Probing Surface Defects of InP Quantum Dots Using Phosphorus Kα and Kβ X-ray Emission Spectroscopy. *Chemistry of Materials* **2018,** *30* (18), 6377-6388.
36. Cossairt, B. M.; Stein, J. L.; Holden, W. M.; Seidler, G. T., 4-1: Invited Paper: Role of Phosphorus Oxidation in Controlling the Luminescent Properties of Indium Phosphide Quantum Dots. *SID Symposium Digest of Technical Papers* **2018,** *49* (1), 21-24.
37. Carbone, M. R.; Yoo, S.; Topsakal, M.; Lu, D., Classification of local chemical environments from x-ray absorption spectra using supervised machine learning. *Physical Review Materials* **2019,** *3* (3).
38. Timoshenko, J.; Lu, D.; Lin, Y.; Frenkel, A. I., Supervised Machine-Learning-Based Determination of Three-Dimensional Structure of Metallic Nanoparticles. *The Journal of Physical Chemistry Letters* **2017,** *8* (20), 5091-5098.
39. Parratt, L. G., Effects of Chemical Binding on the X-RayKα1, 2Doublet Lines of Sulphur Studied with a Two-Crystal Spectrometer. *Physical Review* **1936,** *49* (1), 14-16.
40. Sato, T.; Takahashi, Y.; Yabe, K., An X-Ray Emission Spectroscopic Investigation of the Chemical Bond of Sulfur. I. The Peak Shift ofKα and the Number of Valence Electrons of the Sulfur Atom in Compounds. *Bulletin of the Chemical Society of Japan* **1967,** *40* (2), 298-301.
41. Takahashi, Y.; Yabe, K.; Sato, T., An X-Ray Emission Spectroscopic Investigation of the Chemical Bond of Sulfur. II. The Number of Valence Electrons of the Sulfur Atom in Organic Compounds. *Bulletin of the Chemical Society of Japan* **1969,** *42* (9), 2707-2708.
42. Yarmoshenko, Y. M.; Trofimova, V. A.; Elokhina, L. V.; Kurmaev, E. Z.; Butorin, S.; Cloots, R.; Ausloos, M.; Aguiar, J. A.; Lobatchevskaya, N. I., Possibility of sulphur-oxygen substitution in YBa2Cu3O6+xSy analyzed by means of X-ray emission spectroscopy. *Journal of Physics and Chemistry of Solids* **1993,** *54* (10), 1211-1214.
43. Yarmoshenko, Y. M.; Trofimova, V. A.; Dolgih, V. E.; Korotin, M. A.; Kurmaev, E. Z.; Aguiar, J. A.; Ferreira, J. M.; Pavao, A. C., X-ray emission spectra and valence state of sulphur atoms of YBa2((CuO)1-x(NiS)x)3O4- delta. *Journal of Physics: Condensed Matter* **1995,** *7* (1), 213-218.
44. Dolenko, G. N., X-ray determination of effective charges on sulphur, phosphorus, silicon and chlorine atoms. *Journal of Molecular Structure* **1993,** *291* (1), 23-57.
45. Alonso Mori, R.; Paris, E.; Giuli, G.; Eeckhout, S. G.; Kavčič, M.; Žitnik, M.; Bučar, K.; Pettersson, L. G. M.; Glatzel, P., Electronic Structure of Sulfur Studied by X-ray Absorption and Emission Spectroscopy. *Analytical Chemistry* **2009,** *81* (15), 6516-6525.

46. Solomon, D.; Lehmann, J.; Martínez, C. E., Sulfur K-edge XANES Spectroscopy as a Tool for Understanding Sulfur Dynamics in Soil Organic Matter. *Soil Science Society of America Journal* **2003,** *67* (6), 1721.
47. Huffman, G. P.; Mitra, S.; Huggins, F. E.; Shah, N.; Vaidya, S.; Lu, F., Quantitative analysis of all major forms of sulfur in coal by x-ray absorption fine structure spectroscopy. *Energy & Fuels* **1991,** *5* (4), 574-581.
48. Jugo, P. J.; Wilke, M.; Botcharnikov, R. E., Sulfur K-edge XANES analysis of natural and synthetic basaltic glasses: Implications for S speciation and S content as function of oxygen fugacity. *Geochimica et Cosmochimica Acta* **2010,** *74* (20), 5926-5938.
49. George, G. N.; Gorbaty, M. L.; Kelemen, S. R.; Sansone, M., Direct determination and quantification of sulfur forms in coals from the Argonne Premium Sample Program. *Energy & Fuels* **1991,** *5* (1), 93-97.
50. Prietzel, J. r.; Botzaki, A.; Tyufekchieva, N.; Brettholle, M.; Thieme, J. r.; Klysubun, W., Sulfur Speciation in Soil by SK-Edge XANES Spectroscopy: Comparison of Spectral Deconvolution and Linear Combination Fitting. *Environmental Science & Technology* **2011,** *45* (7), 2878-2886.
51. Berry, A. J.; O'Neill, H. S. C.; Jayasuriya, K. D.; Campbell, S. J.; Foran, G. J., XANES calibrations for the oxidation state of iron in a silicate glass. *American Mineralogist* **2003,** *88* (7), 967-977.
52. Mijovilovich, A.; Pettersson, L. G. M.; Mangold, S.; Janousch, M.; Susini, J.; Salome, M.; de Groot, F. M. F.; Weckhuysen, B. M., The Interpretation of Sulfur K-Edge XANES Spectra: A Case Study on Thiophenic and Aliphatic Sulfur Compounds. *The Journal of Physical Chemistry A* **2009,** *113* (12), 2750-2756.
53. Ray, K.; DeBeer George, S.; Solomon, E. I.; Wieghardt, K.; Neese, F., Description of the Ground-State Covalencies of the Bis(dithiolato) Transition-Metal Complexes from X-ray Absorption Spectroscopy and Time-Dependent Density-Functional Calculations. *Chemistry - A European Journal* **2007,** *13* (10), 2783-2797.
54. Sproules, S.; Wieghardt, K., Dithiolene radicals: Sulfur K-edge X-ray absorption spectroscopy and Harry's intuition. *Coordination Chemistry Reviews* **2011,** *255* (7-8), 837-860.
55. Takahashi, Y.; Yabe, K., An X-Ray Emission Spectroscopic Investigation of the Chemical Bond of Sulfur. III. The Profile of SKβ Band in Sulfur Compounds. *Bulletin of the Chemical Society of Japan* **1969,** *42* (11), 3064-3072.
56. Yarmoshenko, Y. M.; Trofimova, V. A.; Kurmaev, E. Z.; Slater, P. R.; Greaves, C., X-ray emission spectra of YSr2Cu3O7−δ containing sulphate and phosphate groups. *Physica C: Superconductivity* **1994,** *224* (3-4), 317-320.
57. Yarmoshenko, Y. M.; Korotin, M. A.; Trofimova, V. A.; Galakhov, V. R.; Elokhina, L. V.; Kurmaev, E. Z.; Uhlenbrock, S.; Neumann, M.; Slater, P. R.; Greaves, C., Electronic structure of cuprates containing sulfur and phosphorus oxyanions. *Physical Review B* **1995,** *52* (16), 11830-11836.
58. Sugiura, C.; Gohshi, Y.; Suzuki, I., SulfurKβx-ray emission spectra and electronic structures of some metal sulfides. *Physical Review B* **1974,** *10* (2), 338-343.
59. Sugiura, C.; Suzuki, I.; Kashiwakura, J.; Gohshi, Y., SulfurKβ X-Ray Emission Bands and Valence-Band Structures of Transition-Metal Disulfides. *Journal of the Physical Society of Japan* **1976,** *40* (6), 1720-1724.

60. Sugiura, C., Kβ X-Ray Emission and K X-Ray Absorption Spectra of Sulfur in Sulfate Compounds. *Japanese Journal of Applied Physics* **1993,** *32* (Part 1, No. 8), 3509-3514.
61. Sugiura, C., Kβ X-Ray Emission Spectra and Chemical Environments of Phosphorus and Sulfur in Various Compounds. *Journal of the Physical Society of Japan* **1995,** *64* (10), 3840-3852.
62. Sugiura, C.; Yorikawa, H.; Muramatsu, S., SulfurKβX-Ray Emission Spectra and Valence-Band Structures of Metal Sulfides. *Journal of the Physical Society of Japan* **1997,** *66* (2), 503-504.
63. Parratt, L. G., Design of a Double-Crystal X-Ray Vacuum Spectrometer. *Physical Review* **1932,** *41* (5), 553-560.
64. Gohshi, Y.; Hukao, Y.; Hori, K., A wide-range, single-axis, vacuum two-crystal spectrometer for fluorescent X-ray analysis. *Spectrochimica Acta Part B: Atomic Spectroscopy* **1972,** *27* (3), 135-142.
65. Taniguchi, K., Simple quasi-two-crystal x-ray spectrometer. *Review of Scientific Instruments* **1983,** *54* (5), 559-562.
66. Sugiura, C., Molecular-Orbital Interpretation of the X-RayKSpectra from α-Sulfur. *Journal of the Physical Society of Japan* **1971,** *30* (6), 1766-1766.
67. Karlsson, G.; Manne, R., Molecular Orbital Interpretation of X-Ray Emission Spectra II. Sulfur and chlorineKβspectra of some inorganic anions. *Physica Scripta* **1971,** *4* (3), 119-124.
68. Adachi, H.; Taniguchi, K., Discrete Variational Xα Cluster Calculations. IV. Application to X-Ray Emission Study. *Journal of the Physical Society of Japan* **1980,** *49* (5), 1944-1953.
69. Eiichirou, U.; Jun, K.; Uda, M., Calculation of sulfur K ß X-ray spectra. *Nuclear Instruments and Methods in Physics Research Section B: Beam Interactions with Materials and Atoms* **1993,** *75* (1-4), 24-27.
70. Mogi, M.; Ota, A.; Ebihara, S.; Tachibana, M.; Uda, M., Intensity analysis of S Kß emission spectra of Na2SO3 by the use of DV-Xα MO method. *Nuclear Instruments and Methods in Physics Research Section B: Beam Interactions with Materials and Atoms* **1993,** *75* (1-4), 20-23.
71. Petric, M.; Kavčič, M., Chemical speciation via X-ray emission spectroscopy in the tender X-ray range. *Journal of Analytical Atomic Spectrometry* **2016,** *31* (2), 450-457.
72. Wadey, J. D.; Besley, N. A., Quantum Chemical Calculations of X-ray Emission Spectroscopy. *Journal of Chemical Theory and Computation* **2014,** *10* (10), 4557-4564.
73. Zhang, Y.; Mukamel, S.; Khalil, M.; Govind, N., Simulating Valence-to-Core X-ray Emission Spectroscopy of Transition Metal Complexes with Time-Dependent Density Functional Theory. *Journal of Chemical Theory and Computation* **2015,** *11* (12), 5804-5809.
74. Cutsail, G. E.; Gagnon, N. L.; Spaeth, A. D.; Tolman, W. B.; DeBeer, S., Valence-to-Core X-ray Emission Spectroscopy as a Probe of O−O Bond Activation in Cu2O2 Complexes. *Angewandte Chemie International Edition* **2019,** *58* (27), 9114-9119.
75. Wansleben, M.; Vinson, J.; Holfelder, I.; Kayser, Y.; Beckhoff, B., Valence-to-core X-ray emission spectroscopy of Ti, TiO, and TiO2 by means of a double full-cylinder crystal von Hamos spectrometer. *X-Ray Spectrometry* **2018,** *48* (2), 102-106.
76. March, A. M.; Assefa, T. A.; Boemer, C.; Bressler, C.; Britz, A.; Diez, M.; Doumy, G.; Galler, A.; Harder, M.; Khakhulin, D.; Németh, Z.; Pápai, M.; Schulz, S.; Southworth, S.

H.; Yavaş, H.; Young, L.; Gawelda, W.; Vankó, G., Probing Transient Valence Orbital Changes with Picosecond Valence-to-Core X-ray Emission Spectroscopy. *The Journal of Physical Chemistry C* **2017,** *121* (5), 2620-2626.

77. Maganas, D.; DeBeer, S.; Neese, F., A Restricted Open Configuration Interaction with Singles Method To Calculate Valence-to-Core Resonant X-ray Emission Spectra: A Case Study. *Inorganic Chemistry* **2017,** *56* (19), 11819-11836.
78. Gallo, E.; Gorelov, E.; Guda, A. A.; Bugaev, A. L.; Bonino, F.; Borfecchia, E.; Ricchiardi, G.; Gianolio, D.; Chavan, S.; Lamberti, C., Effect of Molecular Guest Binding on the d–d Transitions of Ni2+of CPO-27-Ni: A Combined UV–Vis, Resonant-Valence-to-Core X-ray Emission Spectroscopy, and Theoretical Study. *Inorganic Chemistry* **2017,** *56* (23), 14408-14425.
79. Martin-Diaconescu, V.; Chacón, K. N.; Delgado-Jaime, M. U.; Sokaras, D.; Weng, T.-C.; DeBeer, S.; Blackburn, N. J., Kβ Valence to Core X-ray Emission Studies of Cu(I) Binding Proteins with Mixed Methionine – Histidine Coordination. Relevance to the Reactivity of the M- and H-sites of Peptidylglycine Monooxygenase. *Inorganic Chemistry* **2016,** *55* (7), 3431-3439.
80. Hugenbruch, S.; Shafaat, H. S.; Krämer, T.; Delgado-Jaime, M. U.; Weber, K.; Neese, F.; Lubitz, W.; DeBeer, S., In search of metal hydrides: an X-ray absorption and emission study of [NiFe] hydrogenase model complexes. *Physical Chemistry Chemical Physics* **2016,** *18* (16), 10688-10699.
81. Beckwith, M. A.; Roemelt, M.; Collomb, M.-N. l.; DuBoc, C.; Weng, T.-C.; Bergmann, U.; Glatzel, P.; Neese, F.; DeBeer, S., Manganese Kβ X-ray Emission Spectroscopy As a Probe of Metal–Ligand Interactions. *Inorganic Chemistry* **2011,** *50* (17), 8397-8409.
82. MacMillan, S. N.; Walroth, R. C.; Perry, D. M.; Morsing, T. J.; Lancaster, K. M., Ligand-Sensitive But Not Ligand-Diagnostic: Evaluating Cr Valence-to-Core X-ray Emission Spectroscopy as a Probe of Inner-Sphere Coordination. *Inorganic Chemistry* **2014,** *54* (1), 205-214.
83. Pollock, C. J.; Lancaster, K. M.; Finkelstein, K. D.; DeBeer, S., Study of Iron Dimers Reveals Angular Dependence of Valence-to-Core X-ray Emission Spectra. *Inorganic Chemistry* **2014,** *53* (19), 10378-10385.
84. Bauer, M., HERFD-XAS and valence-to-core-XES: new tools to push the limits in research with hard X-rays? *Phys. Chem. Chem. Phys.* **2014,** *16* (27), 13827-13837.
85. Delgado-Jaime, M. U.; DeBeer , S.; Bauer, M., Valence-to-Core X-Ray Emission Spectroscopy of Iron-Carbonyl Complexes: Implications for the Examination of Catalytic Intermediates. *Chemistry - A European Journal* **2013,** *19* (47), 15888-15897.
86. Swarbrick, J. C.; Kvashnin, Y.; Schulte, K.; Seenivasan, K.; Lamberti, C.; Glatzel, P., Ligand Identification in Titanium Complexes Using X-ray Valence-to-Core Emission Spectroscopy. *Inorganic Chemistry* **2010,** *49* (18), 8323-8332.
87. Smolentsev, G.; Soldatov, A. V.; Messinger, J.; Merz, K.; Weyhermüller, T.; Bergmann, U.; Pushkar, Y.; Yano, J.; Yachandra, V. K.; Glatzel, P., X-ray Emission Spectroscopy To Study Ligand Valence Orbitals in Mn Coordination Complexes. *Journal of the American Chemical Society* **2009,** *131* (36), 13161-13167.
88. Bergmann, U.; Bendix, J.; Glatzel, P.; Gray, H. B.; Cramer, S. P., Anisotropic valence→core x-ray fluorescence from a [Rh(en)3][Mn(N)(CN)5]·H2O single crystal: Experimental results and density functional calculations. *The Journal of Chemical Physics* **2002,** *116* (5), 2011-2015.

89. Bordage, A.; Pápai, M.; Sas, N. S.; Szlachetko, J.; Nachtegaal, M.; Vankó, G., On the sensitivity of hard X-ray spectroscopies to the chemical state of Br. *Physical Chemistry Chemical Physics* **2013,** *15* (26), 11088.
90. Takahashi, Y., The X-Ray Emission Spectra of the Compounds of Third-period Elements. VI. The Relationship between theKα andKβ Spectra. *Bulletin of the Chemical Society of Japan* **1973,** *46* (7), 2039-2044.
91. Petric, M.; Bohinc, R.; Bučar, K.; Žitnik, M.; Szlachetko, J.; Kavčič, M., Chemical State Analysis of Phosphorus Performed by X-ray Emission Spectroscopy. *Analytical Chemistry* **2015,** *87* (11), 5632-5639.
92. Taniguchi, K., Chemical-state Analysis by Means of Soft X-Ray Spectroscopy. II.Kβ Spectra for Phosphorus, Sulfur, and Chlorine in Various Compounds. *Bulletin of the Chemical Society of Japan* **1984,** *57* (4), 915-920.
93. Holden, W. M.; Hoidn, O. R.; Seidler, G. T.; DiChiara, A. D., A color x-ray camera for 2–6 keV using a mass produced back illuminated complementary metal oxide semiconductor sensor. *Review of Scientific Instruments* **2018,** *89* (9), 093111.
94. Rohatgi, A. WebPlotDigitizer. https://automeris.io/WebPlotDigitizer (accessed July 15, 2019).
95. Casida, M. E., Time-Dependent Density Functional Response Theory for Molecules. **1995,** *1*, 155-192.
96. Stratmann, R. E.; Scuseria, G. E.; Frisch, M. J., An efficient implementation of time-dependent density-functional theory for the calculation of excitation energies of large molecules. *The Journal of Chemical Physics* **1998,** *109* (19), 8218-8224.
97. Hirata, S.; Head-Gordon, M., Time-dependent density functional theory for radicals. *Chemical Physics Letters* **1999,** *302* (5-6), 375-382.
98. DeBeer George, S.; Neese, F., Calibration of Scalar Relativistic Density Functional Theory for the Calculation of Sulfur K-Edge X-ray Absorption Spectra. *Inorganic Chemistry* **2010,** *49* (4), 1849-1853.
99. Vijayakumar, M.; Govind, N.; Walter, E.; Burton, S. D.; Shukla, A.; Devaraj, A.; Xiao, J.; Liu, J.; Wang, C.; Karim, A.; Thevuthasan, S., Molecular structure and stability of dissolved lithium polysulfide species. *Phys. Chem. Chem. Phys.* **2014,** *16* (22), 10923-10932.
100. Andersen, A.; Rajput, N. N.; Han, K. S.; Pan, H.; Govind, N.; Persson, K. A.; Mueller, K. T.; Murugesan, V., Structure and Dynamics of Polysulfide Clusters in a Nonaqueous Solvent Mixture of 1,3-Dioxolane and 1,2-Dimethoxyethane. *Chemistry of Materials* **2019,** *31* (7), 2308-2319.
101. DeBeer George, S.; Petrenko, T.; Neese, F., Time-dependent density functional calculations of ligand K-edge X-ray absorption spectra. *Inorganica Chimica Acta* **2008,** *361* (4), 965-972.
102. DeBeer George, S.; Petrenko, T.; Neese, F., Prediction of Iron K-Edge Absorption Spectra Using Time-Dependent Density Functional Theory†. *The Journal of Physical Chemistry A* **2008,** *112* (50), 12936-12943.
103. Besley, N. A.; Noble, A., Time-Dependent Density Functional Theory Study of the X-ray Absorption Spectroscopy of Acetylene, Ethylene, and Benzene on Si(100). *The Journal of Physical Chemistry C* **2007,** *111* (8), 3333-3340.

104. Lopata, K.; Van Kuiken, B. E.; Khalil, M.; Govind, N., Linear-Response and Real-Time Time-Dependent Density Functional Theory Studies of Core-Level Near-Edge X-Ray Absorption. *Journal of Chemical Theory and Computation* **2012,** *8* (9), 3284-3292.
105. Vjunov, A.; Fulton, J. L.; Huthwelker, T.; Pin, S.; Mei, D.; Schenter, G. K.; Govind, N.; Camaioni, D. M.; Hu, J. Z.; Lercher, J. A., Quantitatively Probing the Al Distribution in Zeolites. *Journal of the American Chemical Society* **2014,** *136* (23), 8296-8306.
106. Zhang, Y.; Biggs, J. D.; Healion, D.; Govind, N.; Mukamel, S., Core and valence excitations in resonant X-ray spectroscopy using restricted excitation window time-dependent density functional theory. *The Journal of Chemical Physics* **2012,** *137* (19), 194306.
107. Van Kuiken, B. E.; Valiev, M.; Daifuku, S. L.; Bannan, C.; Strader, M. L.; Cho, H.; Huse, N.; Schoenlein, R. W.; Govind, N.; Khalil, M., Simulating Ru L3-Edge X-ray Absorption Spectroscopy with Time-Dependent Density Functional Theory: Model Complexes and Electron Localization in Mixed-Valence Metal Dimers. *The Journal of Physical Chemistry A* **2013,** *117* (21), 4444-4454.
108. Vjunov, A.; Wang, M.; Govind, N.; Huthwelker, T.; Shi, H.; Mei, D.; Fulton, J. L.; Lercher, J. A., Tracking the Chemical Transformations at the Brønsted Acid Site upon Water-Induced Deprotonation in a Zeolite Pore. *Chemistry of Materials* **2017,** *29* (21), 9030-9042.
109. Fulton, J. L.; Govind, N.; Huthwelker, T.; Bylaska, E. J.; Vjunov, A.; Pin, S.; Smurthwaite, T. D., Electronic and Chemical State of Aluminum from the Single- (K) and Double-Electron Excitation (KLII&III, KLI) X-ray Absorption Near-Edge Spectra of α-Alumina, Sodium Aluminate, Aqueous Al3+·(H2O)6, and Aqueous Al(OH)4–. *The Journal of Physical Chemistry B* **2015,** *119* (26), 8380-8388.
110. Ross, M.; Andersen, A.; Fox, Z. W.; Zhang, Y.; Hong, K.; Lee, J.-H.; Cordones, A.; March, A. M.; Doumy, G.; Southworth, S. H.; Marcus, M. A.; Schoenlein, R. W.; Mukamel, S.; Govind, N.; Khalil, M., Comprehensive Experimental and Computational Spectroscopic Study of Hexacyanoferrate Complexes in Water: From Infrared to X-ray Wavelengths. *The Journal of Physical Chemistry B* **2018,** *122* (19), 5075-5086.
111. Govind, N.; de Jong, W. A., Simulating Cl K-edge X-ray absorption spectroscopy in MCl6 2- (M = U, Np, Pu) complexes and UOCl5 - using time-dependent density functional theory. **2015,** *10*, 247-253.
112. Galib, M.; Schenter, G. K.; Mundy, C. J.; Govind, N.; Fulton, J. L., Unraveling the spectral signatures of solvent ordering in K-edge XANES of aqueous Na+. *The Journal of Chemical Physics* **2018,** *149* (12), 124503.
113. Galib, M.; Baer, M. D.; Skinner, L. B.; Mundy, C. J.; Huthwelker, T.; Schenter, G. K.; Benmore, C. J.; Govind, N.; Fulton, J. L., Revisiting the hydration structure of aqueous Na+. *The Journal of Chemical Physics* **2017,** *146* (8), 084504.
114. Henzler, K.; Fetisov, E. O.; Galib, M.; Baer, M. D.; Legg, B. A.; Borca, C.; Xto, J. M.; Pin, S.; Fulton, J. L.; Schenter, G. K.; Govind, N.; Siepmann, J. I.; Mundy, C. J.; Huthwelker, T.; De Yoreo, J. J., Supersaturated calcium carbonate solutions are classical. *Science Advances* **2018,** *4* (1), eaao6283.
115. Singh, N.; Nguyen, M.-T.; Cantu, D. C.; Mehdi, B. L.; Browning, N. D.; Fulton, J. L.; Zheng, J.; Balasubramanian, M.; Gutiérrez, O. Y.; Glezakou, V.-A.; Rousseau, R.; Govind, N.; Camaioni, D. M.; Campbell, C. T.; Lercher, J. A., Carbon-supported Pt during aqueous phenol hydrogenation with and without applied electrical potential: X-ray absorption and theoretical studies of structure and adsorbates. *Journal of Catalysis* **2018,** *368*, 8-19.

116. Hirata, S.; Head-Gordon, M., Time-dependent density functional theory within the Tamm–Dancoff approximation. *Chemical Physics Letters* **1999,** *314* (3-4), 291-299.
117. Valiev, M.; Bylaska, E. J.; Govind, N.; Kowalski, K.; Straatsma, T. P.; Van Dam, H. J. J.; Wang, D.; Nieplocha, J.; Apra, E.; Windus, T. L.; de Jong, W. A., NWChem: A comprehensive and scalable open-source solution for large scale molecular simulations. *Computer Physics Communications* **2010,** *181* (9), 1477-1489.
118. Lykos, P. G.; Schmeising, H. N., Maximum Overlap Atomic and Molecular Orbitals. *The Journal of Chemical Physics* **1961,** *35* (1), 288-293.
119. King, H. F.; Stanton, R. E.; Kim, H.; Wyatt, R. E.; Parr, R. G., Corresponding Orbitals and the Nonorthogonality Problem in Molecular Quantum Mechanics. *The Journal of Chemical Physics* **1967,** *47* (6), 1936-1941.
120. Deslattes, R. D.; Kessler, E. G.; Indelicato, P.; de Billy, L.; Lindroth, E.; Anton, J., X-ray transition energies: new approach to a comprehensive evaluation. *Reviews of Modern Physics* **2003,** *75* (1), 35-99.
121. Bergwerf, H. MolView. http://molview.org/ (accessed July 15, 2019).
122. Kim, S.; Chen, J.; Cheng, T.; Gindulyte, A.; He, J.; He, S.; Li, Q.; Shoemaker, B. A.; Thiessen, P. A.; Yu, B.; Zaslavsky, L.; Zhang, J.; Bolton, E. E., PubChem 2019 update: improved access to chemical data. *Nucleic Acids Research* **2019,** *47* (D1), D1102-D1109.
123. Becke, A. D., Density-functional thermochemistry. III. The role of exact exchange. *The Journal of Chemical Physics* **1993,** *98* (7), 5648-5652.
124. Francl, M. M.; Pietro, W. J.; Hehre, W. J.; Binkley, J. S.; Gordon, M. S.; DeFrees, D. J.; Pople, J. A., Self-consistent molecular orbital methods. XXIII. A polarization-type basis set for second-row elements. *The Journal of Chemical Physics* **1982,** *77* (7), 3654-3665.
125. Gordon, M. S.; Binkley, J. S.; Pople, J. A.; Pietro, W. J.; Hehre, W. J., Self-consistent molecular-orbital methods. 22. Small split-valence basis sets for second-row elements. *Journal of the American Chemical Society* **1982,** *104* (10), 2797-2803.
126. Hariharan, P. C.; Pople, J. A., The influence of polarization functions on molecular orbital hydrogenation energies. *Theoretica Chimica Acta* **1973,** *28* (3), 213-222.
127. Hehre, W. J.; Ditchfield, R.; Pople, J. A., Self—Consistent Molecular Orbital Methods. XII. Further Extensions of Gaussian—Type Basis Sets for Use in Molecular Orbital Studies of Organic Molecules. *The Journal of Chemical Physics* **1972,** *56* (5), 2257-2261.
128. Krishnan, R.; Binkley, J. S.; Seeger, R.; Pople, J. A., Self-consistent molecular orbital methods. XX. A basis set for correlated wave functions. *The Journal of Chemical Physics* **1980,** *72* (1), 650-654.
129. McLean, A. D.; Chandler, G. S., Contracted Gaussian basis sets for molecular calculations. I. Second row atoms, Z=11–18. *The Journal of Chemical Physics* **1980,** *72* (10), 5639-5648.
130. Noro, T.; Sekiya, M.; Koga, T., Segmented contracted basis sets for atoms H through Xe: Sapporo-(DK)-nZP sets (n = D, T, Q). *Theoretical Chemistry Accounts* **2012,** *131* (2).
131. Adamo, C.; Barone, V., Toward reliable density functional methods without adjustable parameters: The PBE0 model. *The Journal of Chemical Physics* **1999,** *110* (13), 6158-6170.
132. Mullen, D. J. E.; Nowacki, W., Refinement of the crystal structures of realgar, AsS and orpiment, As2S3*. *Zeitschrift für Kristallographie* **1972,** *136* (1-2), 48-65.

133. Finklea, S. L.; Cathey, L.; Amma, E. L., Investigation of the bonding mechanism in pyrite using the Mössbauer effect and X-ray crystallography. *Acta Crystallographica Section A* **1976,** *32* (4), 529-537.
134. Skinner, B. J., Unit-cell edges of natural and synthetic sphalerites*. *American Mineralogist* **1961,** *46* (11-12), 1399-1411.
135. Wang, L.-W.; Li, J., First-principles thousand-atom quantum dot calculations. *Physical Review B* **2004,** *69* (15).
136. Govind, N.; Lopata, K.; Rousseau, R.; Andersen, A.; Kowalski, K., Visible Light Absorption of N-Doped TiO2 Rutile Using (LR/RT)-TDDFT and Active Space EOMCCSD Calculations. *The Journal of Physical Chemistry Letters* **2011,** *2* (21), 2696-2701.
137. Wadt, W. R.; Hay, P. J., Ab initio effective core potentials for molecular calculations. Potentials for main group elements Na to Bi. *The Journal of Chemical Physics* **1985,** *82* (1), 284-298.
138. Hay, P. J.; Wadt, W. R., Ab initio effective core potentials for molecular calculations. Potentials for K to Au including the outermost core orbitals. *The Journal of Chemical Physics* **1985,** *82* (1), 299-310.
139. Dolg, M.; Wedig, U.; Stoll, H.; Preuss, H., Energy-adjustedabinitiopseudopotentials for the first row transition elements. *The Journal of Chemical Physics* **1987,** *86* (2), 866-872.
140. Martin, J. M. L.; Sundermann, A., Correlation consistent valence basis sets for use with the Stuttgart–Dresden–Bonn relativistic effective core potentials: The atoms Ga–Kr and In–Xe. *The Journal of Chemical Physics* **2001,** *114* (8), 3408-3420.
141. Bergner, A.; Dolg, M.; Küchle, W.; Stoll, H.; Preuß, H., Ab initio energy-adjusted pseudopotentials for elements of groups 13–17. *Molecular Physics* **2006,** *80* (6), 1431-1441.
142. Yarmoshenko, Y. M.; Cherkashenko, V. M.; Kurmaev, E. Z., The anisotropy of X-ray emission spectra for 2H-MoS2 single crystals. *Journal of Electron Spectroscopy and Related Phenomena* **1983,** *32* (2), 103-112.
143. Dräger, G.; Brümmer, O., Polarized X-Ray Emission Spectra of Single Crystals. *physica status solidi (b)* **1984,** *124* (1), 11-28.
144. Hayasi, Y.; Takahashi, T.; Asahina, H.; Sagawa, T.; Morita, A.; Shirotani, I., Electronic structure of black phosphorus studied by polarized soft-x-ray emission and absorption spectroscopy. *Physical Review B* **1984,** *30* (4), 1891-1895.
145. Kottmann, A.; Burgäzy, F.; Lam, D. J.; Fang, Y.; Lamparter, P.; Steeb, S., Partial densities of states with polarized oxygen Kα X-ray emission of YBa2Cu3O7−δ. *Physica C: Superconductivity* **1991,** *178* (1-3), 125-136.
146. Lindle, D. W.; Cowan, P. L.; Jach, T.; LaVilla, R. E.; Deslattes, R. D.; Perera, R. C. C., Polarized x-ray emission studies of methyl chloride and the chlorofluoromethanes. *Physical Review A* **1991,** *43* (5), 2353-2366.
147. Glatzel, P.; Bergmann, U., High resolution 1s core hole X-ray spectroscopy in 3d transition metal complexes—electronic and structural information. *Coordination Chemistry Reviews* **2005,** *249* (1-2), 65-95.
148. Hudson, E. A.; Allen, P. G.; Terminello, L. J.; Denecke, M. A.; Reich, T., Polarized x-ray-absorption spectroscopy of the uranyl ion: Comparison of experiment and theory. *Physical Review B* **1996,** *54* (1), 156-165.

149. Feng, Y.; Seidler, G. T.; Cross, J. O.; Macrander, A. T.; Rehr, J. J., Role of inversion symmetry and multipole effects in nonresonant x-ray Raman scattering from icosahedralB4C. *Physical Review B* **2004,** *69* (12).
150. Schülke, W., *Electron dynamics by inelastic X-ray scattering*. Oxford University Press: Oxford ; New York, 2007; p xiii, 591 p.
151. Spanget-Larsen, J.; Thulstrup, E. W., The electronic transitions of dibenzothiophene: linear dichroism spectroscopy and quantum chemical calculations. *Journal of Molecular Structure* **2003,** *661-662*, 603-610.
152. Nguyen, D. D.; Trunk, J.; Nakhimovsky, L.; Spanget-Larsen, J., Electronic transitions of fluorene, dibenzofuran, carbazole, and dibenzothiophene: From the onset of absorption to the ionization threshold. *Journal of Molecular Spectroscopy* **2010,** *264* (1), 19-25.
153. Schena, T.; Bihlmayer, G.; Blügel, S., First-principles studies of FeS2 using many-body perturbation theory in the G0W0 approximation. *Physical Review B* **2013,** *88* (23).

CHAPTER 11 VACUUM FORMED TEMPORARY SPHERICALLY AND TOROIDALLY BENT CRYSTAL ANALYZERS FOR X-RAY ABSORPTION AND X-RAY EMISSION SPECTROSCOPY

Originally published as: Jahrman, E. P.; Holden, W. M.; Ditter, A. S.; Kozimor, S. A.; Kihara, S. L.; Seidler, G. T. Vacuum Formed Temporary Spherically and Toroidally Bent Crystal Analyzers for X-Ray Absorption and x-Ray Emission Spectroscopy. *Review of Scientific Instruments* 2019, 90 (1), 013106. https://doi.org/10.1063/1.5057231.

I contributed to the design of spectrometer and temporary optics and led the effort to characterize the optics with x-ray camera measurements. Evan P. Jahrman and I contributed equally to this work.

We demonstrate that vacuum forming of 10-cm diameter silicon wafers of various crystallographic orientations under an x-ray permeable, flexible window can easily generate spherically bent crystal analyzers (SBCA) and toroidally bent crystal analyzers (TBCA) with ~1-eV energy resolution and a 1-m major radius of curvature. In applications at synchrotron light sources, x-ray free electron lasers, and laboratory spectrometers these characteristics are generally sufficient for many x-ray absorption fine structure (XAFS), x-ray emission spectroscopy (XES), and resonant inelastic x-ray scattering (RIXS) applications in the chemical sciences. Unlike existing optics manufacturing methods using epoxy or anodic bonding, vacuum forming without adhesive is temporary in the sense that the bent wafer can be removed when vacuum is released and exchanged for a different orientation wafer. Therefore, the combination of an x-ray

compatible vacuum-forming chamber, a library of thin wafers, and a small number of forms having different secondary curvatures can give extreme flexibility in spectrometer energy range. As proof of this method we determine the energy resolution and reflectivity for several such vacuum-formed bent crystal analyzers (VF-BCA) in laboratory-based XAFS and XES studies using a conventional x-ray tube. For completeness we also show x-ray images collected on the detector plane to characterize the resulting focal spots and optical aberrations.

11.1 INTRODUCTION

Doubly-curved Bragg optics see extensive use in advanced x-ray spectroscopies at x-ray free electron lasers, synchrotron x-ray light sources, laser plasma facilities, and laboratories performing in-house x-ray absorption fine structure (XAFS) and x-ray emission spectroscopy (XES). This has been made possible by a large body of work aimed at characterizing and evaluating the properties of doubly-curved optics.[1-7] These optics are available commercially; the traditional production methods use glue or anodic bonding to affix crystal wafers after pressing into precision glass or metallic substrates.[8-11] Other production techniques such as vacuum-bent analyzers[12, 13] and hot plastic deformation techniques[14] have also been explored. Another approach is to use a spherical bending apparatus that allows the curvature to be characterized before fixing to a permanent shape.[15]

Even with a variety of available production techniques, acquiring a large number of such optics for multi-analyzer systems can be challenging. Synchrotron endstations for XES, high energy resolution fluorescence detection (HERFD) of XAFS, or nonresonant inelastic x-ray scattering (NRIXS) now often use from five to as many as ~100 such optics.[16-23] In addition to cost issues, for XES there is a pragmatic issue: different synchrotron users may come with experiments requiring acquisition of an entirely new set of optics for some energy range that has

not previously been explored at that facility. The same issue arises with the increasing use of laboratory-based spectrometers,[24-32] where again the elements and energy ranges that are capable of being studied depend on the availability of analyzers having a variety of crystal cuts to achieve the necessary Bragg angles and energy resolutions. As an additional issue, using spherically bent crystal analyzers (SBCA's) in the Johann configuration,[33] the most common doubly-curved optics, in a Rowland circle spectrometer results in large spot sizes out of the Rowland plane when far from backscatter due to sagittal error. Toroidally bent crystal analyzers (TBCA's) are needed for a truer point-to-point focus, but are far less common and their secondary curvature must be tuned to match a chosen Bragg angle.

The purpose of this paper is to address the above concerns, at least for applications requiring only the 'modest' energy resolution of ~1-eV, such as is frequently sufficient in the chemical sciences.[34] Specifically, we demonstrate a simple method to make temporary SBCA's and TBCA's with good performance and very high ease of use. Unlike methods using epoxy or anodic bonding, vacuum forming without adhesive is temporary in the sense that the bent wafer can be removed when vacuum is released and exchanged for a different orientation wafer. While vacuum formed bent crystal analyzers have been utilized before in other applications, this work demonstrates the efficacy of these analyzers in x-ray absorption and emission spectroscopy. The combination of an x-ray compatible vacuum-forming chamber, a suitable library of thin single-crystal wafers, and a small number of forms having different secondary curvatures can give extreme flexibility in spectrometer or monochromator energy range at low cost and with great flexibility for addition of new energy ranges, as needed.

11.2 METHODS

The overall concept and resulting design of the vacuum-formed bent crystal analyzer (VF-BCA) is presented in Fig. 11.1. Front-view and section-view computer aided design (CAD) renderings are shown in Fig. 11.1(a) and (b), respectively. The key point is that an x-ray transparent, flexible polyimide window serves to seal the volume containing the wafer and the machined aluminum alloy or glass lens form from the outside atmosphere. When pumping on the VF-BCA, outside air pressure forces the polyimide window to collapse inward, pressing the wafer firmly onto the underlying form. A photograph of a VF-BCA is shown in Fig. 11.1(c), and for comparison, a commercial, anodically-bonded analyzer (XRS TECH LLC) is shown in Fig. 11.1(d).

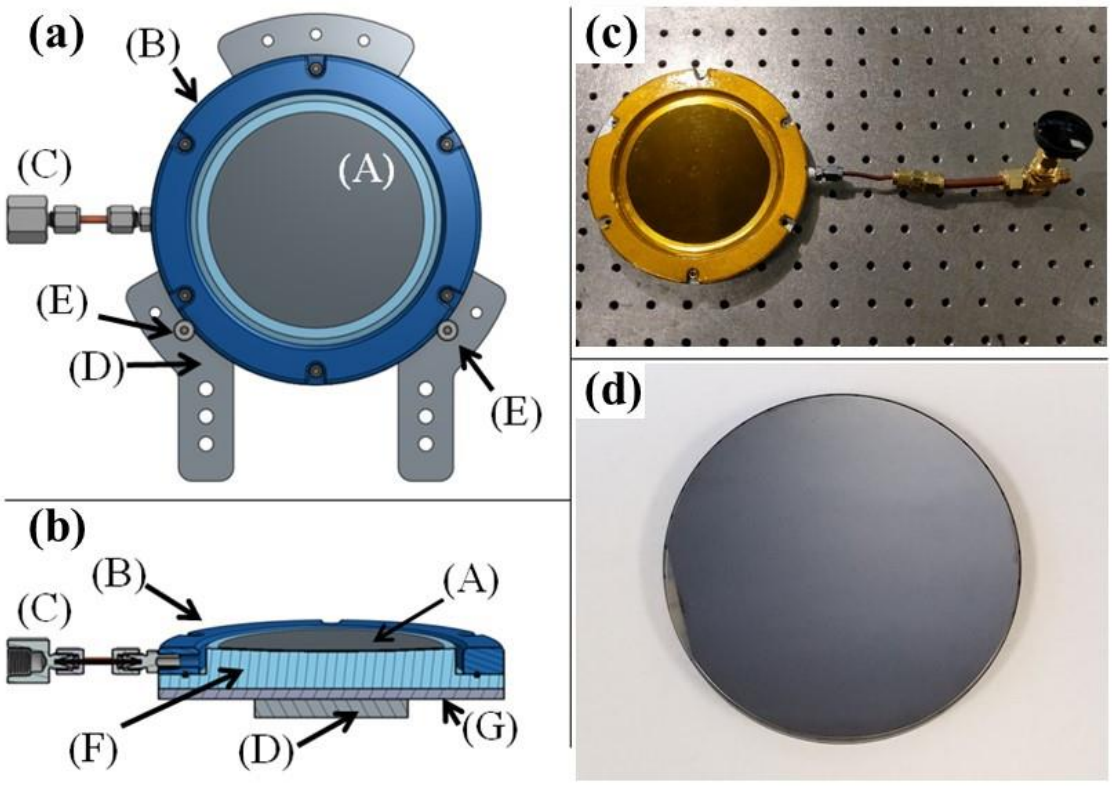

Figure 11.1: **(a)** CAD rendering front view of the vacuum formed bent crystal analyzer (VF-BCA). (A) bent wafer; (B) front flange with polyimide film (not shown); (C) pumping line; (D) aluminum

alloy vertical support plate; (E) support bolts to define the position of the outer diameter of the VF-BCA body. **(b)** CAD rendering section view of the VF-BCA. (F) CNC-machined vacuum form; (G) steel backing plate for magnetic mounting, where magnets (not shown) are attached alongside part (D). **(c)** Photograph of the VF-BCA, note the flexible orange polyimide film that allows air pressure to force the wafer into the shape of the form machined into part (F). A second, similar VF-BCA instead has a simple recess in part (F) to accept a 1-m radius of curvature concave glass lens. **(d)** Photograph of a commercial, anodically-bonded 10-cm diameter SBCA with 1-m radius of curvature.

Several different supporting forms were used, all with the 1-m major radius of curvature required by the laboratory spectrometer[28] that served as an extremely convenient testbed for this project. Table 1 defines the character of the different forms. The lens form was a plano-concave spherical lens made of BK7 glass from Esco Optics with 125 mm diameter, 1-meter ± 1% radius of curvature, and thickness 10 mm. When the forming contact surface was machined from aluminum 6061 alloy, a Mitsubishi M-V5Cn-L vertical machining center was used. The necessary cutting paths were generated under the target scallop deviation of 5 μm with a ball end mill having a ball-end radius of ~7.14 mm. The resulting surfaces were cleaned with solvents but otherwise not modified by, e.g., polishing or lapping.

Table 11.1: List of all bent crystal analyzers and analyzer forms used in this study.

Optic name	Major radius (cm)	Perpendicular radius (cm)	Vacuum form surface
SBCA	100.0	100.0	Wafer anodically bonded to glass
VF-BCA-1	100.0	100.0	Glass lens
VF-BCA-2	100.0	100.0	Al6061 spherical recess
VF-BCA-3	100.0	88.3	Al6061 torus, $\theta^* = 70°$

The wafers used in the VF-BCA were standard 10-cm diameter double side polished Si wafers of various orientations, all nominally 400-μm thick. Different crystal orientations yield different energy ranges over the useful Bragg angle range. A list of absorption edges or

fluorescence lines studied and the corresponding commercial SBCA or wafer used in a VF-BCA is given in Table 2.

Table 11.2: List of experiments performed, commercial SBCA or wafers used in the VF-BCA, and nominal Bragg angle for the absorption edge or fluorescence line from the indicated crystal reflection.

Study	Commercial SBCA	Wafer for VF-BCA	Bragg angle (°)
Ni XAFS	Si (551)	Si (711)	78.0
Ni XAFS	Si (444)	Si (444)	71.6
Cu Kα XES	Si (444)	Si (444)	79.3

The laboratory spectrometer used here[28] is a 1-m diameter Rowland circle spectrometer based on the approach of Seidler, et al.,[24] as modified for tilt-free alignment[35] and by the use of a higher-powered x-ray tube and longer translation stages to give a wider range in Bragg angle (θ_B). Across several instrument generations this overall approach using a conventional x-ray tube and a 'scissors' monochromator has been used in several studies with ~1-eV energy resolution for either transmission-mode XAFS or for XES.[25, 27, 30, 35-37] The present instrument and its performance have been described in detail by Jahrman, et al.[28]

Measurements were performed with a Varex VF-80 x-ray tube with a Pd-anode operating at 35 kV accelerating potential and 100 W total electron beam power. A silicon drift diode (Amptek X-123 SDD) with ~4.6-mm diameter active region was the final detector for all XAFS and XES scans. In Fig. 11.2 we show a schematic of the Rowland circle implementation for this spectrometer, a photograph of the spectrometer in an XAFS configuration, and a photograph of the VF-BCA installed at the optic location.

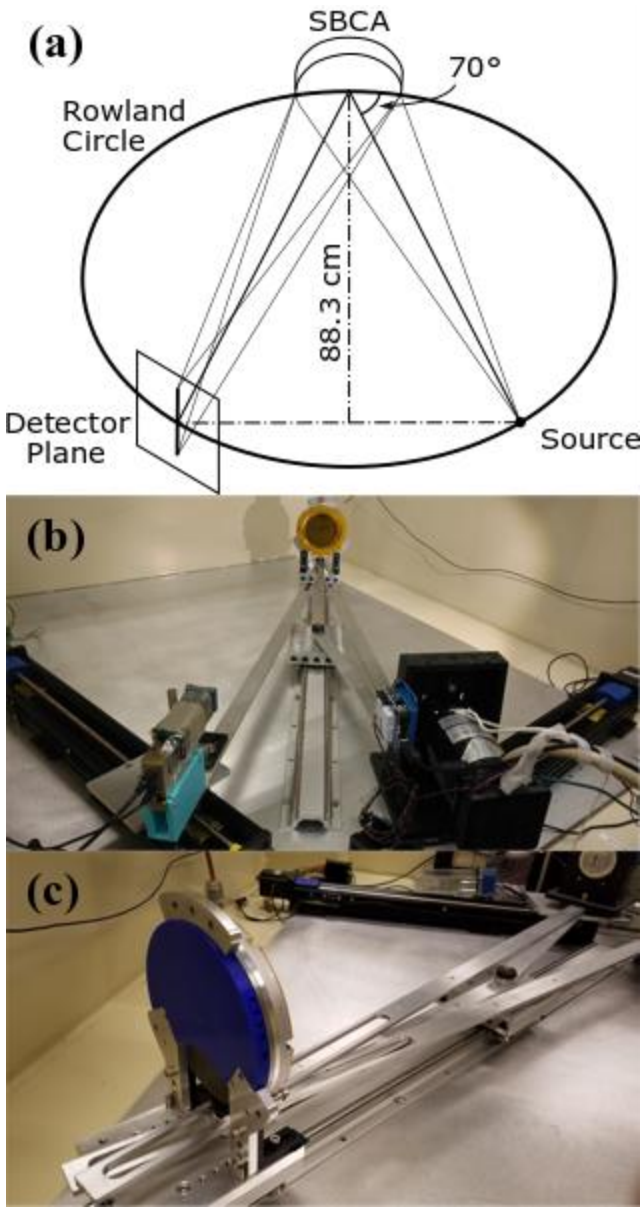

Figure 11.2: **(a)** The Rowland circle implementation for the laboratory spectrometer, shown for a 70° Bragg angle. Note the definition of the detector plane. Also note that perfect point-to-point focusing by the optic would require that its radius of curvature out of the Rowland plane be equal to the normal distance from the source-detector arc to the optic, i.e., the sagitta of the reflexive arc from the source point on the Rowland circle to the detector point, indicated as 88.3 cm on the diagram above. This motivates the use of toroidally curved forms, as discussed in the text. (**b**) Photograph of the laboratory spectrometer. **(c)** Photograph from the reverse side of a vacuum-formed bent crystal analyzer installed into the spectrometer. Note the presence of small magnets

inside visible channels of the plastic 3D-printed part coupled to the steel mounting plate (part (G) in Fig. 11.1) to hold the analyzer in location but allow easy rotation about the azimuthal angle.

Under the protocol for tilt-free alignment,[35] spherical analyzers are rotated about their circular symmetry axis until the wafer's miscut is in the Rowland plane. For a toroidal VF-BCA, the wafer orientation must be determined in a spherical VF-BCA prior to installation into the toroidal vacuum form holder with the miscut oriented in the Rowland plane, i.e., in the plane of the 1-m major radius of curvature. The use of magnets inside a plastic 3D-printed part (Fig. 11.2(c)) allows the VF-BCA to be magnetically mounted rather than mechanically affixed, making it particularly convenient to rotate about the necessary axis in the Rowland plane.

Imaging of the x-ray intensity on the detector plane was performed using a small home-built CMOS x-ray camera. This is an updated version[38] of an earlier camera[39] that has seen good use in a lower-energy XES instrument.[40-43] The camera has a 3.2×5.6 mm^2 field of view. It was mounted on a micrometer-driven vertical translation stage and manually repositioned to achieve mosaic coverage of the x-ray intensity's spatial distribution. Furthermore, the camera's ability to identify both the location and energy of individual x-ray photons allowed the rejection of stray fluorescence by energy-windowing.

Ray tracing software written in `Mathematica` was used to assess Johann error and beam spreading perpendicular to the Rowland plane due to sagittal error, i.e., the use of optics whose second radius of curvature is not equal to the perpendicular distance from the optic center to the line connecting the source and detector points on the Rowland circle (the sagitta). Unlike recent work aiming to give an advanced treatment of the interplay between strain effects and, e.g., dynamical diffraction in SBCAs,[44, 45] here we only seek purely geometric optics effects on slightly sub-mm length scales. Consequently, the Monte-Carlo ray tracing code generated x-rays from a

1-mm diameter source spot, reflected them from the bent optic using simple, specular Bragg reflection assuming zero wafer miscut, and then recorded the position of the intersection of those rays with the detector plane.

Transmission-mode XAFS measurements were performed on a 6-μm thick Ni foil from EXAFS Materials. XES measurements were performed on a 75-μm thick sheet of commercial Cu foil. All measurements were performed with the sample in air under ambient conditions, and a helium flight path space was used to reduce air-absorption. In some cases, small corrections for slow leaks in the helium space have been made to ensure that all comparisons are on a common efficiency basis. All XAFS spectra were dead time corrected and subsequently processed in Athena where standard background removal and normalization procedures were followed.[46] For XES, all spectra are dead time corrected and approximately aligned to a common energy scale.

11.3 RESULTS

Optic performance encompasses both its focal properties, as this is crucial for coupling to the final detector, and also its energy resolution. We begin with focal properties. In Fig. 11.3 we present the x-ray intensity in the detector plane for the commercial, anodically bonded Si (551) SBCA and for a Si (711) wafer in VF-BCA-1, VF-BCA-2, and VF-BCA-3 (see Table 1 for the definitions of these terms). Note that these two crystal orientations have the same *d*-spacing, and consequently are identical for present purposes, giving the same energy range over the same span of Bragg angles. The qualitative agreement is very good. All optics show strong in-Rowland-plane focusing and also the expected degree of out-of-Rowland-plane focusing subject to sagittal distortion. VF-BCA-2 and VF-BCA-3, which are based on machined, unpolished metal forms,

have slightly inferior focal properties. As discussed below, precision polishing of machined surfaces is an obvious future direction for improvement.

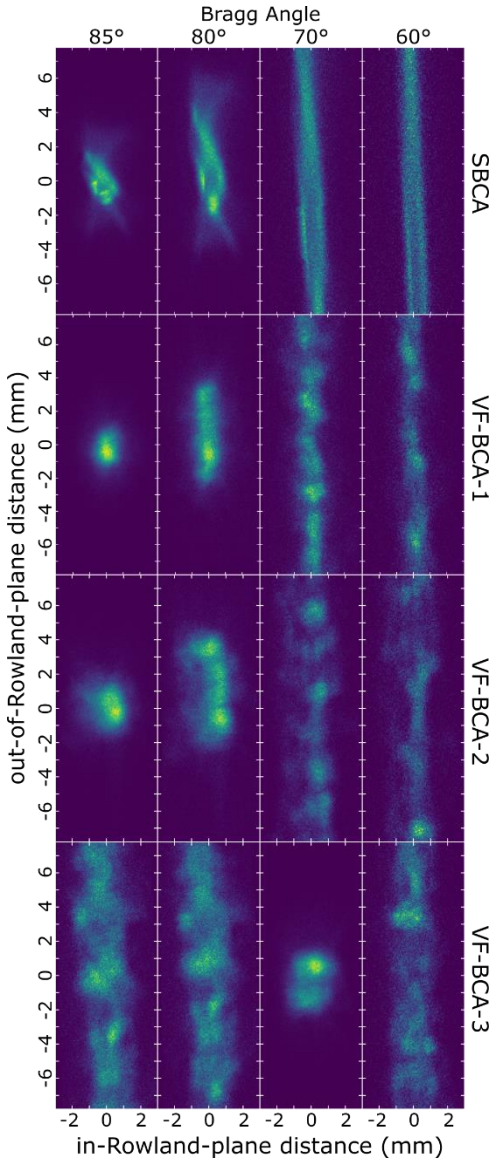

Figure 11.3: Characterization of the spatial distribution of x-ray intensity on the detector plane from **(top)** a commercial Si (551) analyzer (SBCA); **(second from top)** VF-BCA-1 with a Si (711) wafer and **(second from bottom)** VF-BCA-2 with a Si (711) wafer; **(bottom)** VF-BCA-3 with a Si (711) wafer, a torus optimized for $\theta_B = 70°$. The orientations are defined relative to the plane of the Rowland focusing circle. The colorscale of each frame is independently normalized; for a comparison of intensities, see Fig. 11.4.

In Fig. 11.4(a), we show the in-Rowland-plane intensity spread across the detector plane at different Bragg angles for each of the above optics and a Si (711) or equivalent wafer. Although the in-plane focal qualities of SBCA and VF-BCA-1 are similar, the profile of VF-BCA-2 is found to be broader and skewed. The out-of-Rowland-plane intensity spread is shown in Fig. 11.4(b). Near backscatter, the out-of-plane focal quality of both VF-BCA-1 and VF-BCA-2 is found to be comparable to the SBCA. At lower values of θ_B, VF-BCA-1 and VF-BCA-2 demonstrate clear inhomogeneities, although the total refocused intensity remains comparable.

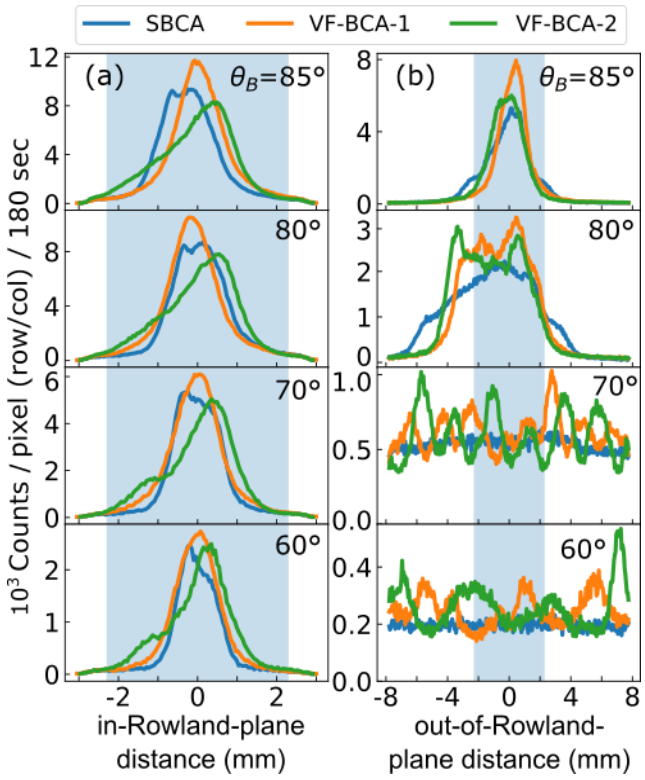

Figure 11.4: (a) Comparison of beam profiles in the Rowland plane for different optics. **(b)** Comparison of beam profiles in the direction perpendicular to the Rowland plane for different optics. The extent of the silicon SDD's active region is represented by the shaded regions.

For the out-of-plane focal quality, it is clear that the use of a SBCA sufficiently far away from backscatter ($\theta_B = 90$ deg) results in rapid spreading of the beam in the out-of-plane direction as expected from sagittal error. In this configuration, the out-of-Rowland-plane spread of the beam

exceeds the height of the detector's active area, as shown in Fig. 11.4(b). This raises the question of using toroidal optics where the primary radius of curvature is dictated by the Rowland circle diameter but where the secondary radius of curvature is chosen for ideal point-to-point focusing for a selected 'design' Bragg angle θ^*. For the Johann geometry, with a Rowland circle of radius D, the secondary radius of curvature R^* is given by $R^* = D \sin^2 \theta_B$. Ray-tracing calculations for the out-of-plane beam height as a function of θ_B are shown in Fig. 11.5(a) for TBCA's having design θ^* varying from 55 to 90°, the lattermost being simply an SBCA. These simulations strongly suggest the TBCA should give a more efficient coupling to the finite-sized detector when the secondary radius of the TBCA is chosen to eliminate sagittal error for θ^* in the middle of the angular range dictated by the energies of interest. Consequently, in the bottom panel of Fig. 11.3 we show the intensity distributions on the detector plane for VF-BCA-3 with a Si (711) wafer. The out-of-plane focal properties of the TBCA are clearly much superior to the SBCA when θ_B is in the vicinity of the designed θ^*.

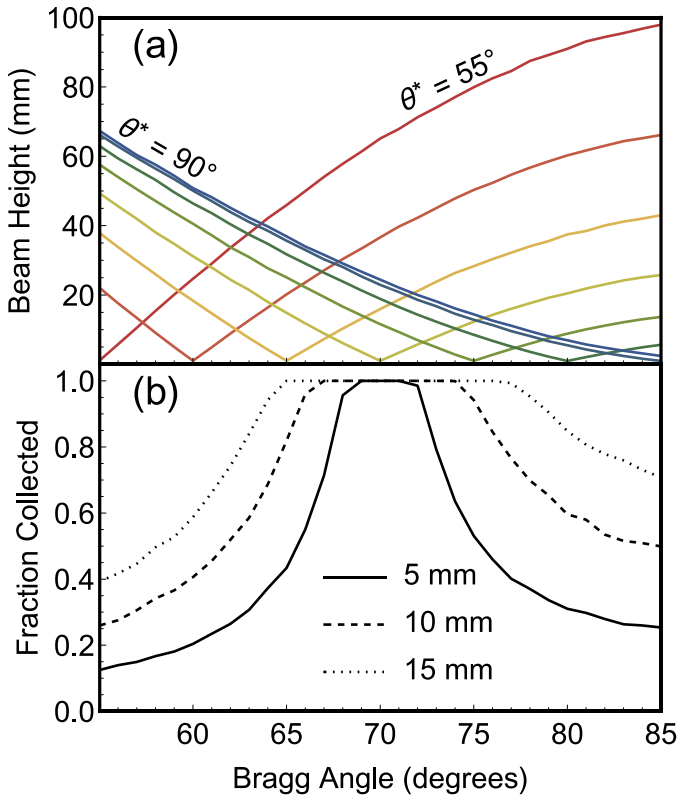

Figure 11.5: **(a)** The modeled beam height as a function of θ_B for doubly-curved optics with a 1-m principal radius of curvature but with secondary curvatures designed for point-to-point focus as design Bragg angles θ^* varying in 5° steps from 55° to 90°, the latter being for a fully spherical analyzer. **(b)** For a $\theta^* = 70°$ toroidal optic, the modeled fraction of x-rays hitting three different circular detectors with diameters of 5 mm, 10 mm, and 15 mm.

The improved spectrometer performance when using a TBCA at θ_B near the designed θ^* is demonstrated in Fig. 11.6. Here, the intensity of x-rays refocused at the SDD by each optic is shown across the full angular range of the instrument. The very short detectors used in the test studies (~4.6-mm active height) gives an especially high sensitivity to out-of-Rowland-plane beam spread, resulting in the narrow experimental Bragg angle range for optimum performance of the TBCA. Ray tracing calculations for TBCA simulating different detector heights are given in Fig. 11.5(b). In each case, there is an optimal, flat-top region of Bragg angles where all of the reflected x-rays are collected by the detector when the height of the reflected beam is smaller than the

detector diameter. This agrees well with the experimental data of Fig. 11.6, which shows the same flat top near the θ^*, and a decrease in count rate far from θ^*. Further, the ray tracing demonstrates the utility of a larger detector which increases both the width of the flat-top region as well as the count rate when θ_B is far from θ^*.

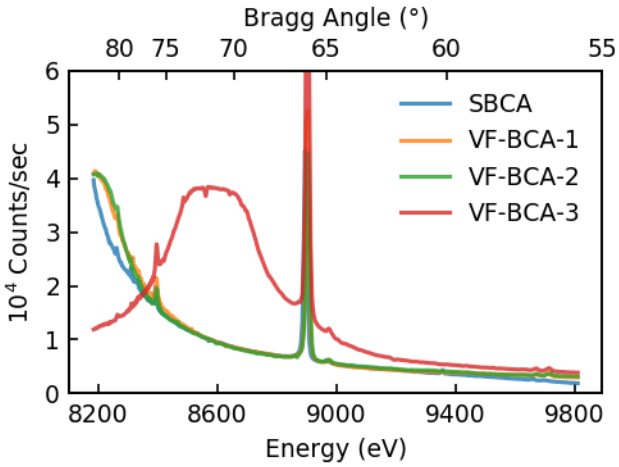

Figure 11.6: Monochromator count rate as a function of photon energy using a Si (551) or equivalent wafer. The sharp features are fluorescence lines, such as the Cu Kβ lines at ~8900 eV coming from the anode heatsink of the x-ray tube. The rapid roll-off for the spherical optics is due to the steadily increasing out-of-plane spread upon decreasing Bragg angle, causing the beam to become taller than the 4-mm active height of the SDD. The toroidal optic shows much improved performance in the designed Bragg angle range.

The preceding discussion has only addressed focal properties. Now we report on the energy resolution using the vacuum clamped optics. The measured Ni K-edge XANES for all optics using a Si (551) or equivalent wafer are shown in Fig. 11.7(a). It can be seen that all optics produced nearly identical spectra, suggesting a negligible loss in energy resolution from the commercial to vacuum clamped optics. The high quality of the XANES spectra is typical of modern laboratory based XAFS systems.[24, 25, 28, 47, 48] Indeed, Fig. 11.8 compares the energy resolution of the current measurements to literature results acquired at a synchrotron and confirms

the present energy resolution provided by the commercial and temporary optics to be satisfactory for chemical analysis. We show that an 0.8 eV broadening of the nominally 1.2-eV resolution synchrotron data removes the small differences between the two spectra; assuming Gaussian response functions as a matter of convenience, this suggests a spectrometer energy resolution of ~1.4 eV. Calculation of the geometrical broadening in the manner of Bergmann and Cramer,[49] this suggests our commercial optic possesses an energy resolution of ~0.4 eV, in fair agreement with the results of Hämäläinen et al.[50, 51] and Rovezzi et al.[9] Similarly, Fig. 11.7(b) presents again Ni K-edge XANES where the spectra are instead measured with the Si (444) reflection by several different optics. Again, spectra are nearly identical, with only minor differences observable in the extent of the shoulder at ~8334 eV and in the magnitude of the oscillation at ~8352 eV.

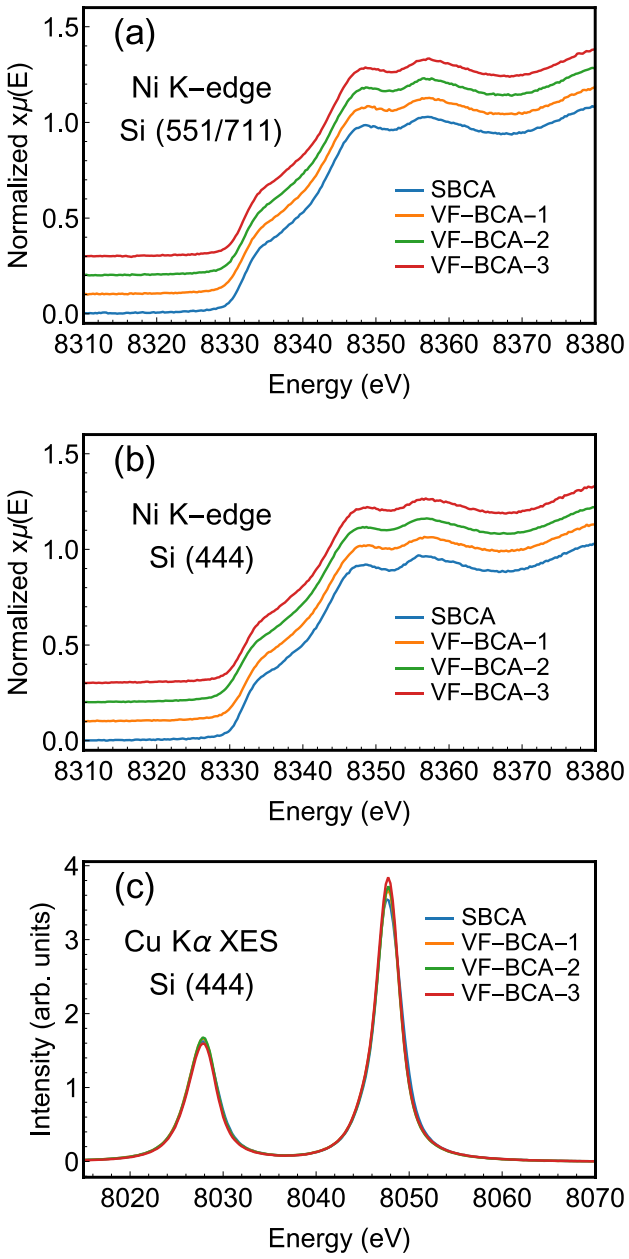

Figure 11.7: Representative spectra demonstrating the capability of the vacuum-clamped optics to perform high-resolution measurements. **(a)** Comparison of Ni XANES measured with each optic using Si (551) or equivalent wafers. **(b)** Comparison of Ni XANES measured with each optic using Si (444) wafers. **(c)** Comparison of Cu Kα XES with each optic using Si (444) wafers.

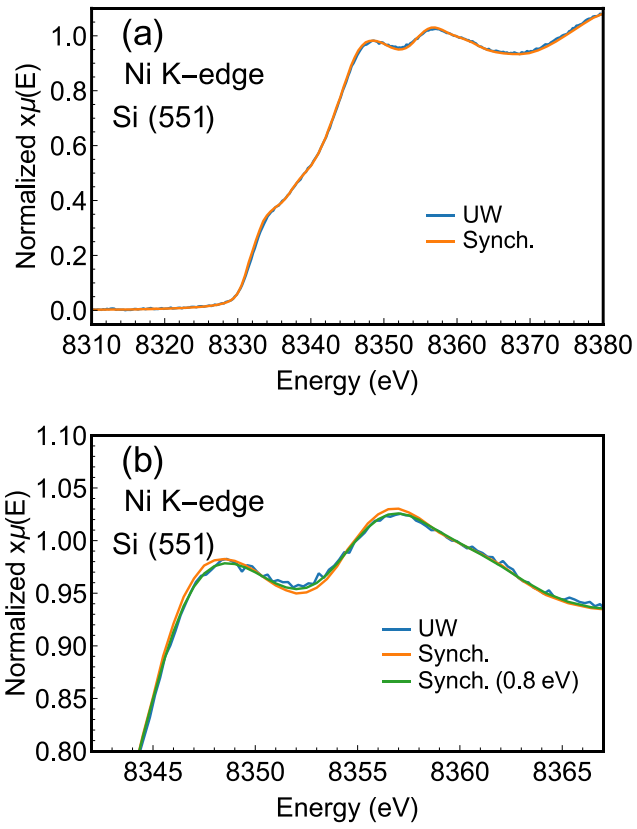

Figure 11.8: Spectra demonstrating the energy resolution achievable in the instrument given a commercial optic. **(a)** Ni XANES measured with the Si (551) SBCA (UW) and at the synchrotron (Synch.) as referenced in Hephaestus.[46] **(b)** Comparison of a small region of the Ni XANES shown in (a) along with a spectrum representing the literature results after convolution with a 0.8 eV Gaussian in Athena.[46]

In Fig. 11.7(c), Cu Kα XES results are presented for all optics using the Si (444) reflection. Here again, spectra were found to be nearly identical, however some small differences in peak ratios can be observed in accordance with small differences in energy resolution and also small differences in the angular response functions between optics. Recall again that the analyzed radiation is being imperfectly focused in the out-of-Rowland-plane dimension, with a spread larger than the detector height. Consequently, small changes in spectrometer alignment can lead to few-percent differences in net monochromator efficiency as a function of energy.

Given the success and limitations shown in this effort to make temporary doubly-bent crystal analyzers, there are several future directions that merit comment. First, the focal quality of optics should be improved by lapping and polishing the surfaces of the machined forms, or by acquiring precision surface-ground glass forms for the toroidal case, in analogy to the high-quality lens used for the spherical case. While this is not particularly relevant for the ~1-eV resolution needed for many measurements in a point-to-point Rowland circle configuration, the same would not be true for higher-energy resolution applications or the important case of dispersive spectrometers based on spherical analyzers, as is commonly used at synchrotron light sources.[52-54] Second, the efficiency of each optic across wider angular ranges of the instrument could be improved by implementing a taller detector. Third, it would be interesting to explore forms with smaller primary radii of curvature or using wafers composed of crystalline materials besides silicon, each with the goal of obtaining higher signal levels. Fourth, although we have only used this method for intact round wafers, one should expect that the same apparatus can be used for segmented wafers, such as is used in the recent development of 0.5-m radius of curvature SBCAs,[9] or for pieces of multiple wafers integrated to obtain a larger BCA solid angle than could be obtained with any single wafer. This lattermost opportunity is likely relevant for materials where the *de facto* standard 10-cm diameter wafers are not available.

11.4 Conclusions

We report the development and performance of spherically and toroidally bent crystal analyzers for use in x-ray absorption and x-ray emission spectroscopies. Unlike the present practice of gluing or bonding the necessary crystalline wafers to a high-precision glass lens, we instead use only air pressure to hold the wafer against the shaping form that provides the necessary profile. The specifications for the shaping form are found to be rather modest, in that modern

machined metal forms suffice and high-precision, high-cost surface ground lenses are not needed. The resulting optics demonstrate resolutions and efficiencies comparable to their commercially available counterparts as determined by XANES and XES measurements using a laboratory spectrometer. These results establish a considerable convenience, simplicity, and flexibility that may prove useful for Rowland circle spectrometers in the lab for XAFS and XES studies, as well as at synchrotron and x-ray free electron laser x-ray facilities for XES, HERFD, and RIXS.

11.5 Acknowledgements

We thank P. Eng for useful discussions during our earliest attempts to vacuum form x-ray optics, and we note that C. Henriquet and C. Shale have been independently pursuing a similar approach at the European Synchrotron Radiation Facility (private communication). E. Jahrman was supported in part by the Joint Center for Energy Storage Research (JCESR), an Energy Innovation Hub funded by the U.S. Department of Energy, Office of Science, and Basic Energy Sciences, and by the U.S. Department of Energy through the Chemical Science and Engineering Division of Argonne National Laboratory. W. Holden and G. Seidler were supported by the Joint Plasma Physics Program of the National Science Foundation and the Department of Energy under Grant No. DE-SC0016251. R&D associated with the Los Alamos National Laboratory (LANL) spectrometer was funded under the Heavy Element Chemistry Program by the Division of Chemical Sciences, Geosciences, and Biosciences, Office of Basic Energy Sciences, U.S. Department of Energy and the U.S. Department of Energy. LANL is operated by Los Alamos National Security, LLC, for the National Nuclear Security Administration of the U.S. Department of Energy (contract DE-AC52-06NA25396).

11.6 REFERENCES

1. D. B. Wittry and S. Sun, J Appl Phys **71** (2), 564-568 (1992).
2. D. B. Wittry and S. Sun, J Appl Phys **69** (7), 3886-3892 (1991).
3. D. B. Wittry and S. Sun, J Appl Phys **67** (4), 1633-1638 (1990).
4. D. B. Wittry and S. Sun, J Appl Phys **68** (2), 387-391 (1990).
5. D. B. Wittry and W. Z. Chang, J Appl Phys **72** (8), 3440-3446 (1992).
6. A. Hauer, J. D. Kilkenny and O. L. Landen, Review of Scientific Instruments **56** (5), 803-805 (1985).
7. G. Askari Germi, S. J. Pestehe and A. Rastkar Ebrahimzadeh, Journal of Applied Crystallography **50** (4), 1104-1116 (2017).
8. R. Verbeni, M. Kocsis, S. Huotari, M. Krisch, G. Monaco, F. Sette and G. Vanko, Journal of Physics and Chemistry of Solids **66** (12), 2299-2305 (2005).
9. M. Rovezzi, C. Lapras, A. Manceau, P. Glatzel and R. Verbeni, Review of Scientific Instruments **88** (1), 013108 (2017).
10. M. Krämer, K. Kuzushita, S. Maeo, T. Utaka and K. Taniguchi, Spectrochimica Acta Part B: Atomic Spectroscopy **63** (12), 1408-1414 (2008).
11. E. Collart, A. Shukla, F. Gelebart, M. Morand, C. Malgrange, N. Bardou, A. Madouri and J.-L. Pelouard, Journal of Synchrotron Radiation **12** (4), 473-478 (2005).
12. P. Suortti, T. Buslaps, V. Honkimäki, N. Hiraoka and U. Lienert, Zeitschrift für Physikalische Chemie **220** (7), 831-847 (2006).
13. J. A. Maj and C. Harmata, United States Patent No. 20120256332 (2012).
14. H. Okuda, K. Nakajima, K. Fujiwara, K. Morishita and S. Ochiai, Journal of Applied Crystallography **41** (4), 798-799 (2008).
15. A. H. Said, H. Sinn and R. Divan, Journal of Synchrotron Radiation **18** (3), 492-496 (2011).
16. S. Huotari, C. J. Sahle, C. Henriquet, A. Al-Zein, K. Martel, L. Simonelli, R. Verbeni, H. Gonzalez, M. C. Lagier, C. Ponchut, M. M. Sala, M. Krisch and G. Monaco, J. Synchrot. Radiat. **24**, 521-530 (2017).
17. R. Verbeni, T. Pylkkanen, S. Huotari, L. Simonelli, G. Vanko, K. Martel, C. Henriquet and G. Monaco, J. Synchrot. Radiat. **16**, 469-476 (2009).
18. T. T. Fister, G. T. Seidler, L. Wharton, A. R. Battle, T. B. Ellis, J. O. Cross, A. T. Macrander, W. T. Elam, T. A. Tyson and Q. Qian, Rev. Sci. Instrum. **77** (6), 063901 (2006).
19. D. Sokaras, D. Nordlund, T. C. Weng, R. A. Mori, P. Velikov, D. Wenger, A. Garachtchenko, M. George, V. Borzenets, B. Johnson, Q. Qian, T. Rabedeau and U. Bergmann, Rev. Sci. Instrum. **83** (4), 043112 (2012).
20. D. Sokaras, T. C. Weng, D. Nordlund, R. Alonso-Mori, P. Velikov, D. Wenger, A. Garachtchenko, M. George, V. Borzenets, B. Johnson, T. Rabedeau and U. Bergmann, Rev. Sci. Instrum. **84** (5), 053102 (2013).
21. I. Llorens, E. Lahera, W. Delnet, O. Proux, A. Braillard, J. L. Hazemann, A. Prat, D. Testemale, Q. Dermigny, F. Gelebart, M. Morand, A. Shukla, N. Bardou, O. Ulrich, S. Arnaud, J. F. Berar, N. Boudet, B. Caillot, P. Chaurand, J. Rose, E. Doelsch, P. Martin and P. L. Solari, Rev. Sci. Instrum. **83** (6), 063104 (2012).
22. M. M. Sala, K. Martel, C. Henriquet, A. Al Zein, L. Simonelli, C. J. Sahle, H. Gonzalez, M. C. Lagier, C. Ponchut, S. Huotari, R. Verbeni, M. Krisch and G. Monaco, J. Synchrot. Radiat. **25**, 580-591 (2018).

23. E. Kleymenov, J. A. van Bokhoven, C. David, P. Glatzel, M. Janousch, R. Alonso-Mori, M. Studer, M. Willimann, A. Bergamaschi, B. Henrich and M. Nachtegaal, Rev. Sci. Instrum. **82** (6), 065107 (2011).
24. G. T. Seidler, D. R. Mortensen, A. J. Remesnik, J. I. Pacold, N. A. Ball, N. Barry, M. Styczinski and O. R. Hoidn, Review of Scientific Instruments **85** (11), 113906 (2014).
25. G. T. Seidler, D. R. Mortensen, A. S. Ditter, N. A. Ball and A. J. Remesnik, Journal of Physics: Conference Series **712** (1), 012015 (2016).
26. D. R. Mortensen, G. T. Seidler, J. J. Kas, N. Govind, C. P. Schwartz, S. Pemmaraju and D. G. Prendergast, Physical Review B **96** (12), 125136 (2017).
27. D. R. Mortensen, G. T. Seidler, A. S. Ditter and P. Glatzel, Journal of Physics: Conference Series **712** (1), 012036 (2016).
28. E. P. Jahrman, W. M. Holden, A. S. Ditter, D. R. Mortensen, G. T. Seidler, T. T. Fister, S. A. Kozimor, L. F. J. Piper, J. Rana, N. C. Hyatt and M. C. Stennett, Review of Scientific Instruments **Submitted** (2018).
29. W. M. Holden, O. R. Hoidn, A. S. Ditter, G. T. Seidler, J. Kas, J. L. Stein, B. M. Cossairt, S. A. Kozimor, J. Guo, Y. Ye, M. A. Marcus and S. Fakra, Review of Scientific Instruments **88** (7), 073904 (2017).
30. R. A. Valenza, E. P. Jahrman, J. J. Kas and G. T. Seidler, Phys Rev A **96** (3), 032504 (2017).
31. M. E. Mundy, D. Ung, N. L. Lai, E. P. Jahrman, G. T. Seidler and B. M. Cossairt, Chem Mater **30** (15), 5373-5379 (2018).
32. W. M. Holden, G. T. Seidler and S. Cheah, The Journal of Physical Chemistry A **122** (23), 5153-5161 (2018).
33. H. H. Johann, Z Phys **69** (3-4), 185-206 (1931).
34. P. Glatzel and U. Bergmann, Coordin Chem Rev **249** (1-2), 65-95 (2005).
35. D. R. Mortensen and G. T. Seidler, J Electron Spec **215**, 8-15 (2017).
36. M. E. Mundy, D. Ung, N. L. Lai, E. P. Jahrman, G. T. Seidler and B. M. Cossairt, Chem Mater (2018).
37. E. P. Jahrman, G. T. Seidler and J. R. Sieber, Analytical Chemistry **90** (11), 6587-6593 (2018).
38. W. M. Holden, O. R. Hoidn, G. T. Seidler and A. D. DiChiara, Review of Scientific Instruments **89** (9), 093111 (2018).
39. O. R. Hoidn and G. T. Seidler, Review of Scientific Instruments **86** (8), 086107 (2015).
40. W. M. Holden, O. R. Hoidn, A. A. Ditter, G. T. Seidler, J. Kas, J. Stein, C. B.M., S. A. Kozimor, J. Guo, Y. Ye, M. A. Marcus and S. Fakra, Rev. Sci. Instrum. **88** (7), 073904 (2017).
41. W. M. Holden, G. T. Seidler and S. Cheah, Journal of Physical Chemistry A **122** (23), 5153-5161 (2018).
42. J. L. Stein, W. M. Holden, A. Venkatesh, M. E. Mundy, A. J. Rossini, G. T. Seidler and B. M. Cossairt, Chem Mater (2018).
43. B. M. Cossairt, J. L. Stein, W. M. Holden and G. T. Seidler, SID Symposium Digest of Technical Papers **49** (1), 21-24 (2018).
44. A.-P. Honkanen, C. Ferrero, J.-P. Guigay and V. Mocella, Journal of Applied Crystallography **51** (2), 514-525 (2018).
45. A.-P. Honkanen, G. Monaco and S. Huotari, Journal of Applied Crystallography **49** (4), 1284-1289 (2016).

46. B. Ravel and M. Newville, Journal of Synchrotron Radiation **12** (4), 537-541 (2005).
47. R. Bès, T. Ahopelto, A. P. Honkanen, S. Huotari, G. Leinders, J. Pakarinen and K. Kvashnina, Journal of Nuclear Materials **507**, 50-53 (2018).
48. Z. Németh, J. Szlachetko, É. G. Bajnóczi and G. Vankó, Review of Scientific Instruments **87** (10), 103105 (2016).
49. U. Bergmann and S. P. Cramer, presented at the SPIE's International Symposium on Optical Science, Engineering, and Instrumentation, 1998 (unpublished).
50. K. Hämäläinen, C. C. Kao, J. B. Hastings, D. P. Siddons, L. E. Berman, V. Stojanoff and S. P. Cramer, Physical Review B **46** (21), 14274-14277 (1992).
51. K. Hämäläinen, D. P. Siddons, J. B. Hastings and L. E. Berman, Phys Rev Lett **67** (20), 2850-2853 (1991).
52. S. Huotari, T. Pylkkänen, R. Verbeni, G. Monaco and K. Hämäläinen, Nature Materials **10**, 489 (2011).
53. S. Huotari, F. Albergamo, G. Vankó, R. Verbeni and G. Monaco, Review of Scientific Instruments **77** (5), 053102 (2006).
54. S. Huotari, G. Vankó, F. Albergamo, C. Ponchut, H. Graafsma, C. Henriquet, R. Verbeni and G. Monaco, Journal of Synchrotron Radiation **12** (4), 467-472 (2005).